# *Synthesis of Naturally Inspired Conjugated Materials for Organic Electronics*

by

Kealan J. Fallon

M.Sci., University College London, 2013

A thesis submitted for the degree of
Doctor of Philosophy
in the subject of
Chemistry

at

University College London

November 2017

# *Declaration*

I, Kealan Jared Fallon, confirm that the work presented in this thesis is my own, carried out at the Department of Chemistry, University College London between September 2013 – July 2017 under the supervision of Dr Hugo Bronstein. Where information is derived from other sources, I confirm that this has been indicated clearly as such. Where work is presented that is the efforts of collaborators, credit is given clearly in the *Contributions* section in the preface of this thesis.

Kealan J. Fallon

November 2017

# *Abstract*

The development of indolonaphthyridine as a building block for organic electronics was investigated. Firstly, indolonaphthyridine was polymerised with a series of simple co-monomers affording semiconductors with narrow optical band gaps absorbing in the near-IR. The materials exhibited high performance charge transport in organic field-effect transistors (OFETs) and high power conversion efficiencies in organic photovoltaics (OPVs). The observed electron transport were some of the highest achieved in the field to date. Theoretical analysis revealed that the high charge transport properties arose from the high degrees of backbone planarity as a result of low degrees of rotational freedom between the indolonaphthyridine and the neighbouring thiophene moieties.

A series of analogous polymers but with branching-point-extended alkyl chains was then investigated. It was found that the charge transport properties were both positively and negatively affected in the series. X-ray studies confirmed that the extended alkyl chains did permit closer interfacial interactions due to the decrease in d-spacing in the (010) plane.

The concept of cross-conjugation was then explored as a strategy to produce wider band gap indolonaphthyridine polymers. It was found that cross-conjugation was a successful method for widening the optical gap and theoretical analysis revealed a LUMO delocalised along the polymer backbone. Testing in OFETs revealed the materials facilitated n-type transport, the first examples of n-type cross-conjugated organic polymers in the field to date.

Finally, the low triplet energies of indolonaphthyridine was investigated in small molecules for their potential to undergo singlet fission. Several family of compounds were screened computationally and the best candidates synthesised. Electronic paramagnetic resonance (EPR) was performed on the samples and showed strong evidence for singlet fission in indolonaphthyridine thiophenes compounds, which exhibited high degrees of tunability and chemical stability, in stark contrast to the linear acenes which dominate the field.

# *Table of Contents*

# *Contributions*

As a synthetic organic chemist, the work herein would be incomplete without the collaboration, expertise and hard work of many device chemists and physicists.

- **Organic field-effect transistors** were fabricated at Imperial College London in Professor Thomas Anthopoulos' group by Nilushi Wijeyasinghe.
- **Organic solar cells** were fabricated at Imperial College London in Professor Ian McCulloch's group by Dr Raja S. Ashraf.
- **Grazing incidence wide-angle x-ray spectroscopy** was performed at Northwestern University, Chicago, USA, in Professor Tobin J. Marks' group by Eric F. Manley.
- **Atomic-force microscopy** reported in Chapter 2 was performed at Imperial College London in Professor Thomas Anthopoulos' group by Nilushi Wijeyasinghe. The reports in Chapter 3 were performed at University College London, in the Bronstein group by Niall Goodeal
- **Photoelectron spectroscopy in air** was performed at SPERC, KAUST, King Abdullah University of Science and Technology, Saudi Arabia, in Professor Ian McCulloch's group by Dr Warren Duffy.
- **Electron paramagnetic resonance spectroscopy** was performed at University College London, in Professor Chris Kay's group by Dr Enrico Salvadori.
- **Transient absorption spectroscopy** was performed by Dr Tracey Clarke at University College London.
- The computational chemistry presented in Chapter 2 was performed in collaboration with Jarvist M. Frost, Anne A. Y. Guilbert and Jenny Nelson, whose support was greatly appreciated. All computational calculations discussed were performed by Kealan J. Fallon, with their guidance.
- The dibrominated DPP monomer used in Chapter 4 was synthesised by Anastasia Leventis from the Bronstein Group.

# *Acknowledgements*

Firstly and foremost, I would like to thank Dr Hugo Bronstein for giving me the opportunity to undertake this research in his group – I could never have imagined working with a more supportive and considerate supervisor. Secondly, I must thank David, without whom the last four years would have been considerably duller. To the same effect, I daren't dream how I would have managed the last four years if it wasn't for an army of friends who brightened every day. It'd be too long to thank them all individually so I'll just thank them here in one big list: Anastasia, Alex F, Niall, Lisa, Oli, Alex G, Notina, Annikki, Bowen, Tom, James, Helen, James, Mike, Caroline, Meghan, Sarah, Charlie, Lizzy and Betsy.

I would also like to thank all the students and staff at UCL and other institutions who have helped me carry out this research – Nilushi, Eric, Enrico, Stoichko, Raja and Warren, without whom I'd never have discovered how interesting the materials I made were.

I cannot express in words my thanks to my family, and my friends who I consider family. To Linda & Damien for all their love, support and encouragement. To Aidan & Alice, the best brother and sister-in-law I could ask for. To Steph and Felicity, whose friendships I will treasure forever. To Neil and Adam, my longest friends.

As if doing a Ph.D. wasn't hard enough, having to experience your sibling undergo a sudden and unexpected heart transplant during it was one of the most challenging events of my life. To everyone who supported and upheld me during that turbulent time, you have my eternal gratitude and unreserved thanks and love.

And finally, this entire thesis is dedicated to my husband Gareth. Starting my Ph.D. single and finishing it married to the most caring, loving person I have ever met, is truly my greatest blessing.

# *Publications*

The following publications have arisen from the work described in Chapter 2 and can be found in *Appendices I & II*:

*I* **Fallon K. J.**, Wijeyasinghe N., Yaacobi-Gross N., Ashraf R. S., Freeman D. M. E., Palgrave R. G., Al-Hashimi M., Marks T. J., McCulloch I., Anthopoulos T. D., Bronstein H. "A Nature-Inspired Conjugated Polymer for High Performance Transistors and Solar Cells" *Macromolecules*, **2015**, 48, (15), 5148–5154

*II* **Fallon K. J.**, Wijeyasinghe N., Manley E. F., Dimitrov S. D., Yousaf S. A., Ashraf R. S., Duffy W., Guilbert A. A. Y., Freeman D. M. E., Al-Hashimi M., Nelson J., Durrant J. R., Chen L. X., McCulloch I., Marks T. J., Clarke T., Anthopoulos T. D., Bronstein H. "Indolo-naphthyridine-6,13-dione thiophene (INDT) building block for conjugated polymer electronics: Molecular origin of ultra-high n-type mobility" *Chem. Mater.*, **2016**, 28, (22), 8366–8378

The following publication is derived from the work described in Chapter 3 and can be found in *Appendix III*:

*III* **Fallon K. J.**, Santala A., Wijeyasinghe N., Manley E. F., Goodeal N., Leventis A., Freeman D. M. E., Al-Hashimi M., Chen L. X., Marks T. J., Anthopoulos T. D., Bronstein H. "Effect of Alkyl Chain Branching Point on 3D Crystallinity in High N-type Mobility Indolonaphthyridine Polymers" *Adv. Funct. Mater.*, **2017**, 1704069

## *Contributing Authorships*

The work for the following publications represents collaborative work that was carried out during my Ph.D., but the details of which will not be included in this thesis:

*i.* Freeman D. M. E., Musser A. J., Frost J. M., Stern H. L., Forster A. K., **Fallon K. J.**, Rapidis A G., Cacialli F., McCulloch I., Clarke T. M., Friend R. H., Bronstein H. "Donor-Orthogonal Acceptor Conjugated Polymers: Reducing the Singlet-Triplet Energy Gap in Conjugated Polymers" *J. Am. Chem. Soc.*, **2017**, 139 (32), 11073-11080

*ii.* Stahl T., Bofinger R., Lam I., **Fallon K. J.**, Johnson P., Ogunlade O., Vassileva V., Pedley R. B., Beard P. C., Hailes H. C., Bronstein H., Tabor A. B. "Tunable Semiconducting Polymer Nanoparticles with INDT-Based Conjugated Polymers for Photoacoustic Molecular Imaging" *Bioconjugate Chem.*, **2017**, 28 (6), 1734-1740

*iii.* Freeman D. M. E., Minotto A., Duffy W., **Fallon K. J.**, McCulloch I., Cacialli F., Bronstein H. "Highly red-shifted NIR emission from a novel anthracene conjugated polymer backbone containing Pt(II) porphyrins" *Polym. Chem.*, **2016**, 7, 722-730

*iv.* Freeman D. M. E., Tregnago G., Rodriguez S. A., **Fallon K. J.**, Cacialli F., Bronstein H. "Deep-red electrophosphorescence from a platinum(II)–porphyrin complex copolymerised with polyfluorene for efficient energy transfer and triplet harvesting" *J. Org. Semiconductors*, **2015**, 3, (1), 1-7

# *List of Abbreviations*

| | |
|---|---|
| ° | degrees |
| δ | chemical shift |
| μ | micro |
| λ | wavelength |
| 2EH | 2-ethylhexyl |
| A | acceptor (as in donor-acceptor) |
| AFM | atomic force microscopy |
| anhyd. | anhydrous |
| Ar | aromatic |
| B(pin) | boronpinacol ester |
| BCE | before common era |
| BDI | Baeyer–Drewson Indigo (synthesis) |
| BHJ | bulk heterojunction |
| br | broad |
| BT | benzothiadiazole |
| C | Celsius |
| cat. | catalytic |
| CB | conduction band |
| CC | cross-conjugation |
| CCL | crystalline correlation length |
| CYTOP | cyclic transparent optical polymer |
| D | drain electrode, donor (as in donor-acceptor) |
| DCM | dichloromethane |
| degas. | degassed |
| Δ | heat to reflux (in caption of scheme), difference between two numbers/values |
| DFT | density functional theory |
| DMF | dimethylformamide |
| DoE | design of experiment |
| DPP | diketopyrrolopyrrole |
| EDG | electron donating group |
| $E_g$ | optical band gap |
| EI | electron ionization |
| EPR | electronic paramagnetic resonance |
| EQE | external quantum efficiency |
| ESI | electrospray ionization |
| ETL | electron transport layer |
| eV | electron Volts |
| EWG | electron withdrawing group |
| FET | field-effect transistor |
| FF | fill factor |
| fTAS | femtosecond transient absorption spectroscopy |
| G | gate electrode |
| g | gram |
| GIWAXS | grazing incidence wide-angle X-ray scattering |
| GPC | gel permeation chromatography |

| | |
|---|---|
| h | hour |
| HOMO | highest occupied molecular orbital |
| HRMS | high resolution mass spectrometry |
| HTL | hole transport layer |
| Hz | hertz |
| $I_{\mathrm{D}}$ | drain current |
| IQE | internal quantum efficiency |
| IND | indolonaphthyridine |
| INDB | indolonaphthyridine benzene |
| INDT | indolonaphthyridine thiophene |
| ITO | indium tin oxide |
| J | coupling constant |
| $J_{\mathrm{SC}}$ | short circuit current |
| L | litre |
| $L$ | channel length |
| LRMS | low resolution mass spectrometry |
| LUMO | lowest unoccupied molecular orbital |
| M | molar |
| m | milli, multiplet |
| $m/z$ | mass to charge ratio |
| MALDI | matrix assisted laser desorption ionisation |
| Me | methyl |
| min | minute |
| $M_n$ | number average molecular weight |
| MO | molecular orbital |
| $\mu_{\mathrm{e}}$ | electron mobility |
| $\mu_{\mathrm{h}}$ | hole mobility |
| µW | microwave |
| $M_w$ | weight average molecular weight |
| NDI | naphthalenediimide |
| NICS | nucleus independent chemical shift |
| nm | nanometre |
| NMR | nuclear magnetic resonance |
| OFET | organic field-effect transistors |
| OLED | organic light emitted diode |
| OPV | organic photovoltaic |
| Ph | phenyl |
| PAH | polycyclic aromatic hydrocarbon |
| PCE | power conversion efficiency |
| PDI | polydispersity index |
| PEIE | ethoxylated polyethylenimine |
| PESA | photoelectron spectroscopy in air |
| PNDB | pyridylnaphthyridine benzene |
| PV | photovoltaic |
| RMS | root mean square |
| RPM | rotations pet minute |
| RT | room temperature |
| S | source electrode, selenophene, singlet |
| SD | source and drain electrodes |

| | |
|---|---|
| SEC | size exclusion chromatography |
| SF | singlet fission |
| T | thiophene, triplet |
| TAS | transient absorption spectroscopy |
| TD-DFT | time-dependant density functional theory |
| TG-BC | top gate bottom contact |
| TLC | thin layer chromatography |
| UV | ultraviolet |
| VB | valence band |
| $V_{\mathrm{D}}$ | drain voltage |
| $V_{\mathrm{G}}$ | gate voltage |
| vis | visible (light) |
| $V_{\mathrm{OC}}$ | open circuit voltage |
| $V_{\mathrm{Th}}$ | threshold voltage |
| $W$ | channel width |
| XRD | X-ray diffraction |
| ZFS | zero field splitting |

*Alice started to her feet,*
*for it flashed across her mind*
*that she had never before seen*
*a rabbit with either a waistcoat-pocket,*
*or a watch to take out of it,*
*and,*
*burning with curiosity,*
*she ran across the field after it,*
*and was just in time to see it pop down*
*a large rabbit-hole under the hedge.*

*In another moment down went Alice after it,*
*never once considering how in the world she was to get out again.*

# I

*Introduction*

## 1.1 Materials: From Pyramids to Pi-Orbitals

The advancement of humanity throughout history is paved with our ability to exploit materials. For almost 2.3 million years, ancient Stone Age civilisations used plants, mud, stone and bone as tools and building materials, and kept treasures of the few metallic elements found in the earth, such as copper and gold. With the discovery of the most basic concepts of chemical and thermal processes around 3000 BCE, we learnt to extract lead, copper and tin from enriched ores, and to combine the latter two into their alloy, bronze, thus creating the art of $metallurgy$, sparking the beginning the Bronze Age. The strength and malleability of these metals allowed for advances in tool making and weaponry, and indeed the history of metallurgy after the Bronze Age is painted in blood in the race to forge the best weapons and armour.

Around 1200 BCE, refinement of thermo-chemical processes and furnace technology led to our ability to extract iron from its ore. The alloy of iron with carbon – steel – is still used to date as one of the strongest metallic materials. With the boom in $ferrous\ metallurgy$ marking the beginning of the Iron Age, tools forged from iron and steel were much stronger allowing for the creation of advanced weaponry and armour, but also hardier agricultural tools, contributing heavily to advancements in farming and thus allowing huge growth in global populations.

Although the advent of metallurgy, and even simple fire, could be considered the birth of chemistry, it wasn't until the medieval period when alchemy was practiced, rooted in the ancient Greek philosophy of Empedocles that everything was made from four elements – earth, fire, air and water. The history of alchemy is steeped in spiritualism, mystery and fraud, most notably for the conquest to create the Philosopher's Stone – granting the power to transform worthless metals to gold – and the pursuit of Elixir of Life. The spread

of the production of fool's gold (Pyrite, $FeS_2$) led to Pope John XXII expelling all alchemists from France in the 14th century for manufacturing counterfeit money, and English law in the 15th century made the "manipulation of metals" punishable by death.

The transition away from alchemy to refined chemistry is credited to the works of Robert Boyle, specifically his landmark publication *The Sceptical Chymist* in 1661, which appealed for a rigorous reproducible scientific approach and asserted that experiments denied the limiting of classical elements to the four, whilst laying out some of the earliest concepts of atoms, molecules and chemical reaction. Throughout the 17th to 19th centuries, advances in chemistry were made swiftly, leading to the creation and isolation of many new materials, elements, compounds and devices. The 19th and 20th centuries saw the chemical revolution, spearheaded by the French chemist Antoine Lavoisier who is now widely regarded the father of modern chemistry. At the end of the 19th century, the mass exploitation of petroleum allowed for large-scale production of chemicals & solvents and created the field of chemical engineering.

In the mid-19th century, the British chemist Thomas Graham noted that some organic materials would not dissolve in solvents, nor would they pass through filter papers, nor could they be purified to a crystalline form. He called these materials *colloids* after *kola*, the Greek word for glue. Cellulose, the scaffolding of all plants and trees and the most naturally abundant polymer in the world, was the feature of the earliest work on polymers. The nitration of cellulose – nitrocellulose or cellulose nitrate – could be dissolved in ethereal ethanol to give a gluey paste called Collodion which was used in surgical dressings and photographic plate emulsions. This discovery was swiftly followed by that of mixing nitrocellulose with camphor to make Celluloid, widely considered the first thermoplastic and was used for applications ranging from cheap jewellery, toy dolls, buttons to billiard balls, due to its similarities to ivory.

A cornerstone in polymer history was the invention of Bakelite (**Figure 1.1**, **P1**) by Leo Baekeland in 1907, and was one of the first plastics made from synthetic components. Baekeland discovered that the mixing of phenol, formaldehyde and a catalyst (HCl, ZnCl, $NH_3$) at high temperatures and pressures formed an insoluble cross-linked solid. Bakelite's plastic could be moulded very quickly and mouldings were smooth, retained their shape and had excellent resistance to electricity, heat and chemical action. Applications of Bakelite stretched from the insulating parts of telephones, to automobile caps and casings, early aeronautic components, cameras and early guns. The diverse and important properties of Bakelite sparked the interest of chemists in this new class of materials and very quickly many new plastics were invented, many of which superseded Bakelite, mainly due to its brittleness. The library of modern thermoplastics (**Figure 1.1**)

now includes polyethylene **P2**, polypropylene **P3**, polyvinyl chloride **P4**, acrylic **P5**, nylon 6-6 **P6** and synthetic rubbers (e.g. polyisoprene, **P7**).

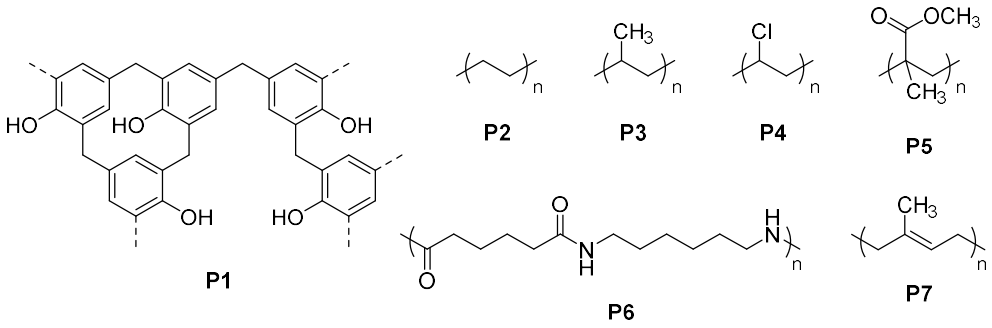


**Figure 1.1** Structures of important historical and commercial thermoplastic polymers

Modern life is highly reliant on plastics and there are few areas of contemporary living which do not exploit them. From widespread use as packaging materials in commercial industries, building materials in construction, lightweight aeronautic materials, to the toy and electronic industries, much of our everyday lives would be vastly different without the invention of plastics. By the 1970s, the field of plastics was considered well studied and almost complete until the discovery of polymers that could act as electrical conductors, opening a whole new field of polymer science: plastic electronics.

The birth of the field of plastic electronics is credited to the discover of electrical conductivity in doped polyacetylene by Heeger and colleagues in 1977.[1,2] The first reports of organic materials in electronic applications began with the report of an organic photovoltaic cell in 1986,[3] followed swiftly by the first report of an organic field-effect transistor (OFET) and organic electroluminescent diode (OLED) in 1987.[4,5] Since these ground-breaking reports, the field has grown and expanded rapidly, advancing these technologies vastly in the process,[6–8] and Alan Heeger, Alan MacDiarmid and Hideki Shirakawa were jointly awarded the Nobel Prize in Chemistry at the turn of the century for "the discovery and development of conductive polymers".

## 1.2 Organic Polymers

### 1.2.1 Principles

#### 1.2.1.1 Terminology & Mechanisms

A polymer is a macromolecule consisting of repeat units of the same chemical structure, called monomers. If a polymer consists of only one monomer, it is termed a homopolymer e.g. polyvinyl chloride **P4**, and if it consists of two or more monomers it is termed a copolymer, e.g. Nylon **P6**.

There are two types of polymerisation reaction: addition and condensation. In a condensation polymerisation, monomers react together with the loss of condensates, typically water or methanol, whereas in an addition polymerisation monomers react together via bond rearrangement without loss of atoms or molecules, typically using specific heats/pressures and catalysts. There are also two mechanisms of polymerisations: step-growth and chain-growth (**Figure 1.2**). In step-growth polymerisations, mechanisms proceed through functional group reactions, whereas in chain-growth polymerisations the mechanism proceeds via free-radicals or ions. General characteristics of these mechanisms are shown in **Table 1.1**. Crucially, a high extent of reaction is necessary for step-growth polymerisations in order to obtain high molecular weight polymers (**Figure 1.3**).

**Table 1.1** Characteristics of step-growth vs. chain-growth polymerisations

| ***Step-growth*** | ***Chain-growth*** |
|---|---|
| Growth through matrix | Growth by addition of monomer at ends of chain |
| Rapid loss of monomer early in reaction | Monomer depleted slowly |
| Similar steps repeated throughout reaction cycle | Different steps operate at different stages of mechanism (i.e. initiation, propagation, termination) |
| Molecular weight increases slowly and high extent of polymerisation needed for high molecular weights | Linear relationship in molar mass of polymer chains and extent of polymerisation |
| Ends remain active | Chains inactive after termination |
| No initiator | Initiator required |

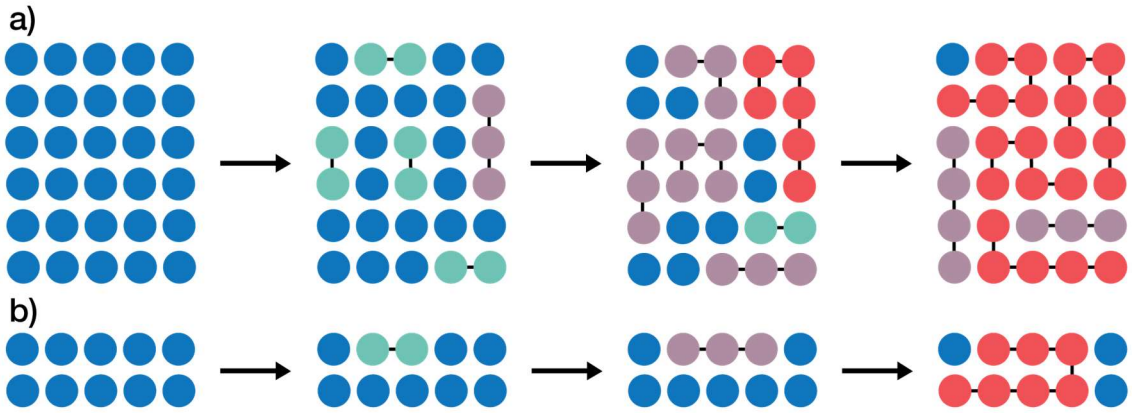


**Figure 1.2** Schematic representation of (a) step-growth and (b) chain-growth addition polymerisations showing monomers (blue circles), dimers (green units), oligomers (purple chains) and polymers (red chains).

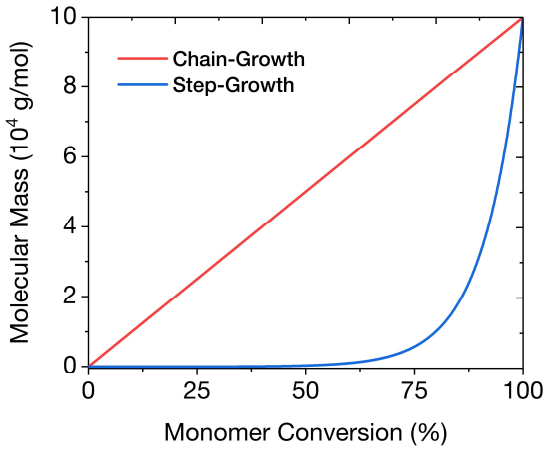


**Figure 1.3** Simulated molecular weight profile as a function of extent of reaction in chain-growth (red) vs. step-growth (blue) polymerisation reactions

### 1.2.1.2 The Statistical Nature of Polymer Chains

Due to the random nature of polymer growth, individual polymer strands formed during polymerisation reactions are seldom the same size. When describing a polymer, it is usually drawn as in **Figure 1.4**, where $n$ represents the number of monomer units in a given polymer chain, and so is termed the degree of polymerisation $\overline{X_n}$.

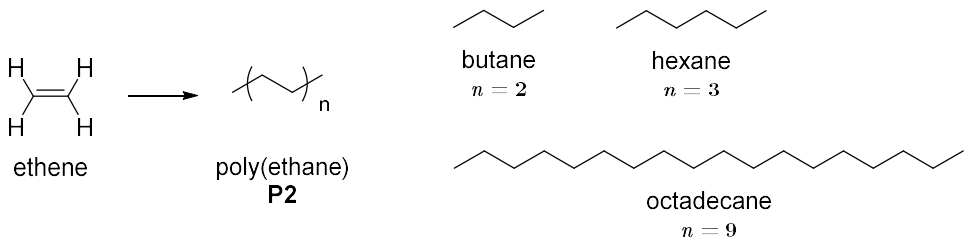


**Figure 1.4** Degrees of polymerisation of poly(ethane) **P2**

A chain where $n = 2$ is termed a dimer, $n = 3$ is termed a trimer and $n > 3$ are called oligomers (i.e. small polymers) and eventually a polymer is formed. The exact value where $n$ denotes a polymer is dependent on the molar mass of the monomer unit, however $n$ can approach and exceed values as high as $10^4$. The important distinction between small molecules and polymers is exhibited nicely by polyethanes **P2**, where $n = 2$ (butane) is a gas, $n = 3 - 7$ are liquids (e.g. hexane), $n = 8 - 10$ are semi-solids with melting points around RT, and $n > 10$ are solid waxes. This demonstrates how the degree of polymerisation can affect the material properties drastically.

As individual polymer chains rarely have the same $\overline{X_n}$ and molar mass, it is necessary to describe the molar mass using statistical distributions around an average molecular weight. The most characteristic statistical distribution of a polymer is its number average molecular weight $M_n$ defined as

$$M_n = \frac{\sum N_i M_i}{\sum N_i} \tag{1.1}$$

where $N_i$ is the number of moles of polymer chains composed of $i$ monomer units and $M_i$ is the mass of a macromolecule composed of $i$ monomer units. As such, $M_n$ represents an average across all unique polymer sizes in a batch of polymer.

The second statistical distribution commonly discussed is the weight average molecular weight, which takes into account the fact that bigger polymer chains contain more of the total mass of the total polymer sample than that of smaller sized oligomers. The weight $W_i$ of a macromolecule with molecular mass $M_i$ is therefore given by

$$W_i = N_i M_i \tag{1.2}$$

and so the weight average molecular weight $M_w$ is defined as

$$M_w = \frac{\sum W_i M_i}{\sum W_i} = \frac{\sum N_i M_i^2}{\sum N_i M_i} \tag{1.3}$$

Other models do exist to describe the molecular weight distributions of polymers, however in this thesis polymer molecular weights will be exclusively discussed in terms of their number average and weight average molecular weights.

The distribution in molecular weight of a synthesised polymer batch can be described as the polydispersity Đ (also referred to as polydispersity index (PDI) or weight dispersion $D_w$), as the ratio of weight to number average molecular weights:

$$Đ = \frac{M_w}{M_n} \tag{1.4}$$

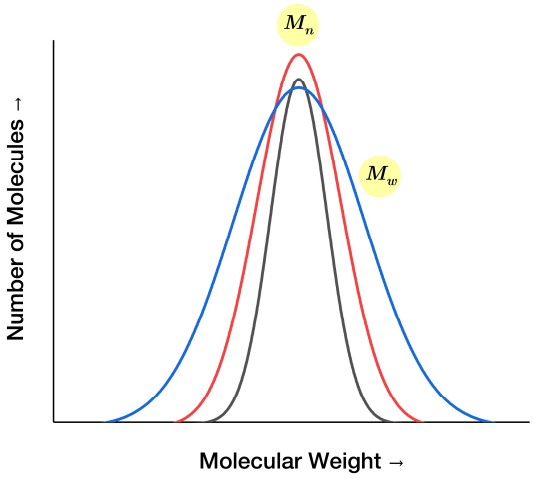


**Figure 1.5** Simulated molecular weight distributions showing $M_n$ and $M_w$ where the polydispersity would be blue > red > black.

### 1.2.1.3 Palladium-Catalysed Cross-Coupling Polymerisations

Of the plethora of methods and catalysts for the synthesis of polymers available to the organic chemist, only one type of reaction will be discussed in this thesis: the formation of carbon–carbon bonds via palladium mediated cross-coupling reactions. Pd, like many other transition metal catalysts, has vacant $\mathrm{dsp}^n$ orbitals which can overlap with filled $\mathrm{sp}^n$ orbitals of ligands forming conventional two-electron two-center σ bonds. Palladium(0) complexes which are coordinatively and electronically unsaturated $(14\ e^-)$ are highly reactive towards oxidative addition (**Scheme 1.1**) with an $\mathrm{sp}^2$–hybridised organohalide whereby the product is coordinatively and electronically stable (note that $\mathrm{Pd}^{\mathrm{II}}$ is a low-spin $\mathrm{d}^8$ metal and so it adopts a square planar conformation and is electronically stable with a $16\ e^-$ configuration).

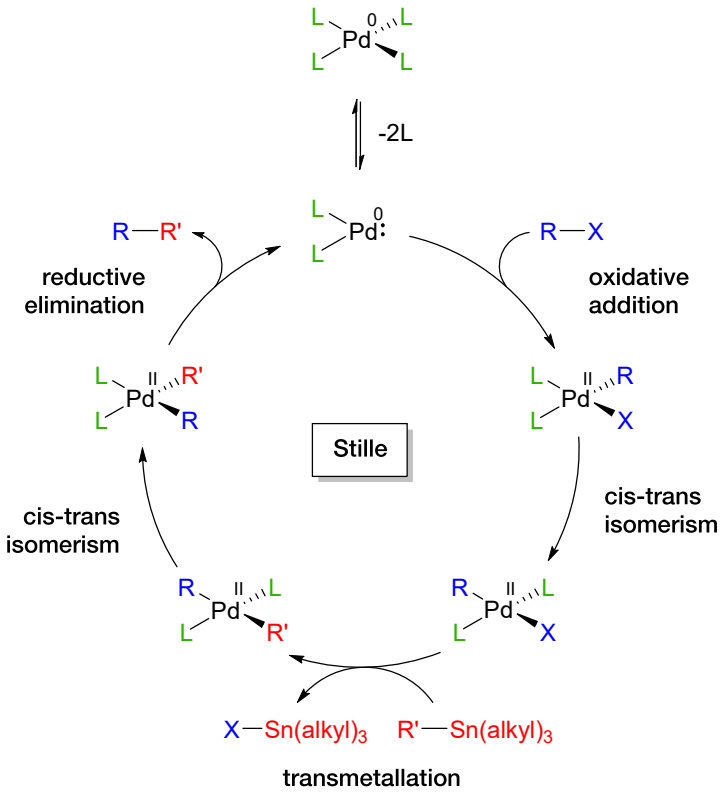


**Scheme 1.1** Stille cross-coupling catalytic cycle where R = R' = $\mathrm{sp}^2$ hybridised C (aryl, allyl, alkenyl) and X = halide (I, Br, Cl) or pseudohalide (OTf, $\mathrm{OPO(OR)_2}$) and L = triarylphosphine ($\mathrm{PPh_3}$, $\mathrm{P}(o\text{-Tol})_3$)

Though formally producing a *cis*-tetravalent species due to the concerted nature of oxidative addition, this species is in rapid equilibrium with its *trans* isomer which is thermodynamically more stable. This *trans* isomer can undergo transmetalation with a variety of reagents, and this gives rise to a library of different Pd cross-coupling libraries. These include alkenes (Heck),[9–12] organozincs (Negishi),[13,14] organosilicons (Hiyama),[15,16] alkynes (Sonogashira),[17,18] amines, alcohols & thiols (Buchwald-

Hartwig),[19–21] Grignard reagents (Kumada),[22–24] arenediazondiums (Heck-Matsuda),[25–27] boronic acids (Suzuki)[28–30] and organotins (Stille)[31–34]. Only the latter two reactions – Suzuki & Stille – are exploited in this thesis and to keep this text concise, the other cross-coupling reactions will not be discussed further.

To continue the discussion of the Stille reaction shown in Scheme 1.1, the *trans*-$Pd^{II}RXL_2$ species undergoes transmetallation with an organostannane to form the *trans*-$Pd^{II}RR'L_2$ species. This must then undergo isomerisation so that the two R groups occupy mutually cis coordination sites, and then the *cis*-$Pd^{II}RR'L_2$ can undergo reductive elimination, yielding the coupled R–R' species and the active $Pd^0L_2$ catalyst.

A Suzuki cross-coupling reaction (**Scheme 1.2**) has a similar mechanism to a Stille up to the *cis-trans* isomerism after oxidative addition. At this point, the organopalladium species reacts with base to form a *cis*-$Pd^{II}R(OZ)L_2$ complex. Meanwhile, a boronic acid species reacts with base to form a borate complex $[R'BY_2OZ]^-Na^+$. This borate complex then undergoes transmetalation with the activated organopalladium species to give the *cis*-$Pd^{II}RR'L_2$ species.

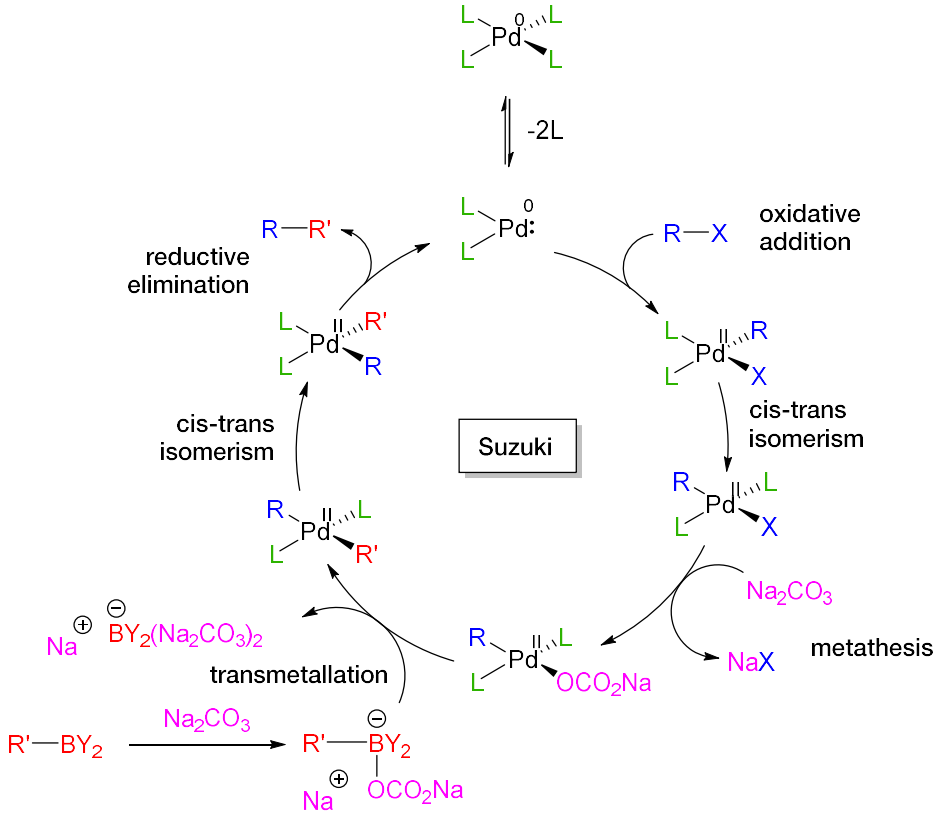


**Scheme 1.2** Suzuki cross-coupling catalytic cycle where R = R' = $sp^2$ hybridised C (aryl, allyl, alkenyl) and X = halide (I, Br, Cl) or pseudohalide (OTf, $OSO_2CF$, $OPO(OR)_2$) and L = triarylphosphine ($PPh_3$, $P(o\text{-Tol})_3$)

The exact mechanism of this step remains to be discovered, however organoboron compounds do not undergo transmetalation in the absence of base.[35] The final reductive elimination step following isomerism is analogous to that discussed earlier for Stille.

Suzuki reactions have some unique advantages over Stille. Boronic acids are readily available and have high stability so can be purified rigorously, whereas organostannes have a tendency to degrade over time and are unstable on silica, so their purification is more difficult. Boronic acids are also much less toxic and less environmentally polluting than organostannanes and the inorganic impurities from Suzuki reactions are easily removed during purification due to their polarity and high solubility in aqueous methanol. The typical solvent system of toluene–water is also more environmentally friendly than Stille solvents, where chlorobenzene is typically employed.

Conversely, Stille reactions are robust and can be performed in under an hour using microwave-assisted methods, whereas Suzuki reactions are typically performed for 3 days. Furthermore, Stille reactions have extremely high functional group tolerance, whereas Suzuki precursors cannot contain any basic-labile functionality.

A variety of palladium catalysts have found uses in these cross-coupling reactions. As Pd(0) is the active catalyst, tetrakis(triphenylphosphine)palladium(0), $Pd(PPh_3)_4$, also referred to informally as *tetrakis*, is frequently used, however it has poor stability due to the tendency for oxidation of the phosphine ligands in air, but can be readily recrystallised from ethanol.

Tris(dibenzylideneacetone)dipalladium(0), $Pd_2(dba)_3$, is another favoured Pd(0) catalyst which has high air-stability due to the strong benzylideneacetone ligands. However, the trade-off is that these ligands are difficult to remove, requiring high temperatures, and so generally aren't employed in Suzuki reactions, but are excellent in Stille. If the Pd source does not contain phosphine ligands they must be added. Bulky phosphine ligands increase the rate of reductive elimination by increasing the Pd–$PR_3$ bite angles thus decreasing the angle between the R and R' group in the *cis* complex. As such tri(*o*-tolyl)phosphine, P(*o*-Tol)$_3$, ligands are routinely used with $Pd_2(dba)_3$.

Lastly, Pd(II) compounds, such as $Pd(OAc)_2$ or $PdCl_2$, have high air-stability and can generate Pd(0) *in-situ*, though are generally more expensive than the Pd(0) reagents discussed above. It should be noted that other Pd regents are available to the organic chemist, but the above reagents are noteworthy for this work.

### 1.2.2 Semiconducting Polymers

As discussed earlier, organic polymers with a saturated backbone consisting purely of $sp^3$ hybridised C-C $\sigma$-bonds atoms are excellent electrical insulators. An unsaturated polymer backbone containing $sp^2$ hybridised C atoms gives rise to a $\pi$-conjugated system, spatially separated from the backbone. The $p_z$ orbitals which do not participate in hybridisation lay perpendicular to the $sp^2$ trigonal planar orbitals, forming $\pi$-bonds. As the $\pi$-system is conjugated, electrons can delocalise along the polymer backbone, giving rise to conductivity.

Small molecules, such as ethene (**Figure 1.6**) have discrete frontier MOs: a highest occupied (HOMO) and lowest unoccupied (LUMO) molecular orbitals. When another ethene unit is added – butadiene – the MOs are hybridised, raising the HOMO and lowering the LUMO. As the conjugation length is extended the hybridisation continues until the differences between energy levels becomes so discrete that the system adopts a band structure – a valence band (VB) for occupied states and a conduction band (CB) for unfilled states. This property is what gives them the conductivity akin to a semiconductor.

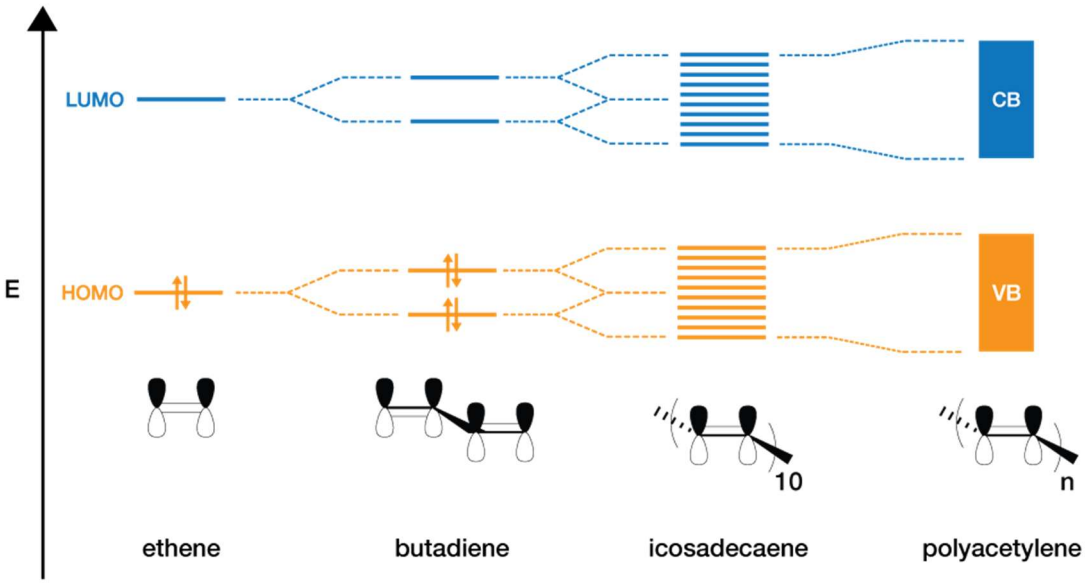


**Figure 1.6** Cartoon of dissolution of discreet energy levels to form a band structure of organic conjugated polymers

As well as acting as a semiconductor in applications such as transistors, the band structure also has unique optical properties. The frontiers of the VB and CB remain known as the HOMO and LUMO (respectively) of the polymer and the difference in energy between them is the optical band gap $E_g$. Upon radiation of an organic semiconductor with a photon of energy $\geq E_g$, an electron can be excited to the LUMO,

creating an exciton. As organic semiconductors typically exhibit $1.0 < E_{\mathrm{g}} < 3.0\ \mathrm{eV}$, they are able to absorb photons in the UV-vis and near-IR regions of the electromagnetic spectrum, from 400 – 1200 nm. As such, organic semiconductors are able to act as light-harvesting active layers in organic photovoltaic cells.

As discussed previously, modern organic polymers are typically formed through transition-metal catalysed step-growth addition polymerisations, where a monomer reacts to form a dimer, then a trimer, then oligomers containing $n$ repeat units. The point at which an oligomer becomes classified as a polymer remains a contested subject. In a theoretical ideal isolated planar conjugated system, the reduction of $E_{\mathrm{g}}$ plateaus after a certain number of repeat units. However, $E_{\mathrm{g}}$ can be further reduced in solid states due to molecular interaction and packing effects, which essentially furthers the effective conjugation length of a polymer. Although the number of monomer units required to bring the band gap energy to its saturation is dependent on the chemical nature of the monomer, a polymer consisting of at least 10-15 monomer units is generally considered a polymer.[36,37]

### 1.2.3 Molecular Orbital Engineering

The crux of organic semiconductor synthesis research is the fundamental understanding of structure-property relationships with the aim to form design rules to facilitate targeted design of future materials with tailored properties to serve the application requirements. When assessing an organic semiconductor for application as a light absorbing material in organic photovoltaic (OPV) cells or as charge transport layer in organic field-effect transistors (OFETs), the precise energies of the HOMO $(E_{homo})$ and LUMO $(E_{lumo})$ and the optical band gap $(E_{\mathrm{g}})$ that lays between them are of paramount importance.

If $E_{homo}$ lays too high, the stability of the polymer to oxidation could be reduced, the open-circuit voltage in OPV cells will fall, and hole injection barriers could be intensified in organic field-effect transistors (OFETs). Similarly, if $E_{lumo}$ lays too low in energy, poor charge separation in OPVs will result in poor performance, and electron injection barriers may form in OFETs. A wide $E_{\mathrm{g}}$ will absorb bluer wavelengths where the intensity of solar radiation is its highest, whilst a narrow $E_{\mathrm{g}}$ will be able to absorb a greater proportion of solar radiation, however cannot efficiently harness the high energy photons in the bluer region of the electromagnetic spectrum.

Concurrently, it is important to remember that a polymer with ideal electronic properties is useless if its physical properties lead to poor solid-state morphology in thin-film which

would negatively impact charge generation in OPVs and prevent charge transport throughout the bulk.

The ground state of a conjugated polymer has two possible resonance structures with nondegenerate energy: the aromatic form and the quinoidal form (**Figure 1.7**).

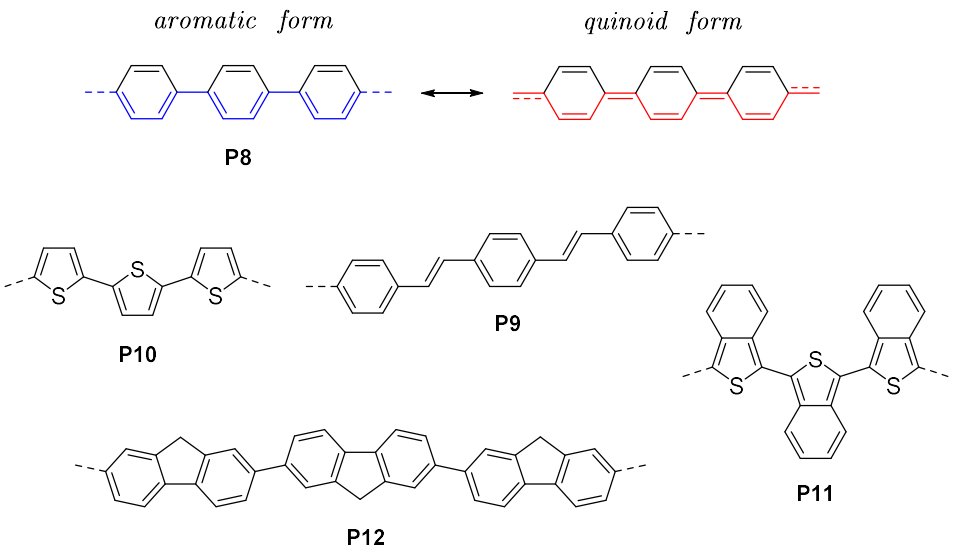


**Figure 1.7** Trimers of basic organic semiconductors, all featuring a backbone of polyacetylene (shown in blue) and its resonance quinoid form (shown in red)

In its aromatic form, the π-electrons of every aryl unit are confined so that the unit maintains its aromatic stabilisation. The delocalisation of the π-electrons results in the conversion of each single bond into a double bond and *vice versa* for double to single bonds, giving the quinoid form. This form is less energetically stable in comparison to the aromatic form and hence has a smaller band gap as a result of loss of aromatic stabilisation energy. This relationship leads to the first "synthetic strategy" for making narrow band gap polymers: the more stabilised the quinoid form of a polyaromatic backbone, the smaller the optical band gap.[38]

The energy levels and hence optical band gap of polymers can be estimated computationally using quantum chemical calculations. For very simple polymers, like those in Figure 1.7, the use of time-dependant density functional theory (TD-DFT) to estimate $E_g$ has its drawbacks, but for the sake of consistency, all theoretical band gaps discussed in this section have been calculated on trimers at the B3LYP/6-311G** level of theory, and though the theoretical values tend to differ to the experimental values, the trends in theoretical data match the trends in experimental data.[39,40] It should also be noted that the trimers discussed in this section do contain differing quantities of π-electrons, e.g. 18 in **P8**, 22 in **P9**, 36 in **P12** etc, which will affect the MO hybridisation

and therefore band gap independent of chemical modification. A more thorough analysis would normalise this factor, however the following analysis is ample for discussing trends.

Due to the strongly aromatic character of benzene, polyphenylene **P8** has minimal quinoid character and thus has a theoretical band gap of 4.4 eV. Poly(phenylenevinylene) **P9**, where each benzene is spaced by an alkene, exhibits a dilution of aromatic character and thus has a narrower $E_{\mathrm{g}}$ of 3.0 eV. As thiophene has a lower degree of aromaticity than benzene, polythiophene **P10** exhibits a narrower $E_{\mathrm{g}}$ than **P8** of 3.4 eV. A creative way to increase the quinoidal stability of **P10** is shown in polyisothianaphthene **P11** (PITN). By considering the aromatic resonance energies of benzene (1.56 eV) and thiophene (1.26 eV), the quinoidal form of **P11** is very favourable due to the formation of aromatic benzene, and thus has a theoretical $E_{\mathrm{g}}$ of 2.4 eV, however experimentally PITN exhibits an incredibly narrow $E_{\mathrm{g}}$ of 1.0 eV.[41]

Another synthetic strategy for narrowing the band gap of organic polymers is planarization: the more planar the backbone, the better the overlapping of $\mathrm{p_z}$ orbitals and thus the greater the delocalisation of conjugation. Steric interactions between units along a polymer backbone restricts most polymers from achieving absolute planarity and distortion along the backbone can be characterised by the dihedral $(\theta)$ twist between aryl units. The distortion from planarity in polyphenylene $(\theta = 39°)$ is greater than that of polythiophene $(\theta = 25°)$ and as a result exhibits a wider band gap as discussed above.

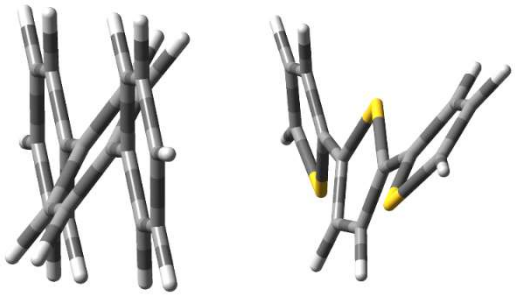

**Figure 1.8** Lowest energy conformations of triphenylene (left) and trithiophene (right) at B3LYP/6-311G**. The distortion from planarity is 39° and 25° respectively.

However, benzene rings feature prominently in the literature and provide favourable properties to many organic semiconductors. A method of decreasing total backbone disorder in benzene-based polymers is to join two rings together with a bridging atom, i.e. carbazole (NH bridge) or fluorene ($CH_2$ bridge). Indeed, polyfluorene **P12** has a theoretical $E_{\mathrm{g}}$ of 3.5 eV, a reduction in 0.9 eV for such a relatively straightforward chemical modification.

A more recent approach to increasing backbone planarity is to design monomers which can participate in long range interactions, namely between heteroatoms and elements with lone pairs (**Figure 1.9**).[42,43]

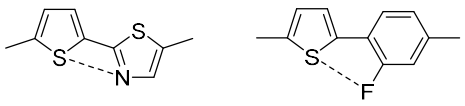


**Figure 1.9** Heteroatom-heteroatom (left) and heteroatom-fluorine (right) long range interactions to create conformational locks and reduce backbone disorder

As explained prior, the optical band gap will narrow with increasing conjugation up until the point at which the effective conjugation length of a polymer becomes saturated and no more narrowing is seen due to longer conjugation. At this point, strategy must move from steric to electronic. The energy levels of polymers can be greatly affected by electronic effects, both inductive or mesomeric, through the addition of electron-donating (EDGs) or electron-withdrawing (EWGs) groups along the polymer backbone. Typically, EDGs raise $E_{homo}$ whilst EDWs lower $E_{lumo}$. For example, 2,1,3-benzothiadiazole (**Figure 1.10**) is an extremely electron poor monomer due to the addition of the electron withdrawing heterocyclic ring. Comparing the theoretical energy levels of benzene–thiophene **P13** and benzothiadiazole–thiophene **P14**, the electron deficient ring shows a drastic drop in $E_{lumo}$ resulting in a much narrower band gap than its benzene equivalent. The benzothiadiazole unit also allows total planarization of the polymer backbone, resulting in a slight raise in $E_{homo}$.

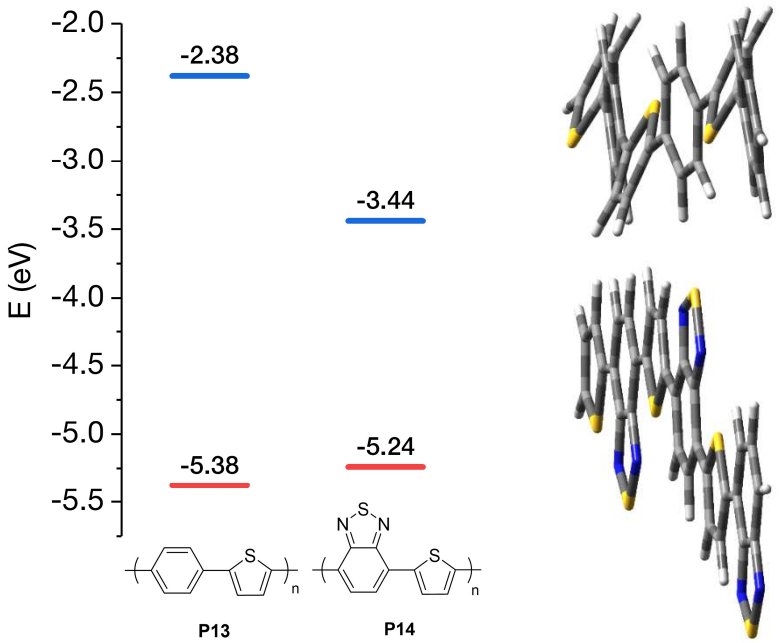


**Figure 1.10** Left: Theoretical band gaps of **P13** (3.0 eV) and **P14** (1.8 eV) with HOMO shown in the red and LUMO in blue; Right: Geometry optimised trimers shown of **P13** (top) and **P14** (bottom) at B3LYP/6-311G**

The last and most powerful synthetic strategy for designing narrow band gap organic semiconductors is the alternation of electron rich "donor" (D) and electron deficient "acceptor" (A) units along a polymer backbone.[44] This alternation creates an electronic "push-pull" driving force for electronic delocalisation, improving quinoidal character i.e. $(\mathrm{D}-\mathrm{A} \rightarrow \mathrm{D}^{+}=\mathrm{A}^{-})$, but crucially leads to significant molecular orbital hybridisation (**Figure 1.11**). On the bonding of the donor to the acceptor, the HOMO of each unit interacts according to perturbation theory to create two new HOMO levels, with the same scenario happening for the LUMO levels. The summative effect simultaneously raises $E_{homo}$ and lowers $E_{lumo}$, thus narrowing the band gap.

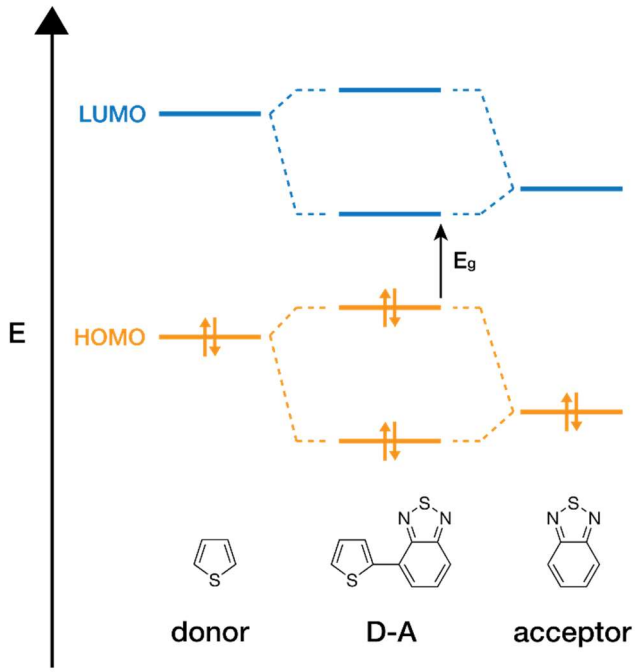


**Figure 1.11** Frontier molecular orbital hybridisation cartoon of an electron rich donor and a electron deficient acceptor molecule to create a D-A unit

The D-A strategy has become the prevailing method of designing novel semiconductors. **Figure 1.12** shows some of the building blocks that have been exploited as both donor and acceptor units, whilst **Figure 1.13** shows some ultra-high-performance polymers. Whilst the performance of organic semiconductors in OPVs and OFETs will be discussed in more detail in the next two sections, it is prudent to have a basic understanding of the benchmarks set for assessing performance in these two types of devices.

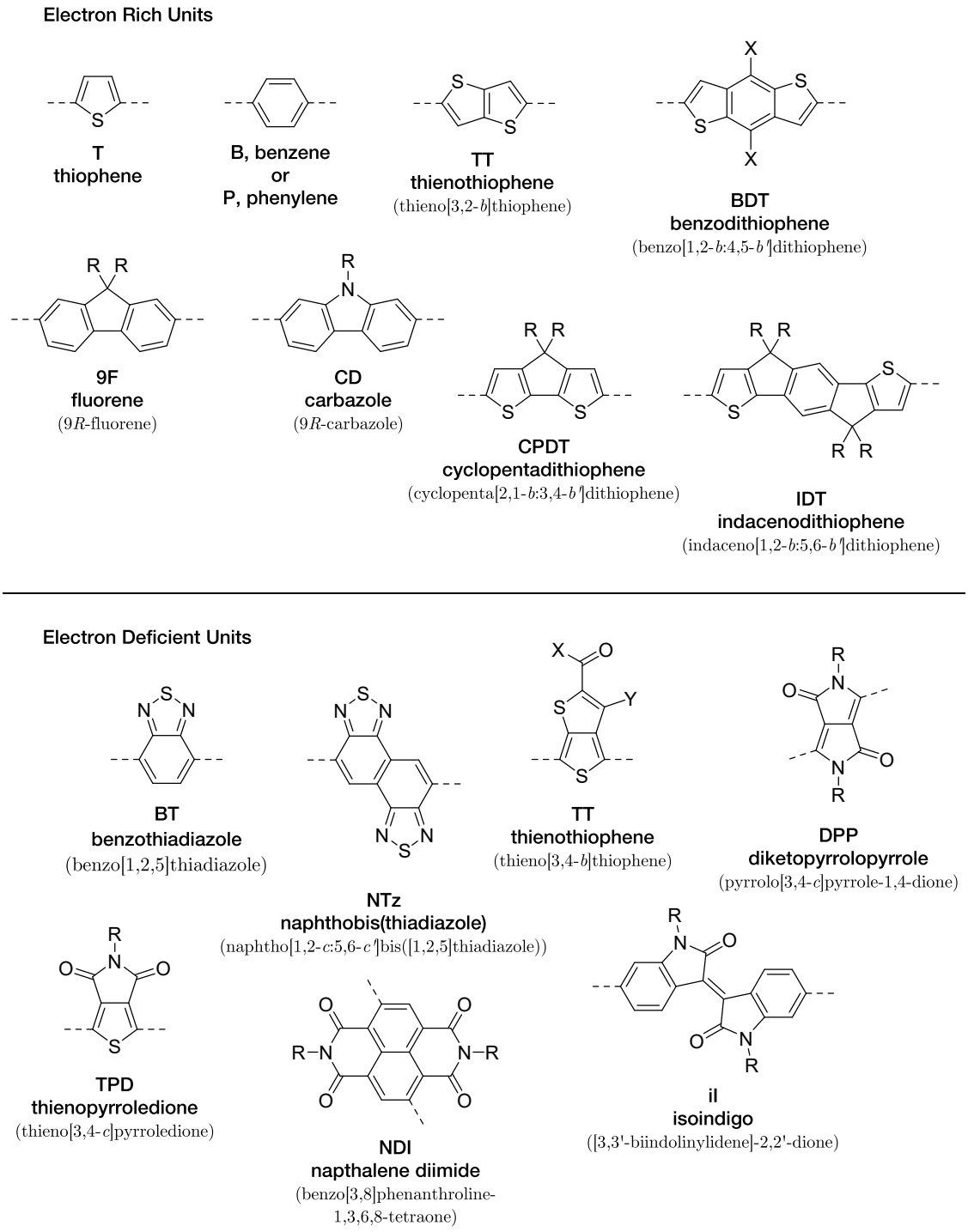


**Figure 1.12** Common organic semiconductor donor and acceptor building blocks. R groups are alkane alkyl groups, X groups are R groups or alkoxyl groups (OR), Y group denotes F more prevalent than H.

In OPVs, the power conversion efficiency (PCE) of a solar cell is the flagship assessment property, and PCEs above 7% are typically viewed as competitive. PCEs in OPV devices have climbed steadily over the last decade and efficiencies exceeding 10% for single-junction OPVs have been reported.[45] You *et al.* showed PCEs up to 7.9% in **PDTP-DFBT**,[46] and He *et al.* reported ground-breaking PCEs up to 9.2% in **PTB7**, rapidly approaching the threshold required for industrial application.[47,48]

Performance of charge transport in FETs must be considered separately for the two types of charge carriers – electrons (n-type) and holes (p-type). For both types, mobilities above 1 $cm^2/Vs$ – the benchmark set by amorphous silicon – are considered ultra-high, with examples above 3 $cm^2/Vs$ remaining extremely rare.

Furthermore, there are many examples of p-type organic polymers exhibiting hole transport above 1 $cm^2/Vs$.[49] Most of the typical building blocks have furnished high-performance p-type materials, including polythiophene,[50,51] cyclopentadithiophene (CPDT),[52,53] diketopyrrolopyrrole (DPP),[54–58] isoindigo (iI),[59,60] and indacenodithiophene[61–63]. Recently, state-of-the-art p-type organic semiconductors have been reported with hole mobilities approaching 10 $cm^2/Vs$, the benchmark set by amorphous metal oxide TFTs.[64]

In stark contrast, there are extremely few examples of n-type polymers reporting electron mobilities above 1 $cm^2/Vs$.[65] Only three polymer families have shown such a level of n-type character: pyridyl-DPP polymers,[66,67] naphthalenediimide (NDI) polymers,[68–71] and fused PPV-type polymers.[72,73]

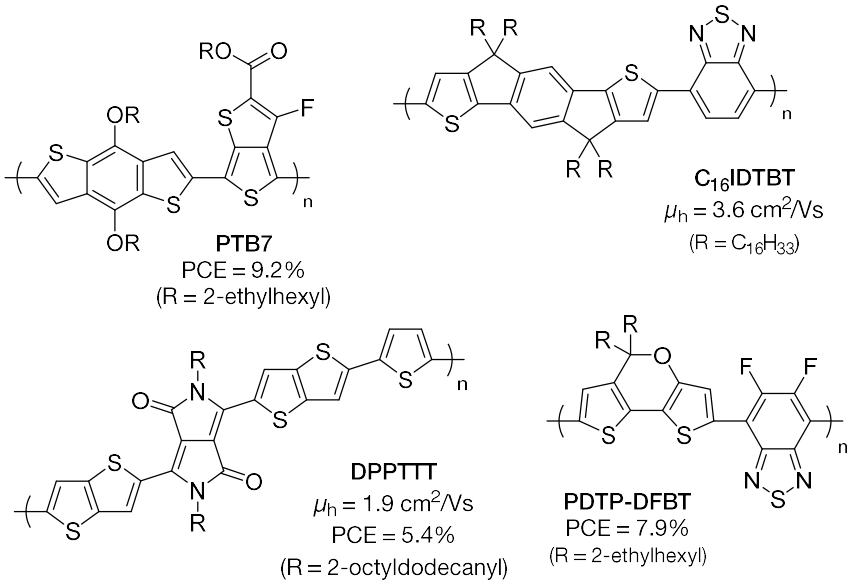


**Figure 1.13** A selection of organic semiconductors showing ultra-high performance in OPVs and OFETs.

## 1.3 Organic Photovoltaics

### 1.3.1 Solar Energy

Global demand for energy has been rising steadily since the industrial revolution of the 18th century due to increasing populations, heavy industrialisation, advancements in technology and the rapidly expanding developing world. To meet demand, the burning of fossil fuels, namely coal and petroleum oil, has prevailed over the last two centuries. It is only in the last few decades where the extent of the consequences of their exploitation has been fully realised. Whilst vast areas of the natural environment are destroyed each year in their mining, their combustion releases huge quantities of greenhouse gases into the atmosphere. Only with geological research in the 20th century did we discover the greenhouse effect and the contribution of manmade $CO_2$ to it. Rising global temperatures risk changing the global climate severely and the need to limit the production of $CO_2$ around the world has led to global $CO_2$-reducing initiatives such as the Kyoto Protocol and Paris Agreement. Worldwide annual energy consumption in 2012 was 18.4 TW and is projected to rise to 27.3 TW by 2040.[74] Demand for energy will see the use of finite non-renewable fuels surge and the search for alternative sources of energy will be one of humanity's most important issues in the coming century. In 2012, 78% of global electricity generation was fuelled by non-renewable energy. Of the renewable contribution only 2% was generated by solar technology. However, the projection of electricity production from renewable sources in 2040 shows the biggest growth in the solar sector (to 9%, **Figure 1.15**).

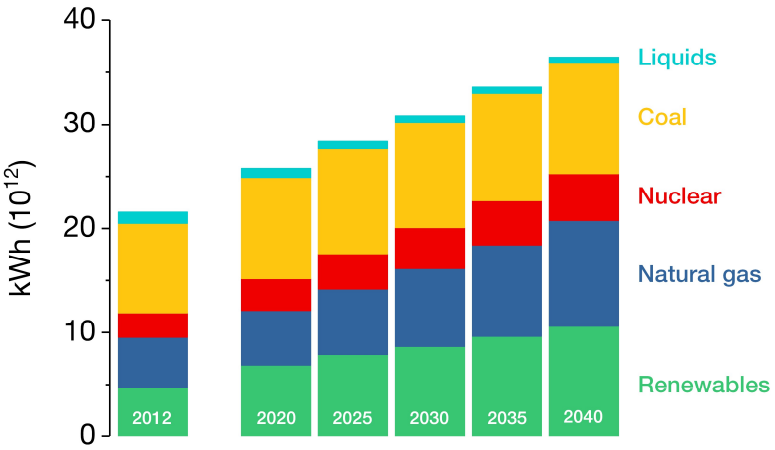


**Figure 1.14** World net electricity generation by energy source in trillion kWh

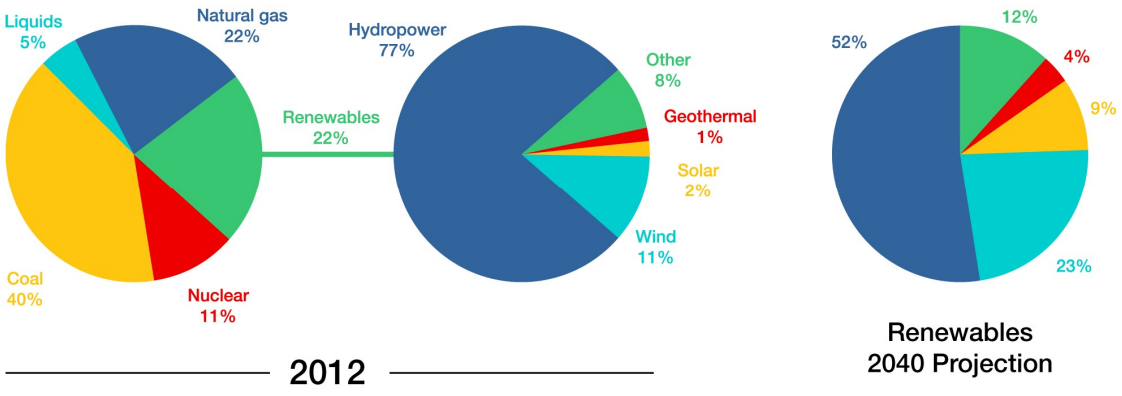


**Figure 1.15** Percentage world net electricity generation in 2012 and projections of renewable energy contribution in 2040.[74]

Solar energy arguably offers the best global solution to the impeding energy crisis: If 2% of land area on Earth were covered in solar cells with an efficiency of 12%, allowing for weather patterns and daylight hours, it is estimated that 67 TW of energy could be generated annually,[75] which is almost 2.5 times more than the projected demand for energy in 2040.

However, it is crucial to stress that the global challenge is not that fossil fuels are a finite resource, but rather that our continuing exploitation of them on a global scale threatens humanity and quality of life for the entire planet. Fossil fuel emissions have been linked to the generation of corrosive acidic rains, particulate pollutants which exacerbate pulmonary conditions, poisonous heavy metals, carcinogenic and teratogenic chemicals, and air, water & thermal pollution. The pinnacle issue of greenhouse gas emissions, such as carbon dioxide, methane and nitrous oxide, has led to severe increase in global temperatures (**Figures 1.16** & **1.17**), leading to drastic climate change around the planet, contributing to droughts, floods, storms, rising sea levels.

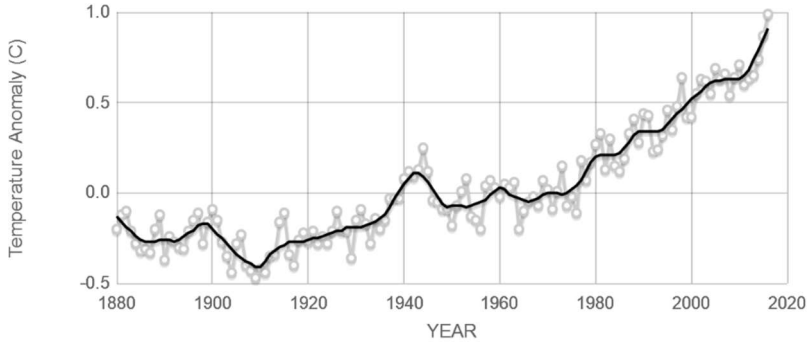


**Figure 1.16** Global temperature anomaly based on land-ocean temperature 1880-2016.[76]

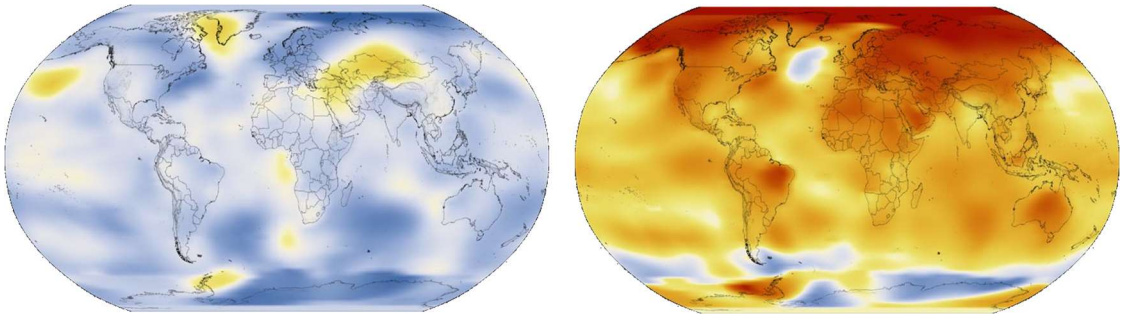

**Figure 1.17** Five-year average variation of global surface temperatures in 1966 (left) and 2016 (right).[76] Dark blue indicates areas cooler than average. Dark red indicates areas warmer than average.

Photovoltaics (PV) are semiconducting materials which produce a voltage or electricity from solar photons with sufficient energy equal to or greater than the optical band gap of the material. The main inorganic photovoltaics are based on silicon and fall within 3 types: monocrystalline, polycrystalline and amorphous. The first two are the typical pin-up solar cell – rigid glass structures in metal frames – whereas amorphous silicon is a thin-film material with a degree of mechanical flexibility. Higher performance semiconductors exist, such as cadmium telluride (CdTe), gallium arsenide (GaAs) or copper indium gallium diselenide (CIGS), the latter being the only other commercially available PV solar cell. The best inorganic PVs are based on wide band gap semiconductors such as $TiO_2$ or $SnO_2$ and ultra-high-efficiency multi-junction cells but these are too expensive for commercial use, though are implemented in space applications.[77]

The case for organic photovoltaics (OPVs) over inorganic PVs is strong due to their low weight, flexibility, short energy payback times, low environmental impact and lower manufacturing costs.[78] Their high solubility in typical solvents enables easy thin-film production, and can be ink-jet printed onto substrates on a roll-to-roll basis – in huge contrast to silicon-based IPVs which rely on expensive thin-film deposition techniques whose cost does not reduce with increased scale.

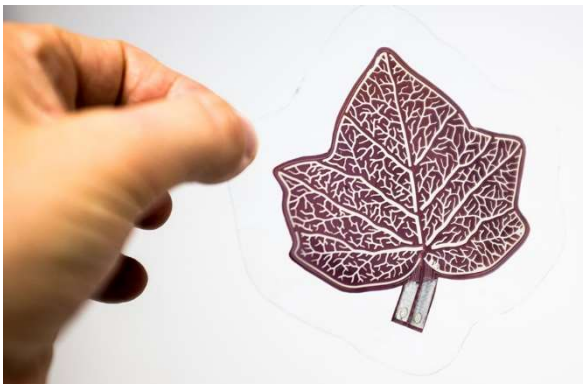

**Figure 1.18** A flexible printed organic solar cell in a leaf motif.[79]

### 1.3.2 Principles

Whilst photoexcitation of an inorganic $p$-$n$ junction solar cell produces free electron-hole pairs, in OPVs it leads to the formation of $excitons$, overall neutral mobile electron-hole pairs bound by Coulombic interaction. This character arises from the low relative permittivity $\varepsilon_r$ of organic materials (2-5) compared to crystalline silicon (12), where the Columbic interaction can be overcome more easily. Non-bonding interactions in organic materials are also considerably weaker than the electronic interactions of inorganic materials, leading to more localised electronic states. For an exciton to dissociate to form free hole $h^+$ and electron $e^-$, it must overcome the Columbic attraction $V$ given by,

$$V = \frac{e^2}{4\pi\varepsilon_r\varepsilon_0 r} \tag{1.5}$$

where $e$ is the charge of an electron, $\varepsilon_r$ is the relative permittivity of the surrounding medium, $\varepsilon_0$ is the permittivity of vacuum and $r$ is the distance between the $h^+$ and $e^-$. The method of overcoming coulombic interaction in OPVs is by using a blend of two materials: a donor and an acceptor, similar to that of a $p$-$n$ junction. The conceptualisation of the modern heterojunction is attributed to Tang *et al.* in 1986 achieving 1% efficiency with a bilayer device using copper phthalocyanine as a donor material and perylenetetracarboxylic bis-benzimidazole as an acceptor.[3] Tang's reported bilayer architecture is still used for small molecule solar cells,[45] however the exciton dissociation in such devices is limited by the bilayer interface. An exciton diffusion length, being the physical distance before an exciton decays to the ground state, is approximately 10 nm.[80–83] Quickly the concept of a bulk heterojunction (BHJ) caught on where the donor and acceptor are thoroughly mixed so that any interface between the two materials is no more than the exciton diffusion length.

Fullerenes have gained large popularity as BHJ acceptor materials due to their high conductivity and their large optical band gap with well-placed frontier MOs to the metallic device electrodes. Naked fullerenes exhibit high crystallinity which hinders intermixing in the BHJ, and so functionalised fullerenes are typically used to reduce crystallinity and increase miscibility with the polymer donors. The most commonly employed acceptor materials are [6,6]-phenyl-C$n$-butyric acid methyl esters, where $n$ is 60 or 70, commonly abbreviated as $PC_{60}BM$ and $PC_{70}BM$ (**Figure 1.19**) respectively.

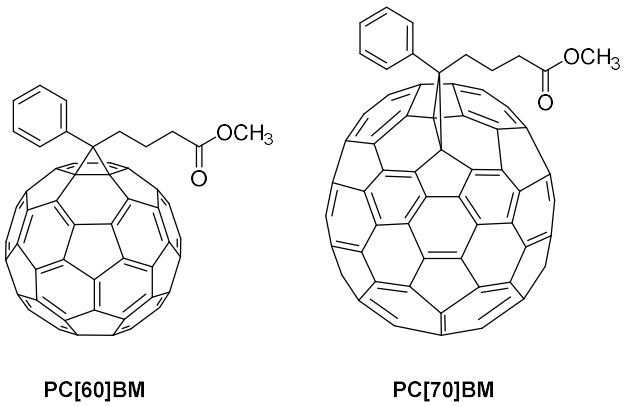


**Figure 1.19** The structures of [6,6]-phenyl-C$n$-butyric acid methyl esters (n=60/70)

However, these fullerenes are expensive and research into alternate acceptor materials remains ongoing.[84] Polymers with similar energy levels to PCBM can act as a BHJ acceptor, however only modest PCEs have so far been achieved using polymer acceptors due to energetically favourable polymer-polymer demixing leading to large scale phase separation in the BHJ.[85]

The mechanism of charge generation in a BHJ is complex and beyond the scope of this thesis, but a simple outline is presented in **Figure 1.20** and discussed below.

Firstly, a proton of energy equal to, or greater than, the optical band gap of the donor $E > E_{\mathrm{g}}$ excites an electron in the HOMO of the donor to its LUMO, forming an exciton where the two generated charges are bound energetically (Figure 1.20a). The exciton then diffuses through the active layer to a donor/acceptor interface (b). At the interface, if the energy offset between the LUMO of the donor and the LUMO of the acceptor is greater than the Columbic attraction of the exciton, it is energetically favourable for the electron to transfer to the LUMO of the acceptor (c). The separated charges can now migrate away from the interface and diffuse through the active layer and to be extracted at the electrodes (d).

This is a simplified view of a very complex system, and there exists many challenges for charge generation in a BHJ. The morphology and blend of the active layer is of critical importance. As well as ensuring that D/A interfaces occur no less than 5-10 nm from any one point, there must also exist percolation pathways to ensure charges can be transported through the bulk to the electrodes efficiently. Therefore, a BHJ which is too finely mixed will hinder the transport of mobile charges in the bulk. Most crucially, the energy offset between $E_{lumo}$ of the donor and $E_{lumo}$ of the acceptor must be equal to or greater than the Columbic attraction of the exciton. If this requirement is not met, charge transfer between the two materials will be inefficient.

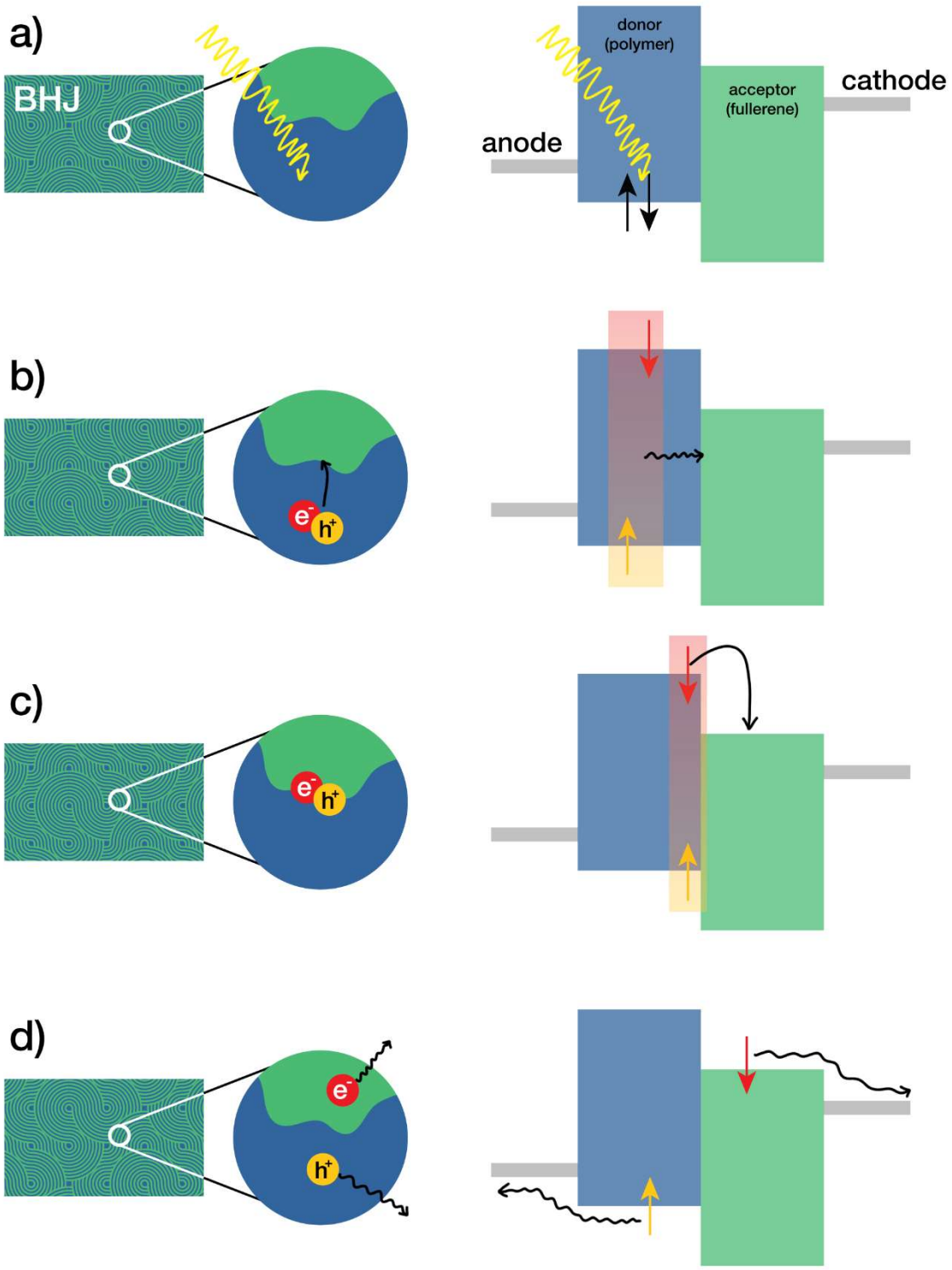


**Figure 1.20** Cartoon of charge separation in a polymer donor (D, blue) – fullerene acceptor (A, green) BHJ showing morphological (left) and energetic (right) processes occurring in tandem. (a) Light with energy $E > E_g$ excites polymer forming energetically-bound exciton; (b) The exciton diffuses to a D/A interface; (c) Dissociation of $e^-$ and $h^+$ at D/A interface creating mobile charges; (d) Charges diffuse through BHJ active layer to the electrodes

### 1.3.3 Device Architecture

There are two kinds of OPV device architecture: conventional and inverted (**Figure 1.21**), differing on their polarities. The core of both devices contains the active layer, the polymer-fullerene BHJ, where photons are absorbed and charge carriers are generated.

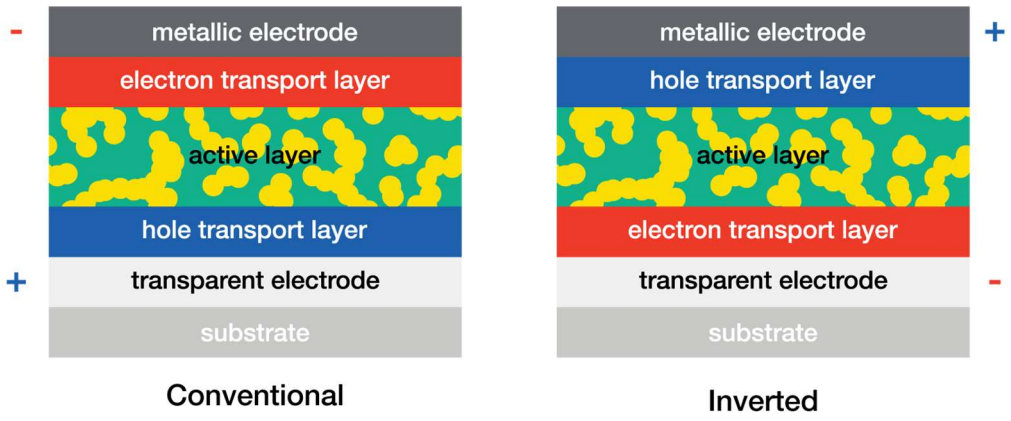


**Figure 1.21** Conventional and inverted architectures of organic photovoltaics

Sandwiching the active layer are the hole and electron transport layers (HTL/ETL) whose function is to provide intermediary energy levels between those of the active layer and an electrode, favouring the transport of one charge carrier over the other and thus acting as blocking layers, directing charge carriers toward the correct electrode, leading to improved charge extraction. Finally, the outermost layers (ignoring the transparent substrate) of the device consist of two electrodes where the charge carriers are collected. The order of these layers determines if the device is conventional or inverted.

In a *conventional* device, an electron transport layer provides a stepping stone to an external metallic cathode of low work function metal (e.g. Al, Ca, Mg). These are easily oxidised leading to poor long-term stability. In an *inverted* device, a hole transport layer provides the stepping stone to an external metallic anode of high work function metal (e.g. Au, Ag) which are much less prone to oxidation and thus lengthens the durability of the device. Therefore, inverted architecture is much more favoured for longevity.

Whereas the main issue associated with the external metallic electrode is stability to oxidation, the internal electrode must be transparent to light to enable photons to penetrate to the active layer. The most common transparent electrodes employed throughout electronics as a field are transparent conducting metal oxides, notably indium tin oxide (ITO). However, indium is an expensive rare earth metal and long-term use of ITO risks OPV fabrication becoming prohibitively expensive. As such there is extensive ongoing research into alternative transparent or semi-transparent electrodes, notably in nanoscale carbon constructs (nanoparticles, nanotubes, nanowires etc.).[86]

The most employed p-type material for the HTL is poly(3,4-ethylenedioxythiophene)-polystyrene sulfonate, PEDOT:PSS or PEDOT (**Figure 1.22**), which matches well most active layers to the anode. PEDOT:PSS is a mixture of two ionomers – polymers which carry partial charges – both polystyrene sulfonate (PSS) which is partially deprotonated, and poly(3,4-ethylenedioxythiophene), PEDOT, which carries a partial positive charge. Combined they form a transparent conductive material with high ductility. With doping PEDOT:PSS can have a conductivity comparable to ITO.[87]

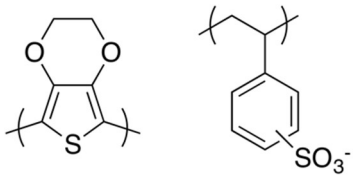


**Figure 1.22** The structure of PEDOT:PSS

PEDOT:PSS is highly hydroscopic and can retain high proportions of water (up to 15 wt%)[88] and is available in an array of pHs, however is typically used in an acidic pH – a downside that can lead to corrosion of metallic electrodes, especially in the case of inverted device architecture.[89]

In conventional devices, ETL are not always needed due to typically good matching with low work function metals. However, an ETL is crucial for inverted devices to match the active layer to the ITO electrode, whilst also remaining transparent to allow photocharge generation. The most employed n-type materials for ETLs are transparent metal oxides such as titanium and zinc oxides.[90]

## 1.3.4 Parameters & Definitions

### 1.3.4.1 Current-Voltage Curve

In the dark, a solar cell acts as a diode and its characteristics can be described by the *Shockley diode equation*

$$J = J_0 \left[ exp\left(\frac{qV}{nkT}\right) - 1 \right] \tag{1.6}$$

where $J_0$ is the dark saturation current, $q$ is elementary charge, $V$ is the voltage, $n$ is a diode ideality factor, $k$ is the Boltzmann constant and $T$ is temperature. The current exhibited by a solar cell in the dark is called the dark current or dark J-V curve (**Figure 1.23**).

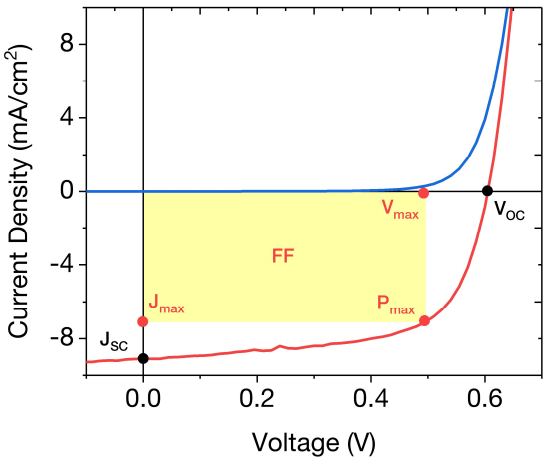


**Figure 1.23** Example of a J-V curve showing both the dark current in blue and illuminated current in red.

The diode ideality factor typically varies between 1-2 depending on the semiconductor and the fabrication process. The *ideal Shockley diode equation* is therefore typically employed where $n = 1$. When the cell is illuminated, it begins to generate power and the J-V curve shifts due to the illuminated current $J_{\mathrm{il}}$. Furthermore, for most illuminated cells with $V > 100\ \mathrm{mV}$ (as is typical), the exponential term is $\gg 1$, and so the $-1$ term can be neglected. As such, the J-V curve of an illuminated cell is given by

$$J = J_{\mathrm{il}} - J_0 \left[ exp\left(\frac{qV}{kT}\right) \right] \tag{1.7}$$

As the current generated by a solar cell is dependent on surface area, the performance of an OPV is given in terms of *current density*, where the amount of current generated is independent of surface area. The *short-circuit current* ($J_{\mathrm{SC}}$) is the current density generated by a solar cell when the voltage across the cell equals zero and is the maximum current possible for any given solar cell. As well as surface area, $J_{\mathrm{SC}}$ is dependent on illumination strength, charge separation yield, optical and thermal losses, and collection of charges at the electrodes.

### 1.3.4.2 Open-Circuit Voltage

As $J_{\mathrm{SC}}$ is the maximum available current from a solar cell when the voltage of the cell is zero, the *open-circuit voltage* ($V_{\mathrm{OC}}$) is the maximum available voltage from a solar cell when current across the cell equals zero and can be calculated by rearranging **Equation 1.7** as

$$V_{\mathrm{OC}} = \frac{kT}{q} ln\left(\frac{J_{\mathrm{SC}}}{J_0}\right) \tag{1.8}$$

#### 1.3.4.3 Fill Factor

Although $J_{\mathrm{SC}}$ and $V_{\mathrm{OC}}$ represent the maximum current and voltage available from a solar cell, the actual power of a solar cell – being the product of these two values – is zero for both $J_{\mathrm{SC}}$ and $V_{\mathrm{OC}}$, where $V$ and $J$ equal zero respectively. Therefore, a more pertinent aspect of a solar cell is the ratio between the maximum experimentally obtainable power $(J_{max}V_{max})$ and the theoretically maximum power $(J_{\mathrm{SC}}V_{\mathrm{OC}})$, known as the *fill factor* $(\mathrm{FF})$.

$$\mathrm{FF} = \frac{J_{max}V_{max}}{J_{\mathrm{SC}}V_{\mathrm{OC}}} \tag{1.9}$$

Visually, this can be seen as the "squared-ness" of the J-V curve (**Figure 1.23**). An ideal $\mathrm{FF}$ of 1 corresponds to a cell which can provide constant maximum current and voltage, however this is not accessible experimentally; A typical silicon $p$-$n$ cell has a $\mathrm{FF} \sim 0.85$ and indeed some exceptional organic solar cells can give $\mathrm{FF} \sim 0.8$ in the best cases.[91]

#### 1.3.4.4 Power Conversion Efficiency

To completely analyse the performance of a solar cell, all the above parameters must be considered together, giving rise to the power conversion efficiency (PCE, $\eta_{\mathrm{e}}$) as the ratio of electricity collected to the incident photon flux $P_{\mathrm{in}}$ acting on the device

$$\eta_e = \frac{J_{\mathrm{SC}}V_{\mathrm{OC}}\mathrm{FF}}{P_{\mathrm{in}}} = \frac{J_{max}V_{max}}{P_{\mathrm{in}}} = \frac{P_{\mathrm{out}}}{P_{\mathrm{in}}} \tag{1.10}$$

#### 1.3.4.5 Quantum Efficiency

The quantum efficiency of a solar cell is the ratio of charge carriers collected relative to the number of photons of a certain wavelength incident on the solar cell. Integrating a solar cell's quantum efficiency over the entire electromagnetic spectrum gives the total amount of current a cell will produce when illuminated by sunlight $(J_{\mathrm{max}})$. There are two main types of quantum efficiency, the external (EQE) and internal (IQE) quantum efficiencies. External QE is the ratio of charge carriers collected relative to the number of incident photons of a wavelength, whereas the internal QE considers reflection of photons and is the ratio of charge carriers collected relative to the number of incident photons of a wavelength which are absorbed by the cell. As EQE is dependent on a cells ability to both absorb light and collect free charges, it is favoured over IQE which provides a more idealistic model. Therefore, EQE is used to evaluate OPV performance

$$\mathrm{EQE} = \frac{e^-/\mathrm{sec}}{\mathrm{photons/sec}} = \frac{\mathrm{current/charge\ of\ an}\ e^-}{\mathrm{total\ power\ of\ photons\ /\ energy\ of\ one\ photon}} \tag{1.11}$$

In an ideal scenario, a cell would have an EQE of 100% for every wavelength with energy greater than the optical band gap. However, QE for all solar cells at most wavelengths is $\ll 100\%$ due to recombination and decay pathways preventing collection of charge carriers, the probabilities of which are also directly related to the photoabsorption probability of the material at each wavelength.

## 1.4 Organic Field-Effect Transistors

### 1.4.1 Principles

#### 1.4.1.1 Architecture

A transistor is the fundamental building block of all modern electronic devices. Modern microchips contain billions of transistors which exploit semiconductors to generate, amplify and control electrical signals. A field-effect transistor (FET) is a transistor in which current is carried along a channel whose effective resistance is controlled by a transverse electric field. Like OPVs, both small molecule and polymer organic semiconductors have been successfully utilised in FETs, however this thesis will focus solely on organic polymer FETs.

There are four FET device architectures which share identical components, but are laid in different configurations (**Figure 1.24**). An FET consists of three electrodes – a source (S), a drain (D) and a gate (G) – and two layers: a semiconductor and a dielectric. The dielectric is an electrical insulator that can be polarised by an applied electric field, thus controlling the resistance of the FET channel. The channel is the distance between the S and D electrodes and is defined by its width $(W)$ and length $(L)$, where typically $W \gg L$.

The source and drain electrodes (SD) are either placed on, or embedded in, the semiconducting layer and the gate (G) electrode is separated from the device by the dielectric layer. The source electrode injects charges into the semiconductor whilst the drain electrode drains them. The gate electrode controls the charge density (i.e. the resistance) of the channel at the dielectric/semiconductor interface (the operating principle is discussed in detail in the next section).

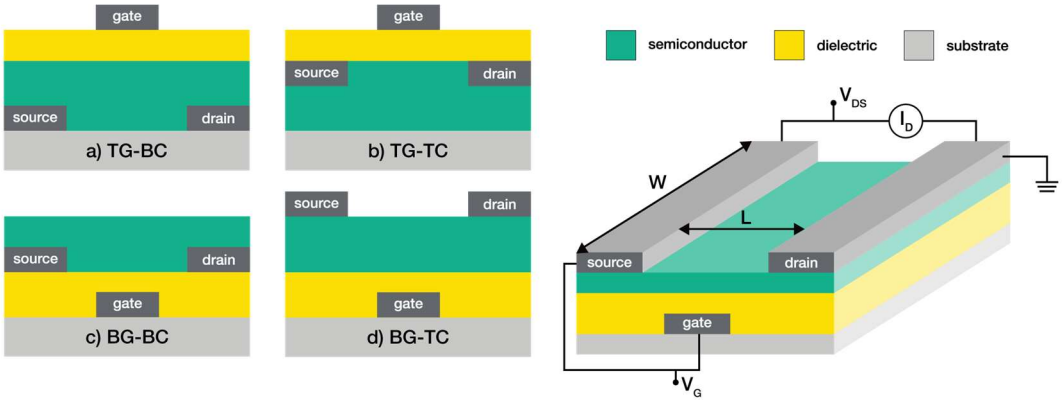


**Figure 1.24** Left: OFET architectures and their abbreviations: a) top-gate bottom-contact; b) top-gate top-contact; c) bottom-gate bottom-contact; d) bottom-gate top-contact; Right: schematic of a BG-TC OFET showing the channel with width $W$ and length $L$

All three electrodes are solely metallic in composition and are typically installed through vapour deposition using shadow masks. It is crucial to select metals whose work function matches the energy levels of the semiconductor, otherwise injection barriers will be formed, negatively impacting device performance. Furthermore, the work function of some metals can be altered by chemical treatment to improve the energetic matching to the semiconductor. Similarly, the dielectric layer needs to be chosen judiciously for each semiconductor, architecture and deposition technique. The capacitance of a dielectric $C_i$ is given by

$$C_i = \varepsilon_0 \frac{\varepsilon_\mathrm{r}}{d} \tag{1.12}$$

where $\varepsilon_\mathrm{r}$ is the relative permittivity (or dielectric constant), $d$ is the layer thickness and $\varepsilon_0$ is the vacuum permittivity. Whilst layer thickness can be controlled during the deposition of the material, $\varepsilon_\mathrm{r}$ is an intrinsic property of each dielectric. Common OFET dielectrics include silicon dioxide $(\varepsilon_\mathrm{r} = 3.9)$, poly(methyl methacrylate) (PMMA, common acrylic $\varepsilon_\mathrm{r} = 2.6$) and CYTOP (cyclic transparent optical polymer) $(\varepsilon_\mathrm{r} = 2.1)$.[92]

### 1.4.1.2 Basic Operating Principles

When a voltage is applied to the gate $(V_\mathrm{G})$, charges of the opposite polarity will be attracted to the semiconductor-dielectric interface from the source electrode and occupy available states in the channel of the semiconductor. There are three classifications of semiconductors: n-type, p-type and ambipolar. In an n-type material, electrons $(e^-)$ are the mobile charge carrier against a positive $V_\mathrm{G}$, whilst in a p-type material travelling vacancies called "holes" $(h^+)$ in the electron population of the occupied MO of the semiconductor act as mobile positive charge carriers against a negative $V_\mathrm{G}$. In an ambipolar material, both electrons and holes can serve as mobile charge carriers

depending on the polarity of the applied gate voltage. Strictly speaking, a semiconductor should not be defined as a n-type, p-type or ambipolar without reference to exact species of electrodes, but often is for convenience.

In an OFET, the precise energies of a semiconductor's frontier MOs levels are much more important than the value of the material's optical band gap. The more closely matched the semiconductor $E_{homo}$ and $E_{lumo}$ are with the work functions of the device electrodes, the better the ability to accept charges (charge injection) and therefore the higher the performance. A n-type semiconductor has a well-matched $E_{lumo}$ and so has a high affinity to accept electrons. Likewise, a p-type semiconductor with well-matched $E_{homo}$ has a high affinity to accept holes. An ambipolar semiconductor has well-matched $E_{lumo}$ and $E_{homo}$ and so can facilitate high transport of either $e^-$ and $h^+$ depending on the polarity of the applied gate voltage $(\pm V_{\mathrm{G}})$. If the energy levels of the semiconductor are not well matched large potential barriers exist and poor charge-injection results.

For a p-type transistor, an applied negative $V_{\mathrm{G}}$ results in holes attracted from the S electrode that occupy HOMO states in the semiconductor. Similarly, for an n-type transistor, a positive applied $V_{\mathrm{G}}$ will result in electrons being attracted from the S electrode that occupy LUMO states in the semiconductor. Crucially, the number of accumulated charges at the semiconductor-insulator interface is proportional to both the applied gate voltage and the capacitance of the dielectric.

The induced charges are free to move under the influence of an external field achieved by applying a potential to the drain electrode, and hence can flow from the S to the D. This is the source-drain current, but is more currently referred to as the drain current $I_{\mathrm{D}}$.

#### 1.4.1.3 Semiconductor Morphology

Of equal importance as the energetics of an OFET device is the precise microstructural morphology of the semiconductor thin-film – ideal energetics are worthless if poor molecular packing prevents efficient charge transport through the thin-film semiconductor. Order in an organic polymer thin-film can be characterised through three-dimensions (**Figure 1.25**): lamellar order between polymer backbones $(100)$; $\pi$-stacking of polymer backbones $(010)$; and order along polymer backbones $(001)$. Polymers can also orientate themselves both face-on and edge-on with respect to the substrate.

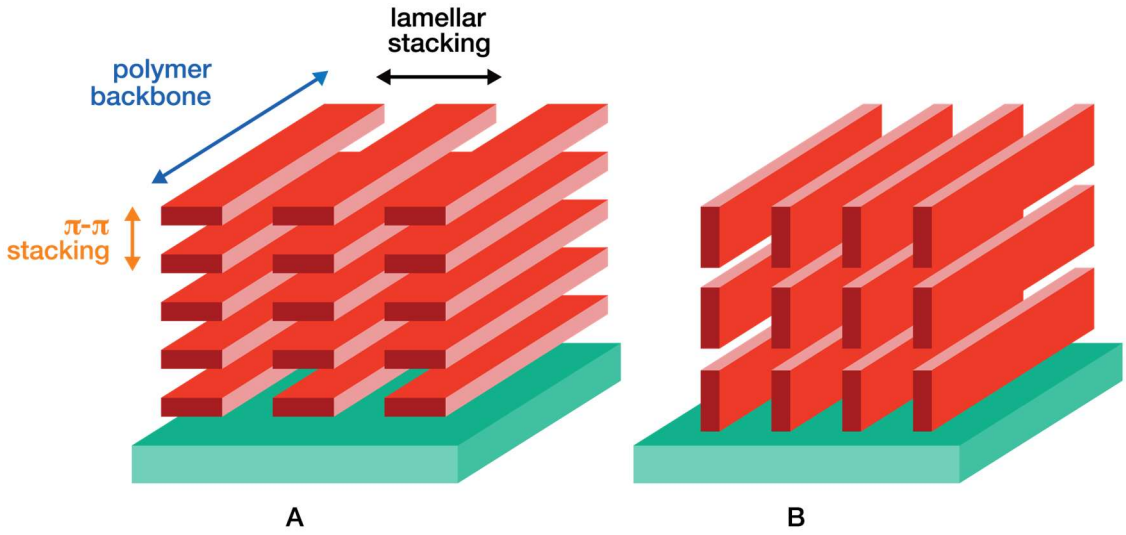


**Figure 1.25** Molecular packing of polymer chains on substrates showing face-on (A) and edge-on (B) orientations and the 3D crystallinity of polymer thin-films

The amorphous nature of polymers means studying molecular packing is much harder relative to small molecule semiconductors which exhibit high crystallinity. In crystalline aromatic semiconductors, four packing motifs are common: herringbone motif with and without $\pi$-stacking, and lamellar motif with 1D and 2D $\pi$-stacking (**Figure 1.26**).[93–96] Of these four motifs, lamellar packing with 2D $\pi$-stacking is believed to be the most efficient nanostructure for efficient charge transport due to high transfer integrals and the ability to transport charge carriers in long, straight lines.[95]

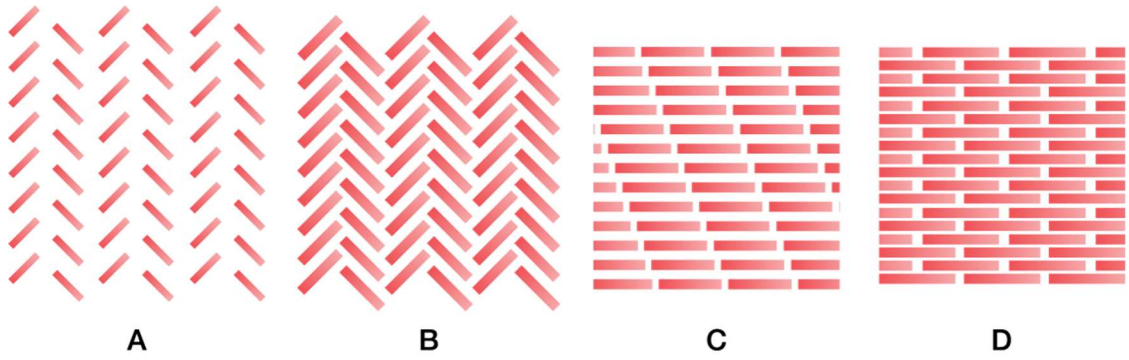


**Figure 1.26** Molecular packing of small molecule organic semiconductors: (A) herringbone packing without $\pi - \pi$ overlap between adjacent molecules (e.g. pentacene); (B) herringbone packing with $\pi - \pi$ overlap (e.g. rubrene); (C) lamellar packing with 1D $\pi$-stacking (e.g. naphthalene diimide); (D) lamellar packing with 2D $\pi$-stacking (e.g. TIPS-pentacene)

Thin-films of typical polymer semiconductors exhibit lamellar crystallinity with both edge-on and face-on crystallites. Synthetic strategy can be used to improve order along polymer backbones: heteroatom-heteroatom and heteroatom-fluorine intramolecular interactions create “conformational locks” reducing disorder; and covalently bridging

aromatic rings (*c.f.* biphenyl vs fluorene) gives rise to lower degrees of rotational freedom, stiffening the polymer backbone, facilitating efficient $(001)$ charge transport.

The choice of solubilising alkyl side chains has a significant effect over total thin-film morphology. Shorter chains decrease lamellar packing distances and increase overall lamellar crystallinity. However, shortening chains reduces the solubility and processability of the polymer, which is one of the most desirable properties of organic polymers. Branched alkyl chains can improve solubility and impact crystallinity favourably, however if the branching point is too close to the polymer backbone the $\pi - \pi$ interchain packing distance will increase leading to reduced charge transport in the $\pi - \pi$ direction.[97]

Unfortunately, there remains no defining theory to predict polymer crystallinity based on alkyl chain selection and researching chain-polymer relationships remains an empirical process.

### 1.4.2 Operating Principles

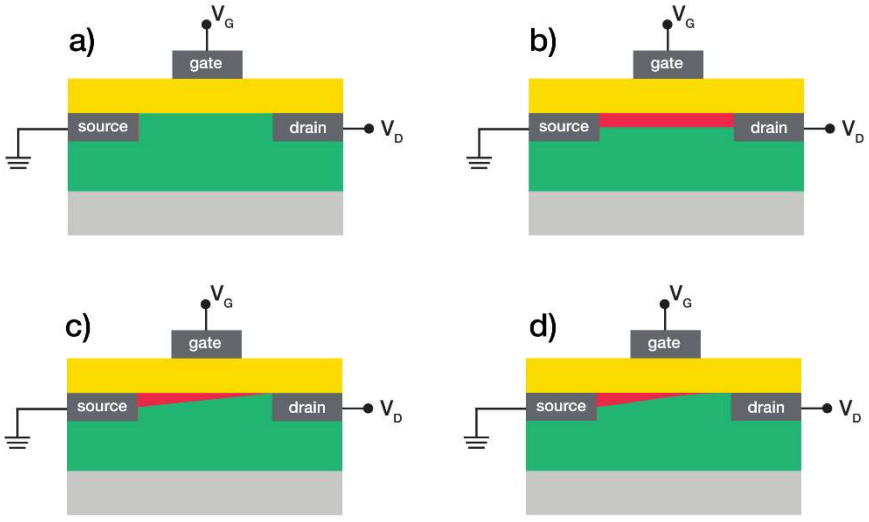


**Figure 1.27** Charge carrier density (red) as a function of distance ($x$) from the source electrode. (a) OFF state, $V_G = V_D = 0$; (b) Uniform concentration of accumulated charges when $|V_{Th}| > |V_G| > 0 = V_D$; (c) Linear variation in carrier density with $x$ when $|V_G - V_{Th}| > |V_D|$; (d) A "pinched-off" channel when $|V_G - V_{Th}| \leq |V_D|$ forming a depletion region adjacent the drain

An OFET is considered in its **OFF** state when $V_G = 0$ and there is no (or insignificant) drain current $I_D \sim 0$ (**Figure 1.27a**). If a bias is applied to the gate electrode $|V_{Th}| > |V_G| > 0$ a charge carrier accumulation layer of uniform density is formed at the semiconductor-dielectric interface, however $I_D = 0$ and device remains in its **OFF** state (b).

If a voltage of the same polarity as the gate is then applied to the drain $|V_{\mathrm{D}}| > 0$, current begins to flow from the source to the drain $|I_{\mathrm{D}}| > 0$, and the OFET is considered in its **ON** state. So long as the voltage at the gate has a greater magnitude than the voltage at the drain, i.e. $|V_{\mathrm{G}} - V_{\mathrm{Th}}| < |V_{\mathrm{D}}|$, there will be a linear variation in the drain current with respect to drain voltage. Transistor behaviour of this type are said to be operating in the *linear regime* (c).

As $V_{\mathrm{D}}$ is gradually increased, the spatial distribution of charge carriers will become non-linear and so the device will exhibit non-linear variation in $I_{\mathrm{D}}$ with respect to $V_{\mathrm{D}}$. Once the magnitude of the $V_{\mathrm{D}}$ reaches and exceeds $(V_{\mathrm{G}} - V_{\mathrm{Th}})$ the channel becomes "pinched-off" (d) and a depletion region forms adjacent to the D. The resistance of this region is very high and as $V_{\mathrm{D}}$ is increased past the pinch-off point, the depletion region grows and the drop in voltage between the S and the pinch-off point remains constant at $V(x) = V_{\mathrm{G}} - V_{\mathrm{Th}}$, hence the current remains constant. A transistor operating in this fashion is said to be in the *saturation regime*.

To characterise a FET, two measurements are made: (1) $I_{\mathrm{D}}$ as a function of $V_{\mathrm{D}}$ at interval values of $V_{\mathrm{G}}$, known as output characteristics; (2) $I_{\mathrm{D}}$ as a function of $V_{\mathrm{G}}$ in the linear (low $V_{\mathrm{D}}$) and saturated (high $V_{\mathrm{D}}$) regimes, known as transfer curves (**Figure 1.28**).

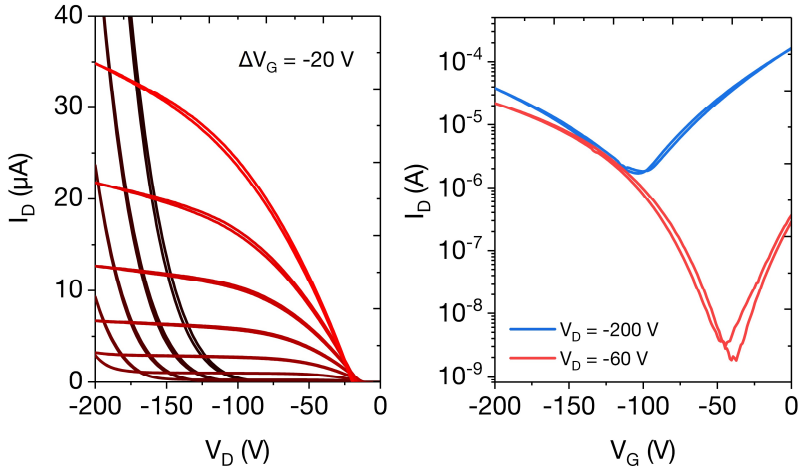


**Figure 1.28** Typical output (left) and transfer (right) characteristics for a p-type OFET

### 1.4.3 Assessing Performance

To extract operational performance parameters from a FET it is necessary to use the gradual channel approximation. This model assumes that (1) voltages vary gradually along the channel between the SD electrode and (2) voltages vary quickly perpendicular to the channel between the insulator and the semiconductor bulk. A mathematical

analysis of this model is beyond the scope of this thesis, but the equations that follow are derived from this concept.

In Figure 1.27b, where $|V_{\mathrm{Th}}| > |V_{\mathrm{G}}| > 0$, the areal number density of induced mobile charge carriers $(Q_{mob})$ in the charge carrier accumulation layer of uniform density formed at the semiconductor interface is given by

$$Q_{mob} = C_i(V_{\mathrm{G}} - V_{\mathrm{Th}}) \tag{1.13}$$

and so, the relationship between the charge density at a distance $x$ from the S can be expressed as

$$Q(x) = C_i[V_{\mathrm{G}} - V_{\mathrm{Th}} - V(x)] \tag{1.14}$$

where $V(x)$ is the channel bias at position $x$. To evaluate drain current in terms of the applied voltages, the change in channel resistance $dR$ with respect to channel position $dx$ is given by

$$dR = \frac{dx}{WQ(x)\mu} \tag{1.15}$$

where $\mu$ is the charge carrier mobility and $W$ is the channel width. For this to be a valid relationship, an assumption is made that the length of the channel $L$ is much greater than the thickness of the film such that the electric field in the $x$-direction is negligible in comparison to the field perpendicular. It is also necessary to assume that charge carrier mobility is not dependant on positions, i.e. $\mu \neq \mu(x)$, which also implies $\mu \neq V(x)$.

The first of the above assumptions does not hold true in FETs with channel lengths below the micron-scale, giving rise to $short\text{-}channel\ effects$ in such systems. There are also examples of electric-field dependence mobility where the second assumption does not apply. But the following equations are given for a FET with an adequate channel length and where $\mu \neq \mu(x)$, whereby $\mu$ represents the mean carrier mobility in the channel.

Using the differential form of Ohm's law,

$$dV(x) = I_{\mathrm{D}} dR \tag{1.17}$$

substituting **Equations 1.14** and **1.15** and integrating over the FET channel,

$$\int_0^L I_{\mathrm{D}}\, dx = W\mu \int_0^{V_{\mathrm{D}}} C_i[V_{\mathrm{G}} - V_{\mathrm{Th}} - V(x)]\, dV(x) \tag{1.18}$$

Hence:

$$I_{\mathrm{D}} = \mu C_i \frac{W}{L}\left[(V_{\mathrm{G}} - V_{\mathrm{Th}})V_{\mathrm{D}} - \frac{V_{\mathrm{D}}^2}{2}\right] \tag{1.19}$$

where $I_{\mathrm{D}}$ is the drain current, $\mu$ is the charge carrier mobility, $C_i$ is the dielectric capacitance per unit area, $L$ and $W$ are the OFET channel length and width respectively, $V_{\mathrm{G}}$ is the gate voltage, $V_{\mathrm{Th}}$ is the threshold voltage, and $V_{\mathrm{D}}$ is the drain voltage.

#### 1.4.3.1 Linear Regime Mobility

For low drain voltages, i.e. $|V_{\mathrm{D}}| \ll |V_{\mathrm{G}} - V_{\mathrm{Th}}|$, where the FET is operating in the linear regime, **Equation 1.19** can be approximated to

$$I_{\mathrm{D}} = \mu_{lin} C_i \frac{W}{L}(V_{\mathrm{G}} - V_{\mathrm{Th}})V_{\mathrm{D}} \tag{1.20}$$

and so, the mobility in the linear regime $\mu_{lin}$ can be expressed by taking the first derivative of $I_{\mathrm{D}}$ with respect to $V_{\mathrm{G}}$

$$\mu_{lin} = \frac{L}{WC_iV_{\mathrm{D}}}\frac{\partial I_{\mathrm{D}}}{\partial V_{\mathrm{G}}} \tag{1.21}$$

#### 1.4.3.2 Saturation Regime Mobility

Once the magnitude of the drain voltage approaches or exceeds the gate voltage, $|V_{\mathrm{D}}| \geq |V_{\mathrm{G}} - V_{\mathrm{Th}}|$, the device enters the $saturation$ regime and the channel current becomes independent of $V_{\mathrm{D}}$, such that $V_{\mathrm{D}} = V_{\mathrm{G}} - V_{\mathrm{Th}}$. Substituting this into **Equation 1.19**

$$I_{\mathrm{D}} = \mu_{sat} C_i \frac{W}{2L}(V_{\mathrm{G}} - V_{\mathrm{Th}})^2 \tag{1.22}$$

and so, the saturation regime can be evaluated from either the second derivative of $I_{\mathrm{D}}$ with respect to $V_{\mathrm{G}}$,

$$\mu_{sat} = \frac{L}{WC_{\mathrm{i}}}\frac{\partial^2 I_{\mathrm{D}}}{\partial V_{\mathrm{G}}} \tag{1.23}$$

or the square-root of the first derivative

$$\mu_{sat} = \frac{2L}{WC_{\mathrm{i}}}\left(\frac{\partial\sqrt{I_{\mathrm{D}}}}{\partial V_{\mathrm{G}}}\right)^2 \tag{1.24}$$

#### 1.4.3.3 On Voltage & Threshold Voltage

The necessary magnitude of $V_{\mathrm{D}}$ at which current begins to flow through the channel and the device enters its $\mathbf{ON}$ state in the linear regime is termed the "on voltage" $V_{\mathrm{on}}$. The threshold voltage $V_{\mathrm{Th}}$ represents the magnitude of $V_{\mathrm{D}}$ at which charges flow freely between the S and D electrodes, i.e. it is the amount of bias required to induce a channel of mobile charges in a semiconductor.

From **Equations 1.20** & **1.22**, an extrapolation of a plot of the square root of the drain current to $\sqrt{I_{\mathrm{D}}} = 0$, i.e. the intercept, $V_{\mathrm{Th}}$ can be approximated. In practice, the saturation regime is used for calculating $V_{\mathrm{Th}}$ due to the conditions that $|V_{\mathrm{D}}| \leq |V_{\mathrm{G}} - V_{\mathrm{Th}}|$ is not valid near the origin of a plot of $I_{\mathrm{D}}/V_{\mathrm{G}}$ in the linear regime.

Between $V_{\mathrm{on}}$ and $V_{\mathrm{Th}}$, the applied potential accounts for the mismatching of the frontier MO levels to the fermi level of the electrodes and the filling of charge traps in the thin-film, which essentially render trapped charge carriers immobile.

#### 1.4.3.4 On/Off Ratio

The on/off ratio $(I_{\mathrm{on}}/I_{\mathrm{off}})$ is self-explanatory in being the ratio of the current in the ON regime versus the OFF regime. A high performance OFET must have a large on/off ratio of several factors to be able to differentiate with ease between the two states. $I_{\mathrm{on}}/I_{\mathrm{off}}$ as high as $10^8$ has been reported, but common values range from $10^3 - 10^7$.[65]

### 1.4.4 Estimating Charge Carrier Mobility

Charge carrier mobility, as defined in the above sections, is the flagship property for the discovery of new OFET materials. Amorphous silicon FETs exhibit $\mu$ of ~1 $cm^2/Vs$, and is used as the benchmark to which OFET mobilities are compared. Mobilities in the range of 0.1 to 1.0 $cm^2/Vs$ are considered good, and values above 1 $cm^2/Vs$ are considered "ultra-high" and feature much less in the literature. Semiconductors with $\mu < 0.1$ $cm^2/Vs$ are often reported, and whilst may not represent a significant breakthrough, can reveal interesting structure-property relationships which are needed to build design rules and further the field as a collective. There is a need for organic semiconductors with $\mu$ approaching 10 $cm^2/Vs$ to compete with inorganic materials in modern electronic circuitry. As research has progressed, novel materials have emerged claiming $\mu$ in the scale of 1 to 10 $cm^2/Vs$, however their accuracy has been drawn into debate.[98,99]

The equations discussed above are derived from a system which obeys the gradual-channel approximation (GCA).[6,100] If an OFET does indeed obey the gradual-channel

model, a plot of the square-root of the drain current $(I_{\mathrm{D}}^{0.5})$ of the transfer curve will be linear, and the gradient of the plot can be used to calculate $\mu$ and the extrapolated intercept used to estimate $V_{\mathrm{Th}}$.

Whilst this model was sufficient for describing transistor behaviour of early OFETs where mobilities were limited by the organic semiconductor, developments have resulted in devices where the semiconductor is not the limiting factor for device performance. In these cases, devices exhibit nonidealities which deviate from the GCA-model, manifesting experimentally as nonlinear plots of $I_{\mathrm{D}}^{0.5}$ as a function of $V_{\mathrm{G}}$ (**Figure 1.29**).

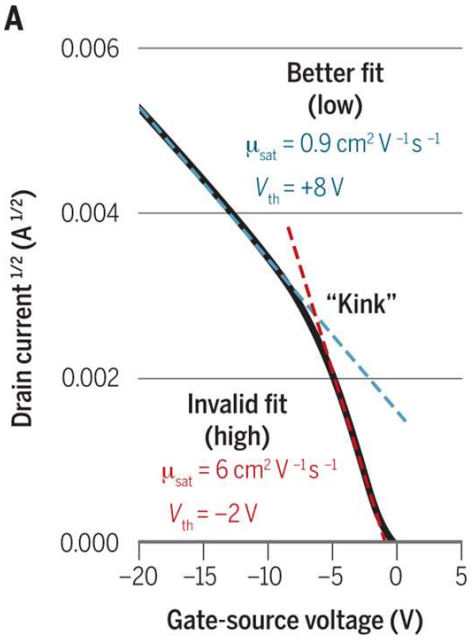


**Figure 1.29** A rubrene small molecule OFET displaying non-ideal character and deviation from the gradual channel model. The true mobility of the device is closer to 0.9 than 6.0 $\mathrm{cm}^2/\mathrm{Vs}$ (from McCulloch *et al.*, 2016).[98]

Several nonidealities have arisen in modern OFET materials. Charge trapping localised around electrodes invalidates a key assumption of the GCA and in one example resulted in $\mu_{\mathrm{e}}^{sat}$ of 19 $\mathrm{cm}^2$/Vs, recorded after localised electron trapping at the D electrode, whilst $\mu_{\mathrm{e}}^{lin}$ of 0.84 $\mathrm{cm}^2$/Vs was recorded before the localised trapping, the latter representing a more accurate estimation of bulk transport.[101] Another nonideality arises from contact-limited performance of an OFET device where contact resistance $(R_{\mathrm{C}})$ shows a gate voltage bias dependence.[102] The resulting nonlinearities of the $I_{\mathrm{D}}^{0.5}$ data can lead to extreme over-estimations of charge carrier mobility and this dangerous practice results in the reporting of incorrect structure-property relationships and the clouding of true molecular design principles.

Due to the material properties of OFET semiconductors being so vastly different from inorganic thin-film transistors, and the lack of better models of which to estimate carrier

mobilities of systems exhibiting nonidealities, it is important to apply conservatism when extracting mobility values from nonlinear systems.

## 1.5 Nature-Inspired Building Blocks

An underlying issue in the field of organic semiconductors is that most monomer units are completely synthetic, produced from petrochemicals derived from crude oil. In the case of OPVs, the ideal scenario for truly renewable energy cannot include the manufacturing of semiconductors from crude oil. The issue is less a philosophical for OFETs, but in order for organic semiconductors to be competitive in a silicon-driven industry, organic FET materials must be cheaper than their inorganic counterparts without loss of performance.

A solution to these issues is to farm precursors from renewable natural sources, such as plants. Natural plant dyes are brightly coloured due to their strong absorption in the UV-vis region of light. The part of each molecule which is responsible for light absorption – the chromophore – provides a platform for building semiconductors from natural products. A library of naturally occurring organic dyes are available to the synthetic chemist including indigo, indirubin, azulene dyes such as guaiazulene, quinacridones, and indanthrene derivatives (**Figure 1.30**).[103–109]

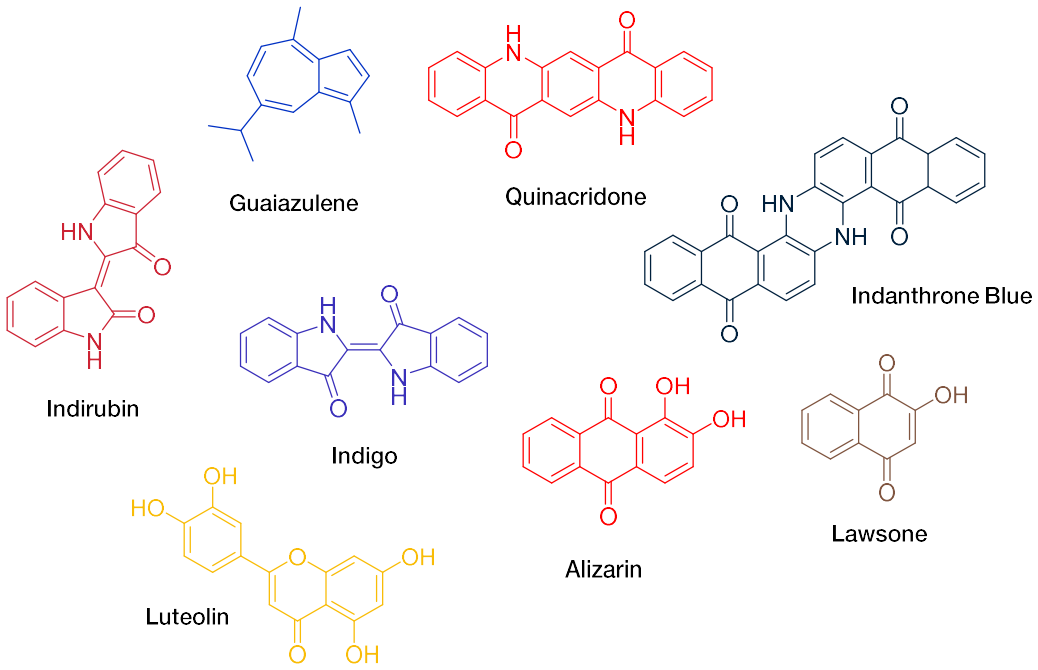


**Figure 1.30** Organic dyes derived from plants

Indigo is the most produced dye worldwide and has a highly planar structure arising from intramolecular hydrogen bonding between the oxygen and the amine protons of the indol-3-one units.[110] Upon photoexcitation, both rotation about the central carbon-carbon

bond and single or double proton transfer results in rapid energy loss, thereby negating any potential for OPV devices (**Figure 1.31**).[111,112]

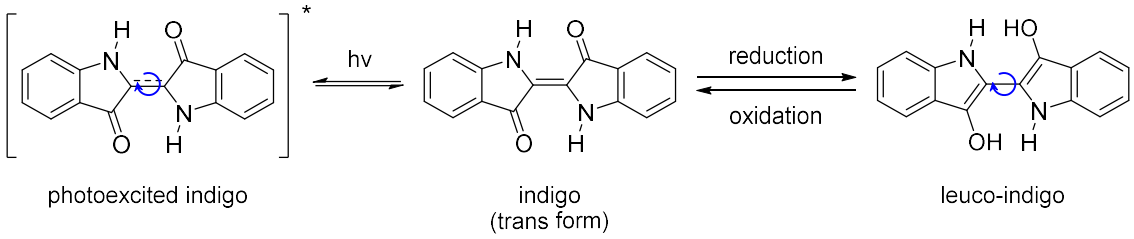


**Figure 1.31** Deactivation pathways of indigo

Indigo has successfully been used as a semiconductor in OFET devices, with reported hole mobilities up to $1\times10^{-2}$ cm$^2$/Vs.[113] More recently, functionalised indigoids have been investigated, and the p-type transport can be slightly enhanced to $1.3\times10^{-2}$ cm$^2$/Vs using 5,5'-dichloroindigo.[114] Cibalackrot is a synthetic dye derived from indigo, first reported in 1914, made by a double condensation reaction of indigo with phenylacetyl chloride, forming cibalackrot with two new ring systems (**Scheme 1.3**).[115]

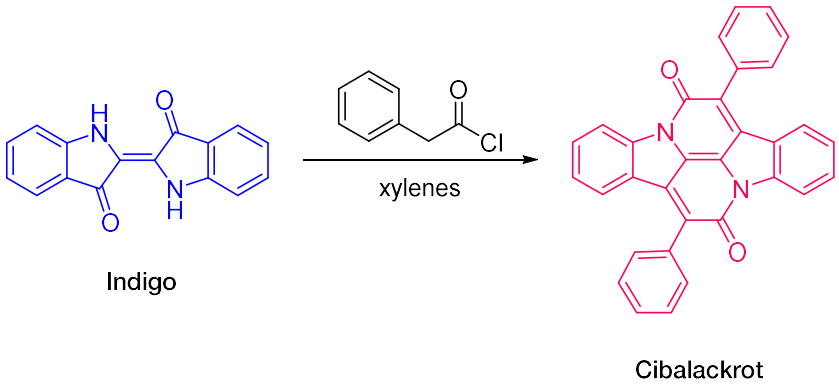


**Scheme 1.3** Condensation reaction of indigo with phenylacetyl chloride to produce cibalackrot

In cibalackrot, the new ring systems afford a central "core" which is locked in a highly planar rigid conformation where proton transfer and rotation are not possible. Structurally, cibalackrot has similar functionality to other bis-lactam systems such as DPP and should exhibit similar electronic deficiencies making it an excellent acceptor-type monomer for narrow band gap D-A polymers. Remarkably however, there are almost no reports of exploiting cibalackrot in semiconductor applications. In 2011, Glowacki *et al.* reported it exhibited ambipolar behaviour with $\mu_h = 5 \times 10^{-3}$ and $\mu_e = 9 \times 10^{-3}$ cm$^2$/Vs in small molecule OFETs,[116] and in 2014 He *et al.* reported a thiophene derivative of cibalackrot in an organic polymer which exhibited high mobilities of $\mu_h = 1.5$ and $\mu_e = 0.4$ cm$^2$/Vs when copolymerised with complex solubilising donor monomers.[117]

## 1.6 Thesis Scope & Aims

The central core of Cibalackrot is *indolonaphthyridine* (derived from the chemical name diindolo[3,2,1-*de*:3',2',1'-*ij*][1,5]naphthyridine-6,13-dione, **Figure 1.32**). The primary aim of this thesis is to investigate the potential of indolonaphthyridine as a building block for novel organic semiconductors for applications in photovoltaics and organic field-effect transistors.

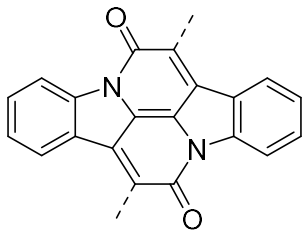


IND
indolonaphthyridine(dione)
(diindolo[3,2,1-*de*:3',2',1'-*ij*][1,5]
naphthyridine-6,13-dione)

**Figure 1.32** Structure of indolonaphthyridine (IND), the focus of this thesis

In the first part of this thesis, the potential of indolonaphthyridine-containing polymers is explored. The low solubility of Cibalackrot is first addressed by the synthesis of an indolonaphthyridine scaffold which can be alkylated to improve solubility. The soluble monomer is then polymerised with fundamental thiophene, selenophene, phenyl and benzothiadiazole co-monomers. Next, the influence of alkyl side chains on the system is studied in order to investigate the effect of polymer structure on solid-state microstructure and charge transport properties. Finally, indolonaphthyridine provides the opportunity to undergo polymerisations across the direction of conjugation. Types of polymers exhibiting this trait are called cross-conjugated polymers, and their chemistry is seldom explored despite the potential they provide as another strategy for band gap engineering. Two cross-conjugated polymers are synthesised to investigate whether this strategy can be employed to create wider band gap indolonaphthyridine systems.

In the last part of this thesis, a physical phenomenon called singlet fission is investigated. Cibalackrot has been suggested to be able to perform singlet fission, however no results confirming this ability have been published in the literature to date. In the final chapter, quantum chemical calculations are used to predict candidates for singlet fission and to deduce structure/property relationships for design rules. The synthesis and characterisation of the best candidates is then undertaken.

# II

*The Design & Synthesis of*
*Indolonaphthyridine Polymers*

## 2.1 Introduction

### 2.1.1 Cibalackrot

In the previous chapter, Cibalackrot **2.3** was identified as a potential building block for organic semiconductor design. Experimentally, **2.3** can be prepared by a dual condensation-annulation reaction of indigo **2.1** with phenylacetyl chloride in mixed xylenes at 165 °C (**Scheme 2.1**).

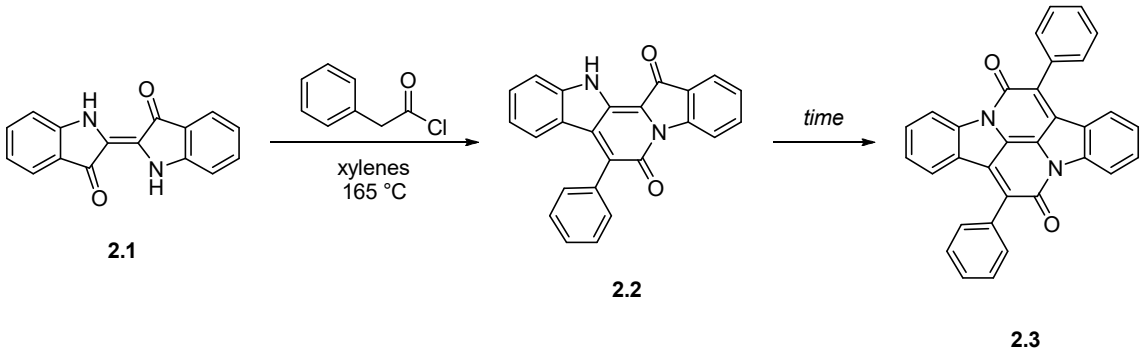


**Scheme 2.1** Duel condensation-annulation reaction of indigo with phenylacetyl chloride in mixed xylenes at 165 °C.

However, this reaction is typically very low yielding due to the poor solubility of indigo in almost every solvent. Indigo adopts a planar conformation due to intramolecular hydrogen bonding between the amine proton and carbonyl oxygen atoms, leading to proficient $\pi$-stacking and thus strong aggregation of the material.

To be regarded as a solution processable organic semiconductor candidate, the material needed a much higher degree of solubility to improve its material properties; The highly

planar, fused aromatic nature of **2.3** led to strong $\pi - \pi$ interactions in the solid-state, forming crystalline aggregates when spun into a thin-film.

The best method to improve solubility and to reduce aggregation of large aromatic systems is to install long aliphatic alkyl side-chains. As indigo provided no synthetic handle for installing alkyl chains on the benzene rings of **2.1** $(indigoid\ rings)$, it was necessary to introduce alkyl chains on the $peripheral$ aryl group installed through the condensation-annulation reaction (see Figure 2.2 for aryl group definitions). The synthetic route to alkylated phenylacetyl chlorides **2.10** and **2.11** is shown in **Scheme 2.2**.

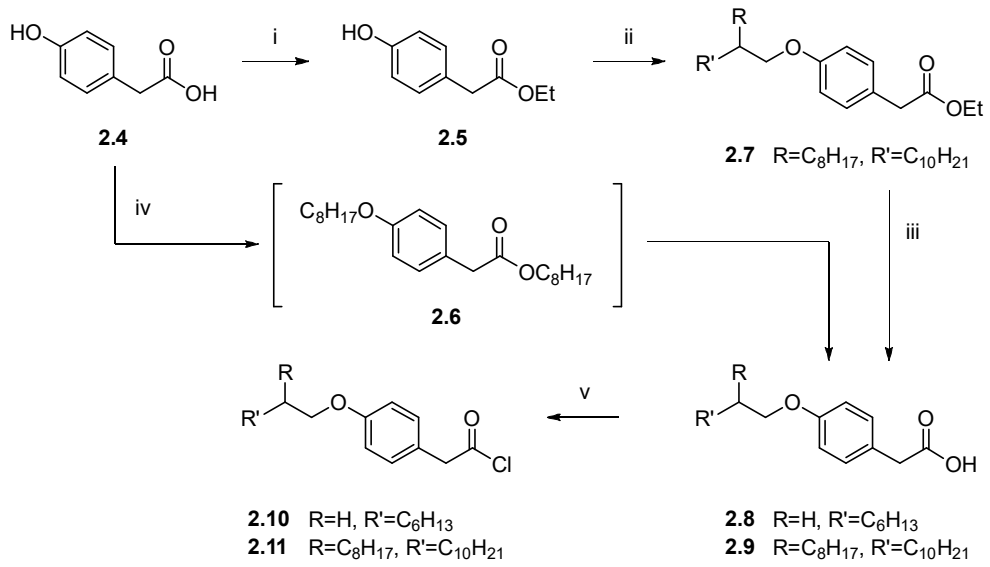


**Scheme 2.2** Synthesis of *para*-alkylated (oxy)phenylacetyl chlorides
i) EtOH, $H_2SO_4$, reflux, 4 h, 99%; ii) 2-Octyl-1-dodecyl bromide, $K_2CO_3$, anhyd. DMF, 80 °C, 64%; iii) NaOH, $H_2O$/MeOH, rt, 95 °C, 99%; iv) $C_8H_{17}Br$, KOH, EtOH, reflux, then 13M KOH, 84%; v) $SOCl_2$, cat. DMF, anhyd. DCM, reflux, 4 h, quant.

Firstly, 4-hydroxylphenylacetic acid **2.4** was protected by making its ethyl ester **2.5** to prevent alkylation of the carboxylic acid group. Two alkyl chains were investigated: a linear octyl chain ($C_8H_{17}$) and a branched 2-octyldodecanyl chain. Alkylations of **2.5** with both 1-bromooctane and 2-octyl-1-dodecanyl bromide proceeded in good yield. The deprotection of the ester groups and subsequent conversion to acyl chloride groups with excess thionyl chloride both proceeded in excellent yield to give the alkylated phenylacetyl chloride reagents **2.10**/**2.11**. Despite the solubilising alkyl chains, the condensation reactions of **2.1** with **2.10**/**2.11** (**Scheme 2.3**) proceeded in poor yield (~5%), still limited by the poor solubility of **2.1**.

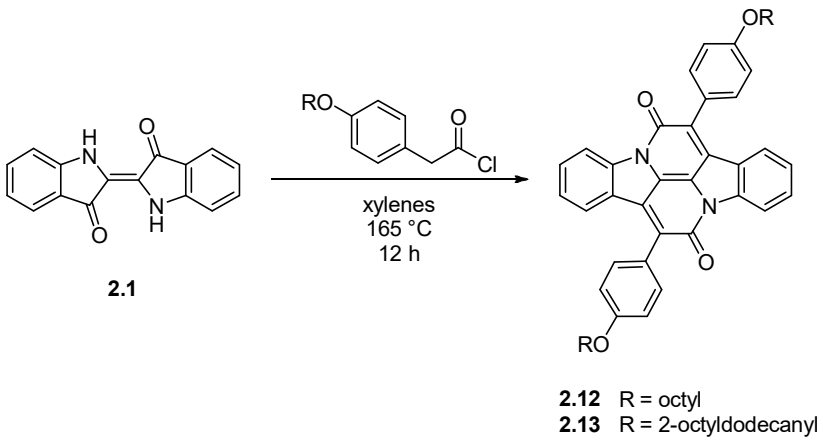


**Scheme 2.3** Condensation reactions with indigo and alkylated phenylacetyl chlorides in mixed xylenes at 165 °C.

The purification of **2.12** and **2.13** on silica gel was much easier as both the octyl and 2-octyldodecanyl chains provided higher degrees of solubility in chloroform and other non-chlorinated solvents such as THF, with retention factors between 0.5-0.7 in chloroform. **Figure 2.1** shows the solution (chlorobenzene) and thin-film (spun from 5 mg/mL solutions in chlorobenzene) UV-vis absorption spectra of the three materials.

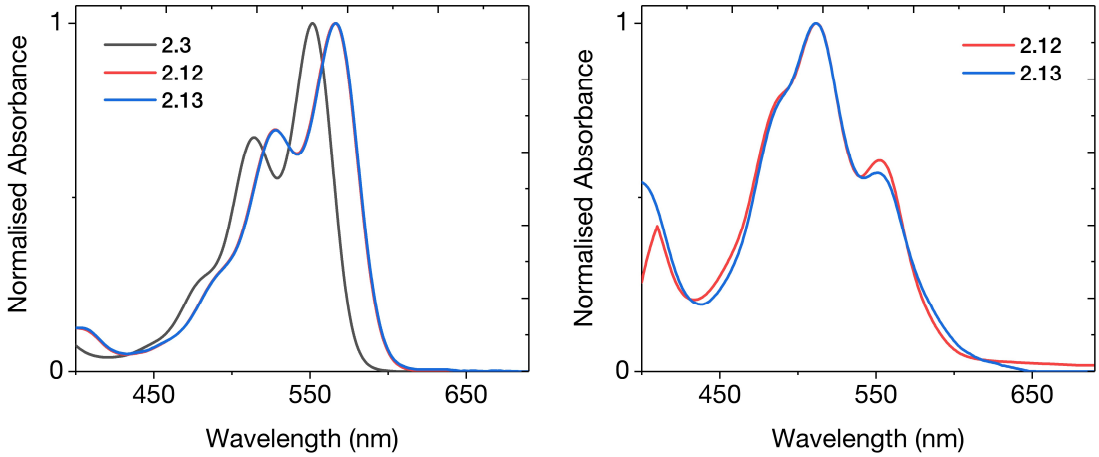


**Figure 2.1** UV-vis absorption spectra of **2.3**, **2.12** and **2.13** in solution (left, chlorobenzene) and thin-films (right, spun from a 5 mg/mL solution in chlorobenzene) of **2.12** and **2.13**. Note that in the solution spectra, **2.12** and **2.13** (red and blue) have practically identical absorbance.

The electron-donating nature of the *para*-alkyloxy group led to a bathochromic (red) shift indicating a narrowing of the optical band gap ($E_g$) of the materials, due to raising of $E_{homo}$. From the absorption onsets of the materials, $E_g$ of **2.3** was estimated to be 2.14 eV, whilst $E_g$ of **2.12**/**2.13** was 2.08 eV. The identical absorbance in solution for **2.12** and **2.13** showed how the length and complexity (i.e. branching) of the choice of alkyl chain does not affect the absorbance of discreet molecules in solution.

As discussed above, the poor solubility of **2.3** meant making a thin-film of the material was impossible. The addition of alkyl chains increased the solubility of the system and as such **2.12** and **2.13** were successfully spun into thin-films from chlorobenzene, however the quality of the film of **2.13** was better than **2.12** due to the greater solubility the branched chains provided. The thin-film absorbance of both materials was comparable, suggesting that solid-state aggregation was either similar, or had small effect on the $E_{\mathrm{g}}$ of these two materials.

It is important to note that the solubility of a polymer decreases as its molecular weight $(M_n)$ increases. For large planar aromatic systems like Cibalackrot, long branched alkyl chains are typically used to provide the highest degree of solubility. The octyldodecanyl chain has gained considerable popularity in organic semiconductor design, not only for its solubilising power but also for the ability of branched alkyl chains to improve thin-film morphology over linear alkyl chains.[118,119,97,120,58]

### 2.1.2 Aims of this Chapter

To simplify the nomenclature of the discussed materials, the “core” section of Cibalackrot, di**i**ndolo[3,2,1-*de*:3',2',1'-*ij*][1,5]**n**aphthyridine-6,13-**d**ione, will hereon be shortened to indolonaphthyridine and abbreviated as IND.

When considering indolonapthyridine as a candidate unit for organic semiconductor synthesis, the direction of conjugation through the material flows through the unit’s $peripheral$ aromatic groups. Therefore, it was assessed that the most logical place to install solubilising alkyl chains to be on the $indigoid$ aromatic rings. However, as natural indigo provides no synthetic handle for performing chemistry, it was necessary to target a synthetic indigoid which could be readily alkylated.

As discussed in detail in Chapter 1, thiophene-based polymer backbones have emerged as superior materials over benzene due to greater degrees of backbone planarity, higher effective conjugation lengths and greater electron density, all leading to polymers with narrow band gaps and frontier molecular orbital energy levels well-placed for OFET and OPV applications.

Quantum chemical calculations using the B3LYP functional at the 6-311G** level of theory found the dihedral angle connecting a benzene ring to IND had lowest energy at $\pm 51^{\circ}$ (**Figure 2.2**), whereas an IND–thiophene (INDT) dihedral had the lowest energy at $\pm 30^{\circ}$.

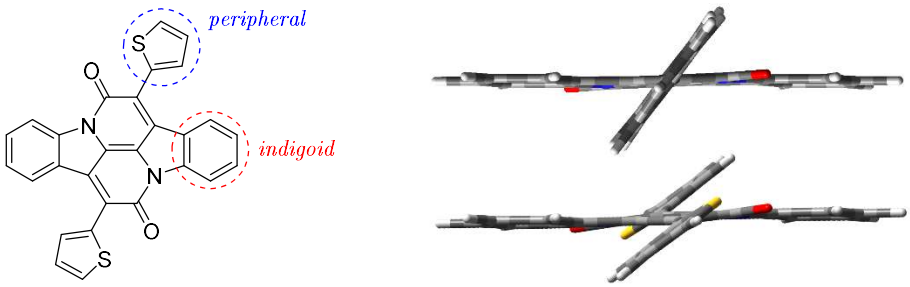


**Figure 2.2** Left: Structure of indolonaphthyridine thiophene or INDT; Right: Calculated geometries at the B3LYP/6-311G** level of theory showing out-of-plane *peripheral* groups – benzene (top) and thiophene (bottom)

Furthermore, INDT showed preference for the conformation where the sulphur atom of the thiophene is oriented toward the oxygen atom of the IND carbonyl, suggesting that S–O long range interactions may also contribute to the stabilisation of this conformation. Altogether, INDT showed greater promise of furnishing high performance polymers over IND–benzene analogues.

Therefore, the aim of the work described in this chapter was to synthesise a novel monomer based on indolonaphthyridine thiophene, solubilised with alkyl chains on the indigo core, and then investigate the properties of several typical INDT-based donor-acceptor copolymers and their prospective application in both OPVs and OFETs.

## 2.2 Synthesis

### 2.2.1 Monomer Synthesis

To install alkyl chains on the indigoid rings of the IND unit, two synthetic options were available: 1) Kumada coupling of a halogenated indigoid, such as dibromoindigo, with alkyl Grignard reagents; 2) alkylation of acidic functional groups, such as hydroxyl groups. Kumada couplings can be temperamental, reagent selective and rely on the use of Pd or Ni catalysts, which are undesirable both environmentally and fiscally.[121] In contrast, alkylation of hydroxyl groups is a facile, clean process, requiring only base and a suitable solvent, can be scaled safely and is free of transition metal catalysts. For these reasons, we chose to pursue installing hydroxyl groups onto the IND core.

The most well-known preparation of indigo is the Baeyer–Drewson Indigo Synthesis which is an aldol condensation reaction between 2-nitrobenzaldehyde **2.14** and acetone in alkaline water (**Scheme 2.4**).[122]

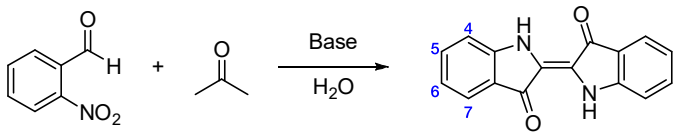


**Scheme 2.4** Baeyer–Drewson Indigo Synthesis

Despite its ease, the scope of the aqueous condensation reaction is limited such that the benzaldehyde cannot contain any acidic or hydrophobic functionality (**Scheme 2.5**) as phenols typically have a much lower pKa (~10) than the α-protons of acetone (19.2) and are preferentially deprotonated, interrupting the complicated reaction pathway. Large alkyl chains, such as 2-octyldodecanyl, are highly hydrophobic and limit the solubility of alkylated benzaldehydes in aqueous media, leading to the formation of micelles, preventing reaction.[123] Therefore, it was necessary to employ protecting group strategy to provide a pathway to compounds which could be alkylated selectively after the synthetic indigoid had been formed.

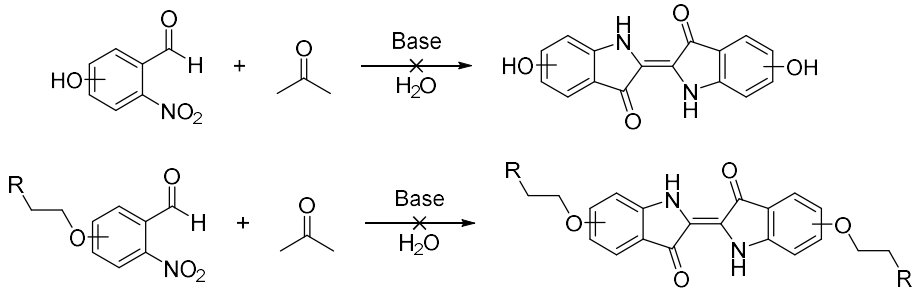


**Scheme 2.5** Limitations of the BDI synthesis of functionalised indigoids in aqueous media

When deciding which position of the indigo ring to install the alkyl chains (see Scheme 2.4 for numbering system), both the 5– and 6–positions lended themselves due to their isolated nature over the 4– and 7–positions which could sterically interfere with the IND condensation reaction. The exact choice over whether to pursue the 5– or 6–position was dictated purely based on whichever approach was more facile. The next section details our consideration of the synthesis of both positions, based on the availability of industrially supplied precursors.

4-Methyl-3-nitrophenol **2.15** is a commercially available precursor for 6,6'-oxy indigoids. Although there are many ways to oxidise aromatic methyl groups,[124–127] the use of *N*,*N*-dimethylformamide dimethyl acetal has the ability to oxidise methyl groups adjacent (ortho) to a nitro group selectively to aldehydes with high yield (**Scheme 2.6**).[124,128–132] However, we found that the reagent methylated the unprotected hydroxyl group faster than the rate of methyl oxidation and so gave 4-methoxy-2-nitrobenzaldehyde **2.18**.[133]

However, methyl groups can act as protecting groups for hydroxyl functionality and are typically cleaved using boron tribromide.[134–137] An aldol condensation of **2.18** with acetone gave 6,6'-dimethoxyindigo **2.19** which was subsequently used in a condensation reaction with 2-thiopheneacetyl chloride to give the 6,6'-methoxy INDT compound **2.20**.

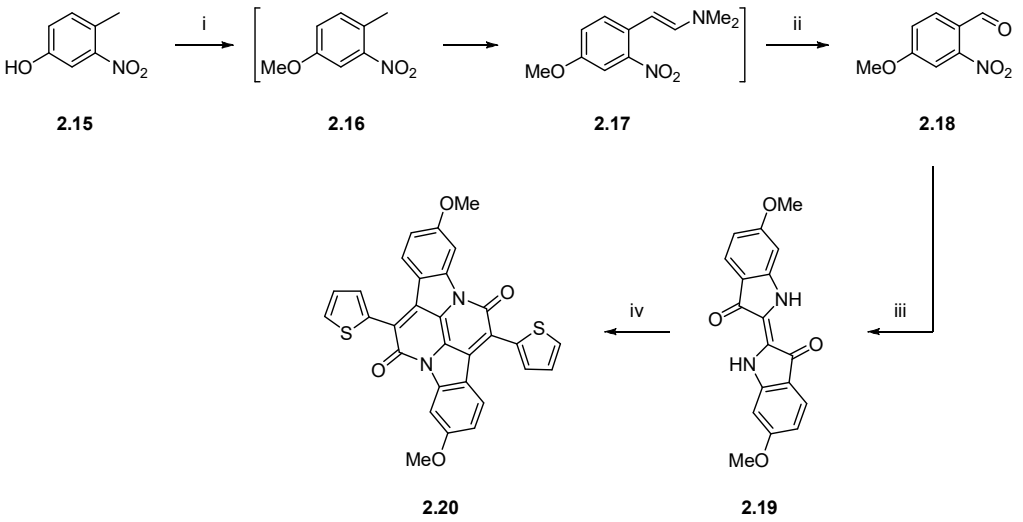


**2.15** **2.16** **2.17** **2.18** **2.20** **2.19**

**Scheme 2.6** Synthetic route to 6,6′-dimethoxy INDT **2.20**
(i) DMF.DMA, anhyd. DMF, 135 ℃, 3 d; (ii) $NaIO_4$, $H_2O$/DMF, 50%; (iii) acetone, KOH, 7%; (iv) 2-thiopheneacetyl chloride, xylene, 165 ℃, 48 h, 56%

However, demethylation of both **2.19** and **2.20** was not possible using dilute or neat $BBr_3$ with the latter leading to decomposition of both materials. As a more labile protecting group (PG) was required, we moved to tetrahydropyran (THP) ethers which are non-toxic compared to other common alternative alkyl ether PGs such as MOM ethers.[138]

5-Hydroxy-2-nitrobenzaldehyde **2.21** is a commercially available precursor for 5,5'-oxy indigoids and underwent quantitative protection with dihydropyran to give the THP-protected aldehyde **2.22**, which subsequently gave indigoid **2.23** (**Scheme 2.7**) in good yield.

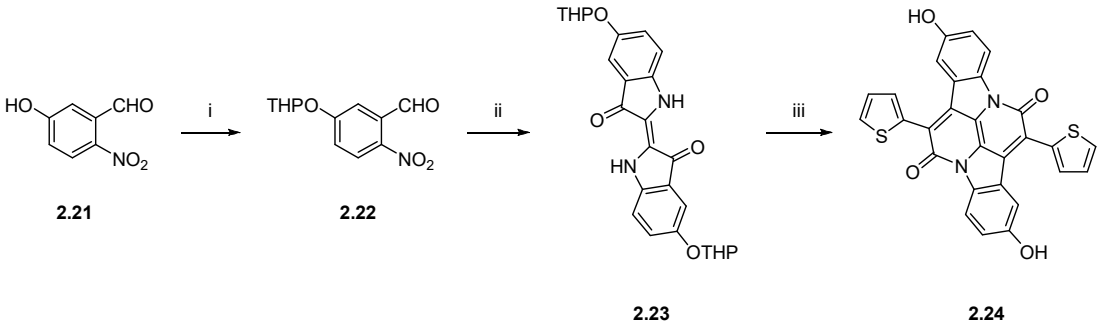


**2.21** **2.22** **2.23** **2.24**

**Scheme 2.7** Synthetic route to 5,5′-hydroxy INDT
(i) Dihydropyran, cat. TsOH/Py, DCM/Hex, quant.; (ii) acetone, KOH, 34%;
(iii) 2-Thiopheneacetyl chloride, xylene, 165 ℃, 48 h; then 5% NaOH, MeOH 29%

At this point the THP groups could be removed and an alkylation attempted, however there was concern about the possibility of N-alkylation over O-alkylation of a dihydroxy indigo, akin to the N-alkylation of DPP and other amine-containing organic semiconductor materials. Considering the potential issue of N-alkylation, it was decided that the INDT unit should be made before cleaving the THP groups. However, tetrahydropyran groups are acid labile and the condensation reaction of **2.23** with 2-thiopheneacetyl chloride liberated hydrochloric acid and, at 165 °C, the THP groups were likely cleaved. Although this was potentially beneficial, as it removed the necessity for an independent deprotection step, the free hydroxyl groups formed from deprotection could then react with the excess acyl chloride present in the reaction mixture, forming esters.

Experimentally, the condensation reaction of THP-indigo **2.23** produced a large quantity of a black crude residue of which analysis was problematic due to its low solubility, coupled with the tendency for IND molecules to aggregate in solution leading to broad $^1$H NMR signals. To ensure any esterified hydroxyl groups were cleaved, the solid was stirred in basic aqueous methanol. Eventually the residue was isolated in sufficient purity to be used in the next step of the synthesis.

Initial alkylation of hydroxyl-INDT **2.24** was attempted using 2-octyl-1-dodecanyl iodide, which was successful however there was evidence in both $^1$H NMR and mass spectroscopy of a mono-iodinated compound, arising from the iodination of thiophene at its 2-position. To combat this unwanted halogenation, we changed our alkylating agent to 2-octyl-1-dodecanyl bromide, which gave the desired di-alkylated product **2.25** without any halogenated side products (**Scheme 2.8**).

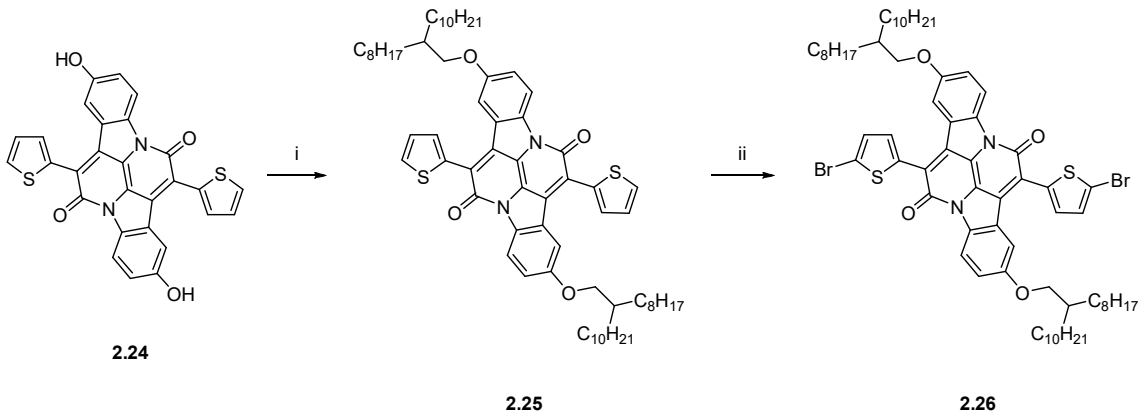


**Scheme 2.8** Alkylation and subsequent bromination of 5,5′-dihydroxy INDT **2.24**
(i) 9-(bromomethyl)nonadecane, $K_2CO_3$, anhy. DMF, 80 °C, 8%; (ii) NBS, DCM, dark, 44%

The yield of this alkylation was extremely poor (8%) although literature yields of similar compounds are commonly found in the 40-60% range.[139] The low yield was certainly due to low purity of compound **2.24** due to the *in-situ* cleavage of the THP groups. Fortunately, the alkylated compound **2.25** had a much greater solubility than its precursor and hence could be easily separated from other organic tars by column chromatography on silica gel. Subsequent bromination of the thiophene units using N-bromosuccinimide gave the desired monomer **2.26** in adequate yield giving 60 mg of material, representing a five-step total synthesis yield of 0.35%.

## 2.2.2 Polymer Synthesis

For the rest of this chapter, monomer **2.26** will be referred to as **INDT**. Polymerisations of material at a scale below 100 mg carries substantial risk of low molecular weight materials due to the restricted availability of co-monomers. Although 60 mg of material was less than ideal, polymerisation of this novel monomer was attempted using standard Stille conditions and 2,5-bis(trimethylstannyl)thiophene as a co-monomer (**Scheme 2.9**).

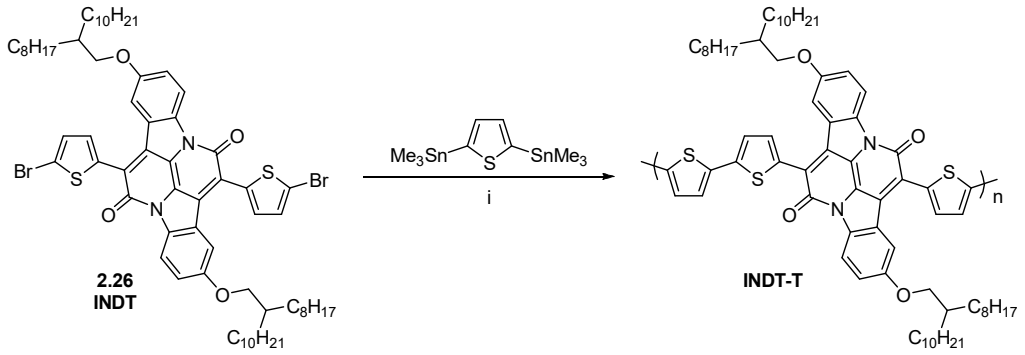


**Scheme 2.9** Microwave-assisted Stille polymerisation of INDT with thiophene
(i) $Pd_2(dba)_3$, P(o-Tol)$_3$, anhy. degas. PhCl, μW, 45 min, 100 → 180 °C

Stille reactions are highly sensitive to both moisture and oxygen and so the polymerisation was carried in an oven-dried microwave (μW) vial with anhydrous chlorobenzene, which was thoroughly degassed for 1 h prior to addition of the Pd catalyst.[140] The μW-assisted polymerisation was performed for 10 min at 100 °C, 5 min at 120 °C, 5 min at 140 °C, 5 min at 160 °C and 20 min at 180 °C, followed by precipitation of the polymer in methanol.

Crude materials from polymerisations can have a very large weight average dispersity (Đ) or polydispersity index (PDI) and require purification to reduce negative device performance arising from: structural defects which trap charges and facilitate recombination of excimers;[141] reduction in device lifetimes from low molecular weight material;[142] or from residual inorganic impurities.[143] Therefore soxhlet extraction of the

crude polymer was performed, firstly in acetone for 12 h then hexane for 12 h, removing low molecular weight oligomers and soluble organic/inorganic impurities. Subsequent soxhlet extraction of the remaining material with chloroform for 12 h afforded the pure high molecular weight polymer, whilst leaving trace insoluble organic/inorganic materials in the soxhlet thimble.

The chloroform extract was then concentrated $in\ vacuo$ to give a turquoise film which was precipitated from a minimum volume of hot chlorobenzene (~2 mL) into rapidly stirring methanol and dried thoroughly to give 49 mg of polymer **INDT-T** (87%). The purified polymer had a number average molecular weight $(M_n)$ of 15.7 kDa, as determined by size exclusion chromatography (SEC) using polystyrene standards (PS) in chlorobenzene at 80 °C, and had a weight average molecular weight $(M_w)$ of 49.4 kDa resulting in a PDI of 3.15 (**Table 2.1**). Whilst, an ideal polymer would have larger $M_n$ and a narrow PDI approaching 1.0, the physical properties of **INDT-T** were acceptable and represented a semiconductor that could be tested in organic electronic devices.

**Table 2.1** Physical and optical properties of **INDT-T**

| $M_n$[a] (kDa) | $M_w$[a] (kDa) | Đ[a] | $E_{homo}$[b] (eV) | $E_{lumo}$[c] (eV) | $E_g$[d] (eV) |
|---|---|---|---|---|---|
| 15.7 | 49.4 | 3.15 | –4.24 | –3.02 | 1.22 |

[a]Determined by SEC using polystyrene (PS) standards and PhCl as eluent; [b]Determined by XPS (incorrect, see text); [c]$E_{homo} + E_g$; [d]Estimated by UV-vis onset, PhCl solution

## 2.3 Results & Discussion

### 2.3.1 Optical Properties

**Figure 2.3** shows the solution (chlorobenzene) and thin film (spin coated from a 5 mg/mL solution in chlorobenzene) UV-vis absorption spectra of **INDT-T**. Both show a broad featureless absorption in the near infra-red region with $\lambda_{max} \sim 790$ nm. The spectrum becomes somewhat broadened on going from solution to thin-film which was attributed to solid-state packing effects.[144] The optical band gap $(E_g)$ of the polymer was estimated from the UV-vis absorption onset to be 1.22 eV, an extremely narrow band gap relative to other similar materials.[58,145,55,146] Near infra-red absorbing materials are highly attractive for transparent solar cells and ambipolar OFETs.[147]

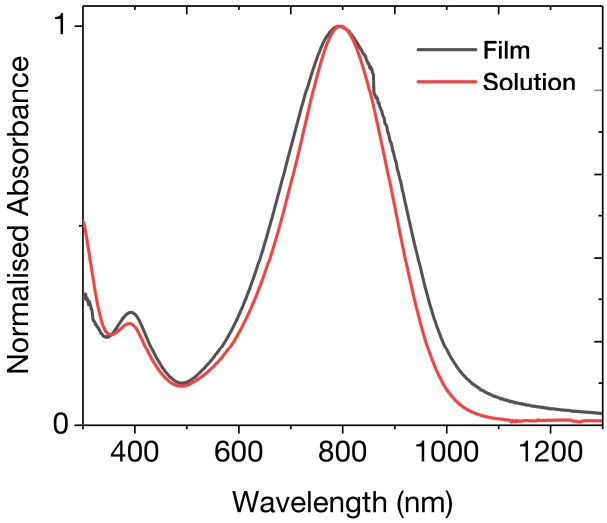


**Figure 2.3** Normalized UV-vis absorption spectra of **INDT-T** in solution (chlorobenzene) and thin-film (spun from 5 mg/mL solution in chlorobenzene)

The energy of the highest occupied molecular orbital ($E_{homo}$) of **INDT-T** was measured using X-ray photoelectron spectroscopy (XPS) and was found to be −4.24 eV. The energy of the lowest unoccupied molecular orbital ($E_{lumo}$) was estimated by the addition of the optical band gap (1.22 eV) to $E_{homo}$ as −3.02 eV. The reader should take these values with caution as these measurements are in disagreement with future experiments using PESA (–5.02 eV and –3.76 eV, see page 78).

To investigate the electronic structure of **INDT-T**, DFT calculations were carried out on model trimers using the B3LYP hybrid functional and 6-31G* basis set. As the length of alkyl chain has negligible effect on the electronics of the molecule (see Figure 2.1), it has become common practice to substitute alkyl chains with methyl groups, simplifying the system considerably, reducing computational workload and thus the time required to run these demanding calculations.

The theoretical band gap $E_{\mathrm{g}}^{calc}$ was calculated using time dependant DFT (TD-DFT) to be 1.32 eV, which was in close agreement with the experimental value. Both the HOMO and LUMO wave functions were well delocalized along the polymer backbone, which displayed a high degree of co-planarity (**Figure 2.4**). Interestingly, there was little contribution to the HOMO from the benzene rings of the indigo core but substantial delocalisation of the LUMO onto these sites. Notably, the LUMO was delocalised onto the 6–position, the position adjacent to where the alkyl chains were installed. Functionalisation of this position with electron-rich or electron-deficient groups may enable tuning of $E_{lumo}$ independent of $E_{hom}$ .

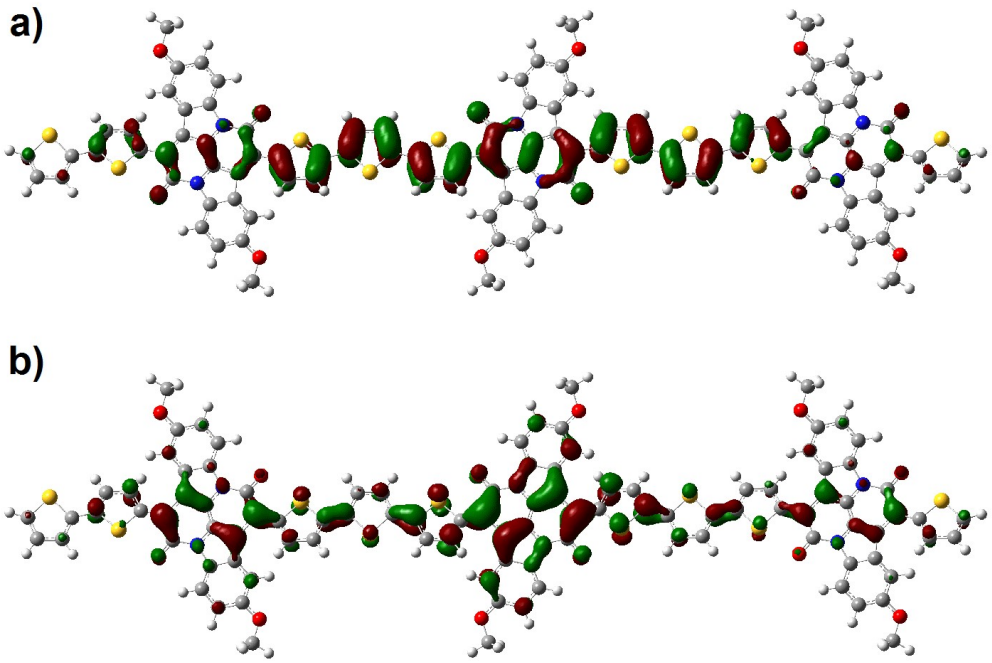


**Figure 2.4** DFT distributions of the a) HOMO and b) LUMO of the geometry optimized trimer of **INDT-T** at the B3LYP/6-31G* level of theory

### 2.3.2 Crystallinity

To investigate the crystallinity of the polymer in solid-state, X-ray diffraction (XRD) was performed on a drop-cast film from a 5 mg/mL solution of **INDT-T** in chlorobenzene (**Figure 2.5**). A broad peak at $2\theta = 3.8°$ was visible corresponding to the $(100)$ reflection, indicative of typical lamellar packing distance of 2.3 nm. The influence of annealing on the molecular packing of the polymer was studied at both 100 and 200 °C.

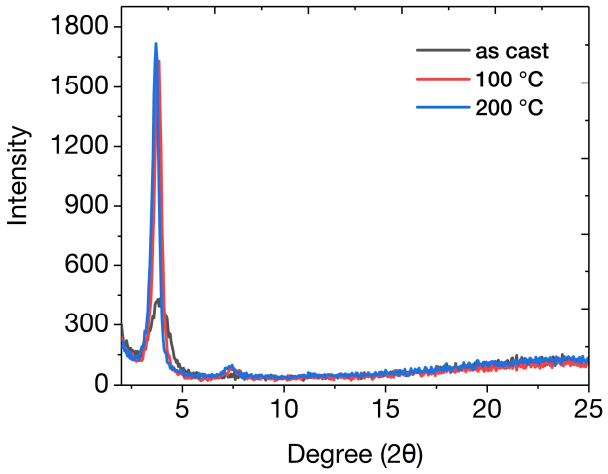


**Figure 2.5** X-ray diffraction of an **INDT-T** thin film drop-cast from a 5 mg/mL solution in chlorobenzene as cast (black) and annealed at 100 ℃ and 200 ℃

Annealing led to a substantial increase in thin-film crystallinity as observed by the increased intensity of the $(100)$ peak and the appearance of the corresponding $(200)$ reflection, indicating increased long-range order. No noticeable change in film crystallinity was observed at higher annealing temperatures.

### 2.3.3 Organic Photovoltaic Devices (OPVs)

To investigate the potential of **INDT-T** as a photovoltaic material, conventional and inverted OPV devices were fabricated. To construct the devices, PEDOT:PSS was spin-coated onto pre-cleaned substrates patterned with indium tin oxide (ITO). The bulk heterojunction (BHJ) photoactive layer was then deposited by spin-coating a 1:2 solution of **INDT-T**:PC[70]BM from a 4:1 $CHCl_3$:oDCB solution (10 mg/mL) at 1000 RPM. Following drying in an inert atmosphere, the counter electrode of LiF (1 nm) and Al (100 nm) was deposited by vacuum evaporation at $3 \times 10^{-7}$ mbar.

Current-voltage (J-V) characteristics were measured under 100 mW/cm$^2$ white light from a tungsten-halogen lamp filtered by a Schott GG385 UV filter and a Hoya LB120 daylight filter, using a Keithley 2400 source meter. Short-circuit currents $(J_{SC})$ under AM1.5G conditions were obtained from the spectral response and convolution with the solar spectrum. Spectral response was measured under operational conditions usig bias light from a 532 nm solid-state laser. The J-V characteristics and external quantum efficiency (EQE) spectrum are shown in **Figure 2.6** and the data from the devices is displayed in **Table 2.2**.

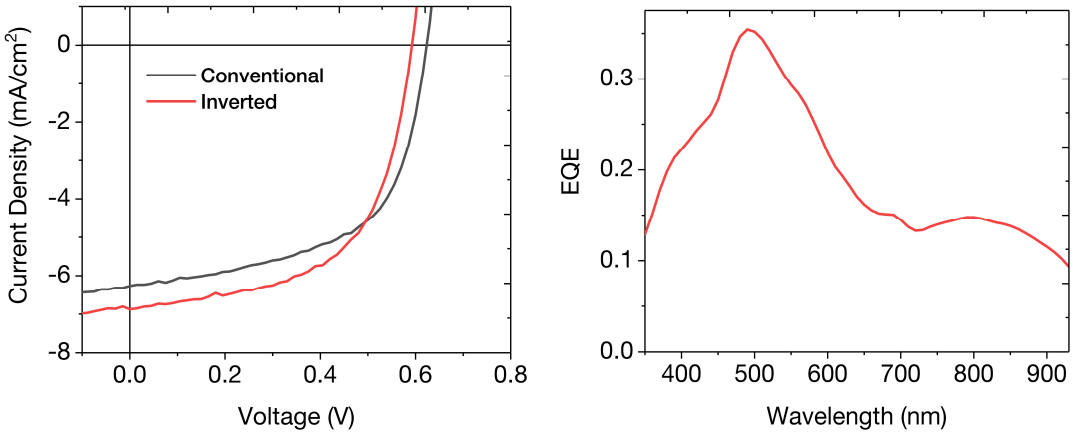


**Figure 2.6** J-V characteristics (left) and EQE (right, inverted architecture) of an **INDT-T** OPV device

**Table 2.2** Properties of **INDT-T** organic photovoltaics spun from 4:1 $CHCl_3$:oDCB solutions with a 1:2 ratio of polymer:PC[70]BM

| Architecture | $J_{SC}$ (mA/cm$^2$) | $V_{OC}$ (V) | FF | PCE (%) |
|---|---|---|---|---|
| Conventional | 6.27 | 0.62 | 0.58 | 2.25 |
| Inverted | 6.88 | 0.59 | 0.58 | 2.35 |

The conventional architecture device had a relatively high $V_{OC}$ of 0.62 V which was impressive considering the extremely narrow optical band gap of **INDT-T**. The inverted architecture had an increased $J_{SC}$ (6.88 mA/cm$^2$, $\Delta = +0.61$) but lower $V_{OC}$ (0.59 V, $\Delta = -0.03$). Both architectures of devices had good fill factors of 0.58 and similar overall power conversion efficiencies of 2.25% and 2.35% for conventional and inverted devices respectively. Despite the modest overall efficiencies, the PCEs obtained represented some of the highest efficiencies from such ultra-narrow near-IR absorbing band-gap materials.[145,146,148] As this initial polymer was both unoptimised and had a less than ideal $M_n$, future optimisation of this system showed strong potential to furnish higher performance OPV materials.

The EQE spectrum revealed that most of the photocurrent originated from the fullerene absorption at 500 nm, but there remained an appreciable contribution from **INDT-T** up to 950 nm. The lower contribution to the photocurrent from the polymer was attributed to its insufficient energetic offset with respect to the fullerene.[149,150]

### 2.3.4 Organic Field Effect Transistors (OFETs)

To investigate the potential of **INDT-T** in field effect transistors, top-gate bottom-contact devices were constructed on glass substrates with Al & Au bilayer (20 nm + 20 nm) source/drain (SD) electrodes for ambipolar charge injection. The active layer of **INDT-T** was then spin-coated on top from a 10 mg/mL solution in chlorobenzene and the films annealed for 15 min. Onto this layer was spin-coated a CYTOP dielectric and the device further annealed for 1 h. Finally, an Al gate electrode was thermally evaporated to complete the device. Linear regime mobilities $(\mu_{lin})$ were calculated from the first derivative of the linear transfer curve $(I_D^{lin})$, whilst saturation regime mobilities $(\mu_{sat})$ were calculated from the second derivative of the saturated transfer curve $(I_D^{sat})$. The characteristics of OFET devices annealed at both 100 and 200 °C is summarised in **Table 2.3** and the transfer curves and output characteristics for the devices annealed at 200 °C are shown in **Figure 2.7**.

**Table 2.3** Characteristics of TG-BC OFET devices containing **INDT-T** annealed at various temperatures with $W = 1000$ µm and $L = 50$ µm

| Annealing Temp (℃) | $V_{\mathrm{Th}}^{lin}$ (V) | | $I_{on}/I_{off}{}^{lin}$ | | $\mu_{lin}$ (cm$^2$/Vs) | | $\mu_{sat}$ (cm$^2$/Vs) | |
|---|---|---|---|---|---|---|---|---|
| | $h^+$ | $e^-$ | $h^+$ | $e^-$ | $h^+$ | $e^-$ | $h^+$ | $e^-$ |
| 100 | −23 | 22 | $10^5$ | $10^6$ | 0.03 | 0.03 | 0.08 | 0.08 |
| 200 | −131 | 52 | $10^3$ | $10^6$ | 0.03 | 0.03 | 0.23 | 0.48 |

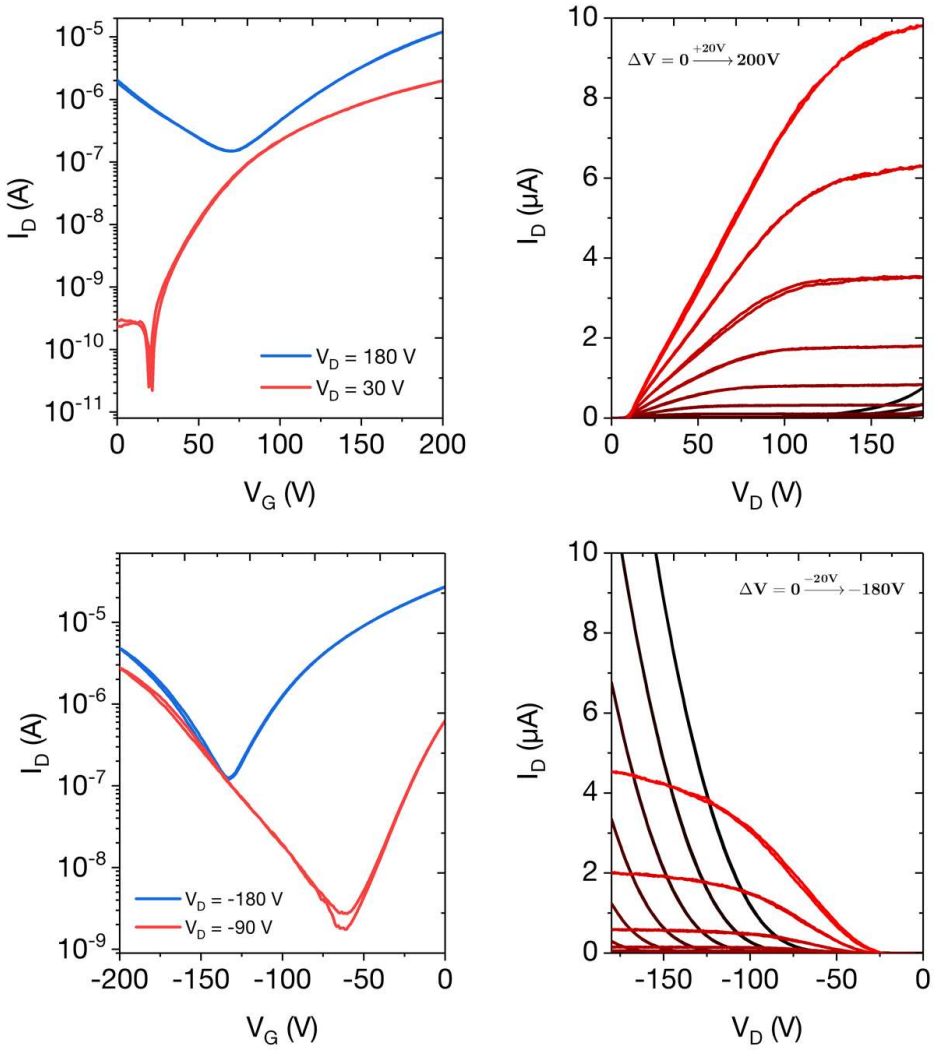


**Figure 2.7** Transfer (left) curves and output (right) characteristics of n-type (top) and p-type (bottom) operation of an ambipolar TG-BC OFET device of **INDT-T** annealed at 200 ℃ with $W = 1000$ µm and $L = 50$ µm

After annealing at 100 °C, both $\mu_h$ and $\mu_e$ extracted from the saturation regimes of the transfer curves were 0.08 cm$^2$/Vs demonstrating good ambipolar behaviour and negligible hysteresis. However, annealing at 200 °C lead to a significant improvement of both characteristics. Conservative best-fit values for $\mu_h$ and $\mu_e$ were 0.23 and 0.48

$cm^2/Vs$ respectively with peak mobilities of 0.52 and 1.2 $cm^2/Vs$ respectively, demonstrating the excellent charge transport properties of **INDT-T**. The improved OFET characteristics at higher annealing temperatures aligned well with the observed increase in crystallinity as seen in XRD experiments.

Threshold voltages $V_{\mathrm{Th}}$ for both p-type and n-type transport were in the range of $|22-52|$ V, which is comparable to values measured in similar DPP and isoindigo based OFETs, except for p-type devices annealed at 200 °C, which had a $V_{\mathrm{Th}}$ of –131 V, indicating a significant injection barrier for holes. This was attributed to non-optimized matching of the electrodes and the $E_{homo}$ of the polymer. To overcome this, an OFET device with UV-ozone treated Au together with an Al adhesion layer (40 + 5 nm) was fabricated for optimized hole injection. The device had a slightly smaller channel length of 30 µm and the same channel width as the ambipolar devices and was annealed at 100 °C. The transfer curve and output characteristics for this device is shown in **Figure 2.8** and the results summarised in **Table 2.4**.

**Table 2.4** Characteristics of a p-type optimised BG-BC OFET device containing **INDT-T** annealed at 100 °C with $W = 1000$ µm and $L = 30$ µm

| $V_{\mathrm{Th}}^{lin}$ (V) | ${I_{on}/I_{off}}^{lin}$ | $\mu_{lin}$ ($cm^2/Vs$) | $\mu_{sat}$ ($cm^2/Vs$) |
|---|---|---|---|
| −53 | $10^4$ | 0.04 | 0.10 (0.14)[a] |

[a]Peak value

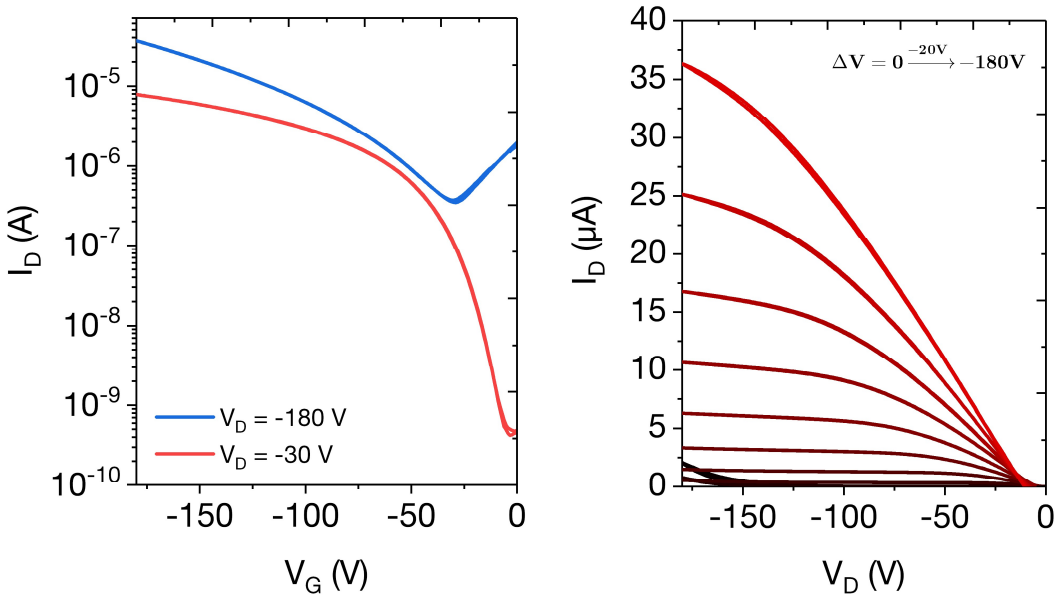


**Figure 2.8** Transfer (left) and output (right) characteristics of a p-type optimised OFET devices of **INDT-T** annealed at 100 °C with $W = 1000$ µm and $L = 30$ µm

Only p-type transport was observed for this device and gave average $\mu_h$ of 0.10 cm$^2$/Vs with peak mobility of 0.14 cm$^2$/Vs, showing improved charge transport over the equivalent ambipolar device. Crucially, $V_{\mathrm{Th}}$ was reduced to –53 V, indicating that the large $V_{\mathrm{Th}}$ for p-type transport in the initial device was likely due to improper work function matching or suboptimal electrode-polymer contact.

## 2.4 Improving the Synthesis of INDT

The initial results of **INDT-T** showed that indolonaphthyridine had true potential as both a near-IR absorbing semiconductor in OPVs and as an ambipolar charge transport material in OFETs. To fully evaluate the potential of the indolonaphthyridine building block in organic semiconducting polymers, a family of donor-acceptor co-polymers was required, shown in **Figure 2.9**.

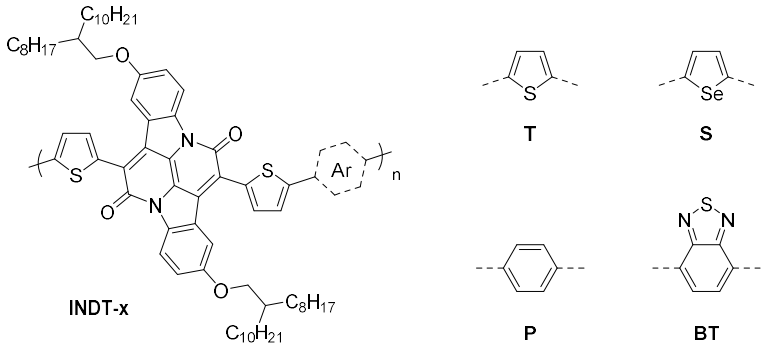


**Figure 2.9** Four polymers targeted for their different theoretical properties tailored toward specific applications

The true performance of **INDT-T** could have been hampered by its low $M_n$ of 15.7 kDa, likely caused due to the lack of available monomer for the polymerisation (60 mg). Therefore, another attempt at synthesising **INDT-T** would be carried out with more monomer, which should yield a polymer with $M_n$ > 20 kDa, to investigate if charge transport & photo-charge generation could be improved. Secondly, co-polymerisation with a phenyl ring (**INDT-P**) will introduce a larger degree of distortion in backbone planarity and conjugation, leading to a deeper $E_{homo}$ and an overall widening of the band gap. These properties are attractive for tailoring the material for OPVs as a wider band gap can absorb a larger portion of light and a deeper $E_{homo}$ will give larger $\mathrm{V_{OC}}$. Thirdly, benzo[*c*][1,2,5]thiadiazole, or benzothiadiazole (**INDT-BT**), is a monomer which has gained popularity for its ability to improve the charge transport properties of its co-polymers in OFETs, particularly semiconductors for p-type OFETs where BT-containing polymers have shown inherently low $E_{homo}$.[151] Finally, selenophene (**INDT-S**) is a relatively newer unit whose co-polymers have similar electronic properties to their

thiophene cousins but have shown intrinsically improved solid-state morphology due to strong intermolecular Se–Se interactions giving rise to a higher degree of crystallinity over thiophene analogues.[152]

To synthesise these four polymers, it was first necessary to improve the initial synthesis of the INDT monomer to achieve larger yields thus more material for polymerisations.

### 2.4.1 Indigo Condensation

Despite its notability, there is surprisingly no stand-out procedure for the Baeyer–Drewson Indigo (BDI) synthesis, with reactions merely typically reported as being performed in a basic acetone/water mixture with base species, concentrations, timings, temperatures and yields varying greatly between works (if given at all).

The yields obtained from various BDI reactions performed during the first section of this work indeed ranged erratically between 5-40%, with a rough mean yield ~20%. Initially, control of the reaction using specific temperatures and concentrations was attempted over two steps:[123,153,154] 1. The initial aldol condensation of acetone and aldehyde at low temperature (-5 °C) using “concentrated” base (0.4 M); 2. Completing the rest of the pathway at a higher temperature (10 °C) using “dilute” base (0.2 M).

A design of experiment (DoE) was not performed on our BDIs, however several methods were attempted from procedures found across the literature and on the internet. Perhaps ironically, conditions which gave consistent high isolated yields (~40%) were found on a hobby website via an internet search engine.[155] The procedure detailed the precipitation of fine particles of an *o*-nitrobenzaldehyde by dissolving it in acetone (10 mL/g) and then adding water (deionised, 10 mL/g), very slowly dropwise. In the case of aldehyde oils, a turbid solution was formed. Sodium hydroxide solution (1M, 5 mL/g) was then added extremely slowly dropwise, immediately dissolving the aldehyde, darkening and then precipitating the indigoid after approximately half the base had been added, eventually becoming viscous with precipitate upon total addition. This method gave consistent yields around ~40% after only 4 h.

The synthesis does lend itself to a full DoE, however this was never a desired objective of this project and 40% yields were sufficient at the scale we could perform the reaction on.

### 2.4.2 Protecting Group Strategy

It was clear that the THP protecting group, whilst exhibiting excellent stability in the alkaline indigo concentration reaction, was unstable during the acidic condensation

reaction. A protecting group with greater stability in both acidic and alkaline media was required. We chose to switch to benzyl (Bn) groups, which typically have excellent stability across the entire pH scale, but can be removed via reduction, classically using hydrogenation with Pd/C.[138]

Protection of phenol **2.21** with benzyl bromide proceeded in near quantitative yield (**Scheme 2.10**) to give benzyl-protected aldehyde **2.27**. Using the improved Baeyer–Drewson condensation conditions, 5,5'-benzyloxyindigo **2.28** was produced in excellent yield (53%).

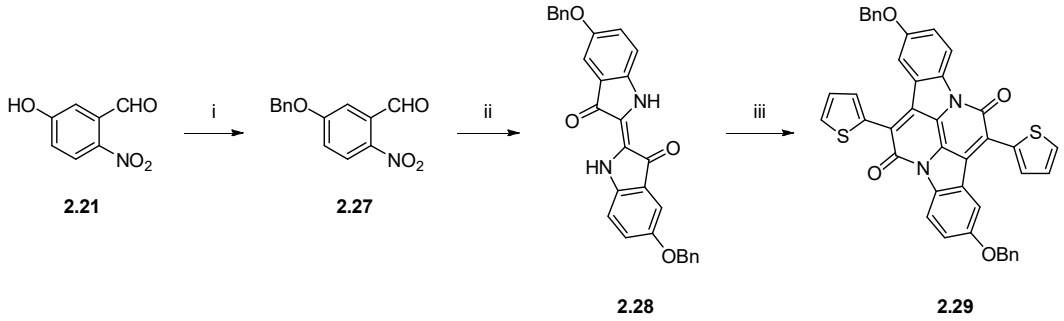


**2.21** **2.27** **2.28** **2.29**

**Scheme 2.10** Synthesis of benzyl-protected 5,5,-hydroxyindigo
(i) BnBr, $K_2CO_3$, anhyd. DMF, 98%; (ii) acetone, then $H_2O$, then NaOH, 53%; (iii) 2-thiophene acetyl chloride, xylenes, 165 °C, 27%

Subsequent condensation of **2.28** with 2-thiopheneacetyl chloride gave the benzyl-INDT compound **2.29** in modest yield but of considerably higher purity than the THP method (demonstrated by the excellent yields in deprotection/alkylation discussed next), although strong aggregation remained in this material, as evident from the broad $^1$H NMR spectrum.

Unfortunately, the Bn groups of **2.29** were inert to typical deprotection via hydrogenation on activated Pd/C despite efforts to screen various solvents and reaction concentrations. Other methods for the removal of Bn groups were attempted: Treatment of **2.29** with B-bromocatecholborane[138] destroyed the compound giving uncharacterisable intractable tars, however the Bn groups were successfully removed using excess iodotrimethylsilane in excellent yield (88%, **Scheme 2.11**).[156] The high yields obtained in subsequent steps, alkylation (89%) and bromination (71%) (see **Scheme 2.8** for details), demonstrated the higher purity of the materials obtained using benzyl PGs over our initial THP synthetic route and led to an increase in total yield from 0.35% over 5 steps to 7.8% over 6 steps.

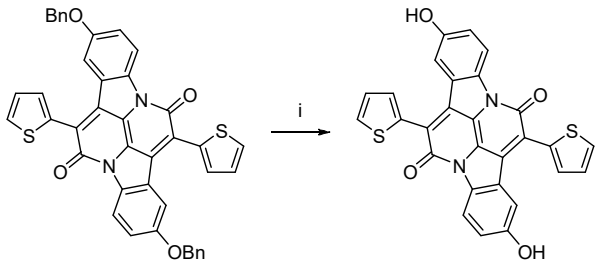


**Scheme 2.11** Removal of the benzyl groups of **2.29**
i) Excess $Me_3SiI$, anhyd. DCM, dark, rt, 5 d, 88%

## 2.4.3 Polymer Synthesis

Using benzyl protecting group strategy, enough INDT monomer was synthesised to make the four desired polymers outlined earlier in the chapter. Both the thiophene **INDT-T** and selenophene **INDT-S** polymers were synthesised using the same $\mu W$-assisted Stille procedure (**Scheme 2.12**) used for the initial polymerisation of **INDT-T**.

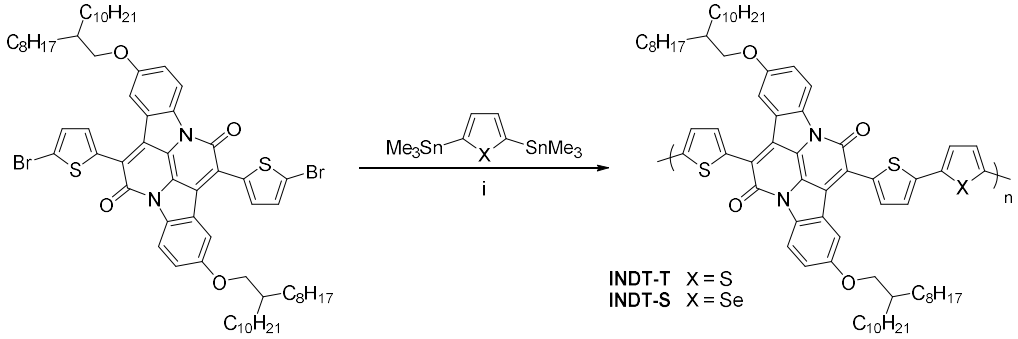


**Scheme 2.12** Microwave assisted Stille co-polymerisation of INDT with 2,5-bis(trimethylstannyl) thiophene and selenophene monomers
i) $Pd_2(dba)_3$, P(o-Tol)$_3$, anhy. degas. PhCl, $\mu W$, 45 min, 100 $\rightarrow$ 180 °C

Reaction conditions for the polymerisations of both **INDT-BT** and **INDT-P** were selected from the literature of polymerisations of similar isoindigo polymers. Both polymerisations shared several conditions: toluene and deionised water were used as solvents, both of which were degassed thoroughly prior to polymerisation; *N*-Methyl-*N*,*N*,*N*-trioctylammonium chloride (Aliquot 336) was used as a phase transfer catalyst to improve the mixing of the organic and aqueous phases; and both reactions were carried out at 135 °C for 3 days. The choice of catalyst and base differed for the two reactions: For **INDT-BT**, tetrakis(triphenylphosphine) palladium(0), $Pd(Ph_3)_4$ was used with sodium carbonate, $Na_2CO_3$. For **INDT-P**, tris(dibenzylideneacetone)dipalladium(0), $Pd_2(dba)_3$, was used as the Pd source and triphenylphosphine was added to form $Pd(Ph_3)_2$ *in-situ*, and potassium phosphate tribasic ($K_3PO_4$) base was used (**Scheme 2.13**).

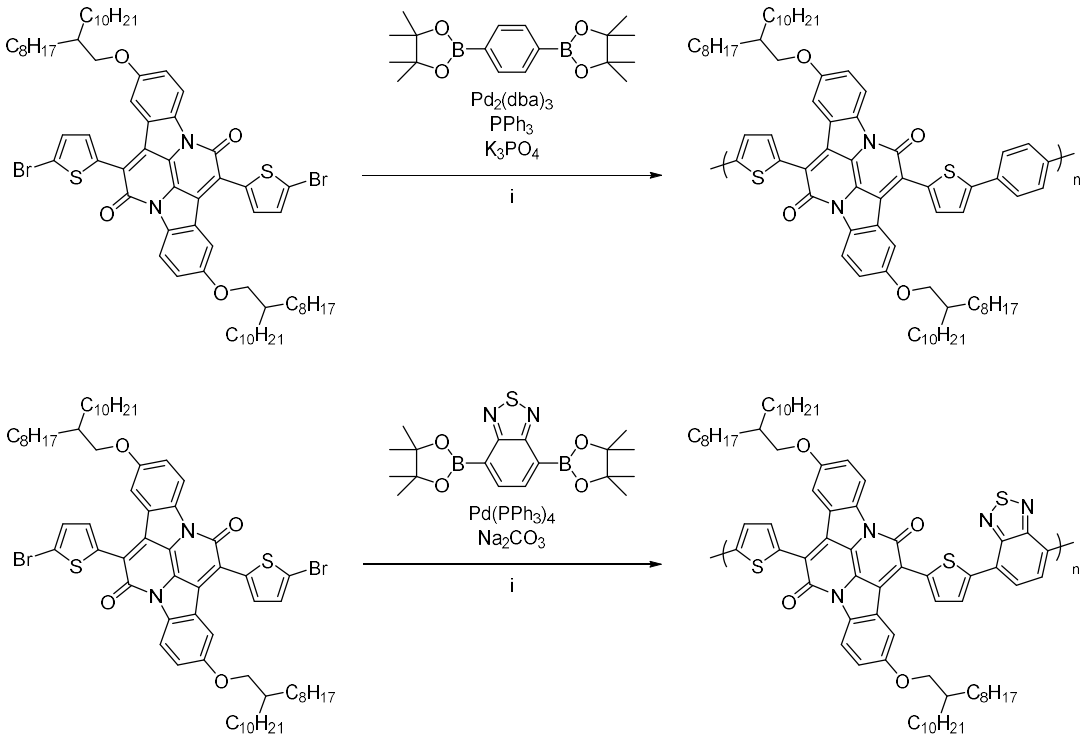


**Scheme 2.13** Suzuki polymerisations of INDT with phenyl– (top) and benzothiadiazole– (bottom) bis(pinacolato)diboron monomers
i) Aliquot 336, degas. PhMe/$H_2O$, 3 d, 135 °C

Following polymerisation, crude polymers were precipitated into methanol and purified by soxhlet extraction, firstly in acetone (12 h), then hexane (12 h) to remove low $M_n$ material and soluble organic/inorganic compounds. Subsequent extraction with chloroform (12 h) gave the purified polymers **INDT-T**, **INDT-S** and **INDT-BT**. Interestingly, **INDT-P** exhibited poor solubility in chloroform and required further extraction with chlorobenzene (6 h), which was somewhat surprising due to the larger twist the phenyl group usually induces in the polymer backbone, hence reducing $\pi - \pi$ interactions and thus increasing solubility.

The purified polymer extracts were then concentrated *in vacuo* and the resulting material precipitated from a minimum volume of hot chlorobenzene (2-5 mL) into methanol, collected by filtration and dried thoroughly. **INDT-T** (87%), **INDT-S** (81%) and **INDT-BT** (84%) were obtained in high yield. **INDT-P** (21%) was poor yielding, however this cannot be wholly attributed to the lower solubility of the polymer as, unfortunately, some material was lost during the soxhlet extraction when residual chloroform in the soxhlet thimble caused a sudden sharp increase in the internal pressure of the system upon cycling, ejecting the condenser and some polymer from the system as consequence. In all future soxhlet extractions described in this thesis, the thimble was thoroughly dried and new glassware used on transition from chloroform to chlorobenzene.

## 2.5 Results of the INDT Polymer Family

### 2.5.1 Physical & Optical Properties

The physical data of the four polymers is summarised in **Table 2.5**. The number and weight molecular weight averages were determined by size exclusion chromatography (SEC) using polystyrene standards (PS) in chlorobenzene at 80 °C. All four polymers showed good $M_n > 20$ kDa, with polydispersities that were slightly high, however symmetrical in distribution.

**Table 2.5** Physical properties of the four indolonaphthyridine containing polymers[a]

| Polymer | $M_n$ (kDa) | $M_w$ (kDa) | Đ |
|---|---|---|---|
| INDT-T | 20 | 80 | 4.00 |
| INDT-S | 25 | 83 | 3.32 |
| INDT-P | 40 | 119 | 2.98 |
| INDT-BT | 29 | 103 | 3.55 |

[a]Determined by SEC using polystyrene (PS) standards and PhCl as eluent

**Figure 2.10** shows the solution (chlorobenzene) and thin-film (spin-coated from 5 mg/mL solutions in chlorobenzene) UV-vis absorption spectra of the four polymers and the optical properties of the polymers are summarised in **Table 2.6**.

**Table 2.6** Optical properties of the four indolonaphthyridine containing polymers

| Polymer | $E_g$[a] (eV) | $E_g^{calc}$[b] (eV) | $E_{homo}$[c] (eV) | $E_{lumo}$[d] (eV) | $\lambda_{max}^{soln}$[e] (nm) | $\lambda_{max}^{film}$[f] (nm) | $\varepsilon$ ($M.cm^{-1}$)[e] |
|---|---|---|---|---|---|---|---|
| INDT-T | 1.26 | 1.32 | –5.02 | –3.76 | 802 | 805 | 50912 |
| INDT-S | 1.22 | 1.36 | –4.99 | –3.77 | 844 | 849 | 67453 |
| INDT-BT | 1.23 | 1.31 | –4.97 | –3.74 | 826 | 820 | 66780 |
| INDT-P | 1.40 | 1.60 | –5.14 | –3.74 | 717 | 736 | 56072 |

[a]Estimated from UV-vis onset, PhCl solution; [b]Determined by TD-DFT using B3LYP/6-31G*; [c]Determined by PESA. Data is given to two decimal places to illustrate the difference in figures however note that this falls within the error margins (±0.1 eV) of the experiments; [d]$E_{homo} + E_g$; [e]PhCl solution; [f]Spin-coated from a 5 mg/mL solution in PhCl

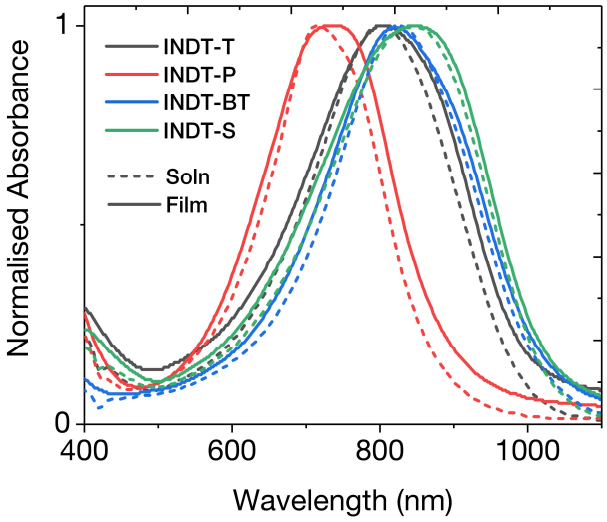


**Figure 2.10** Normalized UV-vis absorption spectra of the four INDT polymers. Solution spectra (dashed lines) were recorded in chlorobenzene, and thin-films (solid lines) were spun from 5 mg/mL solutions in chlorobenzene

The solution absorbance spectra of **INDT-T**, **INDT-S** and **INDT-BT** showed broad featureless absorption in the near-IR region whereas the spectrum of **INDT-P** was considerably hypsochromically (blue) shifted, arising from the widening of the optical band gap. All four spectra became somewhat broadened on going from solution to thin-film, attributed to solid-state packing effects, but overall there was not any significant difference between solution and thin-film absorbance of the polymers.

$E_{homo}$ of each polymer was measured using photoelectron spectroscopy in air (PESA) and the corresponding $E_{lumo}$ was estimated by the addition of the respective optical band gaps, estimated from the UV-vis absorption onset. All polymers exhibited extremely narrow $E_{\mathrm{g}}$ of ~1.2 eV, except for **INDT-P** which had a slightly wider $E_{\mathrm{g}}$ of 1.4 eV, as expected caused by reduction of molecular orbital overlap resulting from decreased polymer backbone co-planarity. Remarkably, all four polymers had $E_{lumo}$ of either –3.7 or –3.8 eV, being almost identical within experimental error $(\pm 0.1\ \mathrm{V})$. Similarly, **INDT-T**, **INDT-S** and **INDT-BT** had comparable $E_{homo}$ around –5.0 eV, whilst **INDT-P** exhibited a deeper $E_{homo}$ of –5.14 eV as postulated.

Theoretical energies of the frontier MOs and the resulting band gaps were estimated by quantum chemical calculations using the B3LYP hybrid functional and 6-31G* basis set. The trend in experimental and theoretical data (**Figure 2.11**) for $E_{homo}$ are generally in good agreement, however the comparison of the two sets of data for $E_{lumo}$ showed poor alignment.

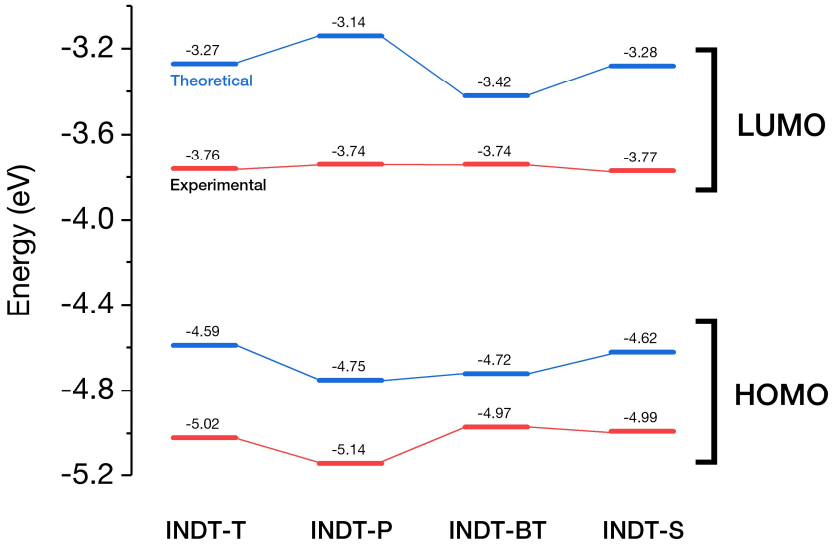


**Figure 2.11** Theoretical (blue) energies of the frontier MOs levels calculated at the B3LYP/6-31G* level of theory using DFT for $E_{homo}^{calc}$ and time-dependent DFT (TD-DFT) for $E_{lumo}^{calc}$. Experimental (red) $E_{homo}$ were recorded using PESA and $E_{lumo}$ resolved by $E_{homo} + E_g$

The molecular orbital distributions of the geometry-optimized structures of each of the four polymers was calculated at the B3LYP/6-31G* level of theory on model trimers, substituting methyl groups for alkyl chains and are shown in **Figure 2.12**. All four polymers have HOMOs and LUMOs well delocalised along their backbones, which suggested that charge transport in these materials should be efficient.

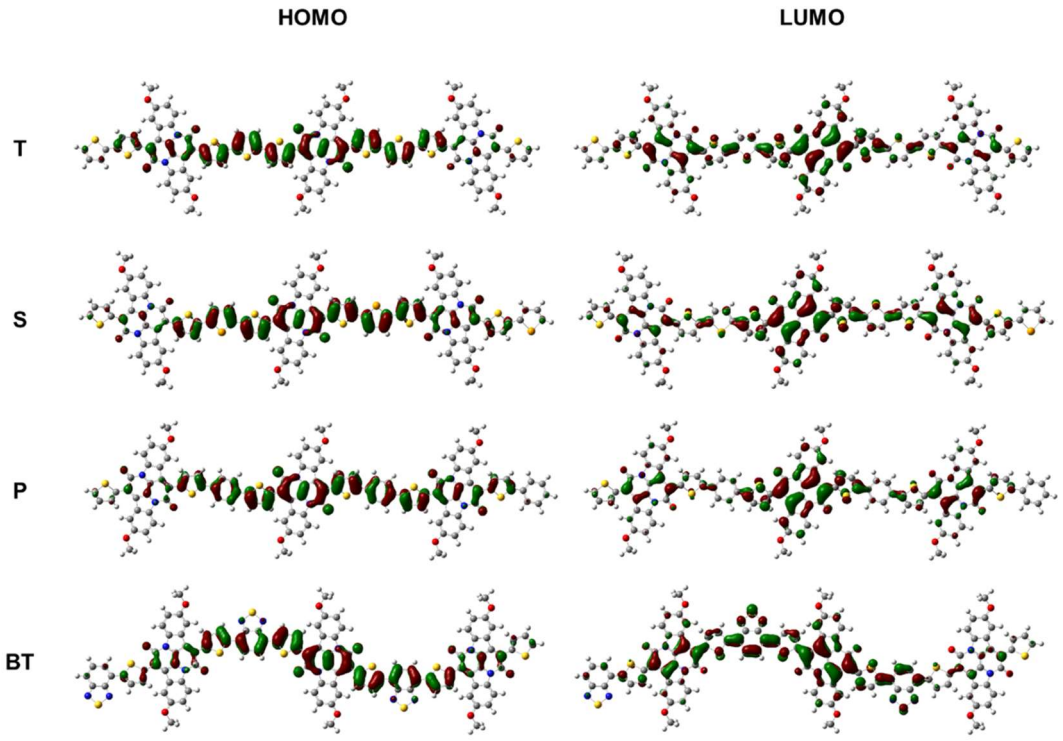


**Figure 2.12** Theoretical molecular orbital distributions of the four polymers calculated at the B3LYP/6-31G* level of theory

To examine the extent of co-planarity of each polymer, the extinction coefficients $(\varepsilon)$ were measured and it was found that $\varepsilon$ for **INDT-BT** and **INDT-S** were considerably higher than those of **INDT-T** and **INDT-P**. It was highly likely that this increase was due to an increase in co-linearity resulting in greater persistence lengths as has previously been shown in BT and Se containing conjugated polymers.[157,158]

### 2.5.3 Crystallinity

The influence of annealing temperature on the molecular packing in the polymer thin-films was studied by X-ray diffraction (**Figure 2.13**). Drop-cast polymer thin-films showed a Bragg reflection at $2\theta = 3.8°$, corresponding to the $(100)$ reflection and indicative of a typical lamellar packing distance of 2.3 nm. Annealing at 100 °C for 10 min led to a substantial increase in thin-film crystallinity as observed by the increased intensity of the $(100)$ peak and the appearance of the corresponding second order $(200)$ reflections for **INDT-T** and **INDT-S**, which indicated increased long-range order in those two polymer films. No noticeable changes in film crystallinity were observed after annealing at higher temperatures.

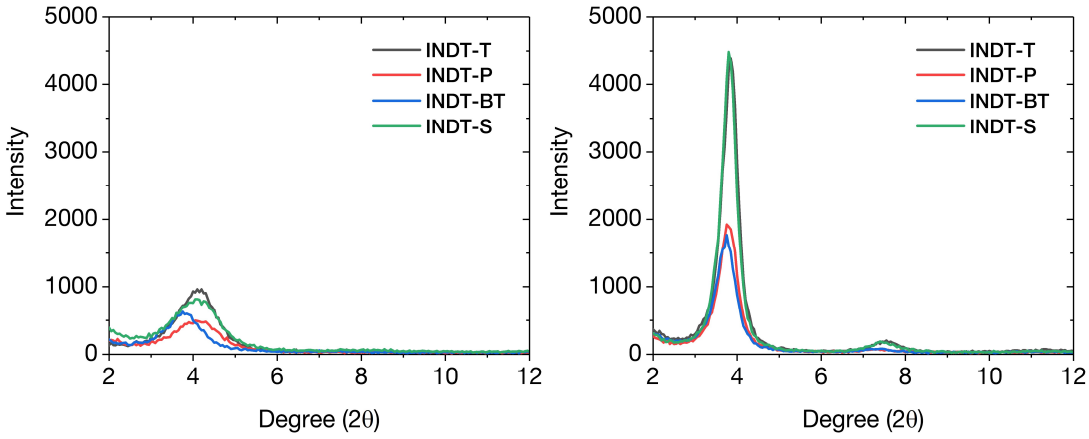


**Figure 2.13** X-ray diffraction of drop-cast INDT polymer films (left) from 10 mg/mL solutions in chlorobenzene. Annealed films (right) were heated at 100 °C for 10 min.

### 2.5.4 Organic Photovoltaic Devices

Bulk heterojunction OPV devices were constructed with the four novel polymers in a conventional architecture consisting of ITO/PEDOT:PSS/polymer:PC[70]BM/LiF/Al and tested under 100 mW/cm$^2$ white light under AM1.5G conditions. The photoactive layer was deposited by spin-coating a 1:2 solution of polymer:PC[70]BM from a 4:1 $CHCl_3$:oDCB solution (10 mg/mL) at 1000 RPM. The current-voltage characteristics of

the four devices are shown in **Figure 2.14** and the data from the devices summarised in **Table 2.7**.

**Table 2.7** Properties of INDT-based organic photovoltaic devices spun from 4:1 $CHCl_3$:oDCB solutions with a 1:2 ratio of polymer:PC[70]BM

| Polymer | $J_{SC}$ (mA cm$^{-2}$) | $V_{OC}$ (V) | FF | PCE (%) |
|---|---|---|---|---|
| INDT-T | 9.1 | 0.60 | 0.64 | 3.5 |
| INDT-S | 8.9 | 0.56 | 0.61 | 3.1 |
| INDT-BT | 6.0 | 0.69 | 0.43 | 1.8 |
| INDT-P | 4.4 | 0.57 | 0.53 | 1.3 |

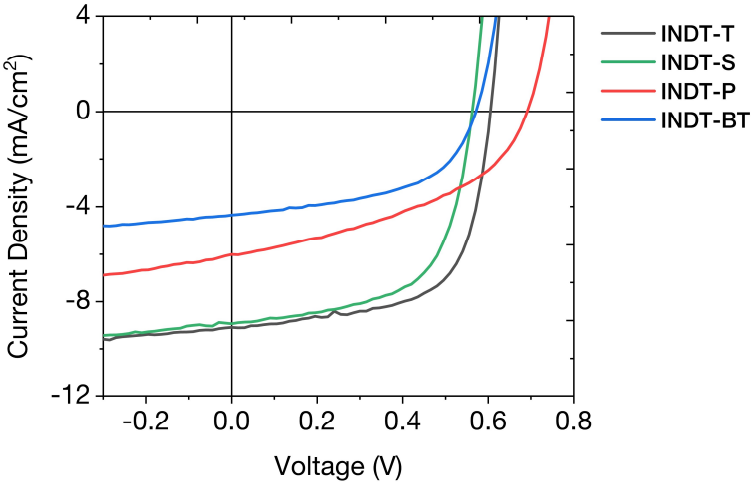


**Figure 2.14** Current-voltage characteristics of polymer:PC[70]BM (1:2) OPV devices

Interestingly, the increase in $M_n$ of **INDT-T** had minimal impact on $V_{OC}$ (0.60 V, $\Delta = -0.2$) however gave significant improvements to both $J_{SC}$ (9.1 mA/cm$^2$, $\Delta = +2.8$) and $FF$ (0.64, $\Delta = +0.06$), resulting in an improved overall device efficiency of 3.5%. The increased $J_{SC}$ was likely due to the increased $M_n$ resulting in an improved bulk heterojunction (BHJ) morphology. **INDT-S** devices showed lower $V_{OC}$, in line with the raised $E_{homo}$ observed experimentally, and high $J_{SC}$ and $FF$, with an overall power conversion efficiency (PCE) of 3.1%. The reasonably high $FF$ for both **INDT-T** and **INDT-S** indicated that both materials performed correctly in the BHJ devices.

**INDT-P** exhibited a significantly larger $V_{OC}$ resulting from the lowering of $E_{homo}$. Although a large $V_{OC}$ is desirable for OPVs, both the $J_{SC}$ and $FF$ were low, leading to an overall PCE of 1.8%. The relatively low solubility of **INDT-P**, with only restricted solubility in chlorobenzene, meant obtaining high quality thin-films was difficult, and so it

was not possible to determine whether the reduced performance was due to electronic or morphological factors.

Finally, **INDT-BT** did not perform well in OPV devices due to poor performance in all three figures of merit, especially $J_{SC}$ (4.4 mA/cm$^2$). The lower $V_{OC}$ was likely contributed by the higher $E_{homo}$ of **INDT-BT** reducing the offset with $E_{lumo}$ of the fullerene. As will be explained in more detail in the next section, **INDT-BT** exhibited extremely high crystallinity and the reduced $J_{SC}$ and $FF$ were very likely products of this high crystallinity leading to large crystalline domains which would have suppressed adequate intermixing of the donor and acceptor phases in the BHJ, thus poor photocurrent generation.

As both **INDT-T** and **INDT-S** showed promise as materials in near-IR OPV devices, the effect of varying the polymer:fullerene blend on device performance was investigated. The current-voltage characteristics are shown in **Figure 2.15** and the data from the devices summarised in **Table 2.8**.

**Table 2.8** OPV device characteristics of **INDT-T** and **INDT-S** solar cells with varying polymer:fullerene blends

| Polymer | D:A[a] | $J_{SC}$ (mA/cm$^2$) | $V_{OC}$ (V) | $FF$ | PCE (%) |
|---|---|---|---|---|---|
| INDT-T | 1:2 | 9.1 | 0.60 | 0.64 | 3.5 |
| | 1:3 | 10.0 | 0.61 | 0.66 | 4.0 |
| | 1:4 | 10.2 | 0.61 | 0.66 | 4.1 |
| INDT-S | 1:2 | 8.9 | 0.56 | 0.61 | 3.1 |
| | 1:3 | 10.3 | 0.57 | 0.60 | 3.5 |

[a]Ratio of polymer donor (D) to PC[70]BM (fullerene) acceptor (A)

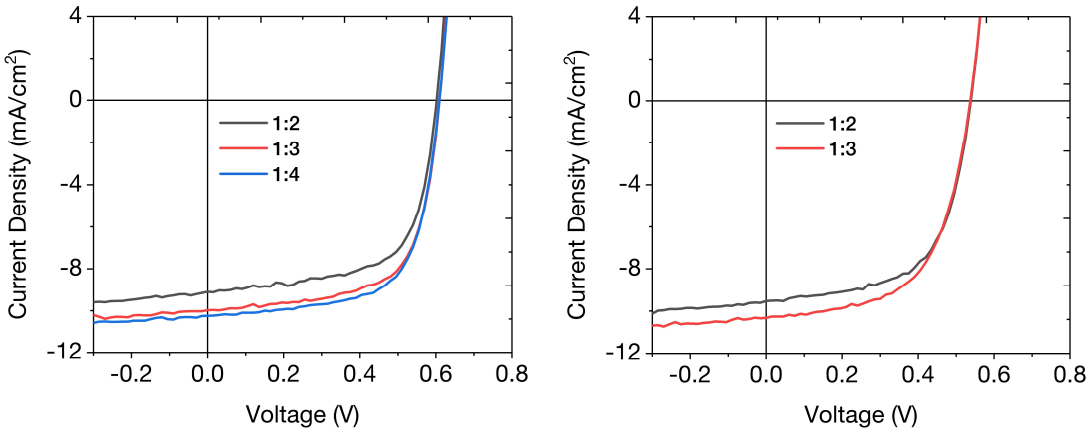


**Figure 2.15** Current-voltage characteristics of **INDT-T** (left) and **INDT-S** (right) OPV devices with varying polymer:PC[70]BM blends

In both **INDT-T** and **INDT-S** devices, increasing the concentration of fullerene led to increased device performance. Whilst $V_{OC}$ and $FF$ remained relatively independent of the variation, significant increases in $J_{SC}$ were observed. For **INDT-T**, a champion device efficiency of 4.1% was obtained with a $J_{SC}$ of 10.2 mA cm$^{-2}$. For **INDT-S**, although a similar $J_{SC}$ of 10.3 mA cm$^{-2}$ was obtained, lower $V_{OC}$ led to a relatively lower champion PCE of 3.1%.

The external quantum efficiencies (EQEs) of these devices were of considerable interest (**Figure 2.16**). Although the majority of the photocurrent originated from the fullerene absorption (~450 nm), there was a clear and significant contribution from the polymer absorption up to 900 nm.

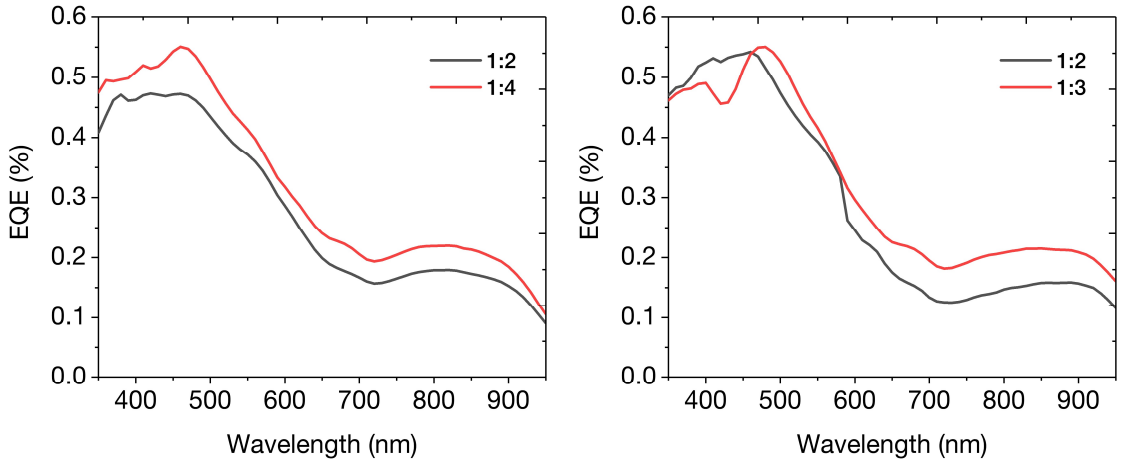


**Figure 2.16** EQEs of OPVs of **INDT-T** (left) and **INDT-S** (right) with varying polymer:PC[70]BM blends

Remarkably, as the concentration of the fullerene was increased, there was a clear increase in the photocurrent contribution from the polymer absorption in the near-IR. Considering the ultra-narrow band gaps of these polymers and the relatively large $V_{OC}$ of their OPV devices, the fact that relatively efficient charge photogeneration was observed at all was somewhat remarkable.

Importantly, the $E_{lumo}$ of all four INDT polymers (–3.7 eV) and the most commonly quoted $E_{lumo}$ of the PC[70]BM fullerene (–3.7 eV) were essentially isoenergetic, implying that the driving force for charge separation $(\Delta G_{CS})$ was virtually zero. Despite this, all contribution to the photocurrent above 700 nm was, without doubt, a result from polymer absorption.

To investigate this phenomenon, femtosecond transient absorption spectroscopy (fTAS) was performed on 1:4 blend films of **INDT-S**:PC[70]BM as a representative case (the respective **INDT-T** blend produced identical spectral trends). The transient spectrum of

a pristine **INDT-S** film pumped at the polymer absorption band, $\lambda_{pump}$ = 800 nm, is shown in **Figure 2.17a**. A broad band was recorded at ~1500 nm that decays with a time constant of 23 ps, and was assigned to the polymer singlet exciton. Addition of the fullerene to create the 1:4 blend film also led to the formation of the polymer singlet exciton (**Figure 2.17b**). However, after the singlet exciton had decayed, a much longer-lived component was observed that absorbed from 1060 nm to above 1400 nm. This component remained present even when the blend spectrum was measured on ns–µs timescales (**Figure 2.17b inset**). Since this excitation had no sensitivity to oxygen, this long-lived component was assigned to polymer polarons.

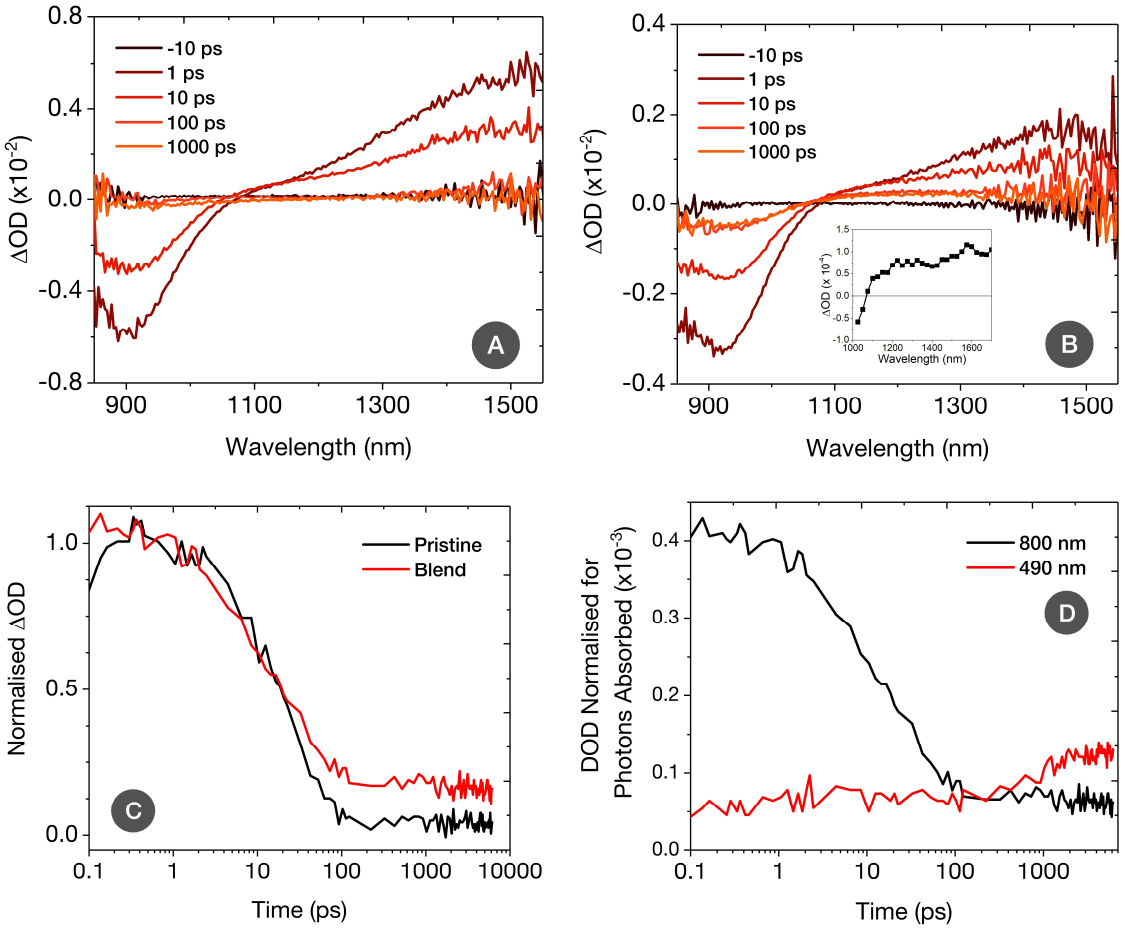


**Figure 2.17** Femtosecond-picosecond transient spectra of **INDT-S**; (a) pristine and (b) a 1:4 blend of **INDT-S**:PC[70]BM both with $\lambda_{pump}$ = 800 nm and an excitation density of 6 µJ cm$^{-2}$; (b, inset) Spectrum of the blend film at 200 ns using a longer time resolution system; (c) Normalised TA kinetics of pristine and 1:4 blend films using $\lambda_{pump}$ = 800 nm / $\lambda_{probe}$ = 950 nm and an excitation density of 2 µJ cm$^{-2}$; (d) TA kinetics of the blend film normalised for photons absorbed using $\lambda_{probe}$ and excitation density as in (c) but varying $\lambda_{pump}$ = 490 nm or 800 nm for selective excitation of either the fullerene or polymer respectively.

**Figure 2.17c** shows the kinetics for both the pristine and blend films using $\lambda_{pump}$ = 800 nm and a probe pulse, $\lambda_{probe}$ = 950 nm, thereby exclusively exciting the polymer. The singlet exciton decay was largely complete by ~100 ps, leaving a signal of close to zero for the pristine film. In the blend film, the singlet exciton similarly decayed by ~100 ps, however the contribution of the long-lived polymer polarons elucidated after ~100 ps, comprising 17% of the initial signal amplitude. As such, most of the polymer excitons formed were lost through relaxation back to the ground state (83%), which was attributed to the lack of driving force for charge separation $(\Delta G_{CS} \approx 0)$, consistent with the polymer contribution to the EQE of approximately 20% at 800 nm. Nevertheless, it was remarkable that such a high proportion of charge carriers were achieved through polymer excitation in such ultra-narrow band gap polymers.

Transient spectra obtained when exciting the fullerene selectively at $\lambda_{pump}$ = 490 nm and $\lambda_{probe}$ = 950 nm is shown in **Figure 2.17d** and suggested the presence of a second charge photogeneration mechanism. On pumping the blend at 490 nm, no decay was observed at all – instead two separate rises in the ground state bleach signal were observed. The first rise occurred from the initial time delay until ~100 ps, whilst the second occurred from 100 ps until the end of the measured time range. Both signals corresponded to the steadily increasing concentration of polymer polarons in the blend film, however the unusually slow nanosecond timescale of the second rise was indicative of hole transfer from photoexcited fullerene to the organic polymer, which has been previously observed in other organic polymers with low electron affinities.[159] Since the appearance of the second rise coincided with the completion of the polymer exciton decay, the first rise was assigned to a combination of polymer exciton decay and hole transfer rise.

The result of the slow rise in the concentration of polymer polarons at this excitation wavelength was that by the end of the measured time range the percentage of polymer polarons present was approximately double that of solely polymer excitation when the polaron signals were normalised for number of photons absorbed. Again, this was consistent with the EQE results, which showed a much greater contribution from fullerene excitons compared to polymer excitons.

As will be discussed heavily in the next section, but is noteworthy here, the INDT polymers have excellent n-type charge transport properties, and due to the isoenergetic nature of the electron affinities of these polymers and PCBM there is potential for INDT-based polymers to be used as an alternative to fullerenes as a polymer acceptor in organic solar cells.

### 2.5.5 Organic Field Effect Transistors

To assess the charge transporting abilities of the four novel polymers, TG-BC OFET devices were constructed on glass substrates, which exhibited superior device performance and lower hysteresis relative to coplanar BG-BC structures on silicon wafer substrates treated with hexamethyldisilazane (HMDS). This was attributed to charge traps at the semiconductor-dielectric interface, combined with higher parasitic contact resistance $(R_{\mathrm{C}})$ in the coplanar geometry.[160]

TG-BC devices were fabricated by spin coating each polymer from 10 mg/mL solutions in chlorobenzene onto pre-cleaned glass substrates with thermally evaporated SD electrodes. Following annealing for 15 min, a CYTOP dielectric was then spin coated onto the semiconductor layer followed by an Al gate electrode thermally evaporated onto the dielectric. The dimensions of the channel in all tested devices were $W = 1000\ \mu\mathrm{m}$ and $L = 40\ \mu\mathrm{m}$. Three varieties of SD contacts were employed, all of 40 nm thickness:

1. as-deposited Au on Al bilayer, for ambipolar operation
2. surface treated Au for p-type enhancement
3. surface treated Al for n-type enhancement

In cases 2 & 3, the treatment of the electrodes to better match the work function of each metal to either $E_{homo}$ (p-type) or $E_{lumo}$ (n-type) of the polymer series reduced charge injection barriers leading to lower contact resistance. Treating Au with UV/ozone facilitated superior hole injection by both removing organic contaminants and forming a native oxide layer.[161,162] Treating Al with ethoxylated polyethylenimine (PEIE) facilitated superior electron injection by reducing the work function to better match the electron affinities of the metal and the polymers. Devices were annealed at 100 ˚C and 190 ˚C, the latter representing the upper limit of the temperature range for which PEIE treatment is most effective.[163]

Despite these efforts to reduce charge injection barriers, the output characteristics observed at low $V_{\mathrm{D}}$ were non-linear. Additionally, when longer channel lengths were tested, $V_{\mathrm{Th}}$ were very low. These two observations were indicative of large $R_{\mathrm{C}}$ and contact-limited device performance, akin to the first **INDT-T** polymer discussed earlier. Importantly, this behaviour renders these devices non-ideal and so the standard gradual channel approximation operation model did not adequately describe the device physics and extracted mobility values using this model were not representative of the bulk property.[164,102]

Extracting performance data in contact-limited devices must be done with care, as the standard method for extracting $V_{\mathrm{Th}}$ typically gives overestimates and the square root

method of extracting $\mu_{sat}$ can be equally unreliable.[165,166] To better analyse the bulk properties of the semiconductor in these devices, a large $V_{\mathrm{D}}$ was applied to compensate for the large $R_{\mathrm{C}}$, and $\mu_{sat}$ was extracted using the second derivative of the saturation regime transfer curve. Transfer data was smoothed prior to data extraction to exclude extreme values and yield a reproducible estimate. Furthermore, **Figure 2.18** shows the gate voltage dependence on mobility and demonstrates that values of $\mu_{sat}$ are not overestimations.[99]

Characteristics and performance data for champion OFET devices of all four polymers is summarised in **Table 2.9**. Complete OFET data for the four polymers is summarised in **Tables 2.10-2.13** and the transfer curves and output characteristics for all four devices is shown in **Figures 2.19-2.22**.

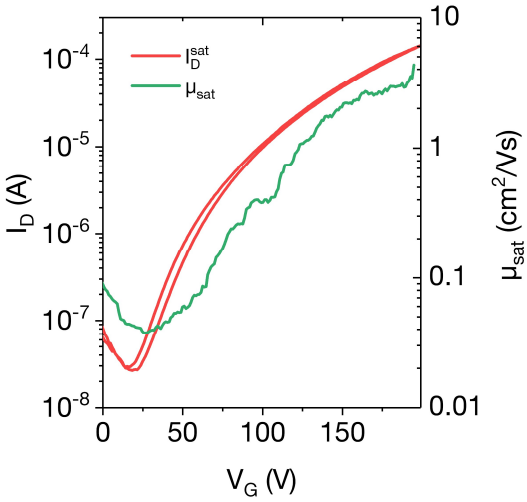


**Figure 2.18** $V_{\mathrm{G}}$–dependence on $\mu_{sat}$ for n-type enhanced OFET device with **INDT-BT** annealed at 190 °C, where $L = 40$ μm, $W = 1000$ μm and $V_{\mathrm{D}} = +180$ V

**Table 2.9** Characteristics of champion TG-BC OFET devices containing the four INDT polymers annealed at 190 ℃ with $W = 1000$ μm and $L = 40$ μm

| Polymer | Type[a] | ${I_{on}/I_{off}}^{lin}$ | $V_{\mathrm{Th}}^{lin}$ (V) | ${I_{on}/I_{off}}^{sat}$ | $V_{\mathrm{Th}}^{sat}$ (V) | ${\mu_{sat}}^{b}$ ($\mathrm{cm^2/Vs}$) |
|---|---|---|---|---|---|---|
| INDT-P | p | $10^2$ | $-104$ | $10^2$ | $-155$ | $2 \times 10^{-3}$ |
| | n | $10^3 - 10^4$ | $+10$ | $10^3$ | $+89$ | $3 \times 10^{-2}$ |
| INDT-T | p | $10^4$ | $-25$ | $10^1 - 10^2$ | $-92$ | 0.29 |
| | n | $10^4 - 10^5$ | $-10$ | $10^3 - 10^4$ | $+37$ | 0.31 |
| INDT-S | p | $10^3$ | $-40$ | $10^1 - 10^2$ | $-101$ | 0.20 |
| | n | $10^4 - 10^5$ | $-10$ | $10^3$ | $+74$ | 0.99 |
| INDT-BT | p | $10^4$ | $-36$ | $10^1$ | $-121$ | 0.52 |
| | n | $10^5$ | $-10$ | $10^4$ | $+74$ | 3.11 |

[a]Parameters extracted from the highest mobility p-type or n-type enhanced devices; [b]Highest value extracted from a ten-point average of smoothed data

Devices containing ambipolar SD electrodes performed well (**Tables 2.10-2.13**) except **INDT-P** which showed smaller $I_{\mathrm{D}}^{max}$ and lower $\mu_{sat}$ due to non-uniformities in the polymer film. The low solubility of **INDT-P** yielded poor quality thin-films and its higher $E_{hom}$ gave rise to a large hole injection barrier as evidenced from the larger $V_{\mathrm{Th}}$ and the highly non-linear output characteristics at low $V_{\mathrm{D}}$. These issues were also present in the enhanced devices of **INDT-P** and thus led to overall poor performance.

In single charge polarity enhanced devices, **INDT-T** showed good balanced charge transport of $\mu_h/\mu_e \sim 0.3$ $\mathrm{cm^2/Vs}$ and both **INDT-S** and **INDT-BT** showed high average p-type performance of 0.20 and 0.52 $\mathrm{cm^2/Vs}$ respectively and excellent peak n-type charge transport performance of up to 0.99 and 3.11 $\mathrm{cm^2/Vs}$ respectively. Pleasingly, OFET performance was highly reproducible over extended periods of time and the mobilities given for **INDT-BT** represent 23 individual devices and are given with low margins of error. The average and peak results of **INDT-BT** indicated that it was one of the highest mobility n-type organic semiconductors reported in the peer-reviewed literature.[65] The output characteristics of **INDT-BT** shown in **Figure 2.22** indicate that the device was strongly contact-limited, and thus it is likely that $\mu_e$ of 3.1 $\mathrm{cm^2/Vs}$ was an underestimate of the bulk property.

**Table 2.10** Characteristics of highest performance OFET devices containing **INDT-T**

| $T^{a}$ (°C) | Type[a] | ${I_{on}/I_{off}}^{lin}$ | ${I_{on}/I_{off}}^{sat}$ | $V_{Th}^{lin}$ (V) | $V_{Th}^{sat}$ (V) | $\mu_{lin}$ (cm²/Vs) | $\mu_{sat}$ (cm²/Vs) |
|---|---|---|---|---|---|---|---|
| 100 | p[b] | $10^4$ | $10^2$ | −79 | −137 | 0.020 | 0.11 |
| | n[b] | $10^6$ | $10^2 - 10^3$ | +6 | +55 | 0.029 | 0.11 |
| 190 | p[b] | $10^4 - 10^5$ | $10^1 - 10^2$ | −47 | −99 | 0.041 | 0.25 |
| | n[b] | $10^4$ | $10^1 - 10^2$ | +26 | +99 | 0.054 | 0.31 |
| | p[c] | $10^4$ | $10^1 - 10^2$ | −25 | −92 | 0.048 | 0.29 |
| | n[c] | $10^4 - 10^5$ | $10^3 - 10^4$ | −10 | +37 | 0.054 | 0.31 |

[a]Annealing temperature; [b]Ambipolar SD; [c]Enchanced SD

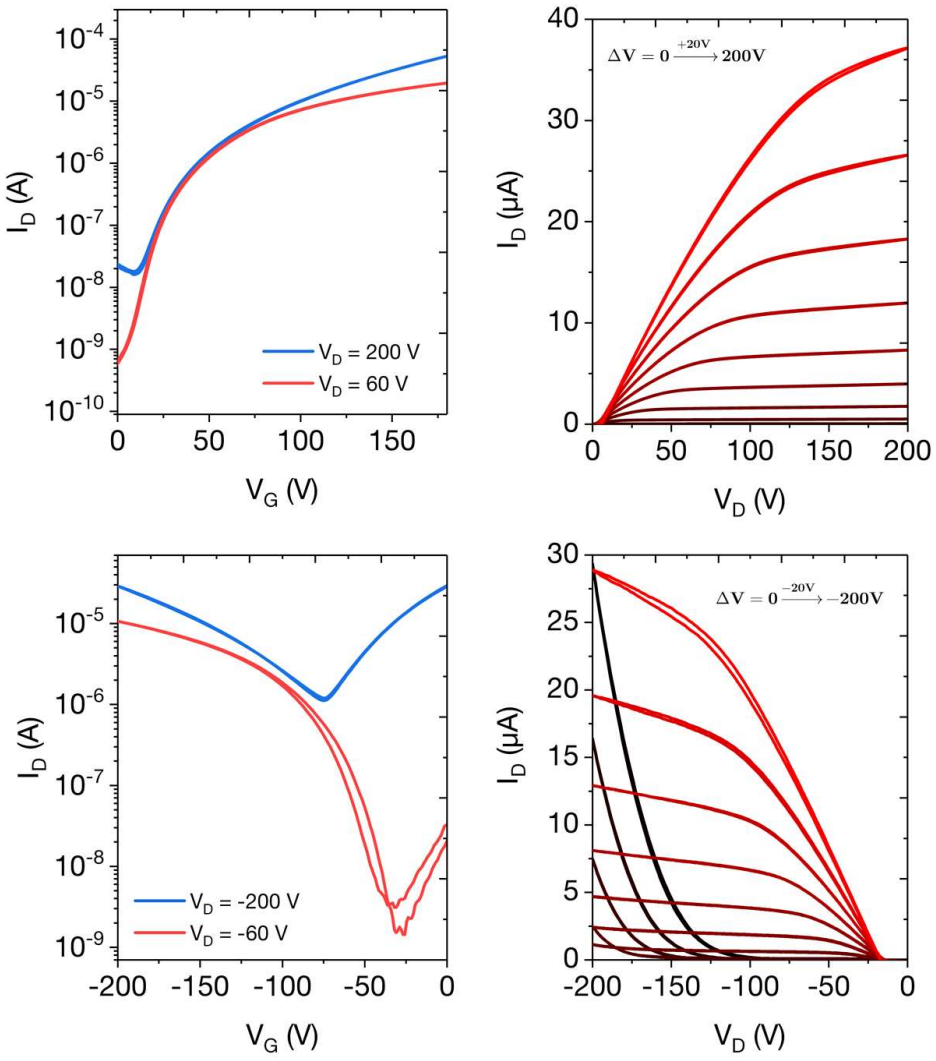


**Figure 2.19** Transfer (left) curves and output (right) characteristics of n-type (top) and p-type (bottom) TG-BC OFET enhanced devices of **INDT-T** annealed at 190 °C with $W = 1000$ µm and $L = 40$ µm

**Table 2.11** Characteristics of highest performance OFET devices containing **INDT-S**

| $T^{a}$ (°C) | Type[a] | $I_{on}/I_{off}{}^{lin}$ | $I_{on}/I_{off}{}^{sat}$ | $V_{Th}^{lin}$ (V) | $V_{Th}^{sat}$ (V) | $\mu_{lin}$ (cm$^2$/Vs) | $\mu_{sat}$ (cm$^2$/Vs) |
|---|---|---|---|---|---|---|---|
| 100 | p[b] | $10^4 - 10^5$ | $10^1 - 10^2$ | −73 | −126 | 0.017 | 0.11 |
| | n[b] | $10^5$ | $10^2$ | +10 | +96 | 0.056 | 0.35 |
| 190 | p[b] | $10^3 - 10^4$ | $10^1 - 10^2$ | −48 | −119 | 0.030 | 0.16 |
| | n[b] | $10^4 - 10^5$ | $10^2$ | +17 | +108 | 0.054 | 0.73 |
| | p[c] | $10^3$ | $10^1 - 10^2$ | −40 | −101 | 0.029 | 0.20 |
| | n[c] | $10^4 - 10^5$ | $10^3$ | −10 | +74 | 0.045 | 0.99 |
| | n[d] | $10^5 - 10^6$ | $10^2$ | +10 | +112 | 0.039 | 0.85 |

[a]Annealing temperature; [b]Ambipolar SD; [c]Enchanced SD; [d]Enchanced SD without PEIE layer

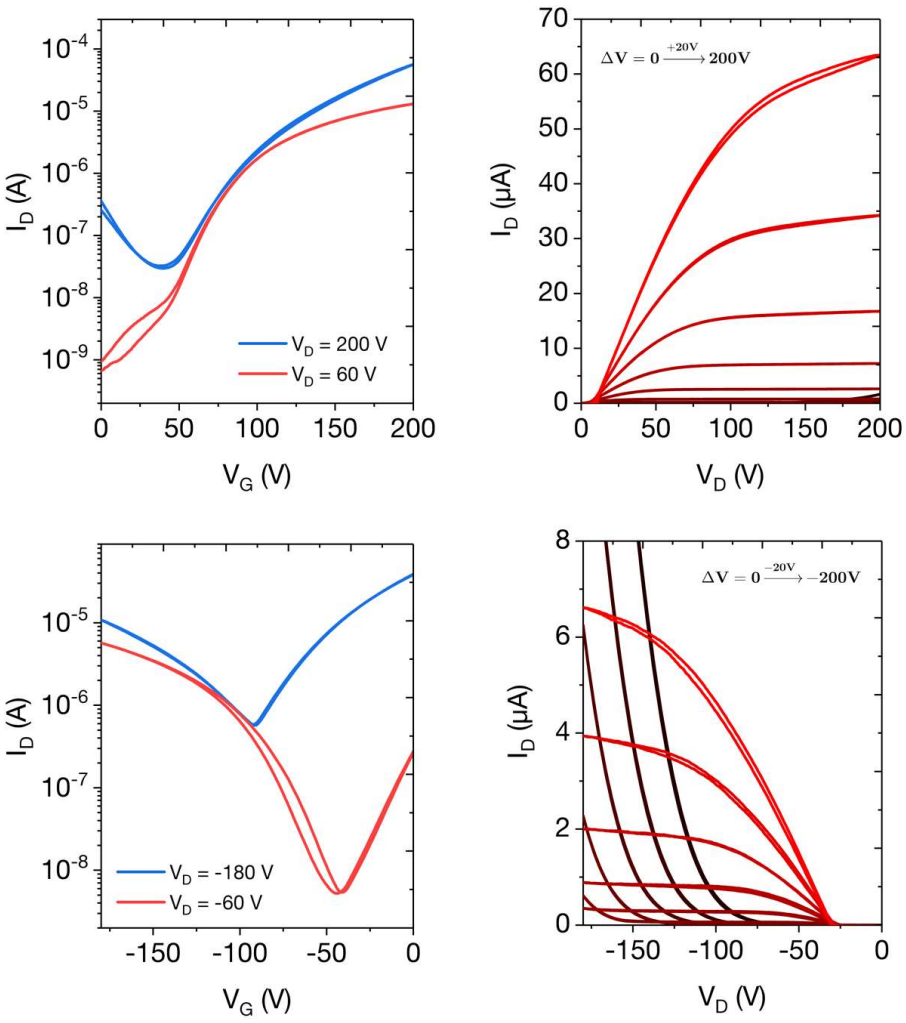


**Figure 2.20** Transfer (left) curves and output (right) characteristics of n-type (top) and p-type (bottom) TG-BC OFET enhanced devices of **INDT-S** annealed at 190 °C with $W$ = 1000 µm and $L$ = 40 µm

**Table 2.12** Characteristics of highest performance OFET devices containing **INDT-P**

| $T^{a}$ (°C) | Type[a] | $I_{on}/I_{off}{}^{lin}$ | $I_{on}/I_{off}{}^{sat}$ | $V_{Th}^{lin}$ (V) | $V_{Th}^{sat}$ (V) | $\mu_{lin}$ (cm$^2$/Vs) | $\mu_{sat}$ (cm$^2$/Vs) |
|---|---|---|---|---|---|---|---|
| 100 | p[b] | – | – | – | – | – | – |
| | n[b] | $10^3 - 10^4$ | $10^2 - 10^3$ | −39 | +121 | $1 \times 10^{-3}$ | $9 \times 10^{-3}$ |
| 190 | p[b] | – | – | – | – | – | – |
| | n[b] | $10^4$ | $10^2 - 10^3$ | +32 | +102 | $2 \times 10^{-3}$ | 0.018 |
| | p[c] | $10^2$ | $10^2$ | −104 | −155 | – | $2 \times 10^{-3}$ |
| | n[c] | $10^3 - 10^4$ | $10^3$ | +10 | +89 | $2 \times 10^{-3}$ | 0.028 |

[a]Annealing temperature; [b]Ambipolar SD; [c]Enchanced SD; Some p-type data unavailable due to high leakage currents

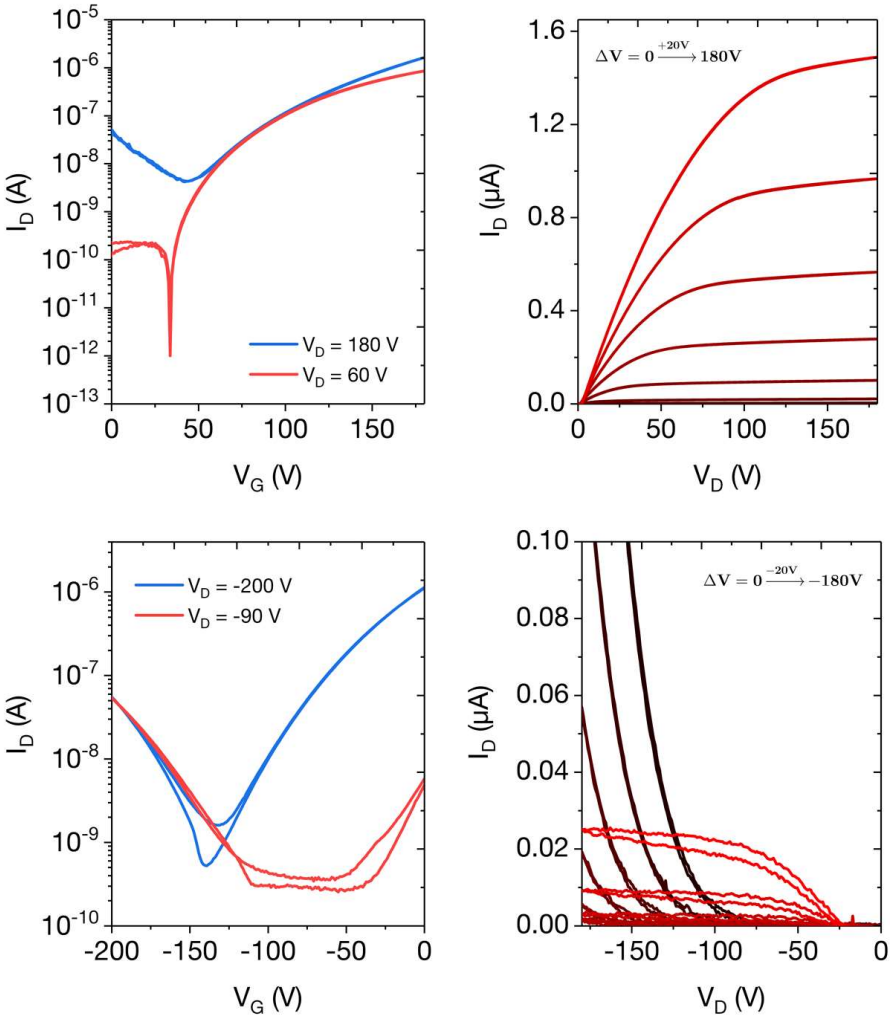


**Figure 2.21** Transfer (left) curves and output (right) characteristics of TG-BC OFET devices of **INDT-P**. N-type data (top) was recorded in an ambipolar device and p-type data (bottom) was recoreded in a p-type optimised device. All devices were annealed at 190 °C with $W = 1000$ μm and $L = 40$ μm.

**Table 2.13** Characteristics of highest performance OFET devices containing **INDT-BT**

| $T^{a}$ (°C) | Type[a] | ${I_{on}/I_{off}}^{lin}$ | ${I_{on}/I_{off}}^{sat}$ | $V_{Th}^{lin}$ (V) | $V_{Th}^{sat}$ (V) | $\mu_{lin}$ ($cm^2/Vs$) | $\mu_{sat}$ ($cm^2/Vs$) |
|---|---|---|---|---|---|---|---|
| 100 | p[b] | $10^2 - 10^3$ | $10^1$ | −80 | −150 | 0.013 | 0.18 |
| | n[b] | $10^5 - 10^6$ | $10^3$ | +9 | +83 | 0.33 | 1.05 |
| 190 | p[b] | $10^3 - 10^4$ | $10^1$ | −44 | −133 | 0.027 | 0.2 |
| | n[b] | $10^5$ | $10^2 - 10^3$ | +18 | +115 | 0.31 | 1.8[e] |
| | p[c] | $10^4$ | $10^1$ | −36 | −121 | 0.12 | 0.52 |
| | n[c] | $10^4 - 10^5$ | $10^4$ | −9 | +77 | 0.33 | 2.8[f] |
| | n[d] | $10^4 - 10^5$ | $10^2$ | +21 | +104 | 0.24 | 1.9[g] |

[a]Annealing temperature; [b]Ambipolar SD; [c]Enchanced SD; [d]Enchanced SD without PEIE layer; [e]Mean of ten devices; [f]Mean of seven devices; [g]Mean of five devices; [e,f,g]Standard deviation of mobilities: ±0.3 $cm^2/Vs$

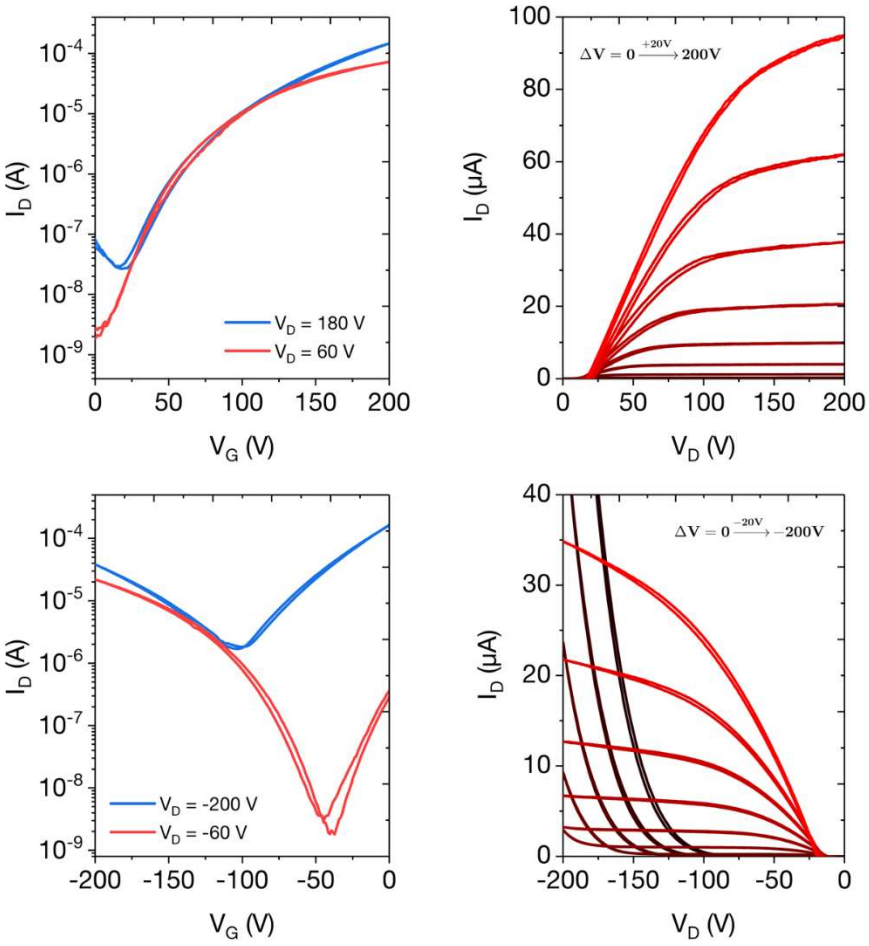


**Figure 2.22** Transfer (left) curves and output (right) characteristics of n-type (top) and p-type (bottom) TG-BC OFET enhanced devices of **INDT-BT** annealed at 190 °C with $W = 1000$ µm and $L = 40$ µm

Extracted $\mu_{lin}$ values are far smaller than the corresponding $\mu_{sat}$ for each device type, and in ambipolar devices values of $V_{\mathrm{Th}}$ are very large, both providing further evidence of contact-limited performance.[102] The non-linearities in the low voltage output data indicate that extracted $\mu_{lin}$ values are a significant underestimate of the bulk property.

The enhancement of devices for single charge polarity operation via SD treatment greatly lowered charge injection barriers as evidenced from the increase in values for $\mu_{sat}$ and the lowering of the magnitudes of $V_{\mathrm{Th}}$. Importantly, the performance of devices with PEIE-treated Al SD was superior to those with untreated Al SD showing that the dramatically improved n-type operation can be attributed primarily to the presence of the PEIE election injection layer and not the use of low work function SD electrodes.

### 2.5.6 Atomic Force Microscopy

High electron transport in OFET devices is typically attributed to facile electron injection resulting from ideal matching of the $E_{lumo}$ of the semiconductor to the work function of the SD electrodes. However, all four INDT polymers had isoenergetic electron affinities within experimental error of $E_{lumo} = -3.75 \pm 0.05$, offering a unique opportunity to examine n-type performance irrespective of $E_{lumo}$. If the variation in $\mu_e$ was not of electrical origin, we postulated that the differences must occur from morphological aspects.

To examine the morphology of the surface of the four semiconductors, atomic force microscopy (AFM) was carried out on thin-films prepared identically to those in of the OFET active layer. **Figures 2.23-2.26** show the AFM images of 5 and 1 μm$^2$ thin-films for all four polymers and **Figure 2.27** shows high resolution 5 μm$^2$ scans on **INDT-BT**.

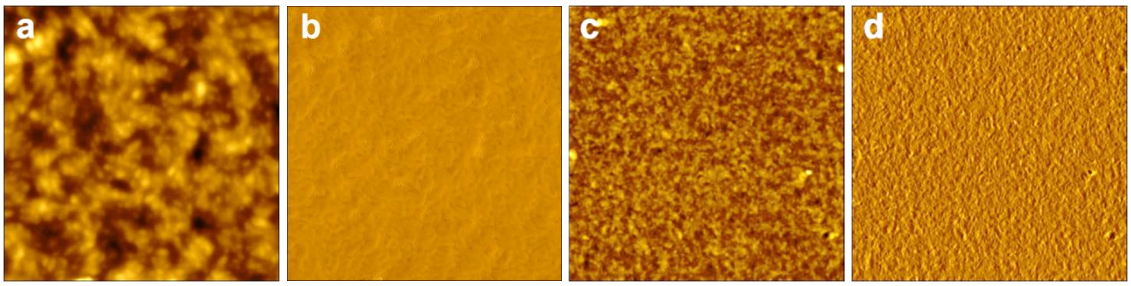


**Figure 2.23** AFM images of **INDT-T** thin-films spin cast from 10 mg/mL and annealed at 190 ℃; (a) 1 $\mu m^2$ topography (RMS = 2.1 nm) and (b) phase; (c) 5 $\mu m^2$ topography (RMS = 2.5 nm) and (d) phase

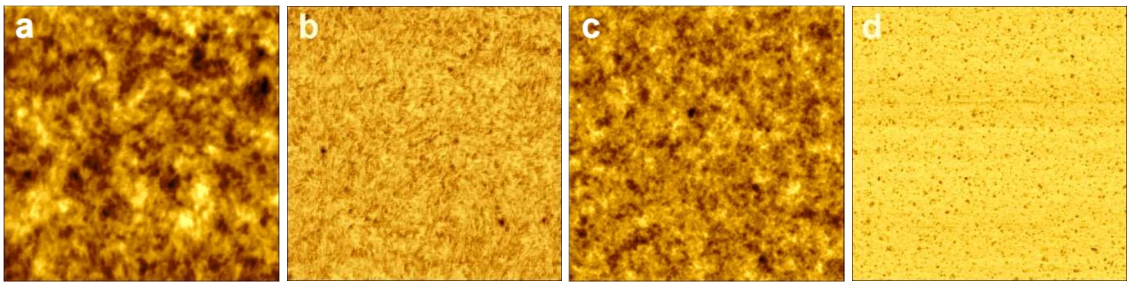


**Figure 2.24** AFM images of **INDT-S** thin-films spin cast from 10 mg/mL and annealed at 190 ℃; (a) 1 $\mu m^2$ topography (RMS = 1.1 nm) and (b) phase; (c) 5 $\mu m^2$ topography (RMS = 2.7 nm) and (d) phase

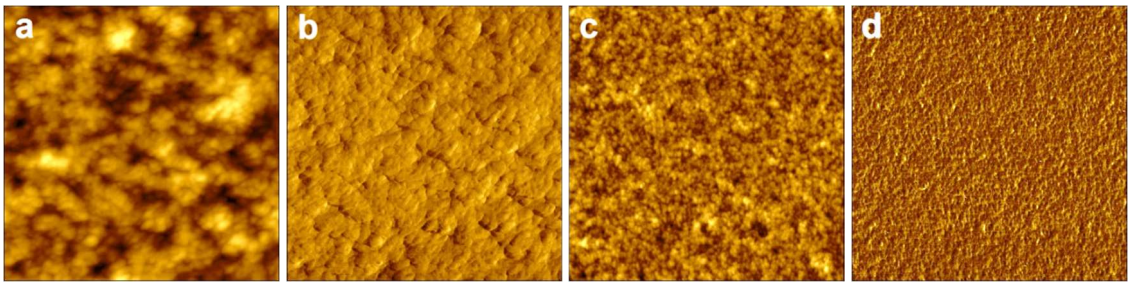


**Figure 2.25** AFM images of **INDT-P** thin-films spin cast from 10 mg/mL and annealed at 190 ℃; (a) 1 $\mu m^2$ topography (RMS = 3.0 nm) and (b) phase; (c) 5 $\mu m^2$ topography (RMS = 3.4 nm) and (d) phase

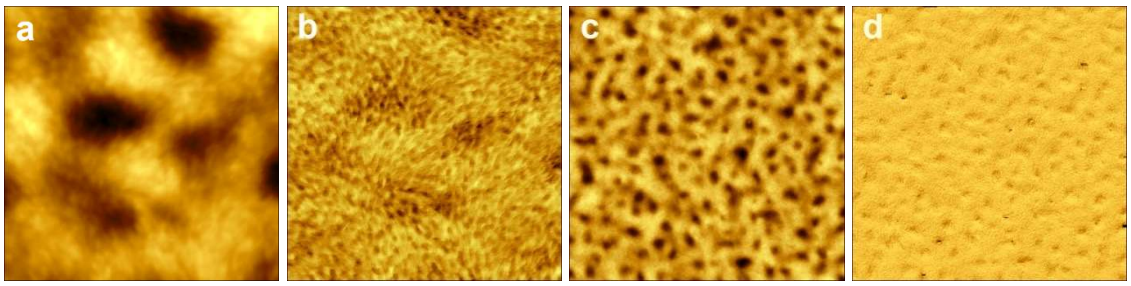


**Figure 2.26** AFM images of **INDT-BT** thin-films spin cast from 10 mg/mL and annealed at 190 ℃; (a) 1 $\mu m^2$ topography (RMS = 7.0 nm) and (b) phase; (c) 5 $\mu m^2$ topography (RMS = 9.1 nm) and (d) phase

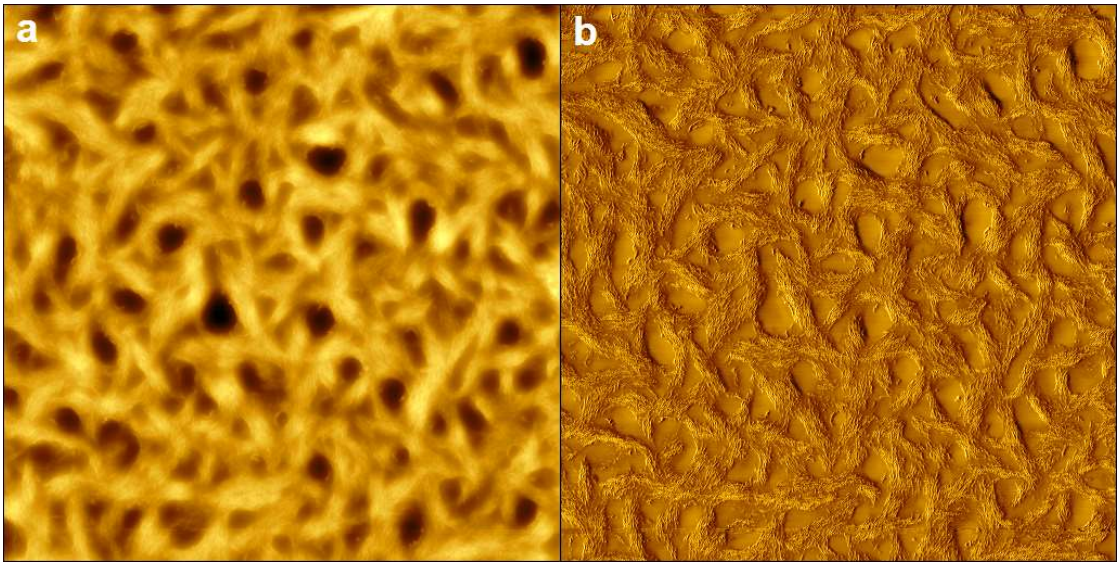


**Figure 2.27** High resolution AFM images of a 5 $\mu m^2$ **INDT-BT** thin-film spin cast from 10 mg/mL and annealed at 100 °C; (a) Topography (RMS = 9.5 nm) and (b) phase; Both topography and phase similar to 190 °C annealed films

Using AFM, if was clear that the **BT** thin-film had a significantly different surface morphology to the other three polymers; Both **T**, **S** and **P** films exhibited relatively flat polycrystalline structure with similar root mean square (RMS) surface roughness of 2.5–3.4 nm, whilst the **BT** film had high RMS of 9.5 nm that contained networks of smooth ribbon-like features. Whilst this suggested a different microstructure of **INDT-BT** at the surface, it was necessary to investigate the bulk morphology of the films, where the majority of charge transport is facilitated.

*For the remainder of this chapter,* ***INDT-P*** *will be omitted from further discussion due to its poor charge transport properties.*

### 2.5.7 Grazing-Incidence Wide Angle X-ray Spectroscopy

The observed high charge transport suggests that the INDT polymer thin-films are not amorphous and are instead self-aligned and highly ordered crystalline systems. To examine the crystallinity of the films, grazing incidence wide-angle X-ray scattering (GIWAXS) was performed on thin-films of **INDT-T**, **INDT-S** and **INDT-BT**.

The 2D scattering patterns and the corresponding out-of-plane $(q_z)$ and in-plane $(q_{xy})$ line cuts are presented in **Figure 2.28**. Crystalline correlation lengths (CCL) and *d*-spacings of the three polymers were calculated from the GIWAXS data and are presented in **Table 2.14**. The CCLs were calculated using a Scherrer analysis modified for a 2D detector.[167]

**Table 2.14** GIWAXS crystalline correlation lengths (CCLs) and *d*-spacings of diffraction planes of INDT polymer thin-films

| Polymer | edge-on[a]/ face-on[b] | *d*-spacing (Å) | | | Correlation length (nm) | | |
|---|---|---|---|---|---|---|---|
| | | (100) | (010) | (001)[c] | (100) | (010) | (001)[c] |
| INDT-BT | edge | 23.3 | 3.66 | 17.8 | 13 | 2.7 | 23 |
| | face | 26.5 | 3.50 | – | 9.9 | 3.3 | – |
| INDT-S | edge | 22.8 | 3.62 | 17.3 | 13 | 2.7 | 9.6 |
| | face | 27.2 | – | – | 4.9 | – | – |
| INDT-T | edge | 22.4 | 3.66 | 17.5 | 15 | 2.5 | 11.8 |
| | face | 22.4 | – | – | 2.1 | – | – |

[a]Edge-on domains include out-of-plane ($q_z$) (100) peaks and in-plane ($q_{xy}$) (010) peaks; [b]Face-on domains include in-plane ($q_{xy}$) (100) peaks and out-of-plane ($q_z$) (010) peaks; [c](001) peaks do not distinguish between an edge-on or face-on orientation

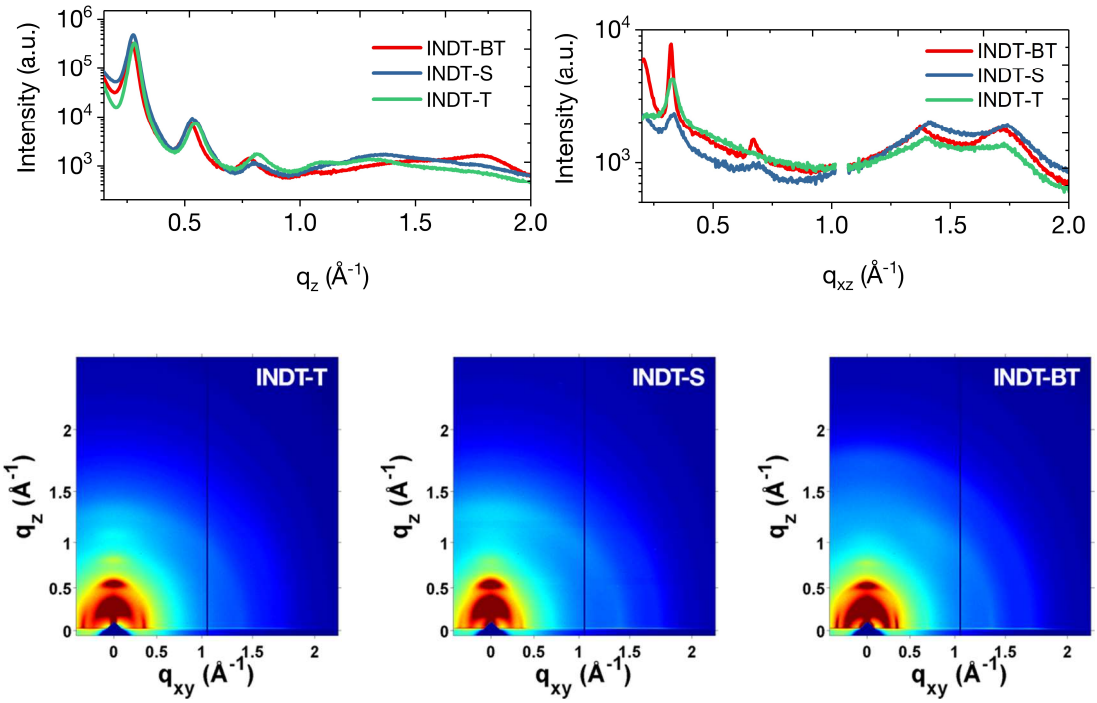


**Figure 2.28** Top: in-plane ($q_{xy}$, left) and out-of-plane ($q_z$, right) GIWAXS line cuts; Bottom: 2D GIWAXS scattering images of **INDT-T** (left), **INDT-S** (middle) and **INDT-BT** (right)

In the out-of-plane ($q_z$) line cuts, all three polymers showed significant edge-on lamellar ordering with (100), (200), (300) and even (400) peaks clearly visible. The *d*-spacings and CCLs for these domains were all similar indicating there was comparative side-chain based ordering in the three polymers. Additionally, **INDT-BT** demonstrated a clear out-

of-plane $\pi - \pi$ stacking $(010)$ peak arising from face-on $\pi - \pi$ crystallites, in contrast to the other two polymers.

In the in-plane $(q_{xy})$ line cuts, all three polymers exhibited edge-on $(010)$ peaks, however there was demonstrative reduction in peak intensity in **BT** > **S** > **T**. There was also indication of face-on $(100)$ domains, however there was a greater reduction in intensity and CCL of this domain in the same trend as the $(010)$ peaks, as shown in **Table 2.14**. Ultimately, **INDT-BT** showed balance between edge-on and face-on domains, while **INDT-S** and **INDT-T** greatly favored the edge-on orientation.

Crucially, there was a significant difference in the $(001)$ and $(002)$ peaks, corresponding to planes resulting from repeating polymer units in an ordered chain backbone (**Figure 2.29**).[168] These peaks indicate the relative degree to which the polymer is forming straight chains in the film –a highly beneficial quality for charge transport.

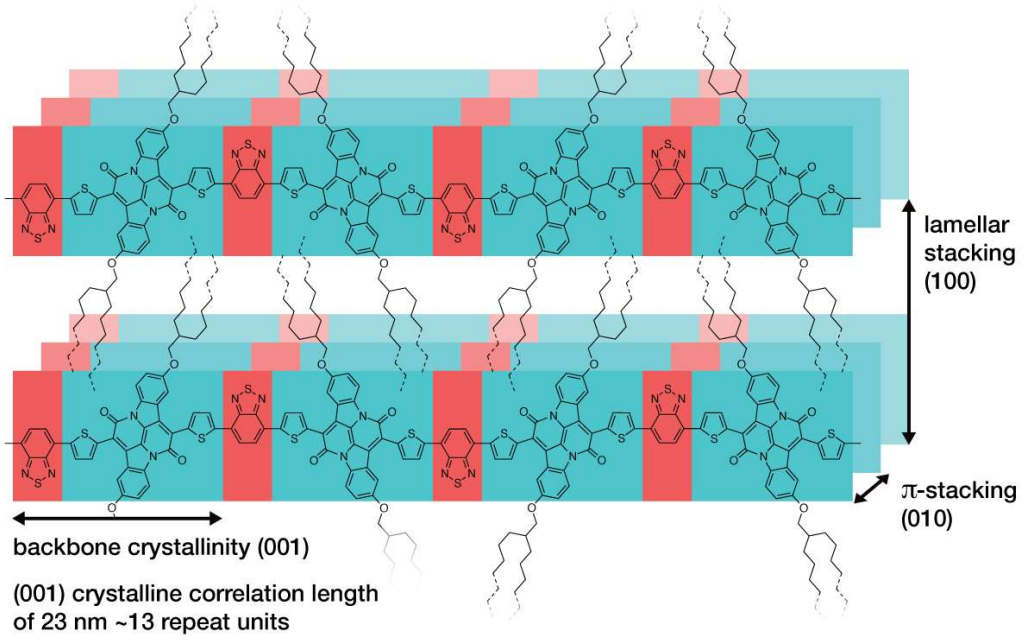


**Figure 2.29** Visualization of the GIWAXS thin-film crystallinity of **INDT-BT**

The $(001)$ $d$-spacings were in good accordance with the geometry-optimized calculated size of a single repeat unit. All three polymers exhibited large CCLs, indicating strong straight chain ordering, especially in **INDT-BT** which had a CCL of 23 nm corresponding to 13 repeat units, a remarkable level of straight chain ordering. **INDT-BT** demonstrated a sharp $(001)$ peak and a sharp $(002)$ second order reflection whilst **INDT-S** exhibited a clear $(001)$ peak and a broad, but clear second order reflection. **INDT-T** presented a $(001)$ peak but no second order reflection indicating that, while it did have strong periodicity along the polymer chain backbone, including a CCL slightly higher than

**INDT-S**, the lack of a second order reflection indicated a lower degree of long range ordering compared to the other two polymers.

These results suggest that the highly ordered chain backbone of **INDT-BT** is the source of its ultra-high electron charge transport properties. These results correlate with similar findings for high p-type mobility organic conjugated polymers and demonstrate how high polymer backbone crystallinity is crucial for high charge transport.[63]

## 2.6 New Structure–Property Relationships

The results of the research detailed in this chapter have implications on the greater context of conjugated polymer design. The introduction of selenophene or benzothiadiazole into a conjugated polymer backbone is a typical strategy for enhancing charge transporting characteristics of organic semiconductors, in particular electron transport.[169–172] The increased n-type mobility is usually attributed to the lowering of $E_{lumo}$ facilitating the injection of electrons into the semiconductor LUMO. However, despite $E_{lumo}$ of the INDT polymers being isoenergetic, significantly enhanced n-type charge transport was seen, attributed to the increased crystallinity along the polymer backbone.

As our study only changed the co-monomer from **T** to **S** to **BT** but kept the acceptor INDT unit constant, the observed increase in backbone crystallinity must originate solely from the modification of co-monomer. This suggests that both benzothiadiazole and selenophene (the former more than the latter) may have an inherent ability to induce order along polymer backbones. Therefore it is possible that the increase in mobility that is commonly observed when introducing either **S** or **BT** units is not solely due to electronic effects on $E_{lumo}$ but also due to a subtle increase in order along the polymer backbone resulting from intra-molecular rigidification of the backbone structure[173] or increased inter-molecular stacking interactions.[53]

To investigate the origin of the rigidity of the polymer backbones we examined the theoretical degrees of rotational freedom along the novel polymers. There are two unique degrees of freedom along each polymer (**Figure 2.30**): the bond connecting the IND core to a thiophene unit $(\theta_{\mathrm{A}})$ and the bond connecting the aromatic co-monomer (T / S / BT) to a thiophene $(\theta_{\mathrm{B}})$.

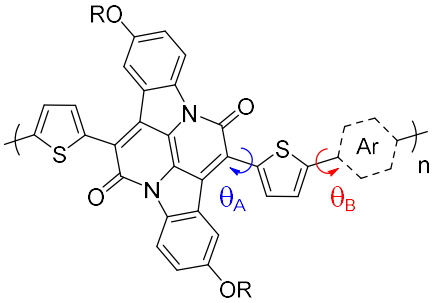


**Figure 2.30** Visualisation of the sites of rotational freedom along the INDT–Ar polymer backbone occurring at the connecting bonds of IND to thiophene (IND–T, $\theta_A$) and thiophene to the different aromatic co-monomers (T–Ar, $\theta_B$)

Initially we set out to understand the origin of the increased backbone crystallinity (and hence charge transport mobilities) of the **BT** vs **S** vs **T** co-monomer units ($\theta_B$). Theoretical torsional potential calculations were carried out on representative dimers of each aryl–thiophene unit at 10° intervals, holding the connecting dihedral angle fixed whilst performing geometry optimization on all remaining degrees of freedom at the B3LYP/6-311G** level of theory. Although this calculation provided reliable optimized geometries, it has previously been reported that DFT calculations suffer from self-interaction error, giving rise to unfair bias toward planar conformations resulting from better delocalization of the wave function. However, second-order Moller−Plesset perturbation theory (MP2) does not and, when used with large basis sets, provides a more reliable method of calculating torsional potential energies.[174] Therefore, the optimized geometries at each 10° interval attained using DFT calculations were taken as input geometries for single point energy calculations using the MP2 functional at the high cc-pVTZ level of theory. The resulting potential energy surfaces are plotted in **Figure 2.31**.

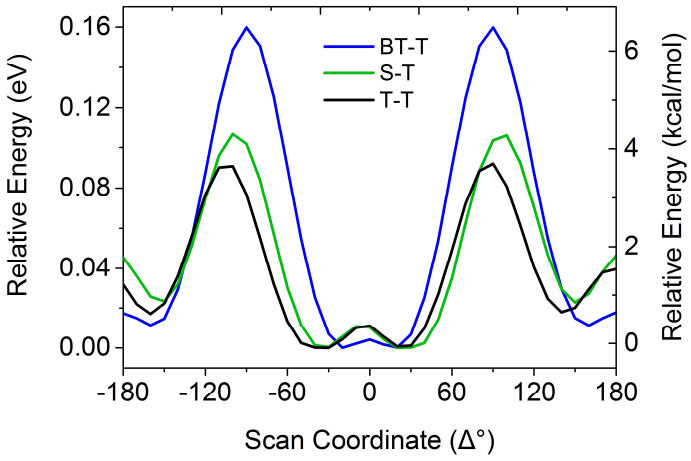


**Figure 2.31** Potential energy surface (MP2/cc-pVTZ) of dihedral angle ($\theta_B$) of dimers of thiophene with benzothiadiazole (BT), selenophene (S) and thiophene (T)

All three dimers were most stable in their trans-orientation as expected, although the completely planar geometry $(\theta_B = 0°)$ was slightly disfavored. The three different dimers all show steep energy barriers with significantly higher maxima for **BT** than for **S** or **T**. The overall degree of restriction of rotation for the dimers follows the trend **BT** > **S** > **T**, which matches the trend in experimental n-type transport as a function of polymer backbone crystallinity, suggesting how lower degrees of rotational freedom along the polymer backbone gives rise to a higher degree of crystallinity.

The high torsional potential of the **BT**–T couple has previously been linked to the origin of high p-type mobility in conjugated polymers.[63] The natural ability of benzothiadiazole to increase rigidity and therefore backbone crystallinity in conjugated polymer chains, thus allowing efficient charge transport, may begin to explain why this heterocyclic unit has consistently been present in the highest performing polymers for organic electronics. However, these results further suggest that the commonly seen increased mobility of selenophene containing polymers over their thiophene analogues is at least in part due to reduced torsional disorder. **Figure 2.32** shows the results of the same calculations of the thiophene–indolonaphthyridine dihedral $(\theta_A)$.

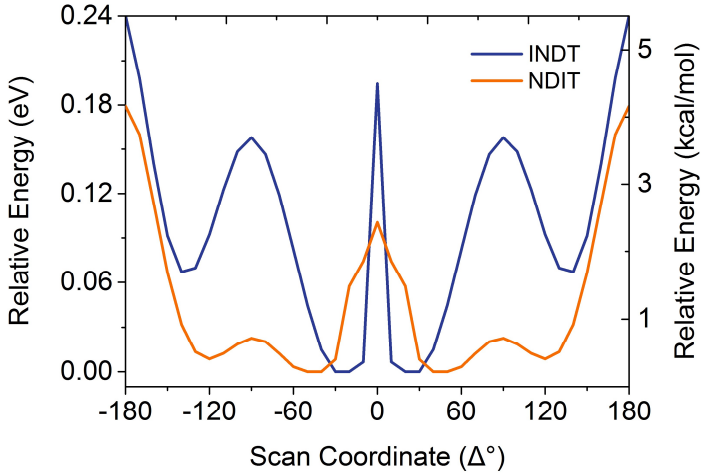


**Figure 2.32** Potential energy surface (MP2/cc-pVTZ) of dihedral angle $(\theta_A)$ of dimers of thiophene with IND and NDI where 0° corresponds to fully planar structures with heteroatoms in *syn*-conformation

Large destabilising interactions for planar conformations $(\theta_A = 0°/\pm 180°)$ arising from steric interactions between either the S–O or H–O were clearly visible, with the latter being the most destabilizing. Remarkably, the lowest energy conformation was one where the dimer was non-planar, having a dihedral angle of approximately 30°. At perpendicular geometries $(\theta_A = 90°)$ another energetic maxima was seen, arising from disruption of conjugation creating large, steep energetic barriers for rotation around this dihedral. The combined outcome of the two destabilising interactions was that the lowest

energy conformation of IND–T lays narrowly flanked by two high energy barriers, resulting in very small degrees of torsional disorder, consequently giving rise to the unusually high amount of polymer backbone crystallinity we observed experimentally.

When considering the combined influence of $\theta_A$ and $\theta_B$, **INDT-BT** could be expected to have the lowest total degree of torsional disorder, as every dihedral bond along the polymer backbone with rotational freedom was effectively "conformationally locked". The increased theoretical rigidity of the backbone, and experimentally observed increased backbone crystallinity in the order **BT** > **S** > **T** may also explain the increased extinction coefficient for **INDT-BT** and **INDT-S** polymers over the **INDT-T** analogue (**Table 2.6**); The lower the degree of twisting of a polymer backbone in solution, the higher the persistence length and hence extinction coefficient.

The torsional potentials of a naphthalene diimide–thiophene (NDI–T) dimer was also considered (Figure 2.32, orange line). Conjugated polymers with a NDI–T backbone are the only other class of materials which display high n-type mobility yet possess a non-planar backbone.[175,176] Furthermore, it is one of the very few other conjugated polymer families which displays crystallinity arising from an ordered chain backbone.[177–179] Both NDI–T and IND–T were energetically unstable at fully planar geometries and in general showed similar features. However, it could clearly be seen that the energy barriers for rotation through were far lower for NDI–T than those for IND–T. By thermally populating the energetic profile (**Figure 2.33**), the energetic disorder in IND–T was significantly reduced relative to NDI–T.

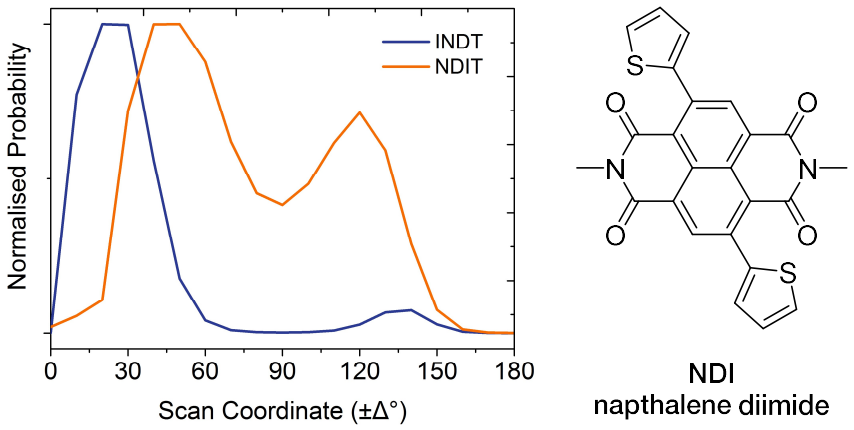


**Figure 2.33** Left: Boltzmann probability density distributions of rotational conformations of IND–T and NDI–T at room temperature; Right: Structure of naphthalene diimide

In order to further understand the calculated differences in rotational energy barriers between IND–T and NDI–T we looked at the distribution of the MOs on going from the lowest energy to the fully orthogonal conformation (**Figure 2.34**).

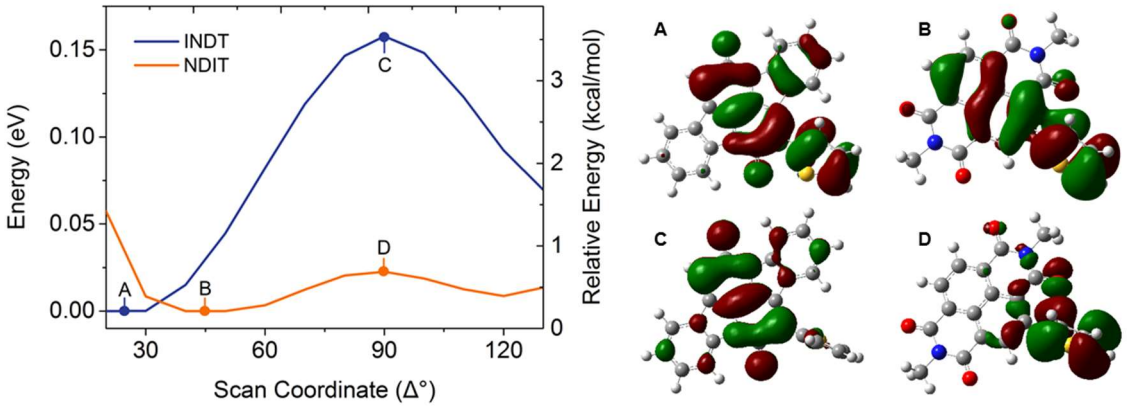


**Figure 2.34** Left: Partial potential energy surfaces (left) from **Figure 2.32** between $20° < \theta < 140°$ (MP2/cc-pVTZ); Right: HOMO distributions at the lowest (A & B) and (C & D) highest potential energy conformations

In the case of NDI–T, on increasing the dihedral from the lowest energy conformation (**Figure 2.34b**) to perpendicular geometries, the HOMO goes from being delocalized across the entire NDI–T unit to being localized predominantly on the thiophene (**Figure 2.34d**), as would be expected from its donor-acceptor characteristics. An increased amount of charge-transfer character and interactions in this conformation could have a stabilizing effect on it. Additionally, there was a clear contribution to the HOMO from the carbonyl oxygen atom of the NDI unit, potentially indicating a stabilising lone pair–arene interaction.

In stark contrast, on increasing the dihedral for the IND–T unit, the HOMO remarkably became fully localized on the IND core (**Figure 2.34c**). This is contrary to what one might expect from the traditional view of donor-acceptor conjugated polymers. Therefore, the high barrier for rotation was attributed solely to the energetic cost of reduced conjugation.

To investigate the unusual orbital distribution of the twisted geometry in IND–T we constructed basic molecular orbital diagrams using DFT/TD-DFT, shown in **Figure 2.35**.

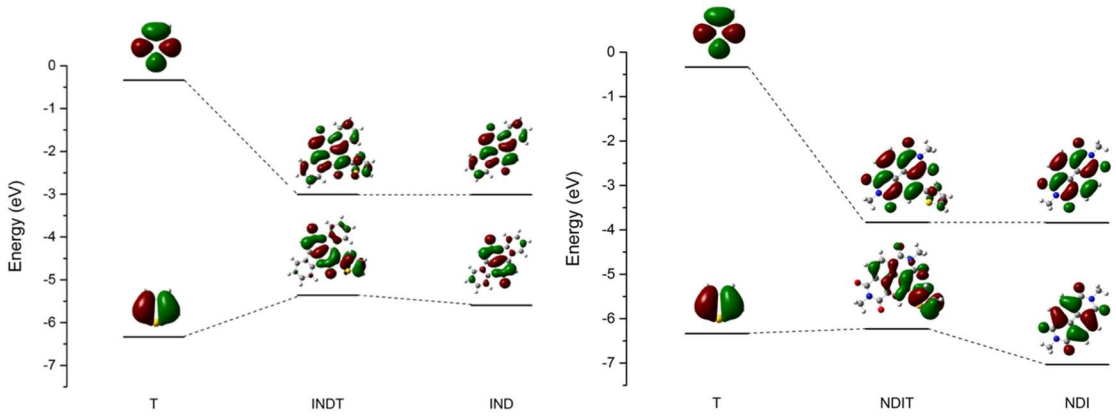


**Figure 2.35** Molecular orbital diagrams of IND–T (left) and NDI–T (right). $E_{hom}$ was calculated with DFT and $E_{lumo}$ was calculated with TD-DFT, both using the B3LYP functional at the 6-31G* level of theory

NDI–T showed conventional donor-acceptor orbital hybridization, however IND–T showed unusual characteristics in that $E_{homo}$ of the IND core was not below that of T implying that IND–T cannot be classified as a typical "acceptor" unit. Instead, the narrow band gap observed in the novel INDT polymers was more a result of the inherent narrow energy levels of indolonaphthyridine, which was then further narrowed through conjugation, rather than the traditional picture of orbital hybridization. However, we note that when including the entire T–T–T (or alternative) repeat unit into the MO diagram IND does take on acceptor-like properties (**Figure 2.36**).

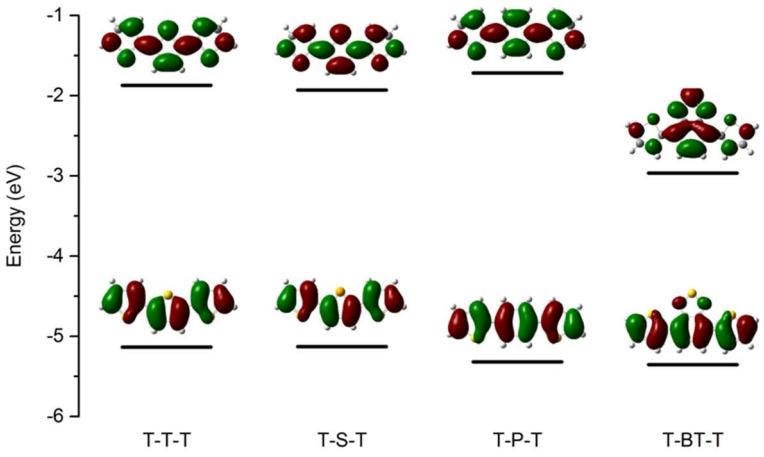


**Figure 2.36** Frontier molecular orbital levels of thiophene–*monomer*–thiophene trimers of thiophene (T), selenophene (S), phenyl (P) and benzothiadiazole (BT), calculated using DFT/TD-DFT at the B3LYP/6-31G* level of theory

## 2.7 Conclusions

Indolonaphthyridine, whose chemical structure is derived from naturally occurring indigo, was successfully exploited as a novel building block for high performance organic semiconductors. The electron deficient system acted as a superior acceptor unit in donor-acceptor organic conjugated polymers with all four materials exhibiting narrow band gaps $E_{\mathrm{g}} \sim 1.2 - 1.4\ \mathrm{eV}$, with high thin-film crystallinity resulting in high p-type and ultra-high n-type charge transport in OFETs. Electron mobility over 3 $cm^2/Vs$ was observed in **INDT–BT**, arising from a highly ordered polymer backbone. The extent of polymer backbone crystallinity varied significantly, as determined by GIWAXS, and could be correlated with the n-type charge transport properties of the conjugated polymer.

Theoretical analysis of the constituent units revealed that indolonaphthyridine polymers are non-planar yet extremely conformationally rigid due to large energy barriers for rotation along connect dihedral bonds, together with large destabilizing interactions in the planar configurations. Despite the distortion from planarity, the obtained optical band gaps were amongst the narrowest seen in organic conjugated polymers. The influence of commonly used co-monomer units on polymer backbone rigidity was explored and was demonstrated to have remarkable effects, directly affecting charge carrier mobility. However, the high backbone rigidity of these polymers arises from an inherent ability of indolonaphthyridine to restrict rotational disorder, which is then augmented by the effect of the co-monomer.

OPV devices were constructed giving PCEs up to 4.1% with demonstrable photocurrent generation occurring at wavelengths up to 1000 nm, whilst retaining good open circuit voltages despite very small energetic driving force for charge separation. Although a high proportion of photocurrent resulted from fullerene absorption, distinct contribution to photocurrent from polymer absorption was confirmed using ultrafast transient absorption spectroscopy.

These results demonstrated the potential of this relatively unexplored chromophore in organic electronics as a semiconductor for high performance n-type transistors and as a near-IR absorber in next generation organic photovoltaics. Perhaps more importantly, these novel materials have allowed for a detailed understanding of the molecular origin of high n-type mobility in conjugated polymers. In particular, they demonstrate that planarity is not a requirement for ultra-high charge carrier mobility provided that the polymer backbone remains rigid. It is anticipated that the structure/property relationships resulting from this work will contribute strongly to future bottom-up design of high performance organic semiconductors.

# III

*Chain-Extended*
*Indolonaphthyridine Polymers*

## 3.1 Introduction

Amongst the most attractive and commercially interesting properties of organic semiconductors is their solution processability, offering the opportunity for low-cost, large surface area, mass production. As most modern donor-acceptor organic semiconducting polymers contain a planar aromatic backbone, solubility is provided by the installation of long aliphatic alkyl side chains (**Figure 3.1**). Many chains are available to the polymer chemist: linear alkane chains e.g. **3.1**-**3.3**; branched chains, such as 2-ethylhexyl (2EH, **3.4**) or 2-octyldodecanyl **3.5**; and chains containing heteroatoms, such as polyethylene glycol (PEG, **3.6**) or fluorinated chains **3.7**.

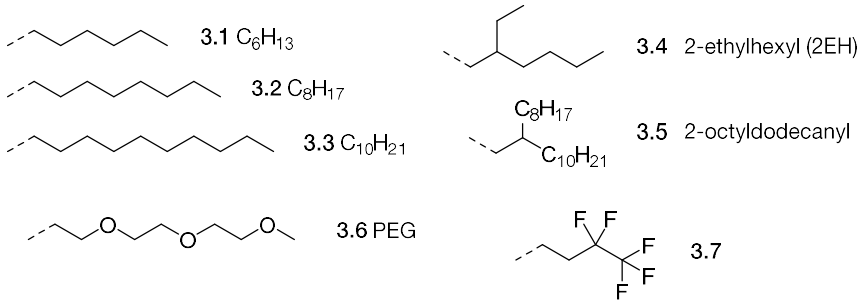


**Figure 3.1** Common alkyl side chains used to solubilise large planar aromatic organic semiconducting polymers

Whilst much research has been carried out into the design of new conjugated polymers, relatively little research has been done into how alkyl chains effect the electronic properties of organic polymers. Until recently, alkyl chain optimisation was not an important step in the research process, as they are (mostly) electrically insulating, i.e. not participating in charge transport. However, it has become increasingly apparent that alkyl chains make a large impact on charge transport properties, due to their critical

influence on a material's solid-state microstructure. In some cases, the optimisation of a polymer's alkyl chains has led to improvements of charge carrier mobilities of more than several orders of magnitude in OFETs and increases in OPV efficiencies of several percentages.[97,157,171,180–184,63,185]

The influence of alkyl chains on the performance of a given polymer is typically unique to the monomer/polymer they are installed on. However, thanks to the vast libraries of polymers and alkyl chains now available in the literature, general correlations have been drawn, which strongly influence alkyl chain selection during novel polymer design.

Of the alkyl chains discussed earlier, branched chains have shown the greatest promise in producing desirable thin-film microstructure, notably 2-ethylhexyl **3.4** and 2-octyldodecanyl **3.5**, the latter of which in particular has featured in some of the highest performing OPV and OFET materials.[186,58,175,7,187,188,91] A shared property of these two common branched chains is their spacer length of one carbon atom. A much lesser investigated variety of alkyl chains are branching-point-extended chains with longer spacer lengths (**Figure 3.2**).

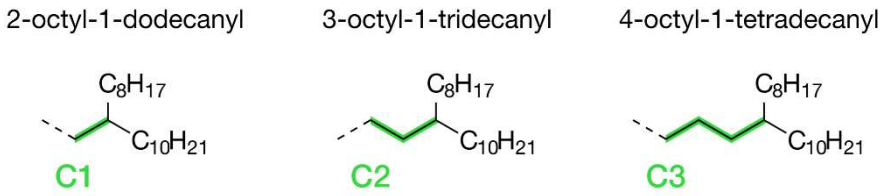


**Figure 3.2** Branching-point-extension of alkyl chains showing C1, C2 and C3 varieties

There are relatively few examples of these chains being exploited in polymer design. Notable examples are of Meager and Vezie *et al.* who showed how **DPPTT-T** with 4-octyl-1-tetradecanyl (C3, Figure 3.2) chains exhibited increased PCEs in OPVs attributed to high persistence lengths and improved film crystallinity, particularly in the $\pi - \pi$ direction.[97,157] The increased interfacial crystallinity arose as a product of reduced inter-chain distances permitted by the branching-point-extended chains (**Figure 3.3**).

Conversely, Shin *et al.* reported a decrease in OPV efficiency of the same polymer where the branching point was held constant, but the total chain length was extended.[184] Their *chain*-length-extended **DPPTT-T** exhibited coarse microstructure with large degrees of phase separation in the BHJ, leading to a decrease in current density and thus efficiency. These studies by Meager and Shin on the same polymer backbone containing alkyl chains with the same number of carbon atoms but with different extension locations, nicely demonstrate the large effect alkyl chains can have on the electronic properties of organic semiconducting polymers.

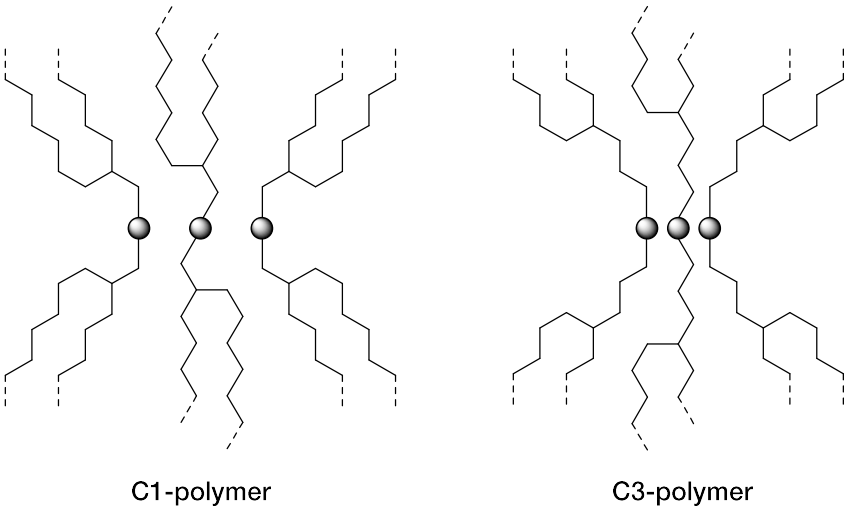


**Figure 3.3** Cartoon of shorter inter-chain distances permitted by C3 chains over C1

In Chapter 2, four indolonaphthyridine thiophene (INDT) polymers were synthesised which exhibited reproducible ultra-high n-type transport up to 3.1 $cm^2/Vs$ and high p-type transport up to 1.0 $cm^2/Vs$ in OFETs.[189,190] The high charge carrier mobilities were directly linked to high polymer backbone crystallinity. Although it has recently emerged that ultra-high charge transport occurs along polymers which have large degrees of polymer backbone ordering, most GIWAXS studies on polymers reported to date in the literature typically display scattering reflections in the lamellar $(100)$ and $\pi - \pi$ planes $(010)$, but only a handful report crystallinity arising from ordered polymer backbones $(001)$.[71,191,168]

Of the four polymers synthesised, the thiophene, selenophene and benzothiadiazole polymers were investigated with GIWAXS and were found to display high backbone crystallinity irrespective of choice of co-monomer. This unique property offered an excellent platform to deduce design parameters for inducing backbone order. The aim of the work in this chapter was to synthesise a branching-point-extended family of INDT polymers using the 4-octyl-1-tetradecanyl (C3) alkyl chain and to investigate what effect the larger spacer length had on charge transport in this unique family of materials.

## 3.2 Synthesis

The necessary alkylating agent for this study, 4-octyl-1-tetradecanyl bromide **3.14**, can be produced using several methods.[97,180,192–194] Due to its robustness, low cost and scalability, the procedure reported by McCulloch *et al.* starting from diethyl malonate **3.8** was chosen (**Scheme 3.1**).[97]

The first step involved an aldol reaction of diethyl malonate with 2-octyl-1-dodecanyl bromide which proceeded in high yield. The second step reported by McCulloch *et al.* was a Krapcho decarboxylation of **3.9** using NaCl and water. This reaction proved incredibly unreliable and mainly returned starting material. The Krapcho method favours methyl esters and works best done at elevated pressures, the latter being unavailable to us, and potentially unfeasible at such large scales.[195–197] To divert around this issue, the two ester groups were cleaved using base, and then the dicarboxyl acid **3.11** was heated neat at 160 °C for 2 h furnishing the monocarboxylic acid **3.12** in respectable yield. Subsequent reduction using lithium aluminium hydride gave 4-octyl-1-tetradecanol **3.13** cleanly in good yield and a final Appel reaction with NBS gave the desired brominated alkyl chain **3.14** in quantitative yield.

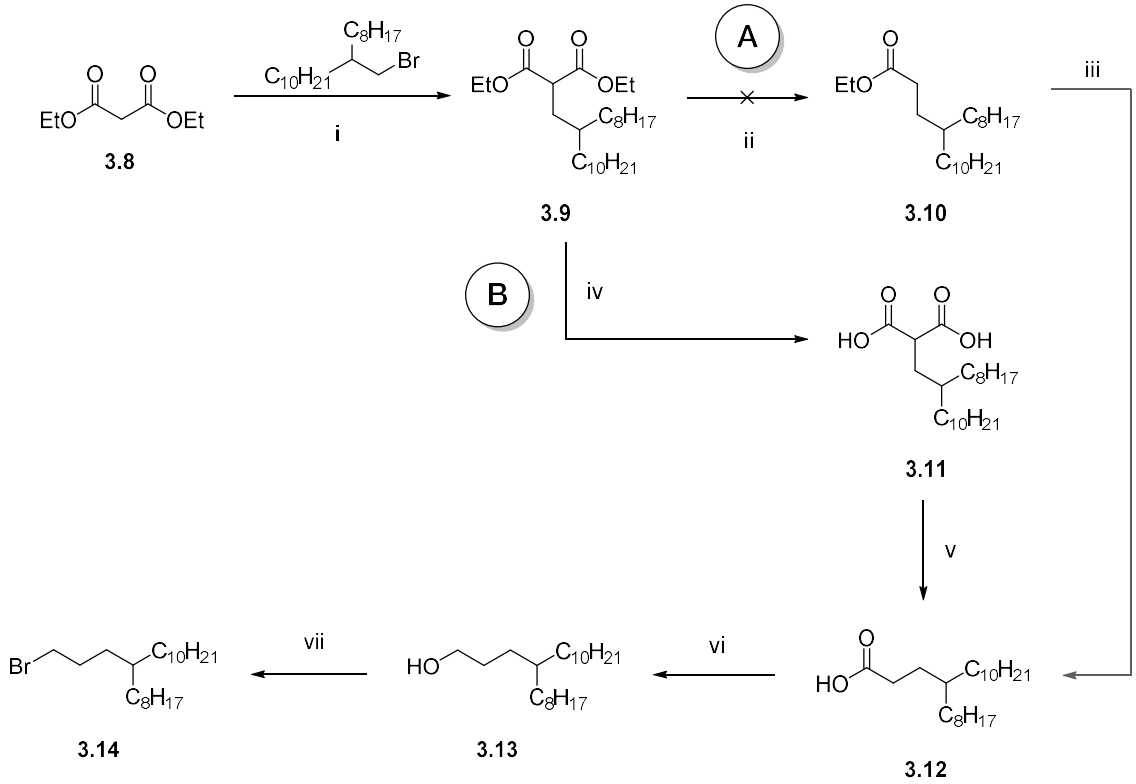


**Scheme 3.1** Synthesis of 4-octyl-1-tetradecanyl bromide **3.14**
(i) NaOEt, EtOH, Δ, 84%; (ii) NaCl, $H_2O$/DMSO, Δ, NR; (iii & iv) NaOH, EtOH, 57%; (v) Δ, neat, 61%; (vi) $LiAlH_4$, THF, 77%; (vii) NBS, $PPh_3$, DCM, quant.

Although the yields of this synthesis were not as high as they theoretically could be for such simple chemistry, the purification of each step was difficult due to the similarities in retention factors of all discussed compounds on silica gel, making column chromatography arduous. Although the crude residues of most of the reactions could be considered pure enough to move to the next step without purification, the highest possible purity was desired and so the crude residues were strenuously purified.

Dihydroxy-INDT **3.15** was then alkylated and brominated in good yield (for the preparation of **3.15** see Chapter 2.4.2, compound **2.24**).

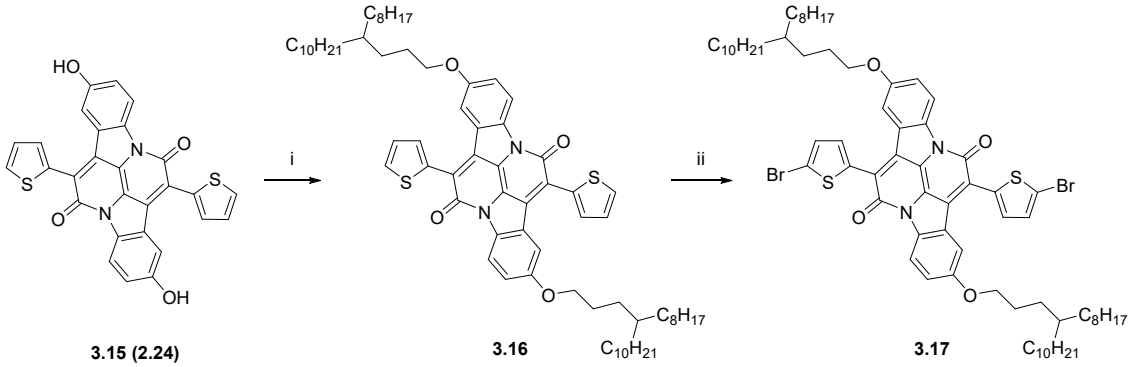


**Scheme 3.2** Alkylation of hydroxy-INDT
(i) **3.15**, $K_2CO_3$, anhyd. DMF, $\Delta$, 44%; (ii) NBS, 0 °C → RT, 97%

The three desired polymers were then synthesised: **C3-INDTT**, **C3-INDTS** and **C3-INDTBT**. The thiophene and selenophene polymers were made using microwave-assisted Stille polymerisation conditions, whilst the benzothiadiazole polymer was made using Suzuki conditions. All reagents and conditions were akin to the C1 varieties reported in Chapter 2 (**Schemes 3.3** & **3.4**).

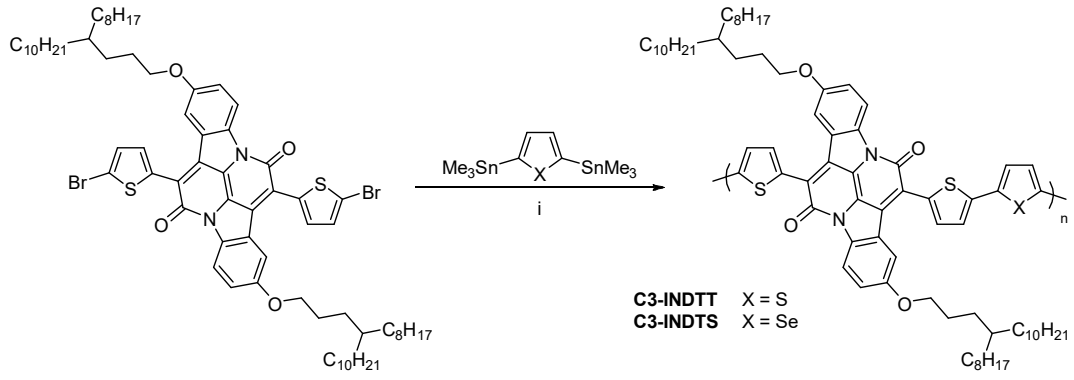


**Scheme 3.3** Microwave assisted Stille co-polymerisations of C3-INDT with 2,5-bis(trimethylstannyl) thiophene and selenophene monomers
i) $Pd_2(dba)_3$, P(o-Tol)$_3$, anhyd. degas. PhCl, μW, 45 min, 100 → 180 °C

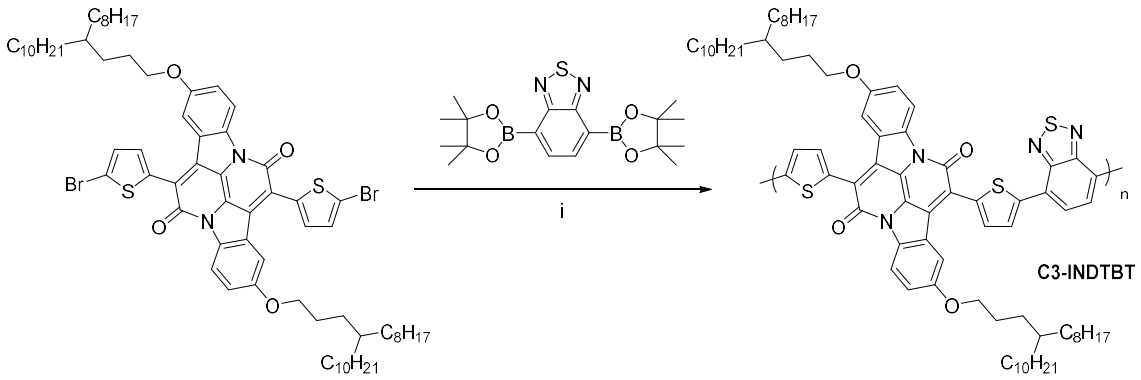


**Scheme 3.4** Suzuki polymerisation of C3-INDT with benzothiadiazole–bis(pinacolato)diboron
i) $Pd(PPh_3)_4$, $Na_2CO_3$, Aliquot 336, degas. PhMe/$H_2O$, 3 d, 125 °C

The crude materials of each polymerisation were purified by soxhlet extraction following precipitation in methanol – firstly in acetone for 12 h, then hexane for 12 h to remove low molecular weight oligomers and soluble impurities. All three polymers were successfully extracted using chloroform for 12 h, and were re-precipitated from a minimum volume of hot chlorobenzene into methanol and collected by vacuum filtration.

## 3.3 Results & Discussion

### 3.3.1 Physical & Optical Properties

The physical data of the novel C3-INDT polymers is summarised in **Table 3.1** (the data for the C1 polymers is included for comparison). The number and weight molecular weight averages were determined by size exclusion chromatography (SEC) using polystyrene standards (PS) eluting with chlorobenzene at 80 °C.

**Table 3.1** Physical properties of the novel C3 INDT-containing polymers[a] and the C1 polymers taken from Chapter 2 (Table 2.5)

| Polymer | C*n* | $M_n$ (kDa) | $M_w$ (kDa) | Đ |
|---|---|---|---|---|
| INDTT | C1 | 20 | 80 | 4.0 |
| | C3 | 27 | 83 | 3.1 |
| INDTS | C1 | 25 | 83 | 3.3 |
| | C3 | 32 | 124 | 3.9 |
| INDTBT | C1 | 40 | 119 | 3.0 |
| | C3 | 50 | 157 | 3.2 |
| | C3[b] | 24 | 107 | 4.5 |

New polymer data highlighted; [a]Determined by SEC using polystyrene (PS) standards and PhCl as eluent; [b]Prior to recycling GPC eluting with PhCl

The physical data of **C3-INDTBT** was poorer than expected, exhibiting a $M_n$ of 24 kDa and $M_w$ of 107 kDa, thus a wide PDI of 4.5, and was not comparable its C1 counterpart with $M_n$ of 40 kDa and a PDI of 3.0. The pure **C3-INDTBT** was therefore further purified by recycling gel permeation chromatography (GPC), raising the $M_n$ to 50 kDa and $M_w$ of 157 kDa, narrowing the polydispersity to 3.2, which was a considerably better fit to the C1 polymer.

All C3 polymers showed good $M_n > 20$ kDa, with the BT and S polymers exhibiting slightly higher polydispersities, whilst the T polymer had a narrower PDI. However, the physical properties of each C3/C1 pair was comparable to a degree where any changes in charge transport properties could tentatively be considered independent of molecular weight. **Figure 3.4** shows the solution (chlorobenzene) and thin-film (spin-coated from 5 mg/mL solutions in chlorobenzene) UV-vis absorption spectra of the three C3 polymers and the optical properties of the polymers are summarised in **Table 3.2**.

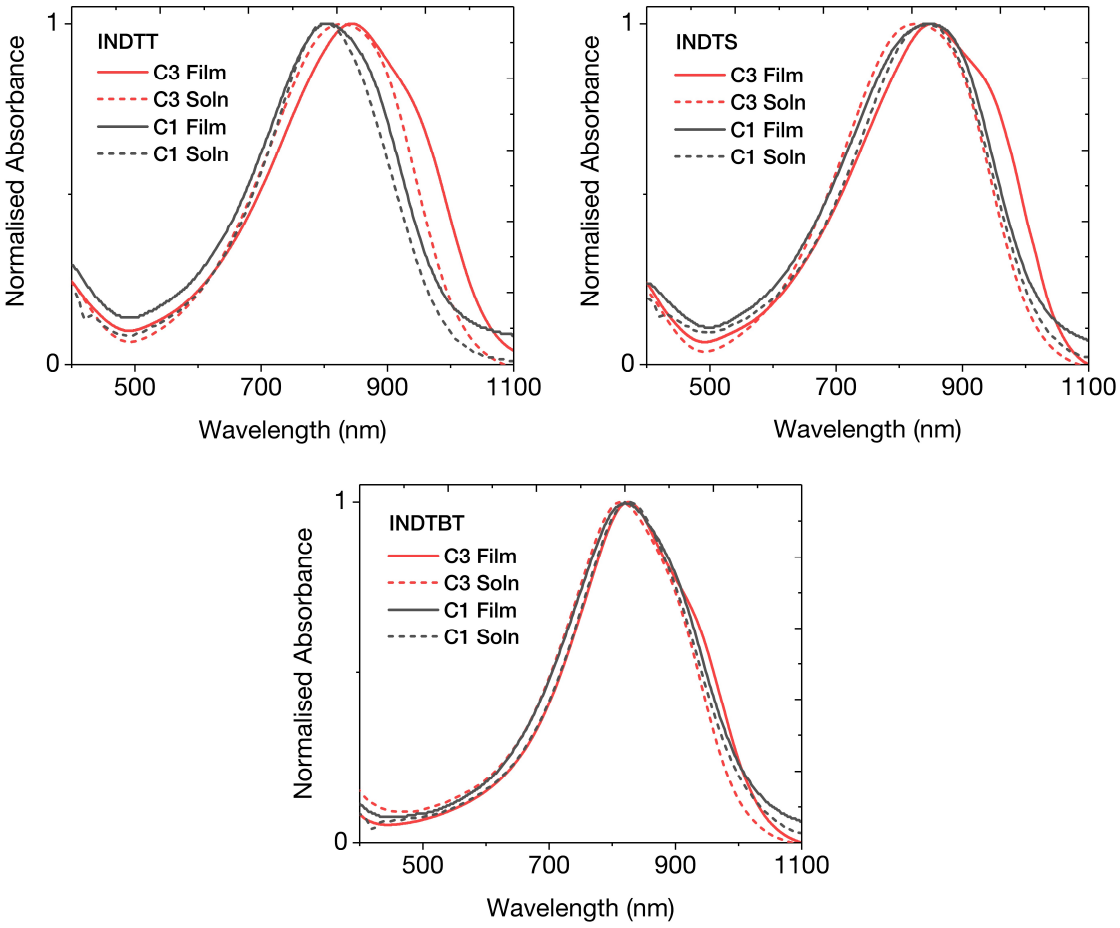


**Figure 3.4** Normalized UV-vis absorption spectra of the C3/C1 INDT polymers pairs. Solution spectra (dashed lines) were recorded in chlorobenzene, and thin-films (solid lines) were spun from 5 mg/mL solutions in chlorobenzene.

**Table 3.2** Optical properties of the novel C3 INDT polymers and the C1 polymers taken from Chapter 2

| Polymer | C$n$ | $E_g$ [a] (eV) | $E_{homo}$ [b] (eV) | $E_{lumo}$ [c] (eV) | $\lambda_{max}^{soln}$ [d] (nm) | $\lambda_{max}^{film}$ [e] (nm) |
|---|---|---|---|---|---|---|
| INDTT | C1 | 1.26 | -5.02 | -3.76 | 802 | 805 |
| | C3 | 1.21 | -4.99 | -3.78 | 847 | 826 |
| INDTS | C1 | 1.22 | -4.99 | -3.77 | 844 | 849 |
| | C3 | 1.23 | -4.99 | -3.76 | 855 | 826 |
| INDTBT | C1 | 1.23 | -4.97 | -3.74 | 826 | 820 |
| | C3 | 1.24 | -5.02 | -3.78 | 825 | 811 |

[a]Estimated from UV-vis onset, PhCl solution; [b]Determined by PESA. Data is given to two decimal places to illustrate the difference in figures however note that this falls within the error margins ($\pm$0.1 eV) of the experiments; [c]$E_{homo} + E_g$; [d]PhCl solution; [e]Spin-coated from a 5 mg/mL solution in PhCl

The UV-vis spectra of the novel C3 polymers showed broad absorption in the near-IR with similar onsets around 1100 nm. Whereas the C1 polymers showed totally featureless thin-film absorption, the C3 polymer films exhibited a slight right-hand shoulder, attributed to solid-state packing effects, indicating a potential new aspect to the thin-film microstructure due to the branching-point-extended alkyl chain. Both the C1 and C3 polymers showed bathochromic shifting of absorbance from solution to thin-film, attributed to the narrowing of optical band gaps due to greater conjugation lengths, suggesting the strong $\pi$-stacking property of the C1 family was still present in the C3 series. However, this effect was less pronounced in **C3-INDTBT** indicating that $\pi - \pi$ interactions could be comparable in both solution and thin-film for this polymer. **C3-INDTT** showed considerable red-shifted absorption to its C1 analogue which could be a feature of the higher $M_n$ and narrower PDI, or indicative of a higher tendency of the C3 polymer to aggregate in solution.

### 3.3.2 Organic Field Effect Transistors

Top gate – bottom contact OFET devices were constructed of the C3 polymers on glass substrates with CYTOP dielectric – an identical architecture to the C1 study to enable direct comparison of device performance. Although the previous study revealed INDT polymers were capable of facilitating ambipolar charge transport, only unipolar optimised devices were investigated in this study. Enhanced n-type devices were fabricated by treating Al SD electrodes with ethoxylated polyethylenimine (PEIE) to enable superior

electron injection whilst UV-ozone treated Au SD facilitated superior p-type performance. A polymer was then spun onto the treated SD electrodes and the device annealed at 190 °C. The device was then completed by spin-coating a CYTOP dielectric onto the semiconductor followed by the thermally evaporated Al gate electrode. **Table 3.3** shows full device data and **Table 3.4** shows a comparison of the maximum field-effect mobilities between the C1 and C3 polymers. The output characteristics and transfer curves of the three novel devices are shown in **Figure 3.5** (n-type) and **Figure 3.6** (p-type).

**Table 3.3** Parameters of TG-BC OFET devices of C3 INDT polymers with $L =$ 40 μM and $W = 1000$ μM annealed at 190 ℃

| Polymer | Type[a] | ${I_{on}/I_{off}}^{lin}$ | ${I_{on}/I_{off}}^{sat}$ | $V_{\text{on}}^{lin}$ (V) | $V_{\text{Th}}^{sat}$ (V) | ${\mu_{sat}}^{\text{b}}$ ($\text{cm}^2$/Vs) |
|---|---|---|---|---|---|---|
| INDT-T | $n$ | $10^4$–$10^5$ | $10^4$–$10^5$ | -8 | +79 | 1.01 (0.93) |
| | $p$ | $10^5$ | $10^1$–$10^2$ | -40 | -112 | 0.11 (0.10) |
| INDT-S | $n$ | $10^4$–$10^5$ | $10^4$–$10^5$ | +3 | +54 | 1.04 (0.89) |
| | $p$ | $10^5$ | $10^1$–$10^2$ | -9 | -65 | 0.13 (0.13) |
| INDT-BT | $n$ | $10^4$–$10^5$ | $10^4$–$10^5$ | +1 | +88 | 0.63 (0.57) |
| | $p$ | $10^5$ | $10^3$ | -29 | -107 | 0.38 (0.29) |

[a]Extracted from each unipolar device exhibiting highest charge carrier mobility; [b]Champion device values with the mean of three device given in brackets

**Table 3.4** Maximum field-effect mobilities of C1 and C3 INDT polymers

| ${\mu_{sat}}^{\text{b}}$ ($\text{cm}^2$/Vs) | **INDT-T** | | **INDT-S** | | **INDT-BT** | |
|---|---|---|---|---|---|---|
| | C1 | C3 | C1 | C3 | C1 | C3 |
| $\mu_e$ | 0.31 | 1.01 | 0.99 | 1.04 | 3.11 | 0.63 |
| $\mu_h$ | 0.29 | 0.11 | 0.20 | 0.13 | 0.52 | 0.38 |

N-type optimised devices exhibited stable operation with low hysteresis and good data reproducibility. Notably, the on/off saturated channel current ratios $({I_{on}/I_{off}}^{sat})$ for C3 polymers were improved by up to an order of magnitude over the C1 polymers. Both the on voltages $(V_{\text{on}})$ and threshold voltages $(V_{\text{Th}})$ did not exhibit a significant trend between the C3 and C1 materials. The electron mobility was significantly improved in **C3-INDTT** (1.01 $\text{cm}^2$/Vs) over its C1 counterpart (0.29 $\text{cm}^2$/Vs) and marginally improved in **C3-INDTS** (1.04 $\text{cm}^2$/Vs, $\Delta = +0.05$).

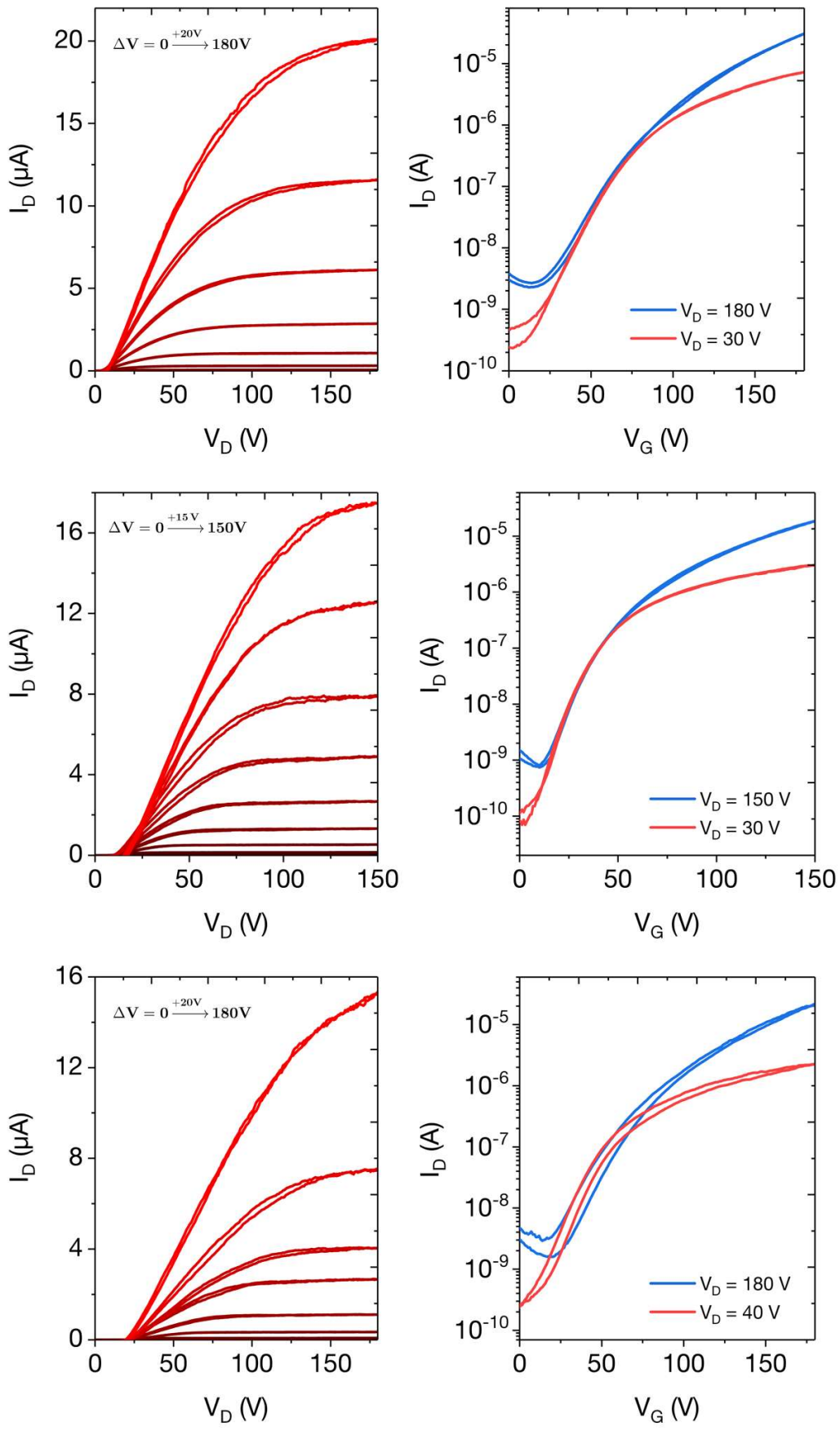


**Figure 3.5** Output characteristics (left) and transfer curves (right) of n-type enhanced TG-BC OFET devices of **C3-INDTBT** (top), **C3-INDTS** (middle), **C3-INDTT** (bottom) annealed at 190 °C with $W = 1000$ µm and $L = 40$ µm

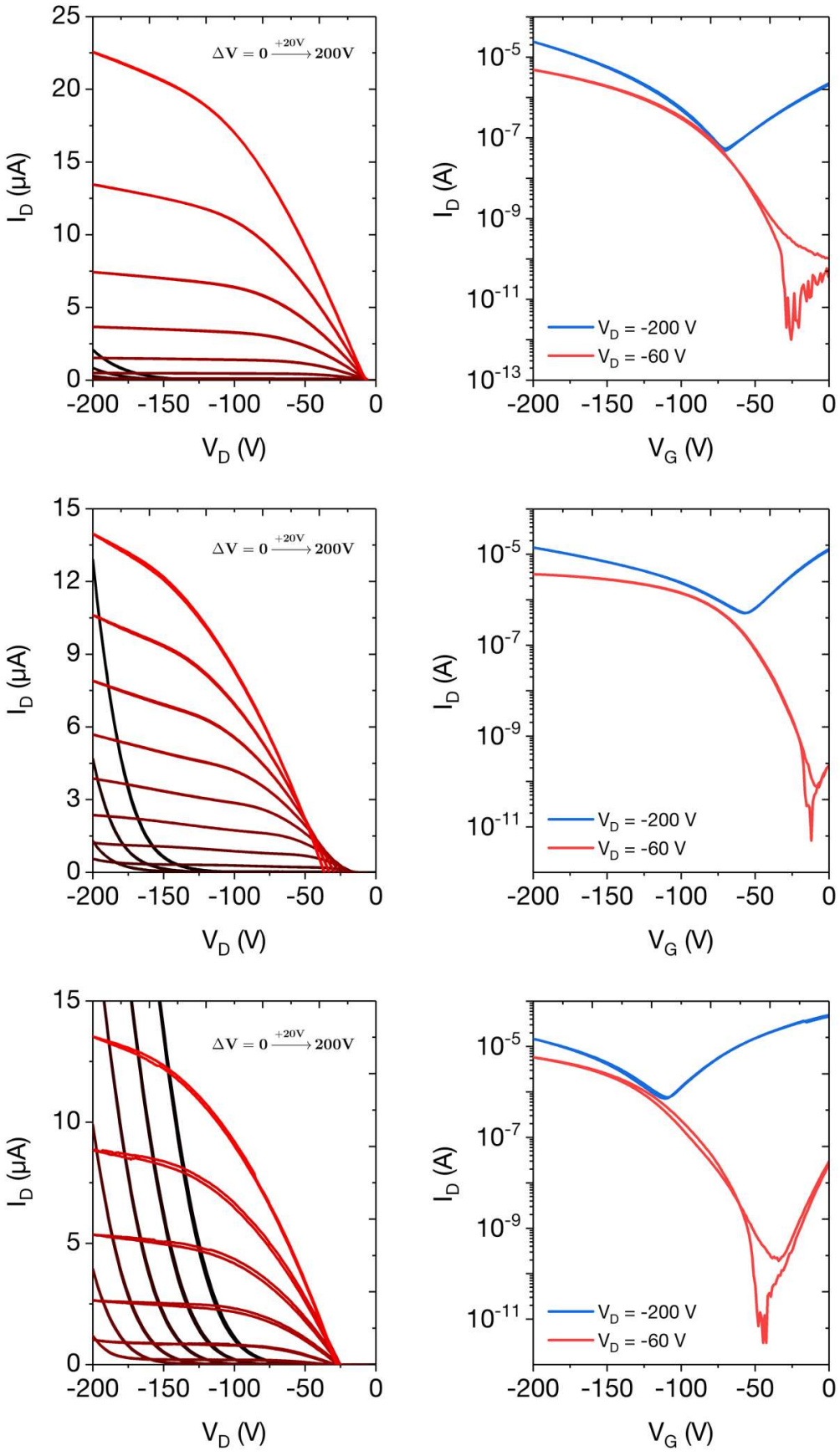


**Figure 3.6** Output characteristics (left) and transfer curves (right) of p-type enhanced TG-BC OFET devices of **C3-INDTBT** (top), **C3-INDTS** (middle), **C3-INDTT** (bottom) annealed at 190 ℃ with $W = 1000$ μm and $L = 40$ μm

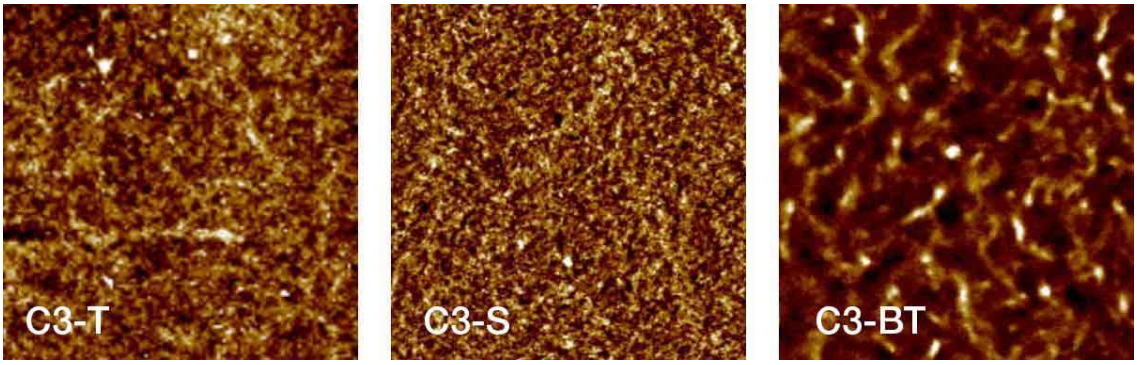


**Figure 3.7** AFM images of 3 $\mu m^2$ samples of C3 INDT films spin-coated from 10 mg/mL solutions in chlorobenzene and annealed at 190 ℃

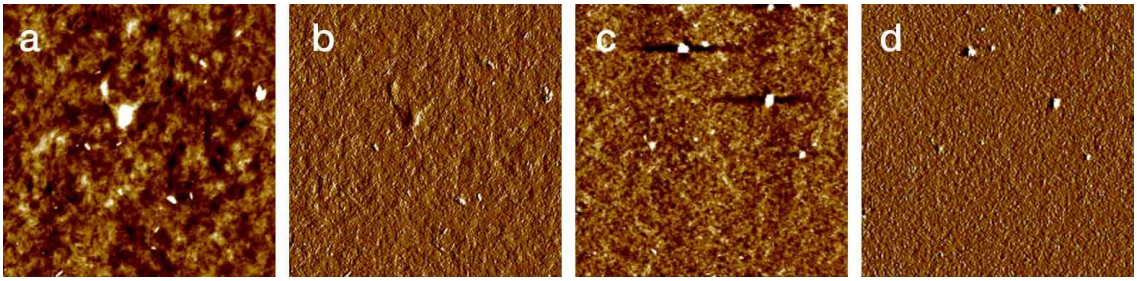


**Figure 3.8** **C3-INDTT** thin-films on glass substrates spin-coated from a 10 mg/mL solution and annealed at 190 ℃; (a) Topography (RMS = 0.96 nm), and (b) phase (1.5 $\mu m^2$ images). (c) Topography (RMS = 1.13 nm), and (d) phase (5 $\mu m^2$ images)

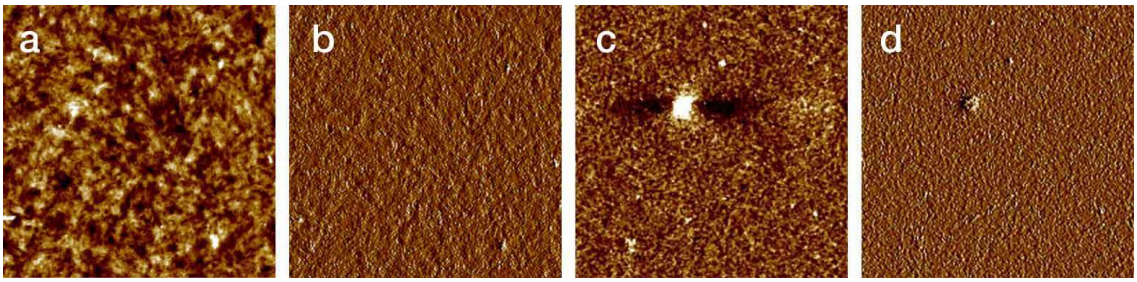


**Figure 3.9** **C3-INDTS** thin-films on glass substrates spin-coated from a 10 mg/mL solution and annealed at 190 ℃; (a) Topography (RMS = 0.99 nm), and (b) phase (1.5 $\mu m^2$ images). (c) Topography (RMS = 1.03 nm), and (d) phase (5 $\mu m^2$ images)

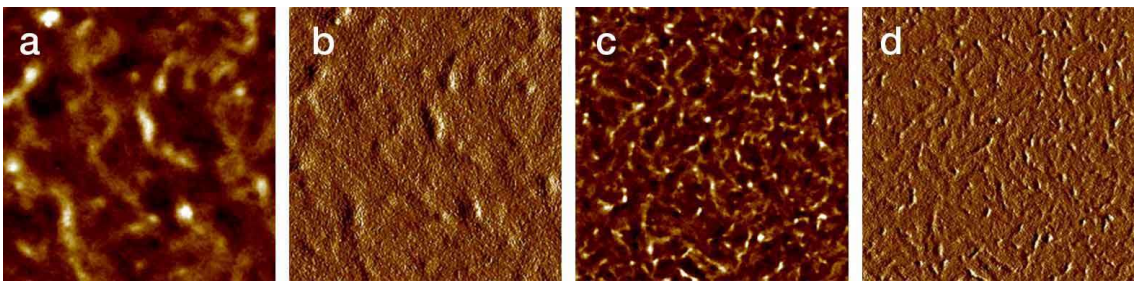


**Figure 3.10** **C3-INDTBT** thin-films on glass substrates spin-coated from a 10 mg/mL solution and annealed at 190 ℃; (a) Topography (RMS = 3.77 nm), and (b) phase (1.5 $\mu m^2$ images). (c) Topography (RMS = 3.86 nm), and (d) phase (5 $\mu m^2$ images)

Surprisingly, $\mu_e$ of **C3-INDTBT** dropped to 0.63 cm$^2$/Vs which, despite being impressive in comparison to the small consortium of high performance n-type organic polymers,[65] represents a large decrease in performance over **C1-INDTBT** (3.11 cm$^2$/Vs, $\Delta = -2.48$). Interestingly, $I_{\mathrm{D}}^{max}$ in **C1-INDTBT** devices was five times greater than those achieved with the new C3 polymer.

P-type optimised devices exhibited operation traits in line with the C1 devices, with the only notable issue being slightly higher leakage current in **C3-INDTS** due to thin-film non-uniformities. Hole mobilities were decreased in all C3 polymers between 0.07 – 0.18 cm$^2$/Vs suggesting that the branching-point-extended chains had minimal impact on p-type transport mechanisms.

### 3.3.3 Thin-Film Morphology

Considering that the physical properties of the C3 and C1 polymer series were tentatively comparable, the observed changes in charge carrier transport were likely a product of morphological differences of the thin-films. **Figure 3.7** shows tapping-mode AFM images of 3 μm$^2$ polymer thin-films on glass substrates and **Figures 3.8**-**3.10** show 1.5 and 5 μm$^2$ scans.

The surface morphology of the thin-films of the C3 polymers had strong similarities with the C1 series when viewed with AFM. Both **C3-INDTT** (RMS = 0.94 nm) and **C3-INDTS** (RMS = 0.97 nm) exhibited flat polycrystalline structure, whereas **C3-INDTBT** films exhibited ribbon-like features with high surface roughness (RMS = 3.55 nm). The surface roughness of all C3 polymer thin-films were considerably smoother than their equivalent C1 counterpart.

Whilst AFM provided useful information about surface morphology, to examine the intermolecular interactions and packing in the bulk of the thin-film, where most charge transport occurs, it was necessary to perform GIWAXS experiments. Thin-films were prepared in an identical fashion to the OFET active layer on Si substrates. **Figure 3.11** shows the 2D scattering patterns and the resulting line cuts for all three C3 polymers are shown in **Figure 3.12**, where the $\mathrm{q_{xy}}$ vector represents scattering in-plane, parallel to the substrate, whilst the $\mathrm{q_z}$ vector represents scattering out-of-plane, perpendicular to the substrate. **Table 3.5** contains the corresponding *d*-spacings and crystalline correlation lengths (CCLs)[167] of the GIWAXS data.

**Table 3.5** GIWAXS *d*-spacings and correlation lengths of diffraction planes of the C3 INDT polymer thin-films

| Polymer | Edge on[a]/ Face on[b] | *d*-spacings (Å) | | | Correlation length (nm) | | |
|---|---|---|---|---|---|---|---|
| | | (100) | (010) | (001)[c] | (100) | (010) | (001)[c] |
| C3-INDTBT | edge-on | 27.0 | 3.60 | 17.7 | 14.2 | 2.4 | 19.1 |
| | face-on | 30.2 | 3.52 | - | 10.7 | 2.3 | - |
| C3-INDTT | edge-on | 26.8 | 3.59 | 17.5 | 26.8 | 2.9 | 15.6 |
| | face-on | 30.1 | 3.57 | - | 10.3 | 1.8 | - |
| C3-INDTS | edge-on | 26.2 | 3.58 | 17.6 | 23.8 | 3.0 | 21.9 |
| | face-on | 30.3 | 3.55 | - | 6.9 | 2.5 | - |

[a]Edge-on domains include out-of-plane ($q_z$) (100) peaks and in-plane ($q_{xy}$) (010) peaks; [b]Face-on domains include in-plane ($q_{xy}$) (100) peaks and out-of-plane ($q_z$) (010) peaks. [c](001) peaks do not distinguish between an edge-on or face-on orientation.

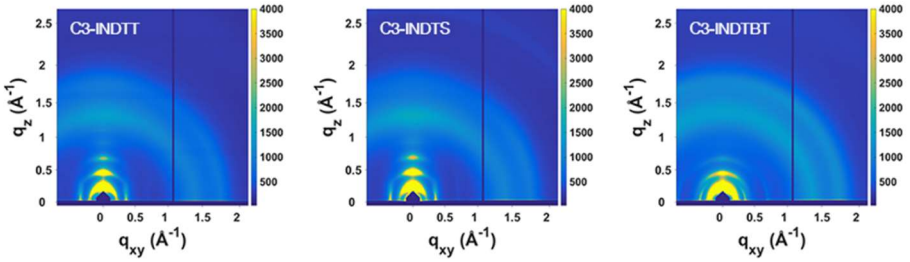


**Figure 3.11** GIWAXS 2D scattering patterns of the three C3 INDT polymers

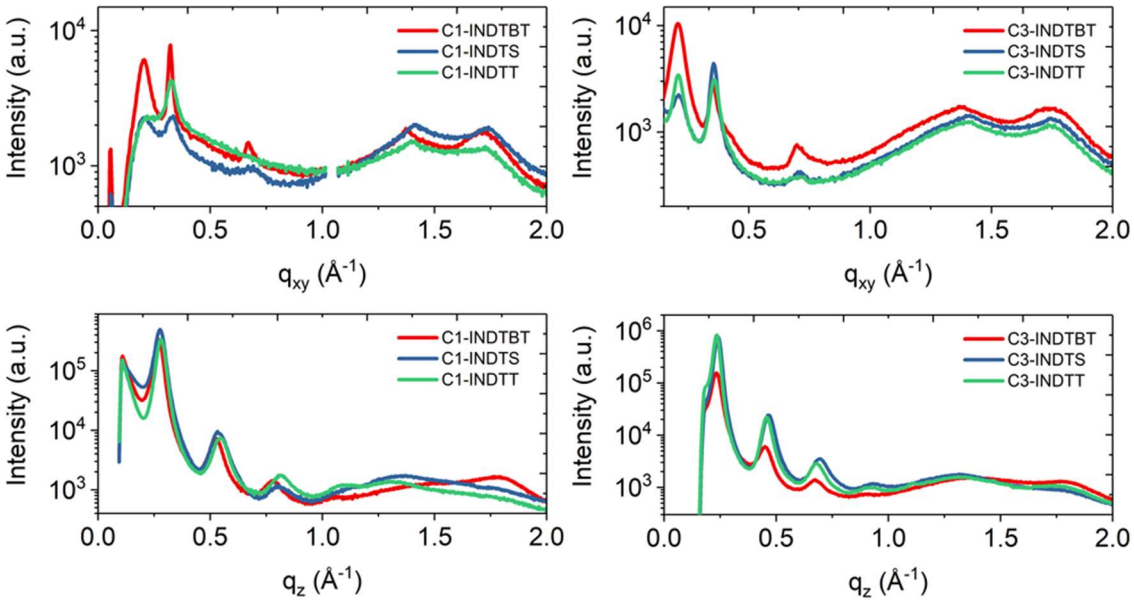


**Figure 3.12** In-plane ($q_{xy}$) and out-of-plane ($q_z$) line cuts of the C1 (left, reproduced from Chapter 2) and C3 (right) INDT polymers

Both the in-plane $q_{xy}$ and out-of-plane $q_z$ line cuts exhibited lamellar crystallinity $(100)$, however the scattering was most significant out-of-plane, where first, second, third and fourth order $(100) \rightarrow (400)$ scattering reflections were visible for edge-on oriented polymers. The *d*-spacing for the lamellar planes of all three C3 polymers increased by 3–4 Å in comparison to their C1 counterpart, which matched the expected growth of the unit cell due to the branching-point-extended alkyl chains. The degree of isotropy in the thin-film crystallites of each polymer was estimated by the comparison of the relative crystalline correlation lengths (CCLs) of the $(100)$ between the edge-on and face-on domains. **C3-INDTT** and **C3-INDTS** clearly favored the edge-on orientation, whilst **C3-INDTBT** exhibited a larger degree of isotropy for polymer orientation on the substrate.

The *d*-spacings of the $(010)$ plane, arising from $\pi - \pi$ stacking, were reduced by ~0.07 Å in all three C3 polymers, confirming that the branching-point-extended alkyl chain did indeed permit increased interchain interactions. There was evidence of $(010)$ crystallites both in-plane and out-of-plane, although the peaks were clearer in the in-plane domain. The consistent isotropy seen in the $(010)$ plane is a distinct difference of the C3 polymers over the C1 series, where only **C1-INDTBT** showed the same degree of orientational diversity. However, **C3-INDTBT** clearly demonstrated the greatest degree of isotropy, in line with previous findings.

The *d*-spacings of the $(001)$ plane, arising from periodicity along polymer backbones were all comparable with high CCLs, indicating a maintained high degree of polymer backbone crystallinity in the branching-point-extended indolonaphthyridine polymers. Whilst **C1-INDBT** exhibited a significantly larger $(001)$ CCL compared to **C1-INDTT** and **C1-INDTS**, all three C3 polymers displayed relatively comparable CCLs. This suggested that the extended alkyl chain allowed the C3 polymers to form more uniform ordered bulk thin-film morphology.

It was unmistakable that the branching-point-extended C3 polymers exhibited increased $\pi - \pi$ interfacial interactions due to the reduced *d*-spacings of the $(010)$ plane, the evidence of face-on $(010)$ crystallites and the relative comparability of the CCLs in both the $q_{xy}$ and $q_z$ $(010)$ domains. Operationally however, **C3-INDTT** exhibited a large increase in n-type charge transport, whilst a modest improvement in $\mu_e$ was recorded for **C3-INDTS**, but a diminished performance was recorded for **C3-INDTBT**. Whilst the high n-type performance of **C1-INDTBT** was linked to its remarkable levels of thin-film crystallinity, this property, inherited from the 2-octyl-1-dodecyl alkyl chain, seems to have been tampered by the increased $\pi - \pi$ interfacial interactions. Conversely, the increased n-type performance and crystallinity of **C3-INDTT** demonstrated how this polymer

benefited from the use of the branching-point-extended chain, resulting in increased $\pi - \pi$ interactions and a narrower optical band gap.

## 3.4 Conclusions

The effect of branching-point-extended alkyl chains on the charge transport properties of three indolonaphthyridine polymers was investigated. The polymers exhibit high levels of three-dimensional crystallinity due to the strong inherent backbone ordering of the indolonaphthyridine, which allowed this alkyl chain study to be conducted for the first time in 3D, whereas previous studies typically only witness lamellar and $\pi$ crystallites.

Interestingly, thiophene and selenophene containing polymers exhibited increased n-type charge transport whilst electron mobility was diminished in the benzothiadiazole polymer. The optical band gaps and frontier molecular orbital energy levels of the C3 polymer series were comparable to the C1 series, suggesting that these electronic differences were a function of thin-film morphology.

GIWAXS experiments on thin-films of the three polymers revealed increased $\pi - \pi$ interactions and high degrees of overall crystallinity for all three C3 polymers. However, the knock-on effect of these interaction of polymer backbone periodicity was not as definitive, showing both positive and negative results. The comparison of the crystalline correlation lengths revealed that the increased $\pi - \pi$ interactions appeared to make all three polymers more uniform in thin-film, suggesting that the $\pi - \pi$ interactions took precedence over thin-film microstructure, ratified by the fact that, to some degree, there was uniformity in the charge carrier mobilities for both n-type and p-type between the three polymers.

The results demonstrated how the relationship between alkyl chain branching point, solid-state morphology and charge transport properties was not as straightforward as had been suggested in the literature, and highlights the importance of alkyl side chain engineering in the design of conjugated organic semiconducting polymers.

However, the three C3 polymers synthesized displayed electron mobilities between 0.63–1.04 $cm^2/Vs$, a remarkable level of n-type character, placing them highly in the consortium of n-type organic polymers reported to date. These results further confirmed that the indolonaphthyridine building block has an unprecedented intrinsic ability to furnish high performance n-type organic semiconducting polymers.

# IV

*Cross-Conjugated*
*Indolonaphthyridine Polymers*

## 4.1 Introduction

In the previous two chapters, $\pi$-conjugated indolonaphthyridine (**Figure 4.1**) has furnished high performance organic semiconductors with narrow optical band gaps. The thiophene co-polymer (**INDT-T**) exhibited the narrowest $E_g$ of 1.21 eV whilst **INDT-P** showed the widest $E_g$ of 1.40 eV. This widening was attributed to the distortion in backbone conjugation due to the larger twist in dihedral angles caused by steric interactions.

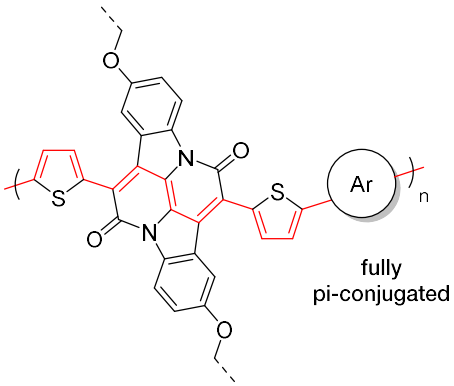


**Figure 4.1** $\pi$-Conjugated indolonaphthyridine polymer with the path of quinoidal conjugation shown in red.

Considering the structure of indolonaphthyridine, a structural isomer of it could be imagined where polymerisation is performed on the indigoid benzene rings and where solubility is provided for by alkyl chains on the peripheral aromatic groups installed through condensation-annulation reactions (**Figure 4.2**).

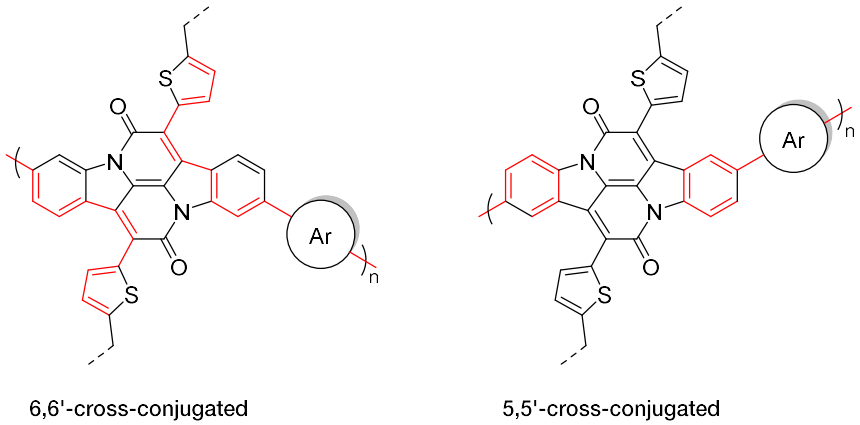


**Figure 4.2** Cross-conjugated indolonaphthyridine polymers with the path of quinoidal conjugation shown in red

However, these theoretical polymers would not be fully $\pi$-conjugated, as the quinoidal structure cannot be extended across the whole polymer backbone. These kinds of polymers are termed cross-conjugated (**Figure 4.3**).

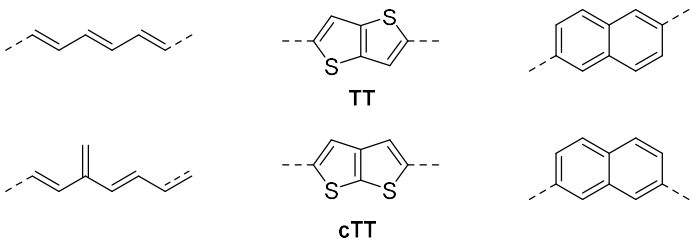


**Figure 4.3** Examples of fully conjugated units (top) and the corresponding cross-conjugated unit (bottom)

Cross-conjugation shortens the effective conjugation lengths of polymers, leading to wider band gap semiconductors. Typically this leads to deeper ionisation potentials which makes a material more stable to oxidative doping when operated in air.[198,199] However, the use of cross-conjugation in semiconductor design has seldom been investigated.

In 2005, Heeney *et al.* demonstrated the first successful use of a cross-conjugated polymer containing thieno[2,3-*b*]thiophene (cTT) as a p-type OFET material, exhibiting $\mu_h$ up to 0.05 cm$^2$/Vs.[200] Recently, Zhang *et al.* reported $\mu_h$ up to 0.54 cm$^2$/Vs in diketopyrrolopyrrole (DPP) based cross-conjugated polymers.[201] Other common building blocks have been exploited in cross-conjugated systems including isoindigo,[202,203] fluorene,[204–207] carbazole,[208] and some more atypical systems,[209–214] however application in OPVs or OFETs is rarely reported.

Considering that conjugated indolonaphthyridine (IND) polymers exhibit narrow band gaps, cross-conjugation could theoretically be employed as a strategy to widen the $E_g$

of these polymers. The potential interest of this arises due to the consistent $E_{lumo}$ of approximately –3.7 eV for the previous four IND polymers, which is isoenergetic with the $E_{lumo}$ of PCBM. If the ionisation potential of an IND polymer could be lowered whilst maintaining $E_{lumo}$ at –3.7 eV, the wide band gap material could be employed as a polymer acceptor in a fullerene-free OPV device.

Due to the lack of published reports of cross-conjugated semiconductors facilitating charge transport in OFETs, it is difficult to predict the behaviour of cross-conjugated indolonaphthyridine (XIND) polymers in this application. However, INDT polymers were proven excellent n-type materials, and an n-type cross-conjugated polymer has not been published to date in the literature.

Two degrees of cross-conjugation (CC) of prospective XIND polymers could be envisaged by considering polymerisation at either the 5,5'– or 6,6'–positions of the indigoid ring (**Figure 4.2**). The effective conjugation length of a 6CC polymer would be greater than that of a 5CC polymer due to quinoidal conjugation which extends onto the peripheral aromatic groups. As such, the largest effect of CC would be achieved in a 5CC polymer.

In considering precursors, 6,6'-dibromoindigo is a natural product and has been known since the Phoenician era, as early as 1570 BC.[215] The precursors of the dye were historically extracted from the sea snail $Murex\ brandaris$, and underwent oxidative coupling in air to form the brilliantly purple solid. Approximately ~8,500 snails were required to harvest a mere 1 g of the dye, leading to the high wealth associated with the colour purple throughout history until cheaper synthetic alternatives were discovered in the late 1800s.[216] The dye became known as $Tyrian\ Purple$ and was worth its weight in gold during the roman era, where its use was restricted to royalty.

The use of natural products as precursors is an important step towards improving the sustainability of organic semiconductors. Obviously, the farming of $Murex\ brandaris$ is not a commercially viable source of 6,6'–dibromoindigo, however it was decided that Tyrian Purple would be used for this study due to its rich history and bioavailability.

In order to target a wide band gap XIND material polymerised at the 6,6'–positions, it was decided to employ benzene as the peripheral aryl group, as the dihedral angle between the IND core and a benzene ring is larger than that of thiophene. This will result in poorer $\pi$-orbital overlap, thus will widen the band gap. Furthermore, the twisted confirmation may reduce $\pi$-stacking and aggregation, thus may lead to a larger degree of solubility.

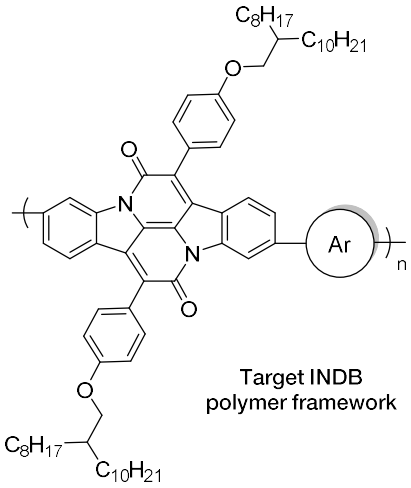


**Figure 4.4** The target 6,6'–INDB polymer framework

## 4.2 Synthesis

Fatefully, Tyrian Purple cannot be prepared by the simple bromination of indigo, which results in bromination on all positions except the 6–position.[217] Whilst several preparations have been reported, none are particularly high yielding.[218,219]

Imming *et al.* reported a five-step synthesis of 6,6'-dibromoindigo from *p*-toluidine **4.1**, a cheap and readily available commercial precursor (**Scheme 4.1**).[220] Firstly, *p*-toluidine was nitrated in high yield with conc. nitric acid in conc. sulphuric acid. The ammonium hydrosulfate sulfate **4.2** salt that was precipitated from the reaction underwent a Sandmeyer reaction with copper(I) bromide to give 4-bromo-2-nitrotoluene **4.3** in literature yield, even at large scale (30 g).

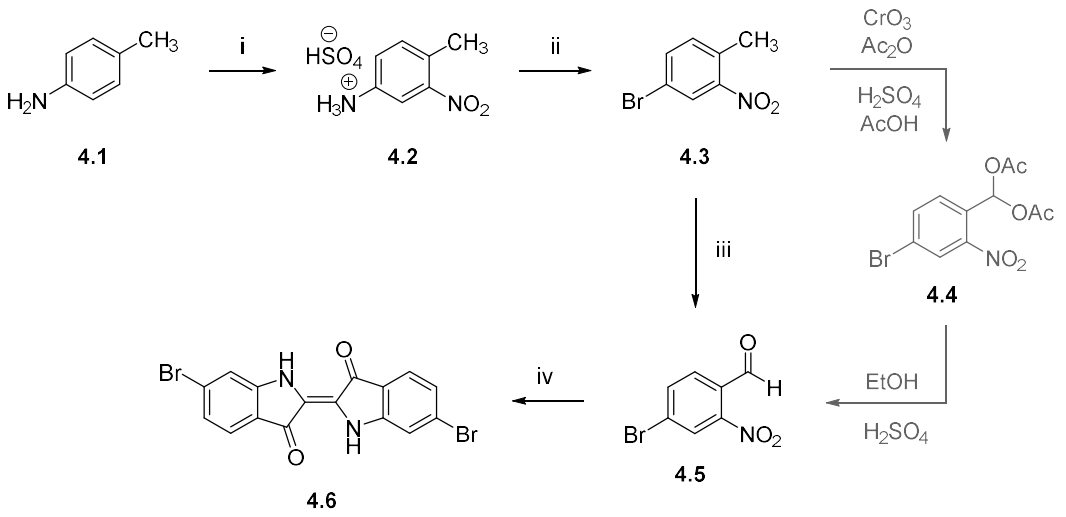


**Scheme 4.1** Synthesis of Tyrian Purple (6,6'-dibromoindigo, **4.6**) from *p*-toluidine **4.1**
(i) $HNO_3/H_2SO_4$, 83%; (ii) $NaNO_2$, HBr, CuBr, 57%; (iii) DMF.DMA, then $NaIO_4$, 67%; (iv) Acetone, $NaOH_{(aq)}$, 58%

The next step of the synthesis reported by Imming *et al.* was the oxidation of the aromatic methyl group using almost three molar equivalents of chromium(VI) oxide and acetic anhydride to give the diacetate **4.4**. Firstly, this procedure was attempted several times but only trace quantities of the diacetate were recovered, far lower than the 65% yield reported. Secondly, this huge excess of chromium is extremely undesirable as, although the reagent is cheap, the reaction has poor scalability due to the generation of huge quantities of toxic chromium waste.

Thankfully, the previously outlined method for oxidising aromatic methyl groups ortho to nitro groups selectively to aldehydes using *N*,*N*-dimethylformamide dimethyl acetal worked efficiently and gave the desired aldehyde **4.5** in higher yield over one step (67%).

Finally, a Baeyer–Drewson indigo reaction of aldehyde **4.5** and acetone in aqueous sodium hydroxide gave 6,6'-dibromoindigo **4.6** in excellent yield (58%). Pleasingly, this four-step route could be scaled effectively to furnish over 10 g of **4.6**.

A condensation-annulation reaction (**Scheme 4.2**) of **4.6** with previously discussed **2.11** gave the brominated monomer **Br-XINDB** (**4.7**) in 6% yield, in line with previous yields of this type of reaction.

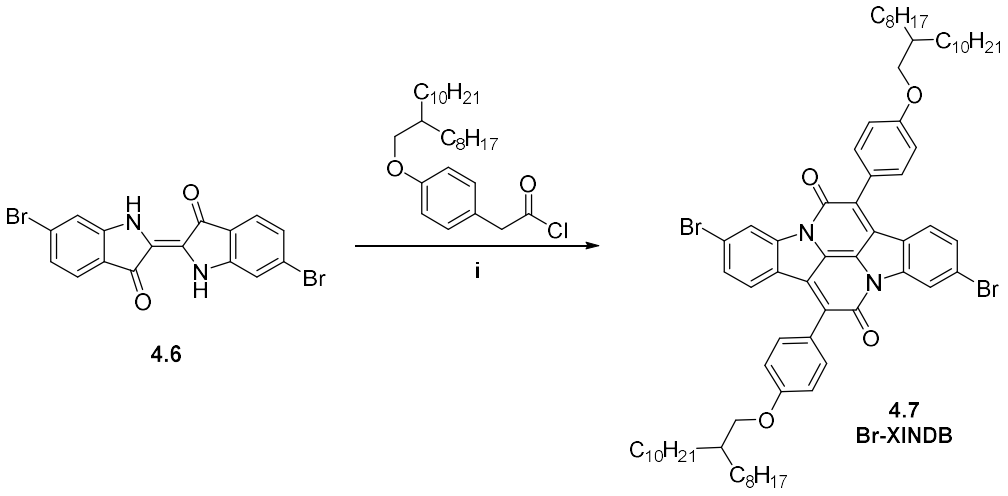


**Scheme 4.2** Synthesis of Br-XINDB **4.7**
(i) Xylenes, 165 °C, 12 h, 6%

Two polymer syntheses were then attempted: (1) a Stille polymerisation of Br-XINDB with 2,5-bis(trimethylstannyl)thiophene; (2) a Suzuki polymerisation of Br-XINDB with benzothiadiazole boronic acid pinacol ester (**Scheme 4.3**). However, the polymeric material obtained from both of these reactions was insoluble, even in high boiling point solvents such as trichlorobenzene.

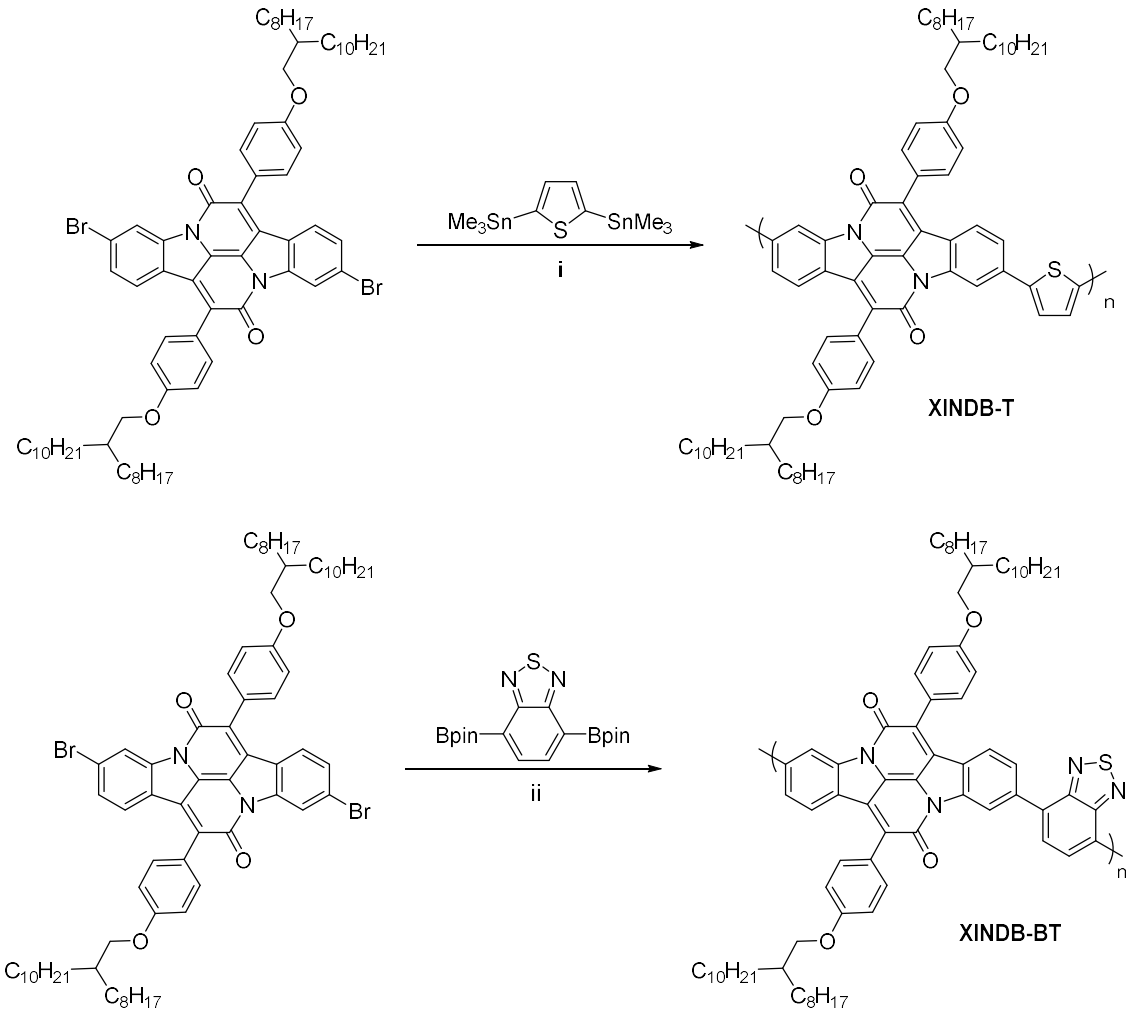


**Scheme 4.3** Attempted polymerisations of XINDB with thiophene and benzothiadiazole (i) $Pd_2(dba)_3$, $P(OTol)_3$, anhyd. degas. PhCl, μW, 45 min, 100 → 180 °C; (ii) Aliquot 336, degas. $PhMe/H_2O$, 3 d, 125 °C

Therefore, co-monomers were required which could provide high degrees of solubility. Due to the availability of materials, (**Br-**)**INDT** (from Chapter 2) and **Br-DPP** were chosen, as these contained large branched 2-octyldodecanyl alkyl chains and were readily available. To be able to react with these monomers, a Miyaura borylation was carried out on **Br-XINDB** (**Scheme 4.4**) to create the borylated monomer **Bpin-XINDB** hereon referred to as **XINDB**.

Suzuki polymerisations were then carried out with XINDB and the two brominated monomers of INDT and DPP to give two novel polymers **XINDB-DPP** and **XINDB-INDT** (**Figure 4.5**). The polymerisations occurred well and the crude polymeric material was purified by Soxhlet extraction in acetone for 12 h then hexane for 12 h, to remove lower molecular weight oligomers and soluble organic impurities, and then the polymers were extracted with chloroform for 12 h. The polymers were then reprecipitated from a minimum volume of hot chlorobenzene into methanol, collected by vacuum filtration and thoroughly dried.

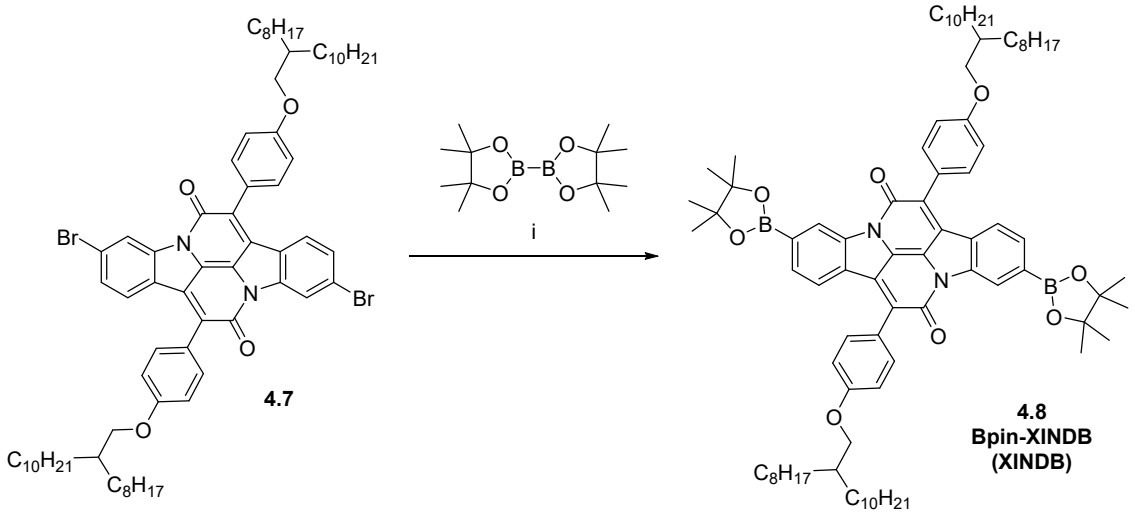


**Scheme 4.4** Synthesis of monomer **XINDB**
(i) $PdCl_2$(dppf), KOAc, anhyd. 1,4-dioxane, 80 ℃, 12 h, 87%

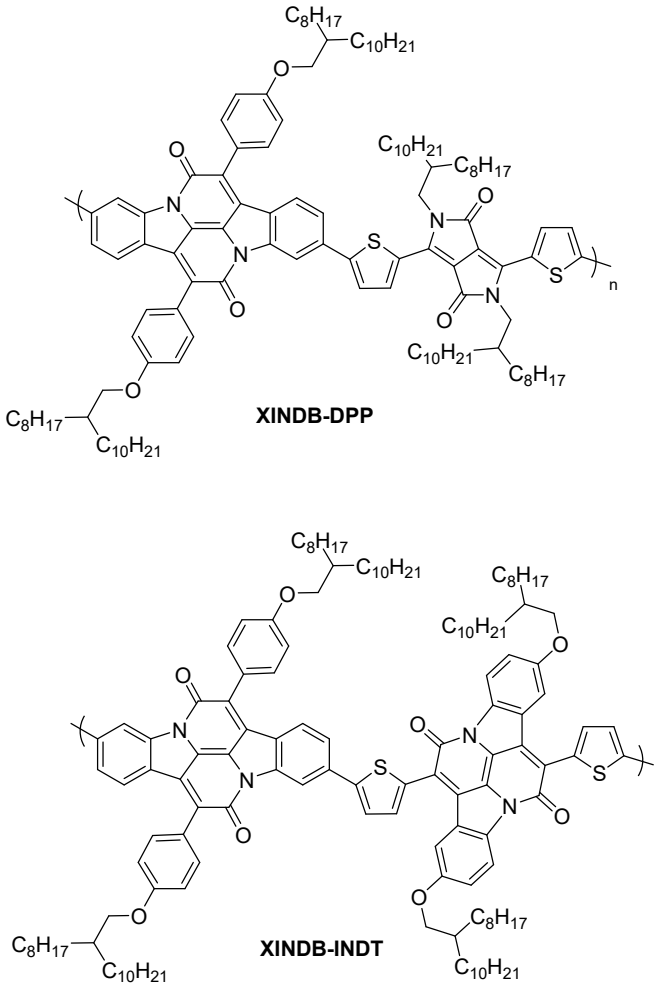


**Figure 4.5** Structures of **XINDB-DPP** and **XINDB-INDT**

## 4.3 Results & Discussion

Hereon, to simplify nomenclature, the two polymers will be referred to by "X" and the comonomer, i.e. **XDPP** and **XINDT**.

### 4.3.1 Physical & Optical Properties

The physical data of the two cross-conjugated polymers is summarised in **Table 4.1**. The number and weight molecular weight averages were determined by size exclusion chromatography (SEC) using polystyrene standards (PS) in chlorobenzene at 80 °C.

**Table 4.1** Physical properties of the two cross-conjugated XINDB polymers[a]

| Polymer | $M_n$ (kDa) | $M_w$ (kDa) | Đ |
|---|---|---|---|
| XDPP | 84 | 551 | 6.6 |
| XINDT | 11 | 53 | 5.0 |

[a]Determined by SEC using polystyrene (PS) standards at 80 ℃ and PhCl as eluent

**XDPP** exhibited a large number average molecular weight of 84 kDa whilst **XINDT** exhibited an $M_n$ of 11 kDa, which was lower than ideal, but its $M_w$ of 53 kDa demonstrated that a considerable quantity of the polymeric material was above the unofficial target of 15 kDa. The $M_w$ for **XDPP** was extremely high at 551 kDa, and the resulting polydispersities of both polymers were also quite high, at 6.6 and 5.0 for the **XDPP** and **XINDT** respectively.

**Figure 4.6** shows the solution (chlorobenzene) and thin-film (spin-coated from 5 mg/mL solutions in chlorobenzene) UV-vis absorption spectra of the two polymers and the optical properties are summarised in **Table 4.2**.

**Table 4.2** Optical properties of the two cross-conjugated polymers

| Polymer | $E_g$[a] (eV) | $E_g^{calc}$[b] (eV) | $E_{homo}$[c] (eV) | $E_{lumo}$[d] (eV) | $\lambda_{max}^{soln}$[e] (nm) | $\lambda_{max}^{film}$[f] (nm) |
|---|---|---|---|---|---|---|
| XDPP | 1.54 | 1.61 | –5.29 | –3.75 | 720 | 727 |
| XINDT | 1.43 | 1.70 | –5.21 | –3.78 | 743 | 750 |

[a]Estimated from UV-vis onset, thin-film; [b]Determined by TD-DFT using B3LYP/6-31G*; [c]Determined by PESA; [d]$E_{homo} + E_g$; [e]PhCl solution; [f]Spin-coated from a 5 mg/mL solution in PhCl

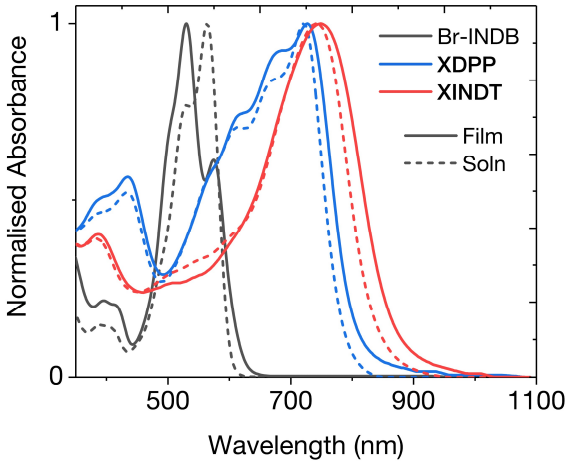


**Figure 4.6** Normalized UV-vis absorption spectra of **Br-INDB** and the two cross-conjugated polymers. Solution spectra (dashed lines) were recorded in chlorobenzene, and thin-films (solid lines) were spun from 5 mg/mL solutions in chlorobenzene

The large bathochromic shifts of the absorbance spectra of the two cross-conjugated polymers relative to the monomer shows considerable narrowing of the optical band gap. However, $E_g$ for **XDPP** and **XINDT** were 1.54 and 1.43 eV respectively, representing the two widest band gap indolonaphthyridine semiconducting polymers synthesised during this thesis, demonstrating the success in using cross-conjugation as a tool for generating wide band gap IND polymers. Also, the extent of the narrowing suggests that electronic coupling may not have been completely broken along the polymer backbone, so charge transport through these materials may remain somewhat efficient.

Both spectra broadened on going from solution to thin-film, which is a common feature of organic polymers, attributed to solid-state packing effects. The absorption of **XINDT** was sharp and featureless in the near-IR, whereas **XDPP** showed features between 600-700 nm and a wider overall spectral bandwidth.

The ionisation potential $(E_{homo})$ of both polymers was measured using photoelectron spectroscopy in air (PESA) and the electron affinity $(E_{lumo})$ estimated by the addition of the corresponding $E_g$, as estimated from the thin-film UV-vis absorption onsets. Interestingly, the $E_{lumo}$ of **XDPP** and **XINDT** were –3.75 and –3.78 eV respectively, validating the theory that an $E_{lumo}$ of approximately –3.75 eV is an intrinsic property of indolonaphthyridine as a building block. The $E_{homo}$ of the two polymers were considerably deeper than the previously studied conjugated polymers, with values calculated by PESA as –5.29 and –5.21 eV for **XDPP** and **XINDT** respectively. These results were in line with the literature observations whereby cross-conjugation leads to deeper $E_{homo}$.

Pleasingly, the deepening of $E_{ho}$ and relative maintained $E_{lumo}$ which remained isoenergetic with the $E_{lumo}$ of PCBM, meant that these materials could be tested as polymer acceptors in polymer-polymer solar cells.

### 4.3.2 Theoretical Analysis

To investigate the electronic structure of the two cross-conjugated polymers, DFT calculations were carried out on model trimers using the B3LYP hybrid functional and 6-31G* basis set. The frontier molecular orbital distributions of the two polymers are shown in Figures **4.7** & **4.8**.

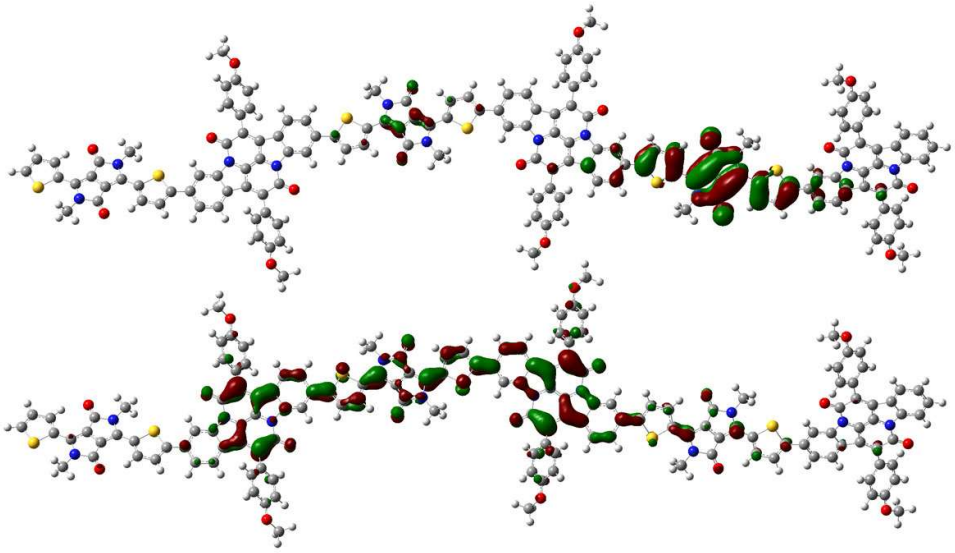

**Figure 4.7** Molecular orbital distributions of the HOMO (top) and LUMO (bottom) of **XDPP** calculated at the B3LYP/6-31G* level of theory

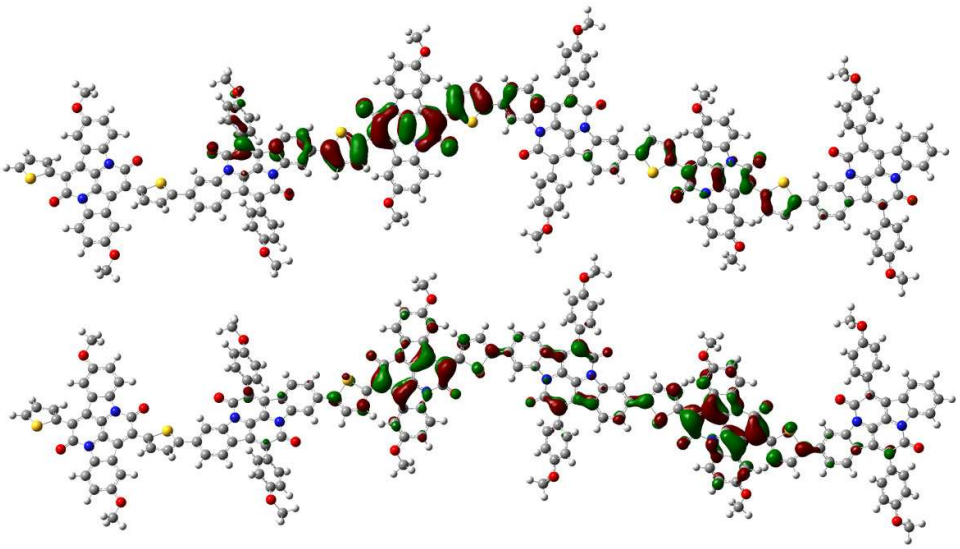

**Figure 4.8** Molecular orbital distributions of the HOMO (top) and LUMO (bottom) of **XINDT** calculated at the B3LYP/6-31G* level of theory

Interestingly, the LUMO wave functions of both polymers were well delocalised along each polymer backbone, whereas the HOMO wave functions were localised on the DPP or INDT units. The relatively high degree of delocalisation of the LUMO in these two polymers suggested that they may be able to facilitate somewhat efficient electron transport.

The theoretical band gap $E_{\mathrm{g}}^{calc}$ was calculated for each of the two polymers using TD-DFT. The theoretical $E_{homo}^{calc}$ was extracted from the DFT calculations of the geometry optimised trimers and the corresponding $E_{lumo}^{calc}$ values estimated by the addition of $E_{\mathrm{g}}^{calc}$ to $E_{homo}^{calc}$. **Figure 4.9** shows the theoretical and experimental frontier MO diagrams for the two polymers. Computational analysis of the polymers suggested that **XINDT** would exhibit the widest band gap, in disagreement with the experimental results.

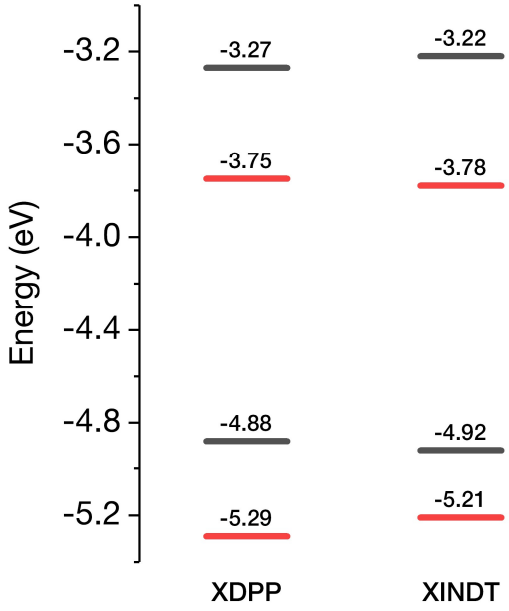


**Figure 4.9** Theoretical (black) and experimental (red) optical band gaps of **XDPP** and **XINDT**

### 4.3.3 Organic Field-Effect Transistors

To investigate the charge transport properties of the cross-conjugated polymers, top gate – bottom contact (TG-BC) OFET devices were fabricated on glass substrates using thermally evaporated source/drain (SD) electrodes. For n-type operation, Al SD electrodes were treated with ethoxylated polyethylenimine (PEIE) to facilitate electron injection by reducing the work function of the electrodes to better match the electron affinity of the polymers. For p-type operation, the treatment of Au electrodes with UV/ozone removes organic contaminants and is expected to improve the hole injection into polymers with HOMO energies around –5.25 eV.[26,27]

Onto the SD electrodes was spin-cast the two cross-conjugated polymers from 10 mg/mL solutions in chlorobenzene. The semiconductor layer was annealed at 190 °C for 15 min before a CYTOP dielectric was spin-cast onto the semiconductor and the device further annealed for 1 h at 100 °C.

Interestingly, despite the outlined efforts, the cross-conjugated polymers only exhibited n-type charge transport in field-effect transistors – no hole transport was observed at all in the devices designed for p-type operation. However, these results corresponded well with the predicted molecular orbital distributions calculated by density functional theory shown in Figures 4.7 and 4.8. The transfer curves and output characteristics of the n-type devices are shown in **Figure 4.10** and the performance data outlined in **Table 4.3**.

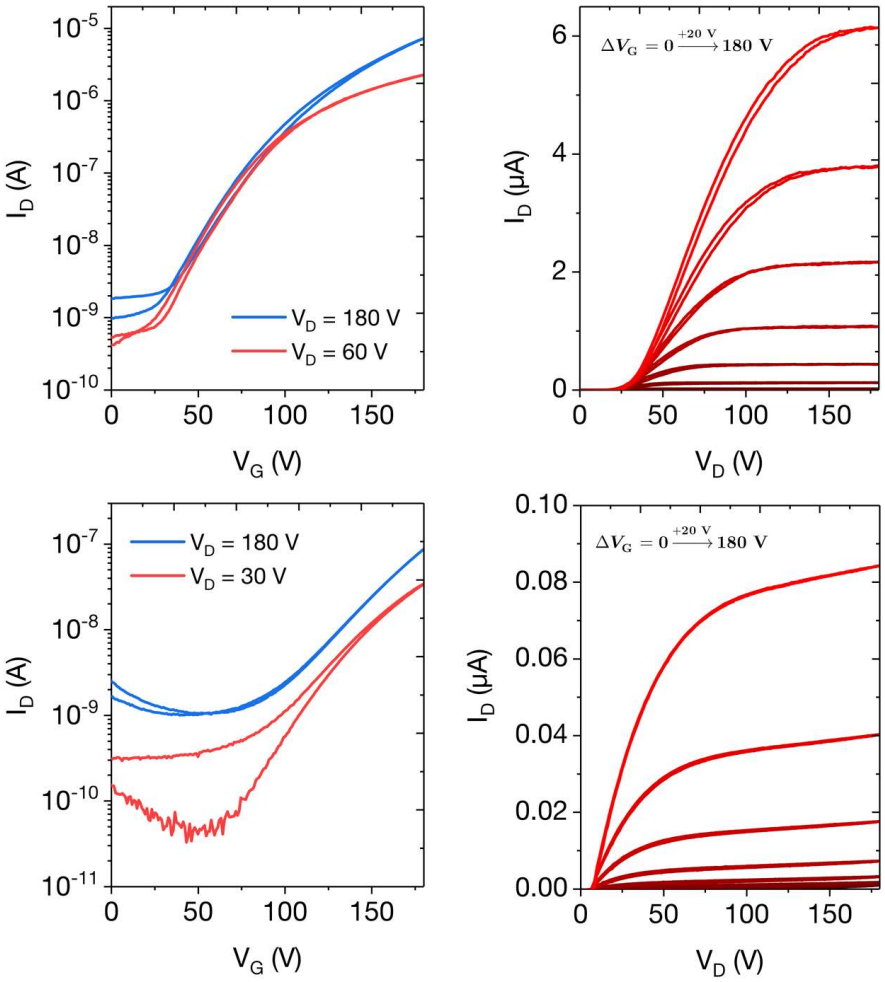


**Figure 4.10** Transfer curves (left) and output characteristics (right) of n-type TG-BC OFET devices based on **XDPP** (top) and **XINDT** (bottom), annealed at 190 °C, with channel dimensions of $L$ = 40 µm and $W$ = 1000 µm

**Table 4.3** Performance parameters of TG-BC n-type OFET devices based on the two cross-conjugated polymers, with channel length $L = 40$ µm and width $W = 1000$ µm

| Polymer | ${I_{on}/I_{off}}^{lin}$ | ${I_{on}/I_{off}}^{sat}$ | $V_{\mathrm{on}}^{lin}$ (V) | $V_{\mathrm{Th}}^{sat}$ (V) | $\mu_{lin}$ ($\mathrm{cm}^2$/Vs)[a] | $\mu_{sat}$ ($\mathrm{cm}^2$/Vs) [a] |
|---|---|---|---|---|---|---|
| XDPP | $10^3 - 10^4$ | $10^3 - 10^4$ | +23 | +91 | 0.012 (0.010) | 0.10 (0.09) |
| XINDT | $10^2$ | $10^2$ | +41 | +123 | 0.0007 (0.0007) | 0.0019 (0.0017) |

[a]Field-effect electron mobility extracted from smoothed data, indicating the best of three devices measured and the mean value given in brackets

The drain currents measured in OFETs based on **XDPP** were two orders of magnitude higher than the drain currents in devices based on **XINDT**, indicating clearly that **XDPP** exhibited superior electron transport in comparison to **XINDT**. Considering the almost identical $E_{lumo}$ of the two polymers, this result was supported by the molecular orbital distributions, which indicated that the LUMO of **XDPP** exhibited greater delocalisation along the polymer backbone relative to **XINDT**.

Field-effect electron mobilities for the two polymers were calculated from the transfer characteristics; Saturation regime electron mobilities $(\mu_e^{sat})$ were 0.10 and 0.002 $\mathrm{cm}^2$/Vs for **XDPP** and **XINDT** respectively, both respectable values for these types of materials. Due to poor device performance at low $V_{\mathrm{D}}$, electron mobilities calculated in the linear regime were relatively lower: 0.012 and 0.0007 $\mathrm{cm}^2$/Vs for **XDPP** and **XINDT**, respectively.

The on-off ratios of the linear and saturated regimes for **XDPP** $(10^3 - 10^4)$ were up to two orders of magnitude higher than **XINDT** $(10^2)$, again demonstrating the better performance of the DPP-based cross-conjugated polymer.

The lack of hole transport in these materials was attributed to the strongly localised HOMO wave function, although further work would be required to confirm this. In contrast, the clear theoretical delocalisation of the LUMO wave functions along the cross-conjugated polymer backbones correlates well with good electron transport in the n-type optimised OFET devices. Notably, these are the first examples of cross-conjugated polymers exhibiting n-type charge transport to date.

## 4.4 Conclusions

The polymerisation of a cross-conjugated indolonaphthyridine monomer synthesized from bioavailable Tyrian Purple was studied. When the cross-conjugated indolonaphthyridine benzene was polymerized with simple co-polymers, such as thiophene and benzothiadiazole, insoluble polymeric material was obtained. However, when the cross-conjugated monomer was polymerized the with large monomers diketopyrrolopyrrole (DPP) and indolonaphthyridine thiophene (INDT), soluble cross-conjugated polymers were obtained in high yields.

Using the cross-conjugated synthetic strategy, the two polymers exhibited the widest band gaps of any indolonaphthyridine-based polymer synthesized to date. Excitingly, the two polymers were successfully utilized in OFETs as n-type materials – making these materials the first examples to date of cross-conjugated organic polymers capable of facilitating electron transport in FETs.

The n-type character of these two materials was linked to the high delocalization of the LUMO wave function along the polymer backbone as calculated using density functional theory. Likewise, the highly localized HOMO wave functions of the materials account for the lack of p-type transport in OFETs.

Pleasingly, the wide optical band gaps of the materials were due to a lowering of $E_{homo}$ as both materials exhibited similar $E_{lumo}$ of approximately –3.75 eV, remaining isoenergetic to the $E_{lumo}$ of common OPV fullerene BHJ acceptors. These wide band gap materials have strong potential to be exploited as acceptor materials in fullerene-free OPVs, and this investigation is currently in progress.

These results further demonstrated the power of indolonaphthyridine to furnish high performance organic semiconductors and attested to the usefulness of cross-conjugation as a synthetic strategy for designing wide band gap organic semiconducting polymers.

# V

*Small Molecule Indolonaphthyridines for Singlet Fission*

## 5.1 Introduction

### 5.1.1 The Energy Landscape

Solar energy is a highly attractive option for meeting the world's increasing demand for energy without increasing the combustion of fossil fuels and worsening climate change. Unfortunately, the economics of energy production is currently a greater priority to global decision makers. Without a major change in the global political climate, it has become evident that the idea of a solar-driven energy landscape will only be achieved by reducing the production cost and/or increasing the efficiency of commercially viable solar technology.

Relative to inorganic photovoltaic materials, organic photovoltaics are still an emerging PV technology. Although conceived in the 1970s, the pursuit of high efficiency OPV materials didn't begin until the early 2000s. Since then, the best research-cell OPV efficiency recorded is currently 11.5% (**Figure 5.1**) is just under half that of the best equivalent inorganic PV cell of (25.3%), research which has had a 30-year head start.[221]

Other technologies do exist which give higher efficiency PV cells, such as multi-junction cells or the state-of-the-art inorganic CIGS material, however these have large costs associated with them, and improving single-junction PV technologies is the most feasible method moving toward a solar dominated renewable energy landscape in the near future.

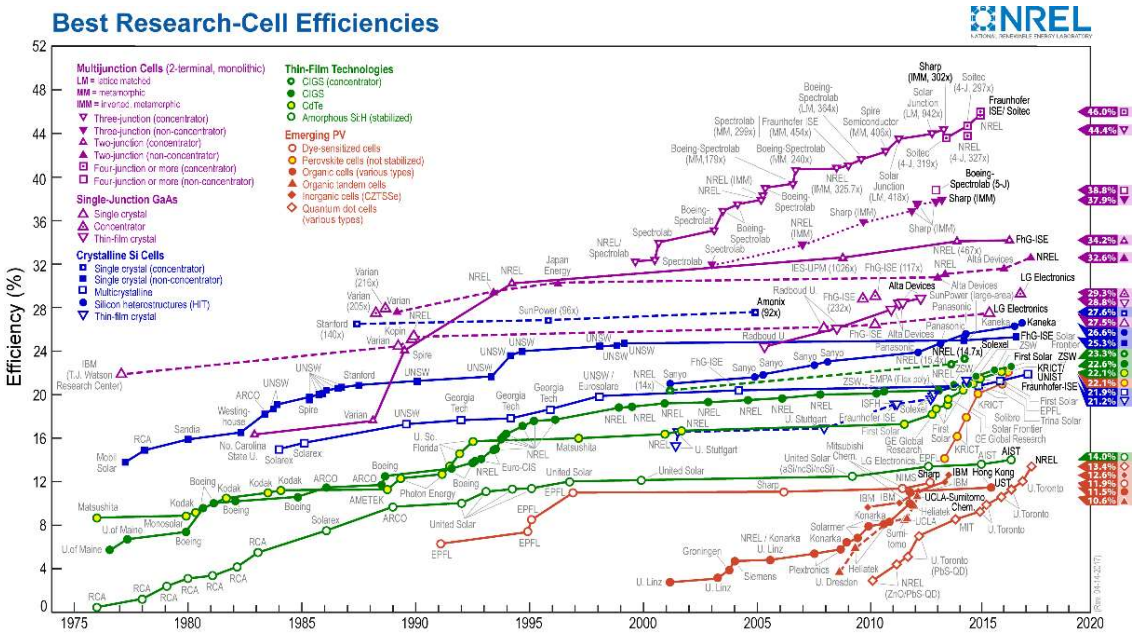


**Figure 5.1** The NREL Best Research-Cell Efficiencies Chart[221]

### 5.1.2 The Shockley-Queisser Limit

Like most physical phenomenon, scientists seeking the highest efficiency PV semiconductor are confined to a theoretical limit. In 1961, William Shockley and Hans Queisser published a theoretical analysis of the maximum possible efficiency in a single junction $p$-$n$ solar cell.[222] Their model found that a maximum efficiency of ~30% occurred in a material with an optical band gap of 1.1 eV and thus became known as the *Shockley-Queisser* (SQ) *limit*. A full physical and mathematical analysis of the model is beyond the scope of this thesis, however a brief overview is provided below.

Whilst solar radiation closely matches a black body emitter at ~6000 K as it passes through Earth's atmosphere the light is attenuated through scattering and absorption by gases and gaseous chemicals; $O_3$ is an excellent absorber of high energy UV radiation and water vapour gives rise to several wide absorption bands at many wavelengths. As the degree of attenuation of light is dependent on the amount of atmosphere through which it passes, a standardised model of measuring solar radiation absorption is necessary. For a path length $L$ through the atmosphere, the air mass (AM) coefficient for solar radiation, relative to the normal Earth's surface, is given by

$$\mathrm{AM} = \frac{L}{L_0} \approx \frac{1}{\cos z} \tag{5.1}$$

where $L_0$ is the zenith path length at sea level and $z$ is the zenith angle in degrees. Therefore, it is important to note that the air mass number is dependent on the Sun's elevation level, which varies with time of day, season of year and latitude of the observer.

Considering that many of the world's major population and industrial centres lie in temperate latitudes (i.e. Europe, China, USA, Southern Africa and Australia), an AM number representing the spectrum at mid-latitudes provides an appropriate “worldwide” model. As such, **AM1.5** where $z = 48.2°$ has been adopted for testing the absorption of solar radiation.

At the time of writing, the current accepted solar radiation reference standard is the ASTM G173 Spectra (**Figure 5.2**)[223] which represents terrestrial solar spectral irradiance on a surface inclined at a sun-facing $37°$ tilt toward the equator, taken under the 1976 U.S. Standard Atmosphere, with an absolute air mass of 1.5.

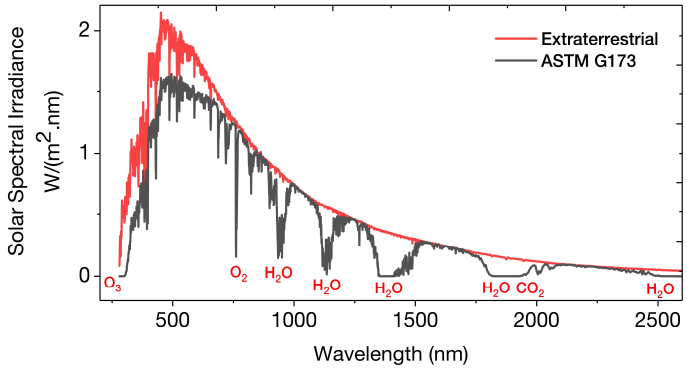


**Figure 5.2** ASTM G173 spectral radiation: terrestrial solar spectral irradiance on a surface inclined at a sun-facing 37° tilt toward the equator, taken under the 1976 U.S. Standard Atmosphere and AM1.5

As the short-circuit current $J_{SC}$ of a solar cell is directly dependent on the power of the incident light source (i.e. the number of photons per unit area), the ideal $J_{SC}$ for each value of $E_g$ is directly proportionate to the number of photons with energy above $E_g$ (**Figure 5.3**).

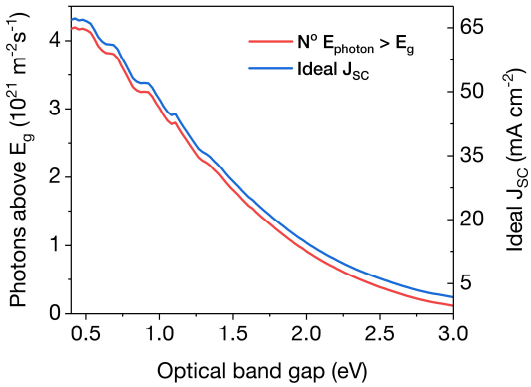


**Figure 5.3** Theoretical number of photons with $E > E_g$ of the ASTM G173 solar spectrum at various optical band gaps (in red). The corresponding ideal $J_{SC}$ of each $E_g$ is shown in blue.

The SQ model takes into account radiative recombination, which places a limit on the rate of exciton production, directly affecting the ideal open-circuit voltage (**Figure 5.4**).

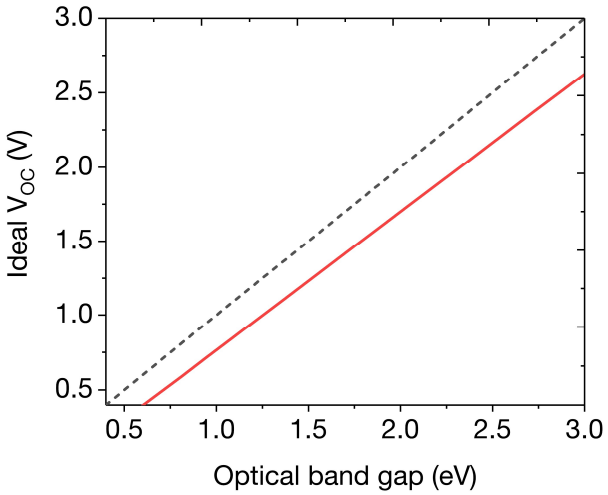


**Figure 5.4** Ideal open-circuit voltage as a function of optical band gap (red). The dashed line shows $V_{\mathrm{OC}} = E_{\mathrm{g}}$.

If the ideal $V_{\mathrm{OC}}$ and $J_{\mathrm{SC}}$ is known for each optical band gap, it is possible to calculate the maximum power point when the product of JV is maximised. The power at this point can be divided by the incident light power to calculate the maximum efficiency at each value of optical band gap (**Figure 5.5**).

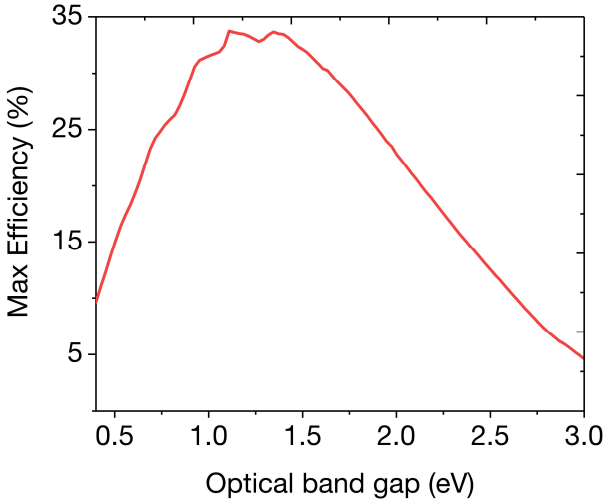


**Figure 5.5** The Shockley-Queisser efficiency limit as a function of $E_{\mathrm{g}}$

Performing these calculations,[224] a maximum efficiency of 33.8% occurs at 1.1 eV. A large constraint of the SQ model is that the excess energy of solar photons with $E \geq E_{\mathrm{g}}$ is converted to heat. If the high energy of such photons could be harnessed instead of lost then the SQ limit could be raised.

One process which can be exploited to this effect is singlet fission (SF) and involves the splitting one singlet excitation into two lower energy triplet excitations. As the decay of a triplet state to a singlet state is spin forbidden, the triplet states are long-lived, and not only could SF-capable photovoltaics harness the normal amount of singlet excitations as generic semiconductors, they can also produce long-lived triplet excitations, reducing the amount of radiative recombination, and thus raising the theoretical limit to ~45%.[225]

### 5.1.3 Singlet Fission

Singlet fission (SF) is a bimolecular process in which a singlet-excited $(\mathrm{S}_1)$ molecule and a ground-state molecule $(\mathrm{S}_0)$ interact to produce a correlated pair of triplet excited molecules $(\mathrm{TT})$. The process begins with a noninteracting combination of an $\mathrm{S}_0$ molecule and an $\mathrm{S}_1$ molecule, whereby SF is induced by the interaction Hamiltonian operator

$$H_{\mathrm{int}} = H_{\mathrm{el}} + H_{\mathrm{sp}} \tag{5.2}$$

where $H_{\mathrm{el}}$ is a spin-free electrostatic part and $H_{sp}$ is a spin-dependant part. Firstly, $H_{\mathrm{el}}$ converts the $\mathrm{S}_0 + \mathrm{S}_1$ state into a pair of local triplet states coherently coupled into a pure overall singlet $^1(\mathrm{TT})$. This action represents the $internal\ conversion$ aspect of SF. The $^1(\mathrm{TT})$ state has been referred to in the literature as a multiexcition state, a doubly excited state, a dark state or a correlated triplet pair.[226–228]

The $H_{\mathrm{sp}}$ component represents the $intersystem\ \ crossing$ component of SF and the outcome is dependent on the strength of the physical coupling between the two molecules, i.e. physical contact and/or noncovalent bonding in crystals or aggregates, or covalent bonding in dimers, oligomers or polymers. If the coupling is weak (e.g. if they simply touch), the singlet $^1(\mathrm{TT})$ state is almost degenerate with the triplet $^3(\mathrm{TT})$ and quintet $^5(\mathrm{TT})$ states, which can also arise from the coupling of two triplets. However, if the coupling is stronger, $H_{\mathrm{sp}}$ can mix the states significantly, meaning that spin coherence is gradually lost and the triplet states can defuse apart.

If the coupling of the molecules is strong, the $^1(\mathrm{TT})$, $^3(\mathrm{TT})$ and $^5(\mathrm{TT})$ states are not degenerate, and the effects of $H_{\mathrm{sp}}$ can be ignored and the only product of SF is a pure $^1(\mathrm{TT})$ spin state. However, if $^1(\mathrm{TT})$ is significantly more stable than $^3(\mathrm{TT})$ and $^5(\mathrm{TT})$, triplet diffusion will be energetically unfavourable. Therefore, an optimal strength of interaction between the two molecules must be obtained if the desired outcome is two free triplet excitons.

Likewise, if the coupling is above thermal energy, $kT$, the $^1(TT)$ state is bound too tightly to dissociate on the timescales available. Similarly, coupling that is too weak will render the formation of the $^1(TT)$ state slower than competing processes such as fluorescence. The simplest view of the overall process of SF is given in **Equation 5.3**.

$$2S_0 \xrightarrow{h\upsilon} S_0 + S_1 \longrightarrow {}^1(TT) \longrightarrow T_1 + T_1 \tag{5.3}$$

#### 5.1.3.1 Detecting Singlet Fission

When investigating singlet fission experimentally, one of the main challenges is differentiating between triplet state formation by SF and or by intersystem crossing (ISC), where spin-orbit coupling converts a singlet excitation to a triplet with the loss of vibrational energy.

As two triplet states are formed from one singlet state, a triplet quantum yield above 100% irrefutably confirms SF. However, some SF-capable materials may not be efficient enough to exhibit this behaviour. As such, the timescales of excited state dynamics can be investigated.

There are multiple relaxation pathways of excited molecules, outlined in **Figure 5.6**. Each pathway has a timeline and unique requirements in order to occur. For example: non-radiative relaxation of high electronic states occurs on the femtosecond $(10^{-15})$ scale; vibrational relaxation of states on the picosecond $(10^{-12})$ scale; fluorescence, i.e. radiative relaxation of $S_1 \rightarrow S_0$ on the nanosecond$(10^{-9})$ scale; phosphorescence, i.e. spin-forbidden relaxation of $T_1 \rightarrow S_0$ on the microsecond $(10^{-6})$ scale.

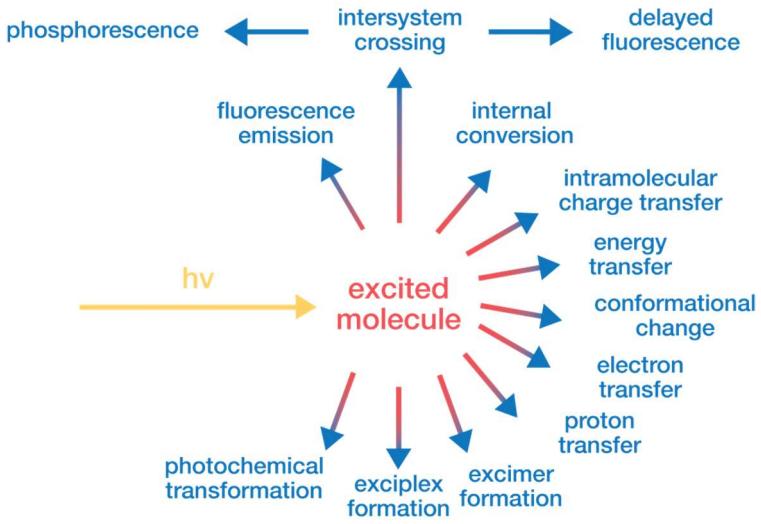


**Figure 5.6** Relaxation pathways of photoexcited molecules

Singlet fission is an incredibly fast process and occurs on the order of picosecond $(10^{-12})$ or faster. In contrast, ISC occurs on the order of $10^{-3} - 10^{-8}$ seconds, representing one of the slowest forms of relaxation in molecular dynamics. As such, time-resolved detection of formation and decay of excited states can also provide evidence of SF, specifically ground-state bleaching which is kinetically concurrent with excited singlet state disappearance and with triplet formation. This analysis is possible using femtosecond transient absorption spectroscopy (fTAS), however this technique is very challenging and there can sometimes be overlap of dynamics in systems with slow SF and fast ISC.[229]

Another technique which can be employed to provide evidence of SF is electronic paramagnetic resonance (EPR), which uses an applied magnetic field to split the magnetic moment of an unpaired electron into sub-states and then uses microwave radiation to probe transitions between sub-states. For triplet states, the populations of these sub-states are entirely dependent on the method of triplet state formation.

In a sample of a SF candidate in a very dilute frozen solution, it would be statistically unlikely that two molecules would be close enough to electronically interact and undergo triplet formation via SF. Therefore, an EPR spectra of a triplet state observed for this sample would result from ISC. If the same experiment was then performed on a thin-film where the candidate can electronically interact strongly, an observable difference in EPR spectra provides evidence that the triplet excitation was formed as a product of a non-ISC process, namely SF. This is a relatively simplistic way of considering complex EPR spectroscopy, but apt for this thesis.

### 5.1.4 Electronic Paramagnetic Resonance

#### 5.1.4.1 Principles

To go back to basics, spectroscopy is the fundamental study of the interaction between matter and oscillating electric and magnetic fields, i.e. electromagnetic (EM) radiation. The fact that particles, atoms and molecules absorb or emit discrete amounts of energy is a fundamental part of quantum theory. The energy of such radiation, as given by Planck's Law,

$$E = h\nu = \frac{hc}{\lambda} \tag{5.4}$$

where $h$ is Planck's constant, $\nu$ is frequency, $c$ is the speed of light, $\lambda$ is the wavelength and $E$ is photon energy. Conventional spectroscopy involves sweeping the wavelength at which an atom or molecule absorbs radiation and the resulting absorption profile gives

insight into the identify, structure and dynamics of a probed sample. UV-vis spectroscopy, arguably the most common spectroscopy, probes molecular scale energy levels which absorb light in the visible region of the EM spectrum (400–700 nm), though also extends to ultra-violet (UV, 10–400 nm) and infrared (IR, 700–$10^5$ nm). Nuclear magnetic resonance (NMR) spectroscopy, the fundamental tool of synthetic chemistry analysis, employs radio waves (75–0.5 m) to probe atomic nuclei of molecules in an applied magnetic field.

Electronic paramagnetic resonance (EPR) is almost identical to NMR spectroscopy, however where NMR examines the excitation of the spin of $atomic\ nuclei$ at radio frequencies, EPR is the study of the excitation of the spin of $unpaired\ electrons$ using microwave radiation (100–0.1 cm).

An isolated electron, like most elementary particles, has spin angular momentum $S$, commonly shortened to $spin$ (note that spin angular momentum is unrelated to any physical motion and is just an intrinsic property of a particle). Because an electron has charge, the combination of spin angular momentum and charge generates a magnetic field. Therefore, electrons have a magnetic moment $\mu$ typically considered as a magnetic "dipole" (**Figure 5.7**).

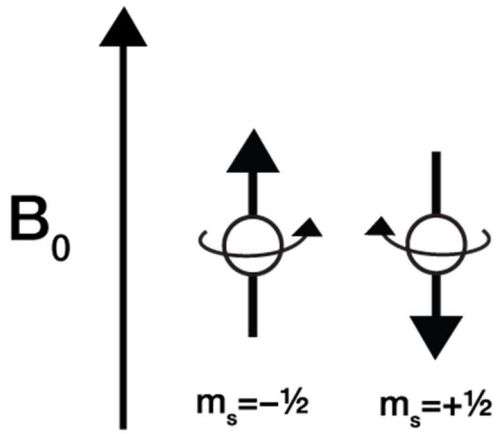


**Figure 5.7** Minimum and maximum orientations of the magnetic moment of an isolated spin-half charged particle relative to a magnetic field

When this electron is placed into an external magnetic field $B_0$, the magnetic moment of the electron is split into two energy levels. As electrons are fermions, i.e. they have a spin quantum number of $s = \frac{1}{2}$, the magnetic component of the particle is split (**Figure 5.8**) into $m_S = -\frac{1}{2}$, the $parallel$ state $(\alpha)$, and $m_S = +\frac{1}{2}$, the $antiparallel$ state $(\beta)$.

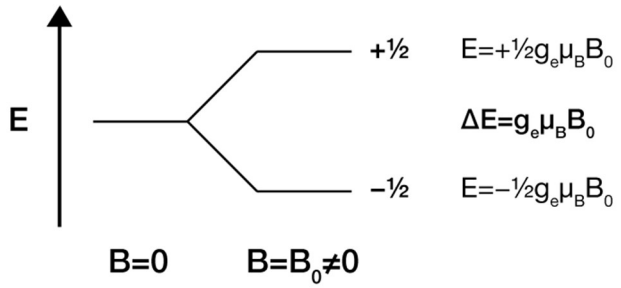


**Figure 5.8** Splitting of the magnetic moment by $\pm\frac{1}{2}g_{\mathrm{e}}\mu_{\mathrm{B}}B_0$ in an applied magnetic field

The electron has a state of lowest energy when $\mu$ is aligned (parallel) with $B_0$ and a state of highest energy when unaligned. This process of splitting the magnetic component of an electron in an external magnetic field is called the Zeeman effect and defined mathematically as

$$E = m_{\mathrm{S}} g_{\mathrm{e}} \mu_{\mathrm{B}} B_0 \tag{5.5}$$

where $g_{\mathrm{e}}$ is the *g*-factor of an electron (2.0023192778 ≈ 2.00) and $\mu_{\mathrm{B}}$ is the Bohr magneton, a physical constant and natural unit for expressing the magnetic moment of an electron caused by its angular momentum. Thus, the difference in energy between $\alpha$ and $\beta$ is given by

$$\Delta E = g_{\mathrm{e}} \mu_{\mathrm{B}} B_0 \tag{5.6}$$

and an unpaired electron can transition $(\Delta m_{\mathrm{S}} = \pm 1)$ between $\alpha$ and $\beta$ by the emission or absorption of a photon of energy $h\nu = \Delta E$, thus giving rise to the fundamental equation of EPR spectroscopy

$$h\nu = g_{\mathrm{e}} \mu_{\mathrm{B}} B_0 \tag{5.7}$$

#### 5.1.4.2 Spin-Orbit Coupling

An unpaired electron on a molecule is not isolated and therefore possesses orbital angular momentum $L$ in addition to spin angular momentum. As a charged particle with orbital angular momentum is essentially a circulating current, $L$ has a magnetic moment associated with it. Importantly, the two magnetic moments of $S$ and $L$ interact, giving rise to *spin-orbit interaction*, a fundamental principle of quantum mechanics. The energy of the spin-orbit interaction depends on the relative orientations of the two components of the angular momentum. Therefore, the magnetic moment of an electron in a molecule is proportional to its *g*-factor and its spin-orbit interaction

$$\mu \propto g_{\mathrm{e}}(S + L) \tag{5.8}$$

In general, orbital angular moment approximates to zero for an electron in the ground state but interactions between the ground and excited states blends small amounts of $L$ to the ground state. To account for the spin-orbit interaction, it is common to assume $(S + L) \propto S$ with a change in the *g*-factor, written mathematically as $g$, i.e.

$$\mu \propto gS \tag{5.9}$$

thus **Equation 5.6** can be modified to account for $L$ as

$$\Delta E = g\mu_{\mathrm{B}}B_0 \tag{5.10}$$

The magnitude of the spin-orbit interaction of an electron is dependent on the nucleus containing it. Typical organic atoms (H, O, C, N) will have small spin-orbit contributions where $g \cong g_{\mathrm{e}}$, but electrons associated with metals will have *g*-factor significantly different to $g_{\mathrm{e}}$. Importantly, $g$ is directly affected by the chemical nature and relationship of the unpaired electron to its nucleus, and to the electronic structure of the molecule to which it belongs. Hence, the *g*-factor can be considered a fingerprint of a molecule.

In an EPR spectrometer, a paramagnetic sample placed in a large magnetic field has its ground state split into two energy levels differing by $\Delta E$. Whereas conventional optical spectroscopy probes samples by scanning frequencies of electromagnetic radiation whilst holding a sample in a constant magnetic field (e.g. UV-vis), EPR experiments probe with microwave frequencies, and the spectral band width of the microwave source is typically constrained to 0.5 GHz. Therefore, it is considerably easier to use a constant probe frequency whilst varying the magnetic field strength until the conditions of **Equation 5.10** are met. The *g*-factor of the molecule can then be calculated with

$$g = \frac{h\nu}{\mu_{\mathrm{B}}B_0} \tag{5.11}$$

These two energy levels arise due to the selection rule $2S + 1$. For a system with one unpaired electron, e.g. a free radical, the multiplicity is a doublet $(2(\frac{1}{2}) + 1 = 2)$, i.e. $\alpha$ and $\beta$ (**Figure 5.9**).

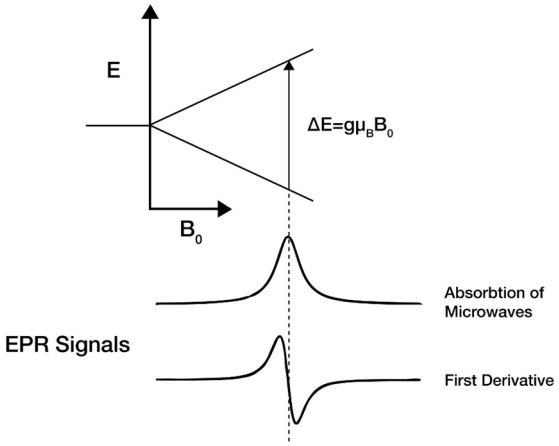


**Figure 5.9** An EPR experiment on a sample with one unpaired electron ($S = \frac{1}{2}$)

If a system contains two unpaired electrons, the state depends of the alignment of the electrons spins. If the spin of the two electrons are aligned antiparallel ($\uparrow\downarrow$), spin is $S = -\frac{1}{2} + \frac{1}{2} = 0$ and the multiplicity of the system is a singlet $(2(0) + 1 = 1)$ and no EPR transition is observed. If the two electrons are aligned parallel ($\uparrow\uparrow$ *or* $\downarrow\downarrow$), $S = 1$, and therefore the multiplicity is a triplet $(2(1) + 1 = 3)$, and according to the $\Delta m_{\mathrm{S}} = \pm 1$ selection rule, two transitions are allowed (**Figure 5.10**), both with $\Delta E = g\mu_{\mathrm{B}} B_0$.

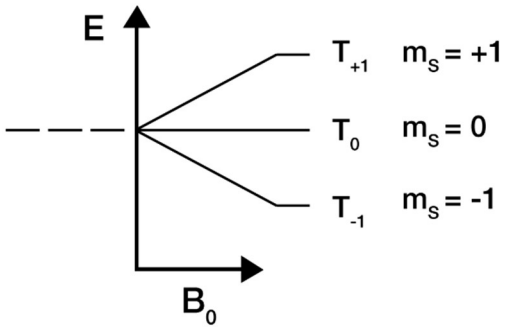


**Figure 5.10** Energy splitting diagram for a triplet ($S = 1$) system

It is prudent to note that the effective magnetic field experienced by each election in a triplet system is not solely the externally applied field $B_0$, but the vector sum of several magnetic fields, including the magnetic moments of the nuclei of the molecule, the other unpaired electron and the electron's own orbital angular momentum. As discussed earlier, in organic molecules $\mu$ as a result of $L$ can be ignored by considering changes in terms of *g*-factor ($\mu \propto gS$). When considering the magnetic moment of a nuclei, it is typically three orders of magnitude smaller than that of an electron.[230] Therefore, only $\mu$ associated with the other electron in a triplet system will be considered in this discussion.

### 5.1.4.3 Zero-Field Splitting

For a triplet system, when considering the effect of $\mu$ of each electron on the other, it is helpful to consider the electrons as dipoles which experience dipole-dipole repulsive interactions due to their parallel alignment (*c.f.* bar magnets). The lowest energy state will be one of *maximum special separation* between the two electrons, thus the quantisation of spin states results from *molecular geometry* and not $B_0$.

**Figure 5.11** shows the energetic splitting of three idealised triplet systems as a function of molecular electronic distribution. In these scenarios, $T_{\mathrm{Z}}$ represents a triplet state where the spin axes of the two electrons are confined to the $\mathrm{XY}$ plane and the component of $S$ in the $\mathrm{Z}$ plane equals zero. Likewise, $T_{\mathrm{Y}}$ represents the two electrons in the $\mathrm{XZ}$ plane with a zero component in the $\mathrm{Y}$ plane, and $T_{\mathrm{X}}$ a zero component in the $\mathrm{X}$ plane and spin axes in the $\mathrm{YZ}$ plane.

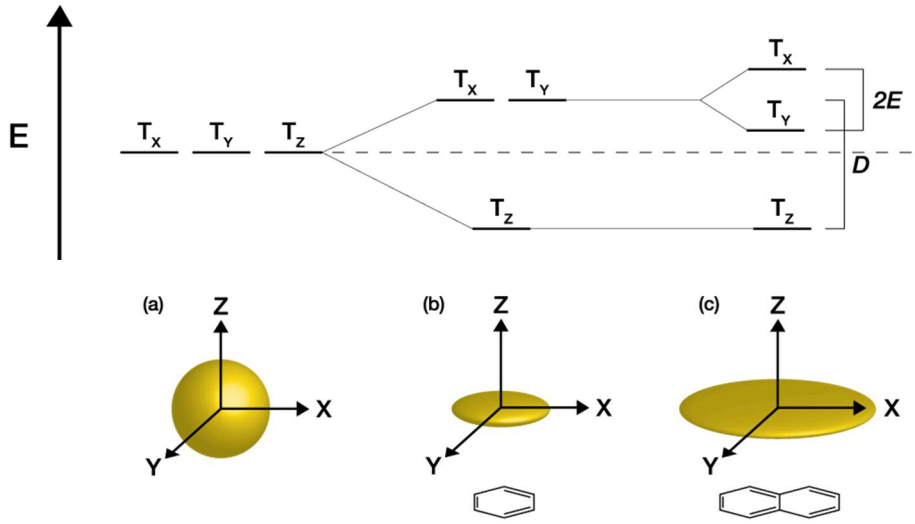


**Figure 5.11** Zero field splitting of three idealised triplet systems as a function of electronic distribution: a) spherical; b) benzene; c) naphthalene

The electronic distribution in Figure 5.11 (a) is spherical, and so there is no direction in which the two electrons can move to minimise their dipole-dipole repulsive interactions and thus all three triplet states are degenerate. In (b), the spin distribution for benzene is compressed in the $\mathrm{Z}$ plane, creating an *oblate* electronic distribution, where the electrons experience more repulsive forces if aligned in either the $\mathrm{XZ}$ or $\mathrm{YZ}$ planes because they will be spatially closer together. The electrons have considerable more freedom of movement in the $\mathrm{XY}$ plane, and therefore the energy of the $T_{\mathrm{Z}}$ level is lower than both the $T_{\mathrm{X}}$ and $T_{\mathrm{Y}}$ levels, which are degenerate. Extension of the aromatic system to naphthalene (c), results in the elongation of the $\mathrm{X}$ plane. The case is similar for

benzene, however the electrons now have more freedom to spatial separate in the $\mathrm{X}$ plane, and therefore the $T_{\mathrm{Y}}$ level $(\mathrm{XZ})$ is lower in energy than the $T_{\mathrm{X}}$ level.

This quantisation of spin states takes place without an applied magnetic field solely due to the degree of the symmetry (anisotropy) of the electronic distribution, and thus is known as $zero\ field\ splitting$ (ZFS) and gives rise to two ZFS parameters, $D$ and $E$.

$D$ is defined as the energy between the lowest energy state and the higher energy degenerate states, as in case (b), or between the lowest energy state and the average of the two higher energy states, as in case (c). $E$ is defined as half the energy between the two highest energy states. The parameters of $D$ and $E$ offer insight into the geometry of the electronic distribution of a system.

#### 5.1.4.4 The EPR Experiment

When a magnetic field is applied, it must be aligned with the molecular geometry of the sample. For example, if $B_0$ is aligned with the molecular Z–axis $(B_{0,\mathrm{Z}}\ or\ H_{\mathrm{Z}})$ the electrons in the $\mathrm{XY}$ plane will remain the same energy, i.e. the $T_0$ state, since their spin vectors are perpendicular to $B_{0,\mathrm{Z}}$. Electrons whose spin vectors are in the $\mathrm{XZ}$ or $\mathrm{YZ}$ planes will be either stabilised or destabilised depending on whether their magnetic moments are aligned $(T_{-1})$ or unaligned $(T_{+1})$ with $B_0$ respectively.

In a spherical molecule of total symmetry, the $T_{\mathrm{X,Y,Z}}$ energy states are degenerate and experience no ZFS and so Zeeman splitting results in two transitions fulfilling $\Delta m_{\mathrm{S}} = \pm 1$ (**Figure 5.12**). Since these two transitions occur at the same field strength, only one EPR signal is detected. The spherical geometry will also result in identical spectra for the other two applied field orientations $(B_{0,\mathrm{X}}\ \&\ B_{0,\mathrm{Y}})$.

For systems of lower symmetry, such as oblate electronic distributions, the ZFS of energy levels leads to considerable energetic differences both at zero field and at high applied fields (**Figures 5.13** & **5.14**).

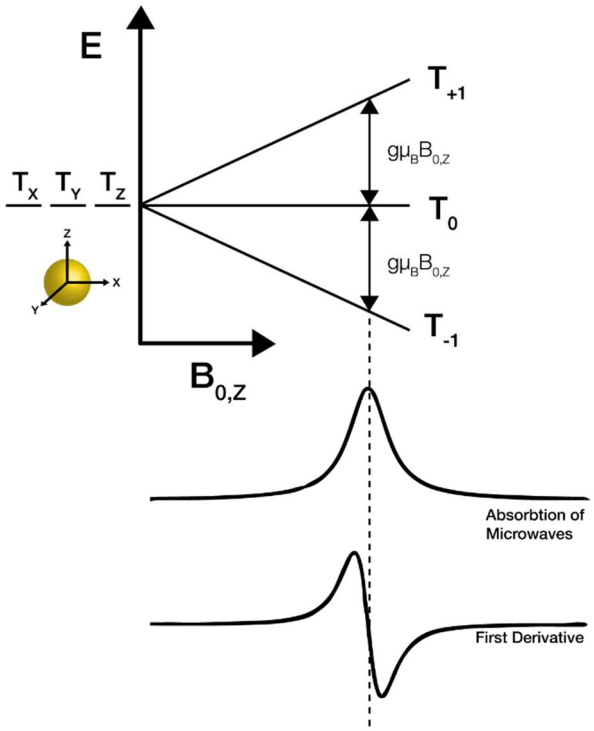


**Figure 5.12** Simulated EPR experiment on a triplet state on a molecule with spherical electronic distribution.

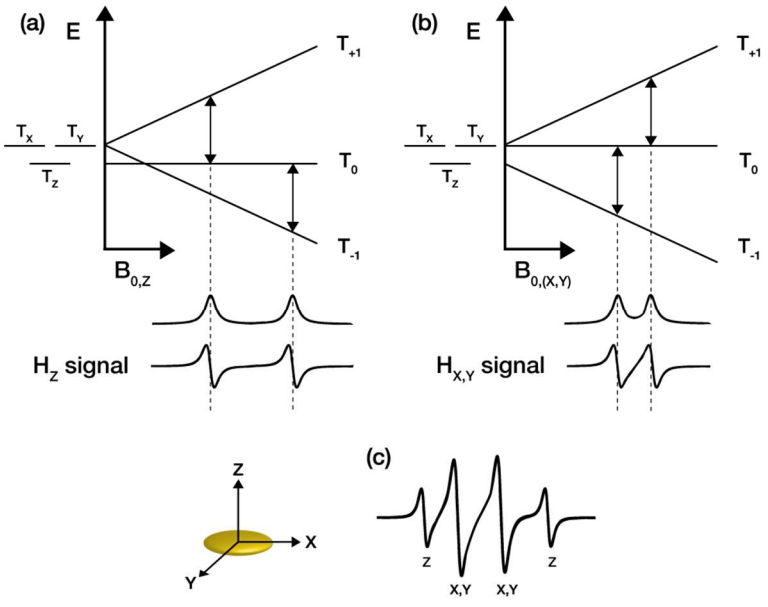


**Figure 5.13** Energy diagrams and simulated absorption/first derivative curves of an oblate triplet system pictured bottom left (e.g. benzene, $S = 1$). Applied magnetic field ($H_x$) aligned with the molecular (a) Z-axis; (b) X- or Y-axes. (c) Simulated EPR spectrum of combined absorbance.

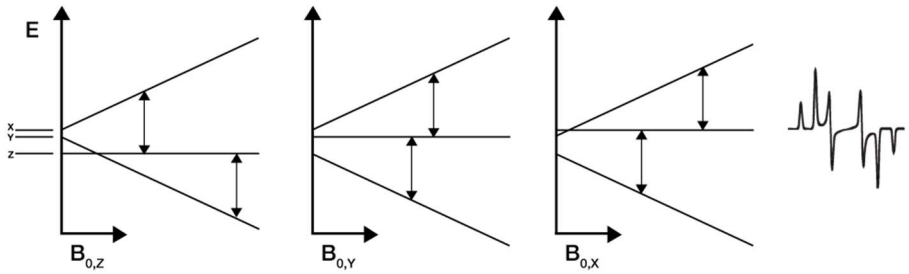


**Figure 5.14** Energy diagrams and simulated combined first derivative EPR spectrum of an elongated oblate triplet system (e.g. naphthalene, $S = 1$).

It is also important to remember that the molecular quantisation at zero field represented by the zero field eigenfunctions $T_{\mathrm{X}},\ T_{\mathrm{Y}},\ T_{\mathrm{Z}}$ are not the same as the eigenfunctions at high applied fields cause by Zeeman splitting, $T_{-1},\ T_0,\ T_{+1}$. A discussion into the mathematical and physical definitions of these eigenfunctions and the energetic properties linking them is beyond the scope of this thesis. However, the above discussion can be concluded by summarising that EPR can be used as a tool for investigating triplet excitations in organic materials, and the spectra obtained from EPR experiments gives direct information into the energetics and populations of triplet states in organic molecules and information on the orientation and size of the triplet excitation relative to the sample.

### 5.1.5 Transient Absorption Spectroscopy

Ultrafast transient absorption spectroscopy (TAS) is a non-linear extension of typical absorption spectroscopy and measures changes in the absorbance/transmittance of a sample over time. In a typical TAS experiment, a sample is irradiated with light generated by a laser at a specified wavelength or over the whole UV-vis spectrum – this is termed the $pump$ pulse. After a delay, the sample is irradiated with another pulse of light, termed the $probe$ pulse. The impact of the probe on the sample is recorded and analysed against time to study the dynamics of the excited state such as

$$\Delta A = A_{probe} - A_{pump}$$

where $\Delta A$ is the change in absorbance, $A_{probe}$ is the absorbance after the probe pulse and $A_{pump}$ is the absorbance after the pump pulse. Typical changes in absorbance of excited samples are: ground state bleaching $(-\Delta A)$ where the ground state is depleted to excited states, i.e. $\mathrm{S}_0 \rightarrow \mathrm{S}_n$; stimulated emission $(-\Delta A)$ at lower energy / higher wavelengths; and sample absorption $(+\Delta A)$ where excited states are further excited. The latter is extremely useful as it allows the probing of non-emissive states.

Whilst TAS used to probe sample dynamics over all wavelengths as a function of time provides information on the evolution/decay of transient species, a transient absorption curve over time as a function of wavelength provides information regarding the number of decay processes occurring at a specific wavelength and the timescale of such processes. At the time of writing this thesis, transient absorption experiments were being carried out on selected materials, but results were too preliminary to discuss in detail. To this effect, only EPR experiments will be discussed in this chapter.

### 5.1.6 Singlet Fission in Organic Materials

Only a very few organic materials have been suggested to undergo singlet fission (**Figure 5.15**). Of these, there exists fewer cases of comprehensive evidence confirming SF. The most researched and thus best cases of SF lay in the linear [n]acenes, notably tetracene **5.2** $(n = 4)$ and pentacene **5.3** $(n = 5)$, which undergo efficient SF with high QEs up to 200%.[173,228,231–240] However linear acenes where $n > 2$ have poor chemical stability and decompose quickly in air, requiring handling in gloveboxes, limiting their practicality. The stability of acenes can be somewhat improved by the addition of (triisopropylsilyl)acetylene groups (typically referred to purely as “TIPS” for ease) at the sites of chemical reactivity with minimal impact on SF, however TIPS-acenes still degrade in under a week in an aerobic environment.

Other organic frameworks which have been suggested to undergo SF are polycyclic aromatic hydrocarbons (PAHs), such as rubrene **5.10** & pyrene **5.6**, benzofurans **5.7**, terpenoids **5.11** and molecules with open-shell character, e.g. **5.15** & **5.16**.[241–246]

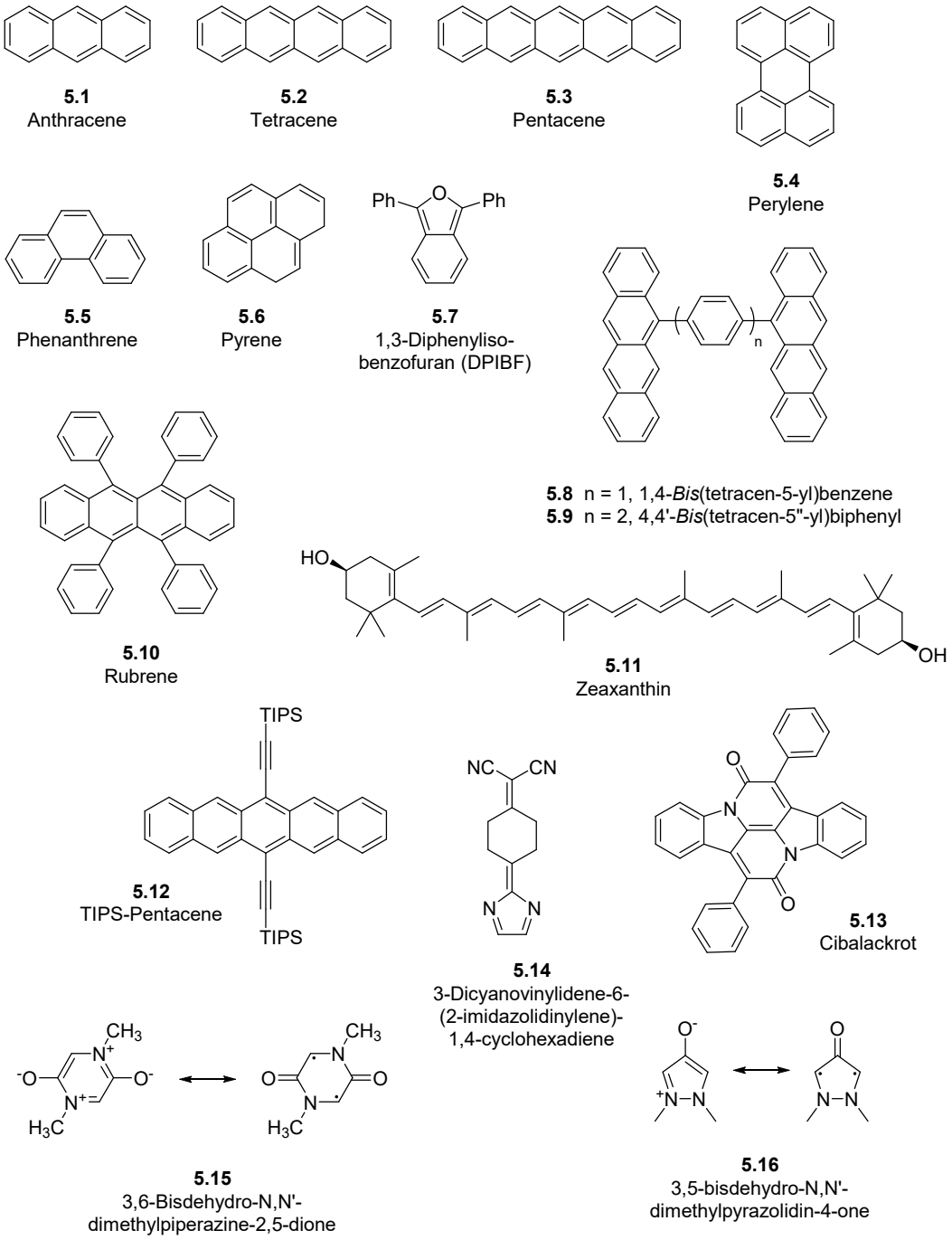


**Figure 5.15** Organic molecules highlighted in the literature to undergo singlet fission

### 5.1.6.1 Clar's Sextets Rule

The rationale behind the stabilisation of the triplet energies of the compounds in Figure 5.15 varies. The low energy triplet states of PAHs can be explained through Clar's sextets, whereby the lowest energy electronic structure contains the most π-sextet aromatic rings.[247,248] In a Clar structure, a sextet is denoted by a circle, and since each sextet comprises two Kekulé valence structures of a benzene ring, there are $2^n$ corresponding Kekulé structures in a Clar structure with $n$ sextets. Therefore, for a given

PAH, the Clar structure with the greatest number of sextets best represents the chemical and physical properties of the structure.

For example, **Figure 5.16** shows two tribenzoperylene isomers. In **5.18**, five sextets can be drawn, whilst only four sextets can be drawn for **5.17** resulting in three "exposed" alkene bonds. Experimentally, **5.18** is very stable, whilst **5.17** readily undergo Diels-Alder cycloadditions.[249]

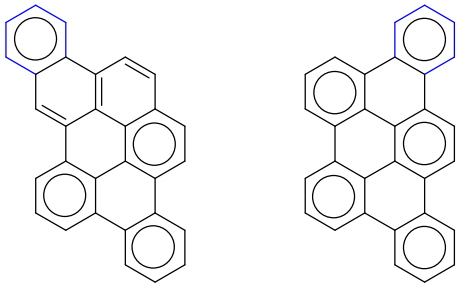


**Figure 5.16** Clar structures of two tribenzoperylene isomers

The case is slightly different for linear acenes, which exhibit migrating sextets. For example, in naphthalene (**Figure 5.17i**), the sextet can be drawn in the left or right-hand benzene ring. As there is only one sextet in naphthalene, but it can occupy either ring, it is drawn with an arrow, showing the migration of the sextet along the system.

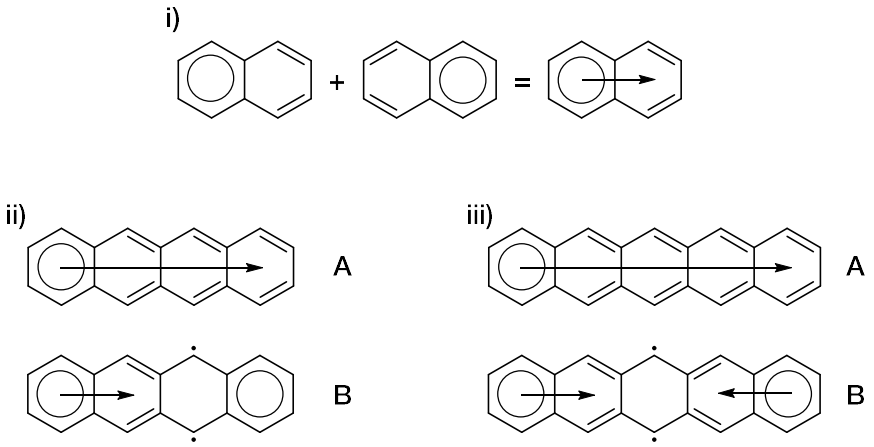


**Figure 5.17** Clar's sextets in (i) naphthalene, (ii) tetracene, (iii) pentacene

Through this premise, the addition of rings to create higher order linear acenes results in structures which all only have one sextet that migrates throughout the system (Figure 5.17, iiA/iiiA). As such, a migrating sextet is destabilising, as the total local aromaticity of any given ring is a superposition of all Clar structures, thereby leading to higher chemical reactivity. Pentacene $(n = 5)$ is incredibly reactive and dimerises readily and must be stored in the dark under inert conditions.

The greater degrees of chemical reactivity in high order linear acenes can also be explained by the alternate Clar structure shown in Figure 5.17 iiB/iiiB, where two sextets can be accomplished if the acenes are considered open shell. Whilst it must be noted that Clar's rules apply to closed shell systems only, this structure is important to discuss, as it shows that through Clar's rules, the energy of the triplet states of acenes are lowered to the point where open shell character arises. Theoretical calculations have suggested that this ground state diradical character exists to the extent that the ground state of acenes $n > 6$ have greatest stability as open-shell.[250] It is of no surprise that energetically-stable open-shell systems have extremely low triplet energies and high ground state diradical character, at the cost of poor chemical stability.[251]

A variety of SF-capable materials with a rationale including high chemical stability is greatly needed for the field to progress further.

### 5.1.7 Aromaticity in the Excited State

Aromatic stabilisation, one of the fundamental concepts of organic chemistry, was first proposed by Erich Hückel in 1931 to explain why some organic molecules exhibited greater stability than theoretically predicted.[252–254] The central principle of aromatic character arises when $[4n + 2]$ $\pi$-electrons are delocalised in an "electron cloud" of out-of-plane $\mathrm{p_z}$ orbitals, a theory which is now commonly known as $Hückel's\ Rule$. The rule can only be applied to planar and cyclic systems and every atom in the ring must participate in the delocalisation of electrons by either having a p-orbital or and unshared pair of electrons.

There are notable examples which disobey Hückel's rule by having $4n$ electrons but display aromatic stability, such as pyrene $(16\ e^-)$ and coronene $(24\ e^-)$, both of which are polycyclic aromatic hydrocarbons (PAHs) and it should be noted that Huckel's rules can only be theoretically justified to monocyclic ring systems.[255]

### 5.1.7.1 Baird's Rule

A much lesser known analysis of aromaticity was published by Colin Baird in 1972.[256] Baird proposed that a $[4n+2]$ $\pi$-electron aromatic system is in fact antiaromatic in its lowest triplet state and that, whilst a $[4n]$ $\pi$-electron system is Hückel antiaromatic in its lowest ground state, a $[4n]$ $\pi$-electron system will exhibit aromatic properties in its lowest triplet state. The theory can be explained by considering the fusion of monoradical fragments of $[4n]$ cyclobutadiene and $[4n+2]$ benzene (**Figure 5.18**). Firstly, both triplet cyclobutadiene and triplet benzene are fragmented into two odd-carbon monoradicals. The symmetry of these fragments is then considered with respect to a vertical mirror plane and assigned $symmetric$ or $antisymmetric$.

The fragments can then undergo two types of interactions: radical-radical (Type 1) and radical-$\pi$ (Type 2). For all interactions only orbitals of matching symmetry are noteworthy, as interactions between opposite symmetries leads to $\Delta \mathrm{E} = 0$. Baird showed using perturbation theory that the interaction of two radicals (Type 1) leads to a destabilising interaction due to the population of a $\sigma^*$ MO, which is more destabilised versus the formed $\sigma$ MO. However, the interaction of a radical with a $\pi$-system (Type 2) leads to a stabilising interaction.

For a $4n$ system, triplet cyclobutadiene cannot undergo a Type 1 interaction due to opposing symmetries $(\Delta \mathrm{E}_1 = 0)$ but forms stabilising interactions with the bonding and anti-bonding orbitals of the allyl fragment $(\Delta \mathrm{E}_2 > 0)$. Hence the total change in energy is positive $(\Delta \mathrm{E}_1 + \Delta \mathrm{E}_2 > 0)$ thus giving stabilisation upon the formation of triplet cyclobutadiene over its polyenyl monoradicals. As such, triplet cyclobutadiene $[4n]$ can be seen as having an $\boldsymbol{aromatic}$ $triplet\ state$.

For a $[4n+2]$ system, reverse characteristics are predicted; The radicals occupying non-bonding orbitals of antisymmetric symmetry can interact – a destabilising interaction $(\Delta \mathrm{E}_1 < 0)$. Furthermore, the two allyl fragments cannot exhibit any radical-pi interactions due to opposing symmetries $(\Delta \mathrm{E}_2 = 0)$. Hence the total change in energy is negative $(\Delta \mathrm{E}_1 + \Delta \mathrm{E}_2 < 0)$ thus is destabilised upon of the formation of triplet benzene from its two polyenyl monoradicals. As such, triplet benzene $[4n+2]$ can be seen as having an $\boldsymbol{antiaromatic}$ $triplet\ state$.

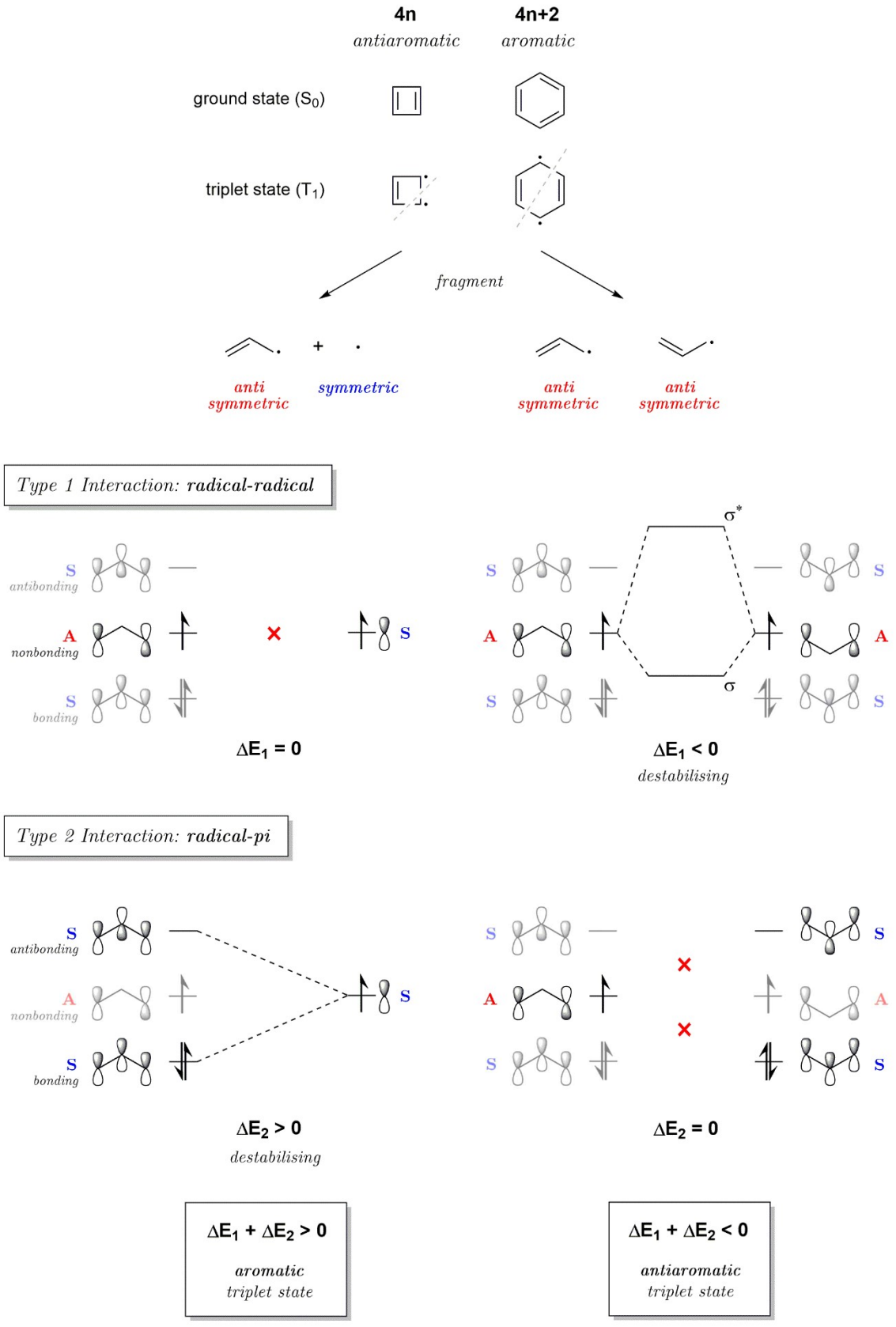


**Figure 5.18** Excited state aromaticity: fusion of odd-carbon polyenyl monoradical fragments of triplet cyclobutadiene and triplet benzene labelled symmetric (S) or antisymmetric (A) with respect to a vertical mirror plane. Two interactions are possible: radical-radical and radical-$\pi$. For a $4n$ system, $\Delta E_1 + \Delta E_2 > 0 \therefore$ ***aromatic*** *triplet state* whereas for a [$4n$+2] system $\Delta E_1 + \Delta E_2 < 0 \therefore$ ***antiaromatic*** *triplet state*

This concept of excited state aromaticity for cyclic organic molecules with a $4n$ component presents the possibility of energetically stabilised triplet states without compromising chemical stability. Ottosson *et al.* used the concept to shown how fulvenes can act as “aromatic chameleons” based on their chemical functionalisation (**Figure 5.19**).[257] The functionalisation of **5.19** with electron donating groups (e.g. methoxy) leads to a stabilisation of a positive charge if the bridging alkene bond is split into charges. This gives rise to a 5-membered ring with 6 electrons, so fulfils the criteria for $[4n + 2]$ ground state aromatic character and triplet state antiaromaticity.

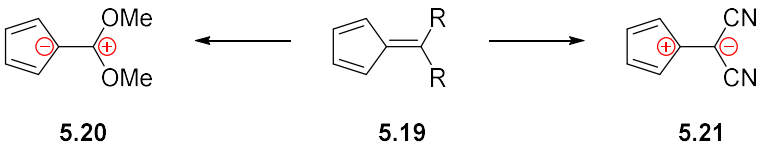


**5.20** **5.19** **5.21**

**Figure 5.19** Fulvenes as aromatic chameleons depending on the electronic nature of the R groups when polarising the bridging alkene bond

In contrast, electron withdrawing groups (e.g. carbonitrile) in **5.21** can stabilise a negative charge giving rise to a 5-membered ring with 4 electrons, thus fulfilling the criteria for $4n$ ground state antiaromatic character, however exhibits Baird triplet state aromatic stabilisation.

### 5.1.8 Aims of this Chapter

In a 2013 paper by Michl *et al.*,[258] cibalackrot **5.13** was suggested to undergo SF in an unpublished study by A. Akdag *et al.*, which to date remains unpublished. Apart from this one publication, there are no other literature reports of cibalackrot in relation to SF.

Time-dependant DFT analysis of **5.13** at the B3LYP/6-311G** level of theory revealed a $\mathrm{S}_1$ energy of 2.28 eV and a $\mathrm{T}_1$ energy of 1.17 eV, giving a $\mathrm{T}_1/\mathrm{S}_1 = \mathrm{T{:}S} = 0.51$. Whilst this does not satisfy the electronic requirement of SF $(\mathrm{T{:}S} < 0.5)$, these calculations demonstrated that the energy of the triplet state of **5.13** was indeed very low.

This stabilised $\mathrm{T}_1$ state cannot be explained using Clar's rules, but analysis of the resonance structures of **5.13** reveals a $4n$ ring contribution (**Figure 5.20**, blue) and so indolonaphthyridines may inherit their stabilised triplet states through Baird-type triplet state aromaticity.

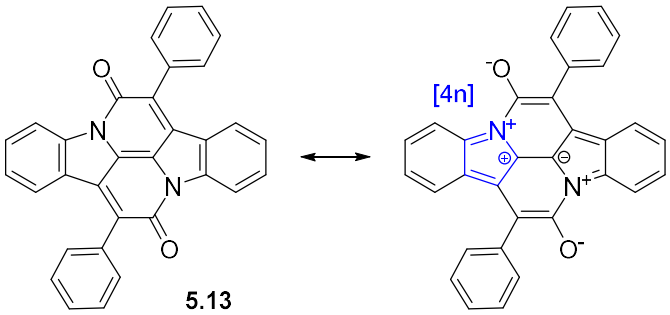


**Figure 5.20** Resonance and delocalisation showing $4n$ contribution to **5.13**

The aim of this chapter is to deduce structure-property relationships for the design of molecules based on **5.13** which satisfy $\mathrm{T{:}S} < 0.5$ and undergo singlet fission. Where evidence of SF was observed, the theoretical triplet state aromaticity was calculated to assess whether Baird-type stabilisation was occurring in such molecules.

Furthermore, the calculated energy of the $\mathrm{T}_1$ state for **5.13** is ~1.2 eV which, as was laid out by the SQ model, is an idyllic excitation energy for PV applications. In an ideal scenario, $\mathrm{T{:}S}$ would be lowered at no expense to this triplet energy, i.e. by increasing the energy of the $\mathrm{S}_1$ state only. As such, an extended aim of this work was to investigate wide band gap materials with good $\mathrm{T{:}S}$ but with triplet energies of practical use.

## 5.2 Indolonaphthyridine Benzene

### 5.2.1 Initial Work

The initial steps of this work began with the synthesis of a series of indolonaphthyridine benzene (INDB) compounds from commercially available functionalised phenylacetyl chlorides and indigo dye (**Scheme 5.1**).

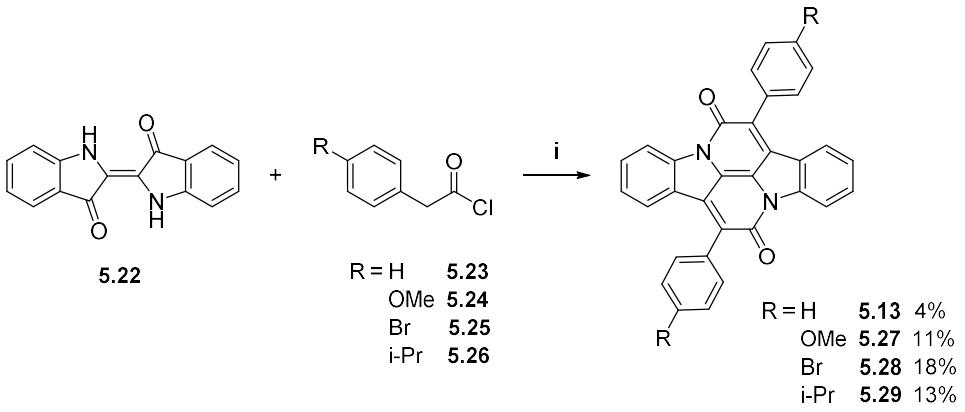


**Scheme 5.1** Synthesis of functionalised INDB compounds
(i) Xylenes, 165 ℃, 12 h

All four materials were very insoluble, especially the Br-containing INDB **5.28**. The methoxy **5.27** and isopropyl **5.29** compounds exhibited greater solubility but solution aggregation remained an issue, even in dilute solution. **Figure 5.21** shows the solution UV-vis absorption spectra of the four materials.

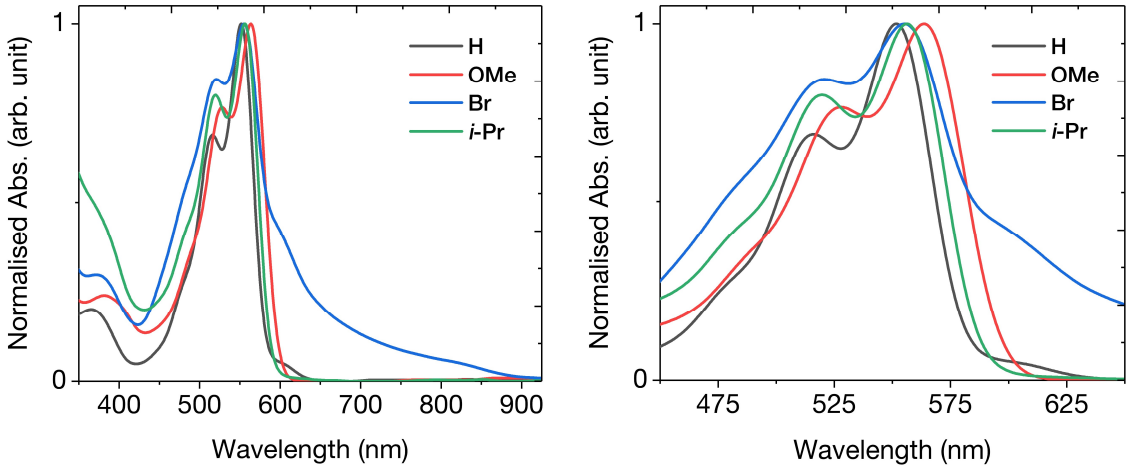


**Figure 5.21** Solution UV-vis absorption spectra of *para*-substituted INDB compounds in chlorobenzene (zoomed in area around $\lambda_{max}$ shown on right)

Interestingly, all three functionalised materials exhibited bathochromic shifts in their absorptions relative to cibalackrot, indicating a slight narrowing of the optical band gaps. $E_g$ was estimated for each compound from the onset of the respective absorption to be 2.13 eV for cibalackrot **5.13**, 2.11 eV for $^{i}$Pr-INDB (**5.29**) and 2.07 eV for OMe-INDB

(**5.27**). It was difficult to estimate the optical gap for the Br-INDB (**5.28**) whose absorption was considerably broader than the other two functionalised INDBs, attributed to strong aggregation of the material in solution. Interestingly, **Br-INDB** exhibited a similar $\lambda_{max}$ as the ***i*Pr-INDB** (**5.29**) of 556 nm, whilst the methoxy INDB **5.27** showed a considerable red-shift in its absorption profile and a $\lambda_{max}$ of 563 nm.

A design rule could be generated from these compounds: functionalisation of the *peripheral* benzene rings at their 4–position results in a narrowing of the optical band gap, which is most notable with electron donating groups.

Transient absorption spectroscopy was carried out on all three functionalised compounds and no evidence of SF was observed.

### 5.2.2 Theoretical Analysis

It was quickly realised that a more strategic approach was needed and so quantum chemical calculations were carried out on cibalackrot with functionalisation in three places: **A**, on the 4-position of the non-indigoid benzene ring; **B**, on the 6**–**position of the indigo ring; **C**, on the 5**–**position of the indigo ring (**Table 5.1**).

**Table 5.1** Time-dependant DFT calculations on cibalackrot **5.13** at the B3LYP/6-31G* level of theory

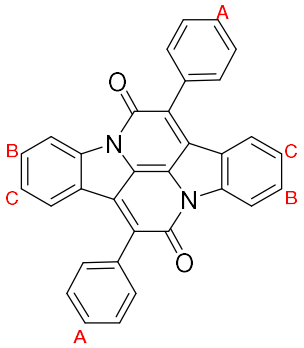


| N° | A | B | C | $S_0 \rightarrow S_1$ | $S_0 \rightarrow T_1$ | T:S |
|---|---|---|---|---|---|---|
| 5.1.01 | – | – | $NO_2$ | 2.1105 | 1.0021 | 0.475 |
| 5.1.02 | – | – | $CF_3$ | 2.2988 | 1.1024 | 0.480 |
| 5.1.03 | $OCH_3$ | – | $CF_3$ | 2.1648 | 1.0490 | 0.485 |
| 5.1.04 | – | $NO_2$ | – | 2.2654 | 1.0983 | 0.485 |
| 5.1.05 | – | $CF_3$ | – | 2.3245 | 1.1322 | 0.487 |
| 5.1.06 | – | – | F | 2.3283 | 1.1341 | 0.487 |

| N° | A | B | C | $S_0 \rightarrow S_1$ | $S_0 \rightarrow T_1$ | T:S |
|---|---|---|---|---|---|---|
| 5.1.07 | – | Br | – | 2.3251 | 1.1338 | 0.488 |
| 5.1.08 | – | F | F | 2.3574 | 1.1551 | 0.490 |
| 5.1.09 | $CH_3$ | F | F | 2.3230 | 1.1422 | 0.492 |
| 5.1.10 | – | – | Br | 2.3497 | 1.1590 | 0.493 |
| 5.1.11 | $OCH_3$ | F | F | 2.2278 | 1.1039 | 0.496 |
| 5.1.12 | $CH_3$ | $CH_3$ | H | 2.3298 | 1.1626 | 0.499 |
| 5.1.13 | $OCH_3$ | – | Br | 2.2323 | 1.1183 | 0.501 |
| 5.1.14 | iPr | – | – | 2.3423 | 1.1741 | 0.501 |
| 5.1.15 | iPr | $CH_3$ | – | 2.3195 | 1.1633 | 0.502 |
| 5.1.16 | $OCH_3$ | – | – | 2.2645 | 1.1375 | 0.502 |
| 5.1.17 | – | F | – | 2.4061 | 1.2107 | 0.503 |
| 5.1.18 | F | F | F | 2.3437 | 1.1815 | 0.504 |
| 5.1.19 | $NMe_2$ | $CH_3$ | – | 2.1818 | 1.1006 | 0.504 |
| 5.1.20 | $OCH_3$ | $CH_3$ | – | 2.2772 | 1.1495 | 0.505 |
| 5.1.21 | $OCH_3$ | – | $OCH_3$ | 2.2520 | 1.1426 | 0.507 |
| 5.1.22 | Br | – | – | 2.3376 | 1.1862 | 0.507 |
| 5.1.23 | $CF_3$ | $CH_3$ | – | 2.3392 | 1.1875 | 0.508 |
| 5.1.24 | $CH_3$ | – | $OCH_3$ | 2.3039 | 1.1697 | 0.508 |
| 5.1.25 | $CH_3$ | $OCH_3$ | – | 2.3577 | 1.1977 | 0.508 |
| 5.1.26 | iPr | – | $OCH_3$ | 2.2903 | 1.1641 | 0.508 |
| 5.1.27 | $NMe_2$ | – | $CH_3$ | 2.1831 | 1.1109 | 0.509 |
| 5.1.28 | iPr | $OCH_3$ | – | 2.3482 | 1.1975 | 0.510 |
| 5.1.29 | $OCH_3$ | $OCH_3$ | – | 2.2877 | 1.1697 | 0.511 |
| 5.1.30 | $CH_3$ | – | – | 2.2739 | 1.1644 | 0.512 |
| 5.1.31 | – | – | – | 2.2807 | 1.1706 | 0.513 |
| 5.1.32 | $NMe_2$ | $OCH_3$ | – | 2.2025 | 1.1324 | 0.514 |

| Nº | A | B | C | $S_0 \rightarrow S_1$ | $S_0 \rightarrow T_1$ | T: S |
|---|---|---|---|---|---|---|
| 5.1.33 | $CF_3$ | $OCH_3$ | – | 2.3734 | 1.2265 | 0.517 |
| 5.1.34 | $CF_3$ | – | $OCH_3$ | 2.2825 | 1.1854 | 0.519 |
| 5.1.35 | iPr | – | Br | 2.2038 | 1.1447 | 0.519 |
| 5.1.36 | – | $NMe_2$ | – | 2.2298 | 1.1612 | 0.521 |
| 5.1.37 | – | $CH_3$ | – | 2.2248 | 1.1715 | 0.527 |
| 5.1.38 | $NO_2$ | $CH_3$ | – | 2.2341 | 1.1769 | 0.527 |
| 5.1.39 | $CH_3$ | – | $CH_3$ | 2.4171 | 1.2745 | 0.527 |
| 5.1.40 | iPr | – | $CH_3$ | 2.4014 | 1.2688 | 0.528 |
| 5.1.41 | $OCH_3$ | – | $CH_3$ | 2.3441 | 1.2416 | 0.530 |
| 5.1.42 | $NMe_2$ | – | $OCH_3$ | 2.2620 | 1.2075 | 0.534 |
| 5.1.43 | $NO_2$ | $OCH_3$ | – | 2.2675 | 1.2165 | 0.536 |
| 5.1.44 | $CF_3$ | – | $CH_3$ | 2.4249 | 1.3020 | 0.537 |
| 5.1.45 | – | – | $NMe_2$ | 2.4736 | 1.3335 | 0.539 |
| 5.1.46 | $NO_2$ | – | $OCH_3$ | 2.1637 | 1.1707 | 0.541 |
| 5.1.47 | – | – | $CH_3$ | 2.2389 | 1.2115 | 0.541 |
| 5.1.48 | – | $OCH_3$ | – | 2.1783 | 1.1795 | 0.541 |
| 5.1.49 | $NO_2$ | – | $CH_3$ | 2.3044 | 1.2927 | 0.561 |
| 5.1.50 | – | – | $OCH_3$ | 2.1526 | 1.2888 | 0.599 |

Dashed line (–) represents proton, synthesised compounds highlighted

Of the 50 structures analysed, only 12 showed $\mathrm{T{:}\,S} < 0.5$, which did not include any of the four initially synthesised compounds. The twelve compounds all constituted functionalisation of the indigoid benzene rings with halogens and strong electron withdrawing groups, such as nitro or trifluoromethyl. At the other end of the spectrum, the structures exhibiting the largest $\mathrm{T{:}\,S}$ featured functionalisation of the indigo benzene rings with electron donating groups.

Interestingly, the 6–position of the indigo ring seemed to have the strongest effect on $\mathrm{T{:}\,S}$. For structure 5.1.17, where the only modification to cibalackrot is the addition of F

atoms at the 5,5'–positions, $\mathrm{T{:}S}$ was calculated to be 0.503, whereas for compound 5.1.06, where an identical modification was made but to the 6,6'–positions, $\mathrm{T{:}S}$ was calculated to be 0.487. **Figure 5.22** shows scatter plots of $\mathrm{S_1/T_1}$, $\mathrm{(T{:}S)/T_1}$ and $\mathrm{(T{:}S)/S_1}$. Due to the small size of the data set, it was difficult to perform rigorous statistical analysis of the data, but there did not seem to exist a noteworthy degree of trend in any of the data.

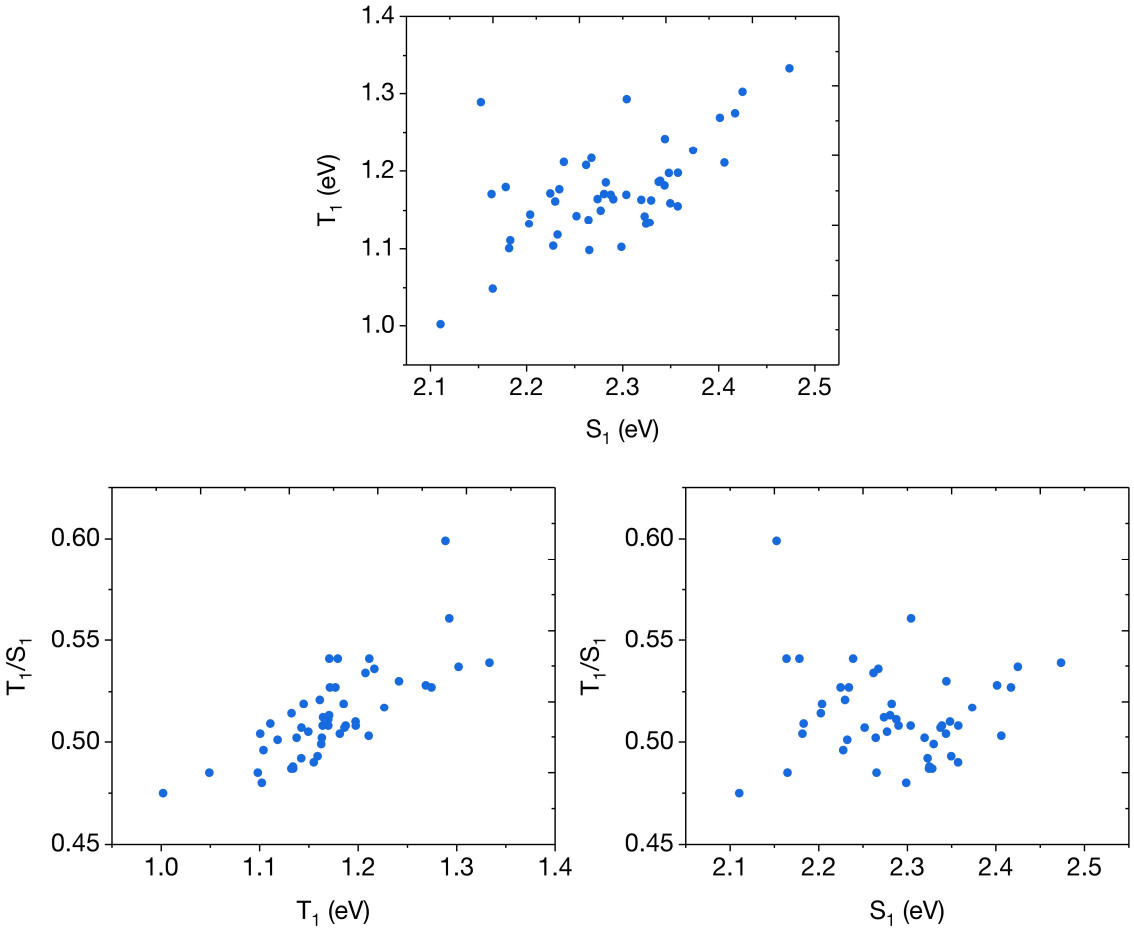


**Figure 5.22** Statistical distributions of theoretical analysis in Table 5.1

## 5.2.3 Targeted Design

From the initial four compounds, it was clear that a higher degree of solubility was necessary to ensure good quality thin-film forming character and to prevent aggregation. From the analysis of the quantum calculations, compound 5.1.03 where cibalackrot contained alkoxy chains in the 4–position of the *peripheral* benzene rings and the *indigoid* rings were functionalised with trifluoromethyl groups at the 6,6'–positions, exhibited a $\mathrm{T{:}S}$ of 0.485, a good value which provided room for a degree of error in the calculation. The theoretical optical band gap of this compound was narrower than cibalackrot, however the synthesis of a wide band gap SF material was an extended aim

of this project and synthesising any indolonaphthyridine which underwent SF was the first and most important aim.

Usefully, 2-nitro-4-(trifluoromethyl)benzaldehyde **5.30** was commercially available and underwent a Baeyer–Drewson indigo condensation in typical yield (**Scheme 5.2**) to give the trifluoromethyl indigoid **5.31**. This indigoid exhibited excellent solubility in chloroform at RT, in stark contrast to typical indigoids, which exhibit extremely poor solubility.

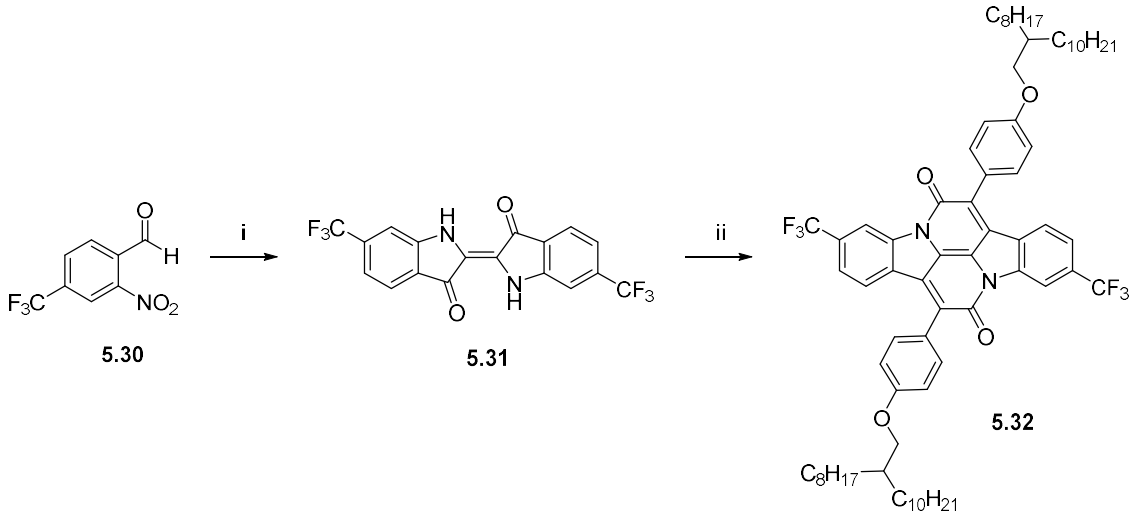


**Scheme 5.2** Synthesis of trifluoromethyl indolonaphthyridine benzene **5.31**
(i) Acetone, NaOH, 53%; (ii) **2.11**, xylenes, 165 °C, 12 h, 1.4%;

In deciding which alkyl chain to use, there remains debate in the literature about how important crystallinity is for SF. An ideal SF material would undergo efficient SF as an amorphous solid to enable scalable solution processing, whereas a crystalline requirement causes the same manufacturing issues as crystalline silicon OPV generation.[259] The highest quality thin-films of indolonaphthyridine materials achieved during this thesis employed 2-octyldodecanyl chains. To this effect, 2-octyldodecanyl chains were chosen for these materials to ensure high quality thin-film formation.

The synthesis of 2-octyldodecanylphenylacetyl chloride was outlined in Chapter 2 (compound **2.11**), which underwent the condensation-annulation reaction with indigo **5.31** to give the desired **$CF_3$-INDB** (**5.32**), which exhibited extremely high solubility and formed high quality thin-films.

**Figure 5.23** shows the solution and thin-film UV-vis absorbance spectra of **5.32**. As predicted, **5.32** exhibited a narrower band gap as indicated by the bathochromic shift in absorption. From the onset of the solution spectra, the optical band gap was estimated to be 2.03 eV. Gratifyingly, the solution absorption profile was narrow and showed similar in features to the solution absorbance of cibalackrot. Interestingly, the thin-film absorbance bandwidth was considerably broader, and exhibited significant broadness

around the onset, possibly indicating that the material was aggregating strongly in the solid-state. This was potentially beneficial, as it suggested there was strong electronic coupling between molecules in the film, an important requirement for efficient SF.

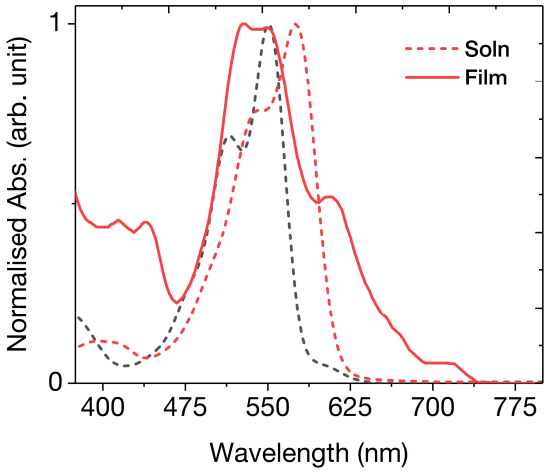


**Figure 5.23** UV-vis absorbance spectra of **5.32** in solution (red dashed line) and thin-film (red solid line) and cibalackrot (solution, black dashed line)

### 5.2.4 Using EPR to Examine Triplet States

To recap the experiment outlined at the end of section 5.1.3, two samples of **5.32** were prepared: (1) a 100 μM solution in degassed toluene; (2) a thin-film prepared on quartz slide from a saturated solution of **5.32** in chloroform, to ensure thick film formation. Both samples were placed in quartz EPR tubes and sealed under high vacuum $(10^{-5}\ \mathrm{mmHg})$. In the EPR experiment, the solution sample was frozen (50 K) and at such a low concentration any observed EPR signal would arise due to triplet formation as a product of intersystem crossing. In an analogous experiment on the thin-film sample, the intermolecular distances are vastly reduced permitting triplet formation via SF, which is typically kinetically faster than ISC.

Crucially, the spectral line shape of an EPR signal is dictated by a molecule's triplet sub-level populations, as the intensity of each transition is proportional to the relevant population difference. Since the population of triplet sub-levels depends strongly on the mechanism responsible for the creation of the triplet, a triplet formed via SF should have a different line shape to a triplet formed via ISC. The extent of the difference is difficult to predict and depends of several factors, however differences in spectral line shape between the two samples gives strong evidence that SF could be occurring in the sample. This is a simplified way of considering complex EPR data, however provides enough evidence to discuss potential of SF candidates in this thesis. The EPR spectra of **5.32** are shown in **Figure 5.24**.

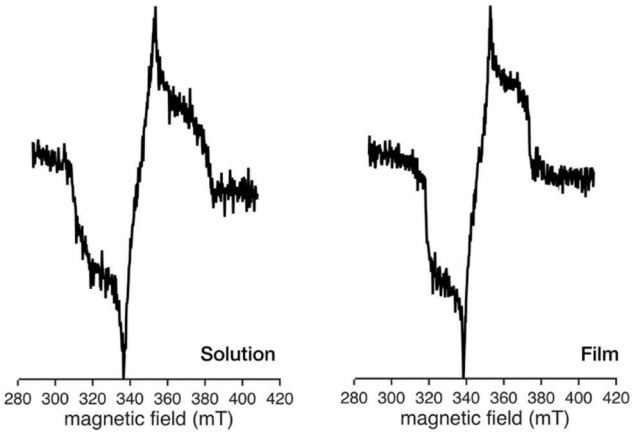


**Figure 5.24** EPR spectra of **5.32** in solution and thin-film

A signal was observed in both solution and thin-film, indicating that triplet formation was occurring in the material. However, the spectral line shape was highly comparable in both physical states, although the spectral width was reduced in thin-film. Unfortunately, this suggested that triplet formation was only as a result of ISC and not SF.

The fact that no evidence of SF was found in any of the five indolonaphthyridine benzene compounds synthesised, either the triplet energy levels of all INDB compounds do not fulfil the energetic requirement of $\mathrm{T{:}S} < 0.5$ or there was insufficient energetic coupling of the INDB molecules in thin-film, caused by either the large branched alkyl chains, or the large intermolecular packing distances resulting from the non-planar conformation of the molecule's peripheral benzene rings.

Several design rules were drawn as a result of the study on INDB. It was clear that the best method for lowering $\mathrm{T{:}S}$ was to introduce halogens or EWGs on the indigo benzene rings, notably at the 6–position. Furthermore, spectroscopic studies revealed $E_{\mathrm{g}}$ was least reduced by employing alkyl chains over alkoxy, which act as stronger EDGs. Lastly, due to lack of evidence of SF in INDB candidates, the system may benefit from greater planarity to enable stronger electronic coupling in solid state.

## 5.3 Indolonaphthyridine Thiophene

As a summative response to the above design rules, an analogous assessment of indolonaphthyridine thiophene (INDT) candidates using quantum chemical calculations was carried out, as shown in **Table 5.2**. The methyl groups at the thiophene 2-position represent solubilising alkyl chains.

**Table 5.2** Time-dependant DFT calculations on indolonaphthyridine thiophene SF candidates at the B3LYP/6-311G** level of theory

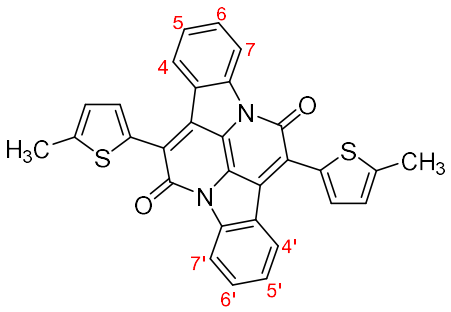


| Ref. | 4,4′ | 5,5′ | 6,6′ | 7,7′ | $S_0 \rightarrow S_1$ | $S_0 \rightarrow T_1$ | T: S |
|---|---|---|---|---|---|---|---|
| 5.2.01 | CN | – | – | – | 1.9283 | 0.8069 | 0.418 |
| 5.2.02 | – | – | CN | – | 1.9685 | 0.8540 | 0.434 |
| 5.2.03 | – | – | – | CN | 2.0351 | 0.8873 | 0.436 |
| 5.2.04 | – | – | $CF_3$ | – | 2.0293 | 0.8967 | 0.442 |
| 5.2.05 | – | – | $CO_2Me$ | – | 1.9938 | 0.8838 | 0.443 |
| 5.2.06 | – | CN | – | – | 2.0218 | 0.9002 | 0.445 |
| 5.2.07 | – | – | – | F | 2.0760 | 0.9275 | 0.447 |
| 5.2.08 | – | – | CN & Br | – | 2.0137 | 0.9046 | 0.449 |
| 5.2.09 | – | F | – | – | 2.0769 | 0.9405 | 0.453 |
| 5.2.10 | – | F | F | – | 2.0916 | 0.9592 | 0.459 |
| 5.2.11 | – | – | Br | – | 2.0824 | 0.9621 | 0.462 |
| 5.2.12 | – | – | Cl | – | 2.0867 | 0.9667 | 0.463 |
| 5.2.13 | F | – | – | – | 2.0846 | 0.9664 | 0.464 |
| 5.2.14 | – | – | – | – | 2.1150 | 0.9906 | 0.468 |
| 5.2.15 | – | – | F | – | 2.1307 | 1.0124 | 0.475 |
| 5.2.16 | – | – | $OCH_3$ | – | 2.1905 | 1.1053 | 0.505 |

Dashed line (–) represents proton

Interestingly, the values of $\mathrm{T}:\mathrm{S}$ in all INDT compounds were considerably lower than those of the screened INDB structures, with the unsubstituted INDT (**H-INDT**, 5.2.13) exhibiting a $\mathrm{T}:\mathrm{S}$ of 0.468. Indeed, all INDT compounds exhibited $\mathrm{T}:\mathrm{S} < 0.5$ except the electron rich methoxy species 5.2.16, asserting the trend that electron deficient IND cores have lower $\mathrm{T}:\mathrm{S}$, with the three compounds with lowest $\mathrm{T}:\mathrm{S}$ being carbonitrile-substituted IND cores at the 4–, 6– and 7–positions.

The energy of the $\mathrm{S}_1$ state was considerably reduced for all INDTs, which was somewhat expected due to the greater degree of planarity affecting improved $\pi$-delocalisation. The knock-on effect meant that the $\mathrm{T}_1$ energies were considerably reduced to 0.8 – 1.0 eV. However, the impressive $\mathrm{T}:\mathrm{S}$ exhibited by these materials meant that there was a high probability that experimental $\mathrm{T}:\mathrm{S}$ would be lower than 0.5 despite any bias provided by errors in the calculations.

It was also evident from the calculations that functionalising INDT compounds at the 6–position would provide a family of compounds with a wide range of $\mathrm{T}:\mathrm{S}$ and $E_\mathrm{g}$. Other 6–functionalised indigos had been synthesised previously in work detailed earlier in this chapter and in Chapter 4, so the synthetic challenge would also be reduced. As such, it was decided that a family of INDT compounds would be synthesised, functionalised at the 6,6'–positions with H, F, Cl, Br and CN. These five materials would provide a good family for investigating singlet fission in indolonaphthyridine thiophenes.

### 5.3.1 Synthesis

Firstly, 2-octyldodecanic acid **5.34** was prepared by the oxidation of 2-octyldodecanol **5.33** to the corresponding carboxylic acid using catalytic pyridinium chlorochromate and periodic acid as the terminal oxidant in high yield (**Scheme 5.3**). Subsequent chlorination with thionyl chloride provided the corresponding acyl chloride **5.35** in quantitative yield.

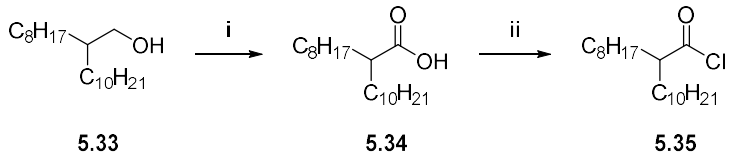


**5.33** **5.34** **5.35**

**Scheme 5.3** Synthesis of 2-octyldodecanoyl chloride **5.35**
(i) $\mathrm{H_5IO_6}$, cat. PCC, MeCN, 0 °C → RT, 12 h, 80%; (ii) $\mathrm{SOCl_2}$, cat. DMF, anhyd. DCM, $\Delta$, 3 h, quant

Next, 2-thiophenylacetic acid was protected as its methyl ester **5.37** in high yield. The reaction also serves to purify the commercially bought acid, which contained a relatively high proportion of impurity due to the tendency of simple thiophene compounds to degrade over time (**Scheme 5.4**). The methyl ester **5.37** and 2-octyldodecanoxyl chloride

**5.35** then underwent a Friedel-Crafts reaction in the presence of aluminium(III) chloride in high yield. The carbonyl group of the acylated thiophene **5.38** was then reduced selectively using triethylsilane in trifluoroacetic acid.

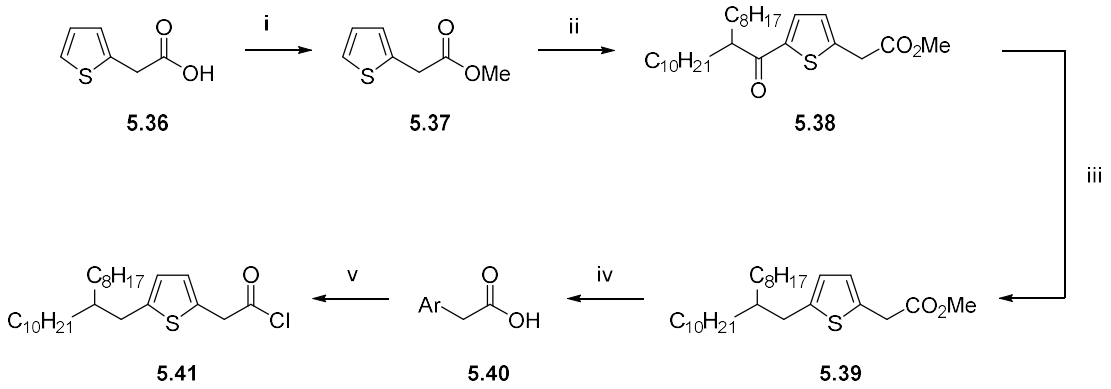


**Scheme 5.4** Synthesis of alkylated thiophenylacetyl chloride **5.41**
(i) MeOH, cat. $H_2SO_4$, Δ, 3 h, 92%; (ii) **5.35**, $AlCl_3$, anhyd. DCM, 0 °C → RT, 24 h 76%; (iii) $Et_3SiH$, TFA, 5 d, 93%; (iv) 4M NaOH, MeOH, 99%; (v) $SOCl_2$, cat. DMF, anhydr. DCM, Δ, 3 h, quant;

Whilst this reaction was high yielding, it required a large excess $Et_3SiH$ and silanyl impurities eluted with the desired thiophene compound during purification due to similar polarities, and so extremely careful column chromatography was required to remove all silanes. This purification was improved by firstly deprotecting the ester to form the acid **5.40** (in quantitative yield) which exhibited higher polarity than **5.39**, and so could be more easily separated from the silanyl impurities. Future iterations of this reaction could benefit from a Wolff–Kishner reduction of **5.38** as its carboxylic acid,[260] or via a Caglioti modified procedure of **5.38**,[261] however as large quantities of the alkylated thiphene are required, the use of large quantities of hydrazine is also non-ideal.

Conversion of the reduced thiophene **5.39** to the acid (**5.40**) and then the acyl chloride (**5.41**) both proceeded in quantitative yield. The total synthesis was very high yielding and could be scaled safely to large quantities, with the oxidation of 2-octyldodecanol and Friedel-Crafts reactions being the only two requiring cautious control of internal temperature.

The required 6,6'–functionalised indigoids were all prepared in good yields from their respective 4-functionalised-2-nitrotoluenes (**5.42**–**5.45**), via oxidation with *N*,*N*-dimethylformamide dimethyl acetal (**Scheme 5.5**).

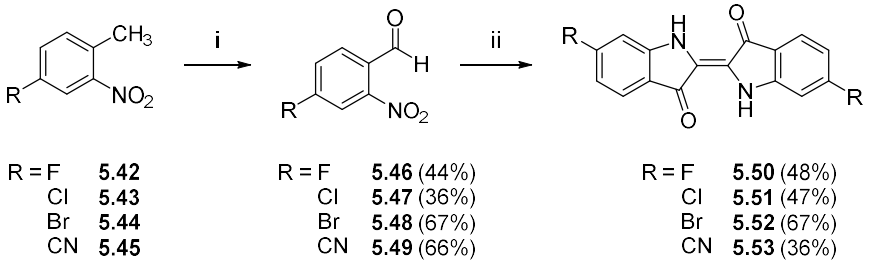


**Scheme 5.5** Synthesis of 6-functionalised indigoids **5.50**–**5.53**
(i) *N*,*N*-dimethylformamide dimethyl acetal, anhyd. DMF, 135 °C, 12 h; (ii) Acetone, $NaOH_{(aq)}$, 3 h, RT

The respective INDT compounds were then prepared by the condensation reactions of functionalised indigoids **5.42**–**5.45** with 2-octyldodecylthiophene acetyl chloride **5.41** (**Scheme 5.6**).

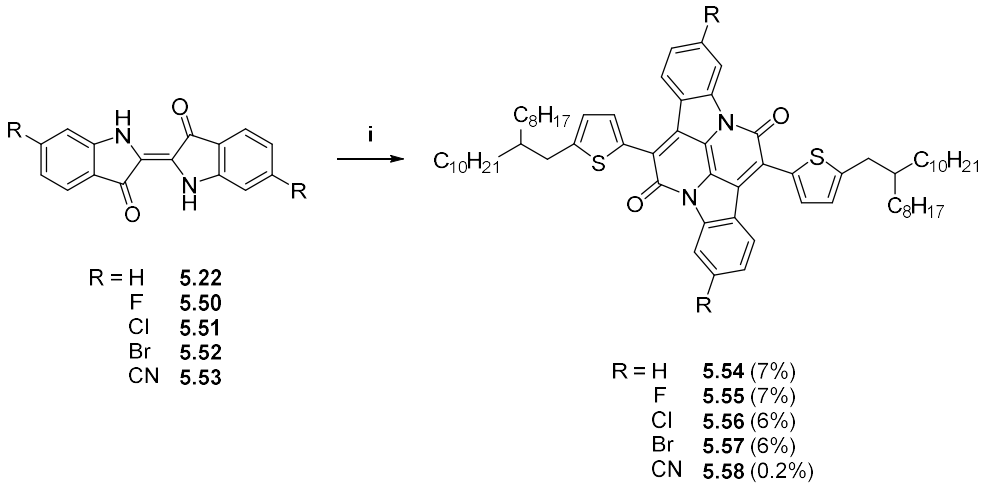


**Scheme 5.6** Condensation-annulation reactions to form 6,6'–functionalised INDTs
(i) **5.41**, xylenes, 165 °C, 12 h

For ease of discussion, INDT compounds **5.54**–**5.58** will be referred to hereon as ***x*-INDT** where *x* is the substituent at the 6,6'–positions. Very similar yields of 6-7% were obtained for unsubstituted indigo (**H-INDT**) and the three halogenated indigoids. However, the formation of **CN-INDT** was extremely poor (0.2%), attributed to the hydration of the carbonitrile groups in the acidic, high temperature reaction. **CN-INDT** was the most desirable material due to its lowest T:S and so a larger quantity of it was synthesised via a Rosenmund–von Braun cyanation of **Br-INDT** (**Scheme 5.7**).

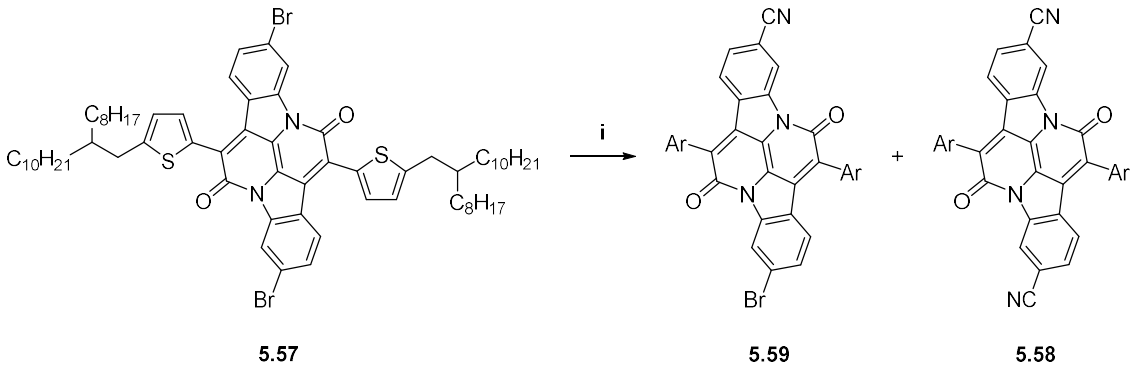


**Scheme 5.7** Synthesis of **CN-INDT** from **Br-INDT**
(i) Excess CuCN, DMF, 150 °C, 12 h; 29% **5.59**, 35% **5.58**

Despite the use of CuCN in large excess (~13 equiv.), the reaction gave a mixture of mono-nitrile and di-nitrile INDTs in 29% and 35% yield respectively, an effect which is common with this type of reaction.[262] This was potentially extremely interesting as the asymmetric **CN/Br-INDT** (**5.59**) offered the possibility of an intermediary electronic system between the dibromo and dinitrile INDTs. It also offered the possibility of future cross-coupling reactions to synthesise dimers. Nonetheless, it is likely that the reaction conditions (dilution, equiv. CuCN, time) could be optimised to provide a greater quantity of dinitrile INDT if required in the future. **Figure 5.25** shows the normalised UV-vis absorption spectra of the six INDT compounds in solution (chloroform) and thin-film (spun from solutions in chloroform).

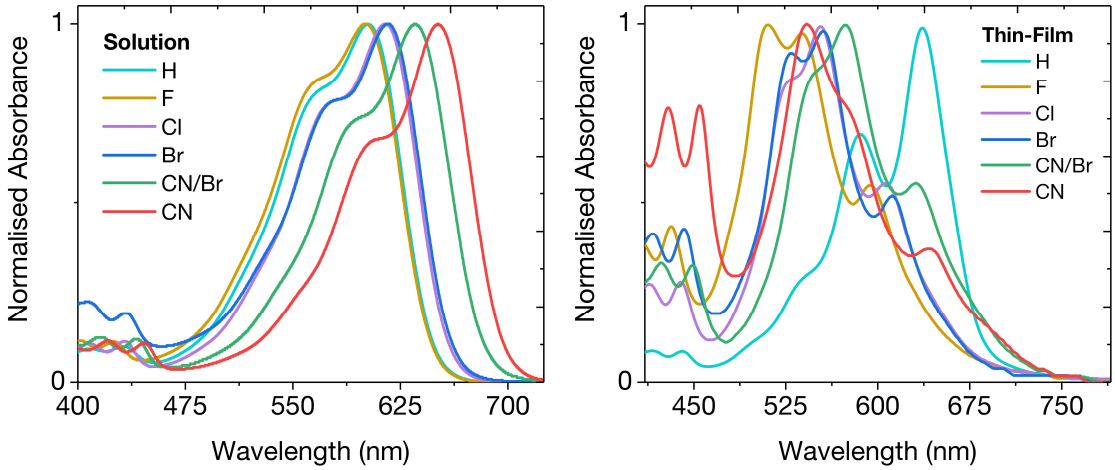


**Figure 5.25** Normalised UV-vis absorption spectra of 6,6'–functionalised INDTs in solution (chloroform, left) and thin-film (right, spun from chloroform)

In solution, all six compounds showed similar absorbance features and identical spectral bandwidth with $\lambda_{max}$ between 600-650 nm. **H-INDT** and **F-INDT** exhibited practically identical absorbance, whilst **Cl-INDT** and **Br-INDT** exhibited identical absorbance profiles but bathochromically shifted by 15 nm relative to H and F. The addition of the strong electron withdrawing nitrile groups led to a large red shift in absorbance attributed

to the narrowing of the optical band gap as expected from theoretical analysis. Relative to the **Br-INDT**, the addition of each CN group red-shifted the absorbance by ~17 nm.

In thin-film, all INDT compounds (except H) showed broad absorbance over the 500-600 nm region of the UV-vis spectrum, with broad absorbance onsets attributed to aggregation of the materials in solid state, indicating that electronic coupling may be strong in these materials, in a similar fashion as **$CF_3$-INDB**. However, **H-INDT** showed a stark difference in absorption, with a sharp absorbance onset and a $\lambda_{max}$ at 636 nm. Remarkably, when the thin-film absorbance measurements were repeated intermittently over a 31-day period to monitor stability, **H-INDT** showed a clear change in its absorption profile. **Figure 5.26** shows the evolution of the UV-vis absorbance spectra of **H-INDT** and a comparison of the absorbance at day 0 and day 31.

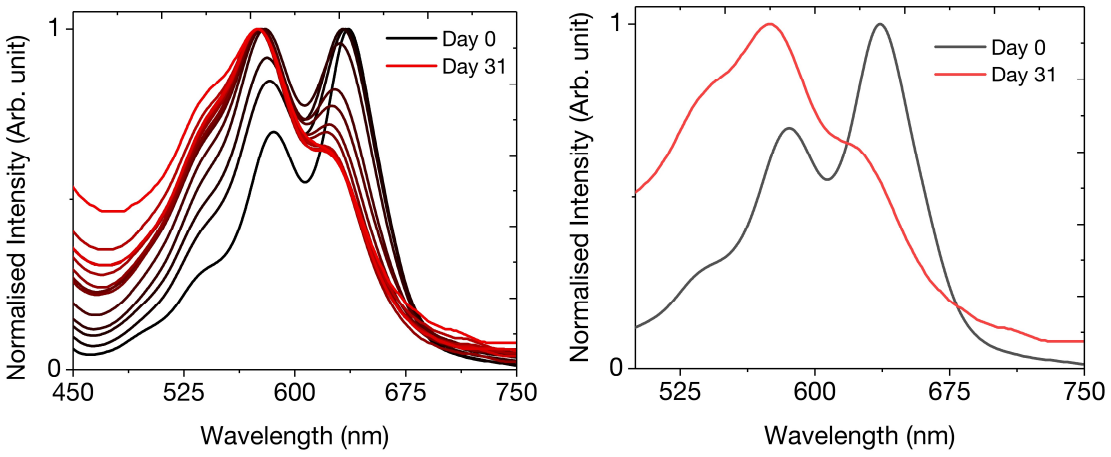


**Figure 5.26** Normalised transient UV-vis absorption spectra of **H-INDT** over 31 days (left) and at day 0 and day 31 (right)

It was clear that the absorbance feature at 636 nm decayed over time, evolving the feature at 585 nm as the dominant absorption after 7-10 days, which in turn was hypsochromically shifted 10 nm to 575 nm. This evolution of absorbance suggested that the initial thin-film morphology was kinetically formed and the morphology changed over time to give the thermodynamically favoured microstructure. This is an exciting feature, as it allowed the assessment of SF character as a function of film morphology.

The 31-day monitoring of the absorption spectra of the other five INDT compounds over is shown in **Figure 5.27**, and the corresponding normalised decay in absorbance of all six compounds is shown in **Figure 5.28**. The thin-films were stored in plastic boxes, in air, out of direct sunlight, but in a well-lit area.

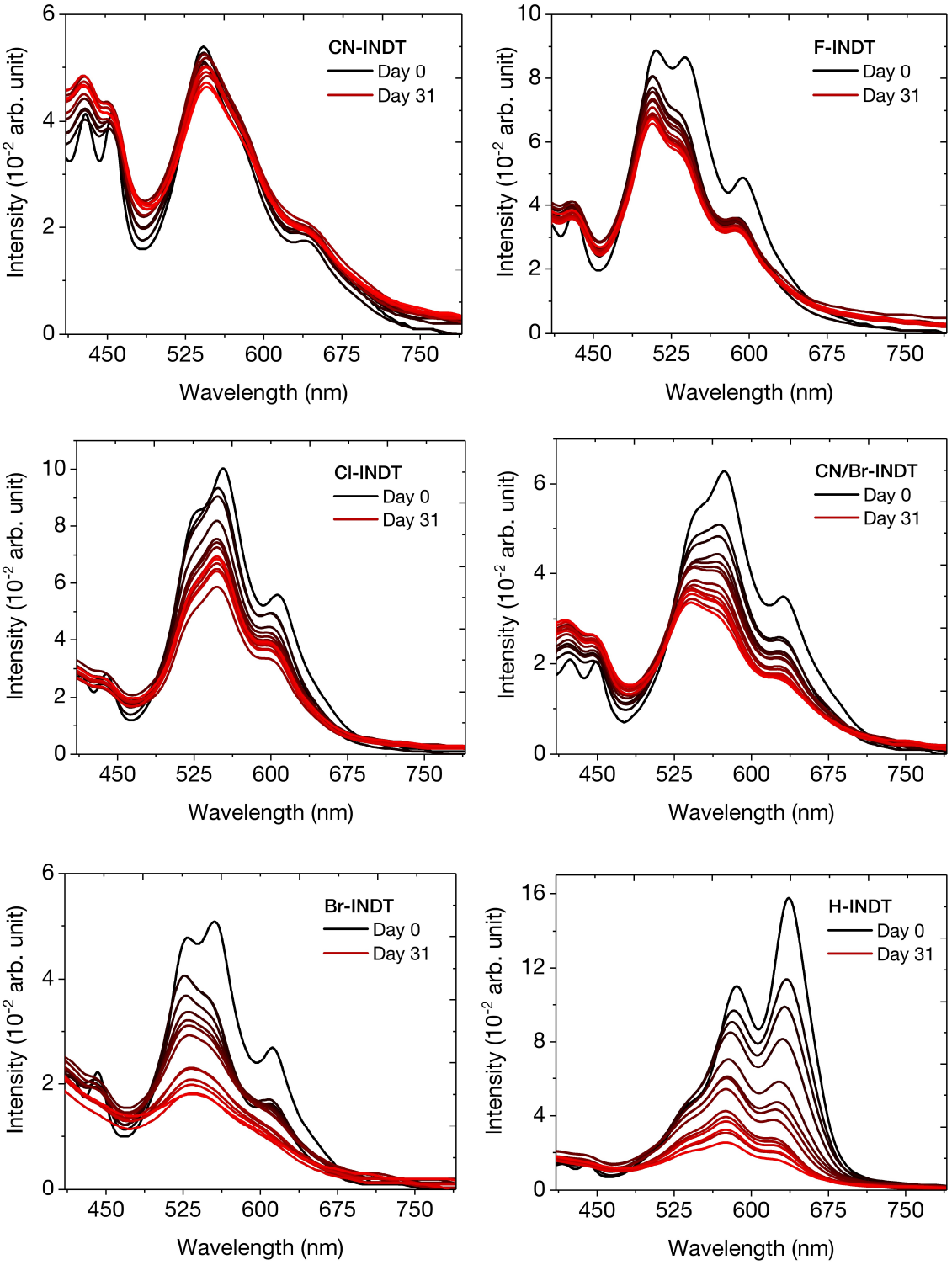


**Figure 5.27** Transient UV-vis absorption spectroscopy of INDT thin-films. Films were stored in air on a shelf in a well-lit area but out of direct sunlight, during July 2017 when RT fluctuated between 13-33 ℃ daily.

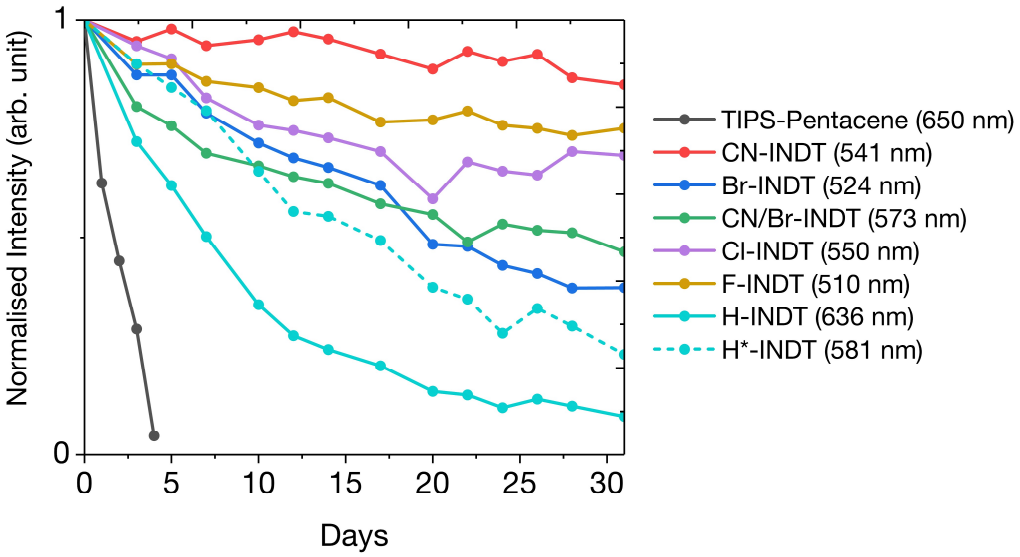


**Figure 5.28** Decay in $\lambda_{max}$ of UV-vis absorption of INDT thin-films on glass substrates normalised against $\lambda_{max}$ of each material on day 0. Films were stored in air on a shelf in a well-lit area but out of direct sunlight, during July 2017 when RT fluctuated between 13-33 ℃ daily.

All films showed decay over time as was expected, and the stability of the compounds was in the order CN > F > Cl > CN/Br ~ Br > H. Excitingly **CN-INDT**, which showed the greatest promise of SF from theoretical analysis showed an impressive 85% of initial $\lambda_{max}$ intensity after 31 days. The decay of the peak of **H-INDT** at 636 nm suggested poor stability, however the discussed changes in its thin-film morphology make it a unique case, and indeed the same analysis of the $\lambda_{581nm}$ (Figure 5.28, H*-INDT, dashed blue line) showed a decay more in line with the other materials.

To compare the stability of INDT compounds to the favoured SF material TIPS-pentacene (TIPS-P), a thin-film of TIPS-P was made in an identical fashion and at the same time as the INDT thin-films so that the films were subjected to the same degradation conditions. The transient UV-vis absorption of TIPS-P (**Figure 5.29**) revealed that the compound completely degraded after 4 days, whereas the absorption of CN-INDT barely dropped by ~2% after 4 days, showing the remarkable stability of INDT materials over TIPS-P.

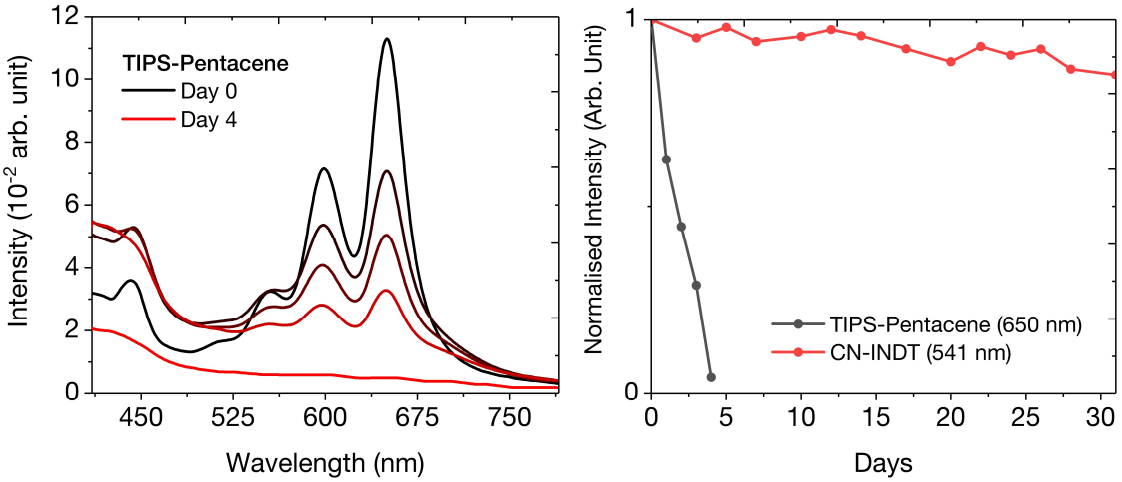


**Figure 5.29** Transient UV-vis absorption of thin-films of TIPS-pentacene (left) and CN-INDT (right). Films were stored in air on a shelf in a well-lit area but out of direct sunlight.

### 5.3.2 EPR Experiments

†*It must be noted that* **CN/Br-INDT** *was prepared after the EPR analysis of the other five materials, so its analysis cannot be discussed in this section.*

To examine the triplet excitations of the five† materials, EPR experiments were carried out on (1) frozen 100 μM solutions in degassed toluene and (2) thin-films deposited from saturated solutions in chloroform. The EPR spectrums are presented in **Figures 5.30–5.34**. EPR signals were observed in all five materials, confirming efficient triplet state generation in the materials, however the EPR signals were typically stronger in solution than in thin-film. This could be attributed to film thickness, or poor alignment of the sample with respect to the spectrometer – further experiments are needed to clarify this. When comparing the spectral line shape between solution and thin-film for the five samples, **H-INDT** and **F-INDT** exhibited comparable signals, though the spectral width of **F-INDT** did appear reduced in thin-film. However, the poor resolution of the thin-film EPR signals for these two compounds meant SF could not be ruled out in these materials and more experiments are needed.

However, **Cl-INDT**, **Br-INDT** and **CN-INDT** all showed clear, distinct EPR signals in solution and in thin-film. Notably, **Br-INDT** and **CN-INDT** showed significant differences in spectral line shape between solution and thin-film spectra, resulting from distinct changes in triplet sub-level populations due to a change of the mechanism responsible for triplet generation. In these two materials, a physical process, much faster and with considerable favouritism over ISC was occurring. This evidence was extremely promising and highly suggested that efficient SF may be occurring in these two materials.

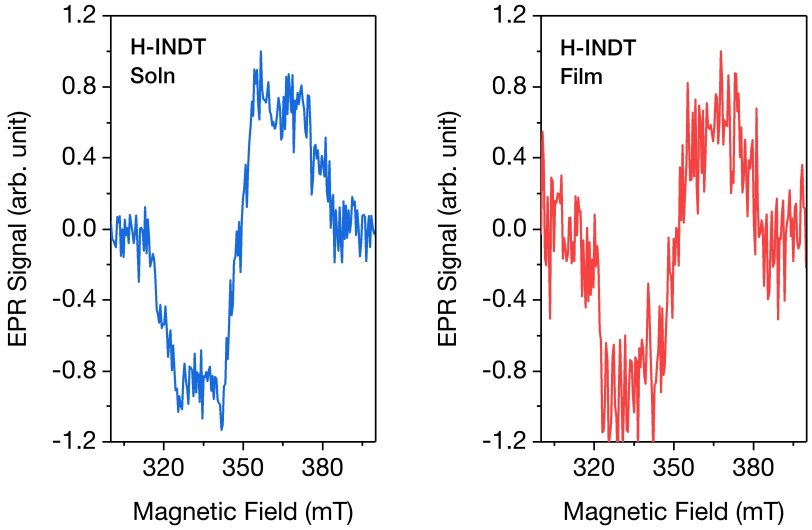


**Figure 5.30** EPR traces for **H-INDT** in solution (left) and thin-film (right)

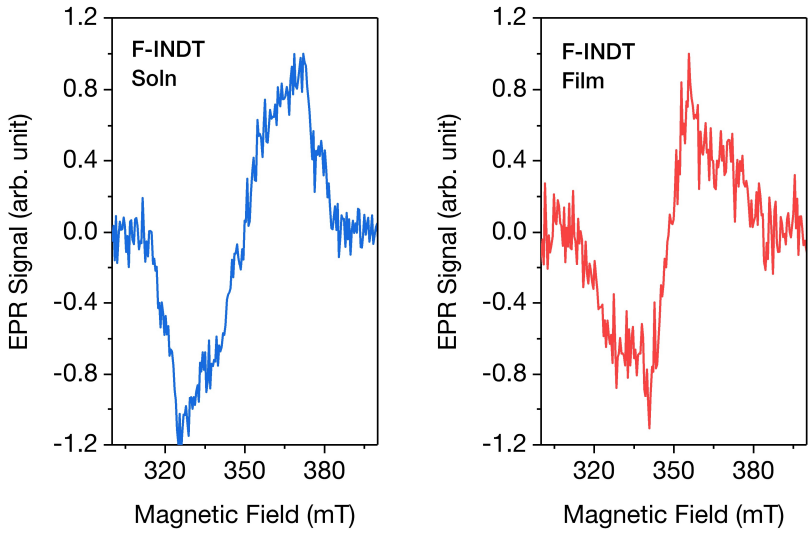


**Figure 5.31** EPR traces for **F-INDT** in solution (left) and thin-film (right)

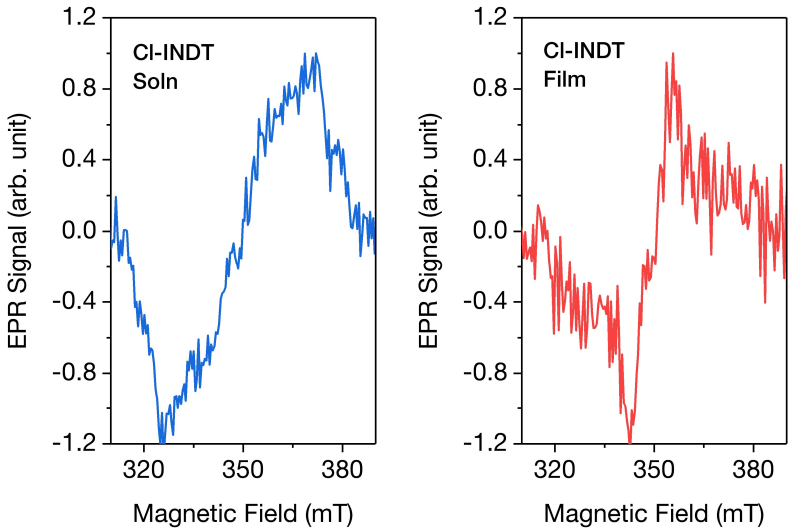


**Figure 5.32** EPR traces for **Cl-INDT** in solution (left) and thin-film (right)

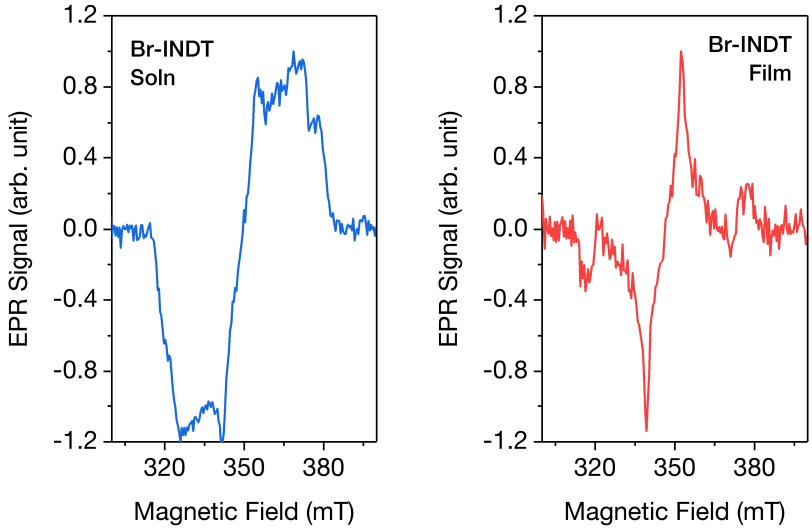


**Figure 5.33** EPR traces for **Br-INDT** in solution (left) and thin-film (right)

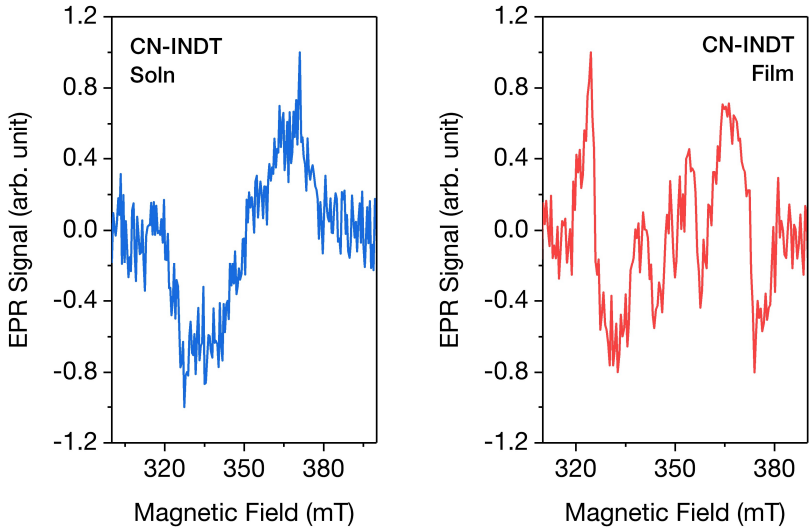


**Figure 5.34** EPR traces for **CN-INDT** in solution (left) and thin-film (right)

**Figure 5.35** shows simulated triplet excitations for the five INDT species superimposed on the observed EPR spectra. All compounds other than **CN-INDT** roughly matched these simulations well, although the poor signal resolution prevented adequate analysis. To conclude, EPR experiments revealed that the triplet excitations generated in the **Br** and **CN** INDT compounds exhibited significantly different triplet sub-populations in thin-film and dilute solution, suggesting that efficient SF could be occurring in these materials. Due to similarity in line shapes for **Cl** and the poor resolution of thin-film spectra for the **H** and **F** INDT compounds, it was not possible to deduce whether the spectral line shapes were significantly different and thus whether or not SF was occurring in these materials. However, these results were extremely promising and transient absorption spectroscopy of the excited states of these materials is currently ongoing.

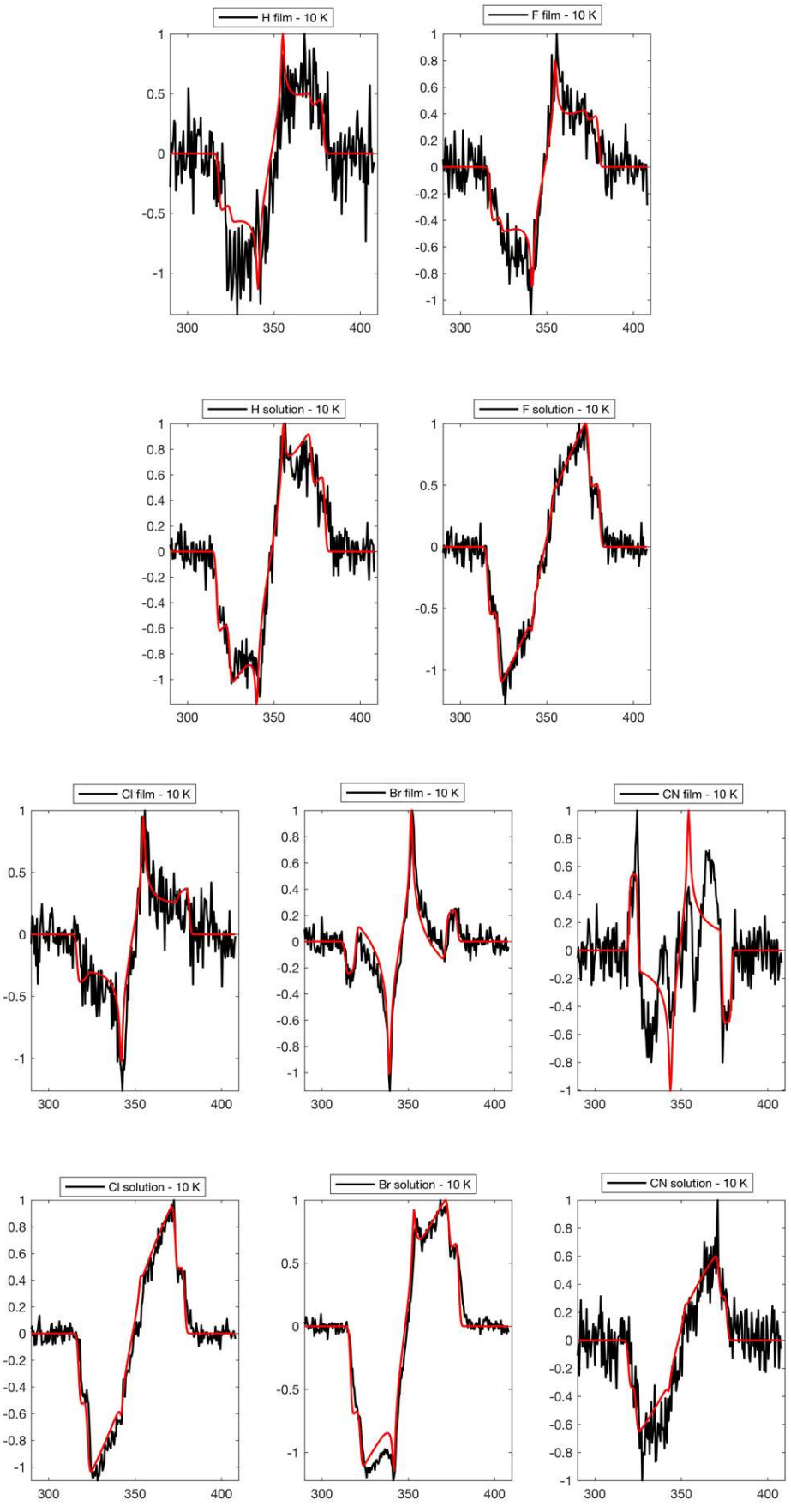


**Figure 5.35** Comparison of recorded and simulated triplet EPR spectra of INDT compounds

### 5.3.3 Baird Stabilisation

If the discussed indolonaphthyridine thiophenes do indeed facilitate SF, then investigating whether the triplet state is stabilised through Baird excited state aromaticity is crucial for expanding our knowledge of SF mechanisms.

Aromaticity can be calculated using nucleus independent chemical shift (NICS) quantum chemical calculations,[263–265] although there remains debate about which NICS index gives the most reliable estimation of aromaticity.[266,267] NICS(1) calculations have emerged as the preferred method as it probes the aromaticity of a ring current 1 Å above the ring (as opposed to NICS(0) which assesses the aromaticity in the plane of the ring). NICS(1) calculations on the synthesised INDT molecules are presented in **Table 5.3**.

**Table 5.3** NICS(1) calculations on synthesised indolonaphthyridine thiophenes at the B3LYP/6-311G** level of theory

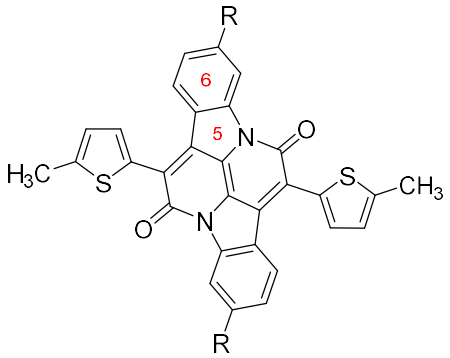


| 6,6'-R | T:S | *5-membered ring* | | | *6-membered ring* | | |
|---|---|---|---|---|---|---|---|
| | | $E_S$ | $E_T$ | $E_T/E_S$ | $E_S$ | $E_T$ | $E_T/E_S$ |
| CN | 0.434 | -3.582 | -9.331 | 2.6 | -18.900 | -21.365 | 1.1 |
| CN/Br | 0.449 | -3.442[a]<br>-4.029[b] | -10.187[a]<br>-7.819[b] | 3.0[a]<br>1.9[b] | -17.435[a]<br>-17.364[b] | -20.178[a]<br>-20.591[b] | 1.2[a]<br>1.2[b] |
| Br | 0.462 | -3.965 | -9.779 | 2.5 | -16.580 | -20.322 | 1.2 |
| Cl | 0.463 | -2.595 | -6.863 | 2.7 | -8.744 | -9.822 | 1.1 |
| H | 0.468 | -2.853 | -7.379 | 2.6 | -10.120 | -11.453 | 1.1 |
| F | 0.475 | -2.427 | -6.648 | 2.7 | -8.738 | -9.872 | 1.1 |

[a]CN side of indigoid; [b]Br side of indigoid; $E_S$ = singlet state; $E_T$ = triplet state

The increase in aromaticity $E_T/E_S$ for the indigoid 6-membered rings was calculated to be 1.1 – 1.2 times larger for each of the systems in their triplet state over their singlet state. Pleasingly, the same NICS(1) calculation on the 5-membered rings of each molecule revealed between 1.9 – 3.0 times greater aromatic character in the triplet state.

Furthermore, in the asymmetric **CN/Br-INDT**, where the NICS(1) calculations were carried out on the rings on both the "CN side" and the "Br side" of the molecule, the increase in triplet state aromaticity was higher in the 5-membered ring CN-adjacent ($E_T/E_S = 3.0$), with a smaller but still notable increase in the 5-membered ring Br-adjacent ($E_T/E_S = 1.9$).

Analogous calculations were carried out on TIPS-pentacene (**Table 5.4**) and a reduction in aromaticity was seen in every ring in the triplet state, validating triplet state antiaromaticity expected for linear acenes.

**Table 5.4** NICS(1) calculations on TIPS-pentacene ($^i$Pr groups substituted for methyl groups) at the B3LYP/6-311G** level of theory

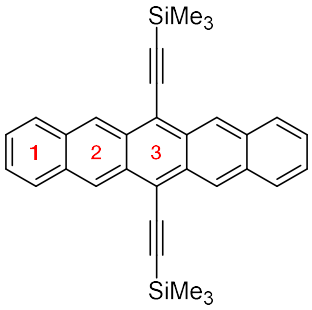


| Ring | $E_S$ | $E_T$ | $E_T/E_S$ |
|---|---|---|---|
| 1 | -19.195 | -13.950 | 0.7 |
| 2 | -28.341 | -2.7974 | 0.1 |
| 3 | -24.299 | -13.070 | 0.5 |

## 5.4 Pyridylnaphthyridine Benzene

The encouraging evidence of SF in indolonaphthyridine thiophenes meant that the pursuit of a wider band gap candidate capable of similar SF was not irrational. One method considered to this aim was replacing a $sp^2$ hybridised carbon in the benzene rings of indigo with a nitrogen, giving rise to pyridylnaphthyridine benzenes (PNDBs). TD-DFT calculations of several PNDB SF candidates are presented in **Table 5.5**.

**Table 5.5** Time-dependant DFT calculations on pyridylnaphthyridine benzene candidates at the B3LYP/6-311G** level of theory

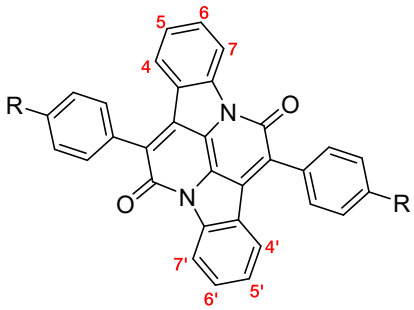


| Ref. | R | 4,4′ | 5,5′ | 6,6′ | 7,7′ | $S_0 \rightarrow S_1$ | $S_0 \rightarrow T_1$ | T:S |
|---|---|---|---|---|---|---|---|---|
| 5.5.01 | H | N | – | – | – | 2.2207 | 1.0249 | 0.462 |
| 5.5.02 | OMe | N | – | – | – | 2.0804 | 0.9786 | 0.470 |
| 5.5.03 | H | – | – | N | – | 2.2424 | 1.0582 | 0.472 |
| 5.5.04 | H | – | – | – | N | 2.2968 | 1.0874 | 0.473 |
| 5.5.05 | H | – | N | – | – | 2.3402 | 1.1636 | 0.497 |
| 5.5.06 | OMe | – | – | N | – | 2.1427 | 1.0367 | 0.498 |
| 5.5.07 | H | – | – | – | – | 2.2807 | 1.1706 | 0.513 |
| 5.5.08 | OMe | – | – | – | N | 2.2185 | 1.0805 | 0.519 |
| 5.5.09 | OMe | – | N | – | – | 2.2111 | 1.1321 | 0.544 |

Dashed line (–) represents standard aromatic $sp^2$ hybridised C atom

For all PNDBs where R = H, T:S was calculated between 0.462 – 0.497. Interestingly, N-substitution at the 5,5'–positions exhibited the smallest improvement, followed by the 7– and 6– positions which exhibited similar T:S however the 6–pyridyl exhibited a slightly narrower band gap. The lowest T:S of 0.462 was exhibited by the 4–pyridyl compound which also had the lowest $S_1$ and $T_1$ energies.

Of significance was compound 5.5.02, where the 4–pyridyl PNDB contained a methoxy group on the 4–position of the peripheral benzene ring. This PNDB had good calculated T:S of 0.470, with significantly larger singlet and triplet energies over the INDT compounds, despite the electron rich alkoxy group.

### 5.4.1 Synthesis

The synthesis of azaindigos was non-trivial and there is sparse literature available on the subject. Pioneering work on the synthesis of azaindoles by Sucharda in 1925 seemed the most promising route.[268–270]

Firstly, a condensation reaction of 3-aminopicolinic acid **5.60** with chloroacetic acid under Sucharda's conditions was carried out, which proceeded in an adequate yield of 37% (**Scheme 5.8**), however this yield could likely be improved with optimisation of reaction conditions.

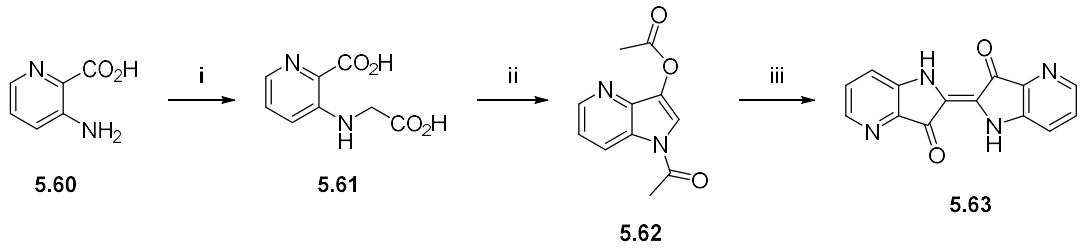


**Scheme 5.8** Synthesis of 4-azaindigo **5.63** from 3-aminopicolinic acid **5.60**
(i) Chloroacetic acid, $K_2CO_3$, $H_2O$, 95 °C, 12 h, 37%; (ii) AcOK, $Ac_2O$, 130 °C, 1 h, 78%; (iii) $NH_4OH$, air, 12 h, 37%

Pleasingly, the subsequent cyclisation–decarboxylation reaction proceeded efficiently in short reaction time to furnish azaindole **5.62**, which exhibited a good degree of stability on silica gel and so was purified using expedited dry-flash chromatography, to give the **5.62** in excellent 78% yield with high purity. As azaindoles with a hydroxyl group in the 3–position exhibit poor air stability, **5.62** was immediately oxidatively coupled in ammonia water in aerobic conditions to furnish 4-azaindigo **5.63** in 37% yield, in line with the ~40% yields obtained throughout this thesis for indigo formation reactions. Importantly, this reaction favoured high concentration and large surface area – poor yields were obtained if the reaction was performed dilute, and the best yield was obtained when using an oversized flask and vigorously stirred components, attributed to better surface area contact with molecular oxygen.

Pleasingly, 2.2 g of 4-azaindigo **5.63** was produced from 25 g of 3-aminopicolinic acid. If this chemistry was repeated, focus should be given to increasing the yield of the initial reaction between the picolinic acid and chloroacetic acid, which lends itself to

optimisation or could be carried out using more classic *N*-alkylation methods, such as with stronger base in DMF (e.g. **Scheme 5.9**).

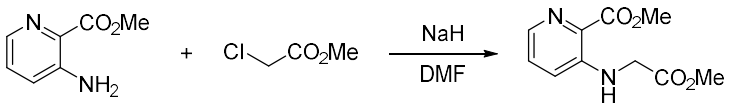


**Scheme 5.9** Suggested alternate *N*-alkylation of 3-aminopicolinic methyl ester

The condensation of 4-azaindigo with the 2-octyl-1-dodecylphenylacetyl chloride reported in Chapter 2 (**2.11**) gave the corresponding 4-pyridylnaphthyridine benzene (**5.64**, 4PNDB) in low yield (**Scheme 5.10**). The poor yield was attributed to arduous purification, however if the reaction was repeated the yield would be expected to improve severely due to now known purification procedures.

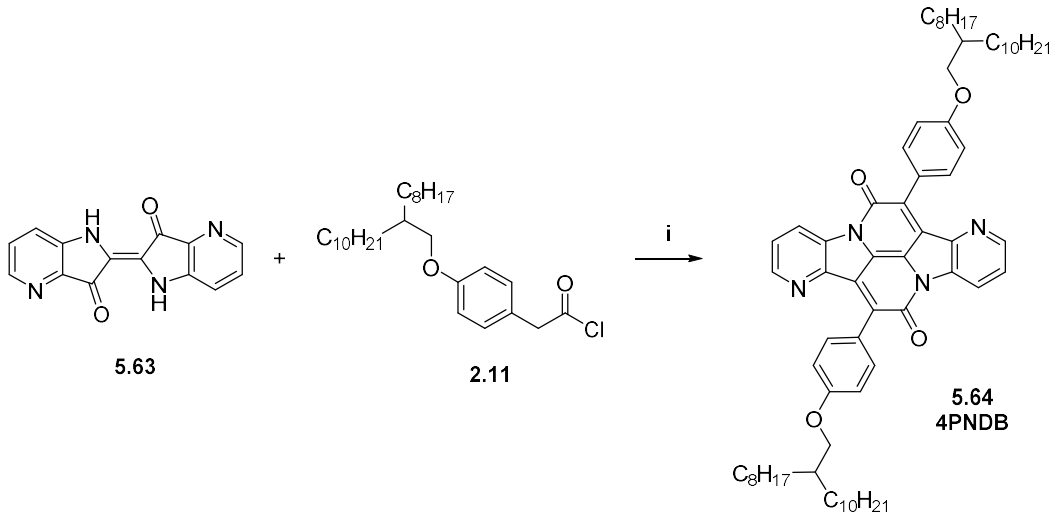


**Scheme 5.10** Annulation-condensation reaction of 4-azaindigo with **2.11** to give 4-pyridylnaphthyridine benzene (4PNDB) **5.64**
(i) Xylenes, 165 °C, 12 h, 0.4%

However, **5.64** was obtained in high purity and its UV-vis absorption spectra is shown in **Figure 5.36**. As predicted by theoretical analysis, the optical band gap of **4PNDB** was narrowed compared to the $sp^2$-containing carbon equivalent (***p*O-INDB**, **2.13**) but to a lesser extent compared to **CN-INDT**. Aside from the bathochromic shift in absorption, both the solution and thin-film spectral features were identical to ***p*O-INDB**, suggesting potentially comparable energetic structure of the two materials.

**Figure 5.37** shows a preliminary EPR experiment on **4PNDB**. Whilst triplet excitations are present in both physical states, the resolution of the solution is very poor and further studies are required to deduce meaningful populations data. Analysis of this compound remains ongoing.

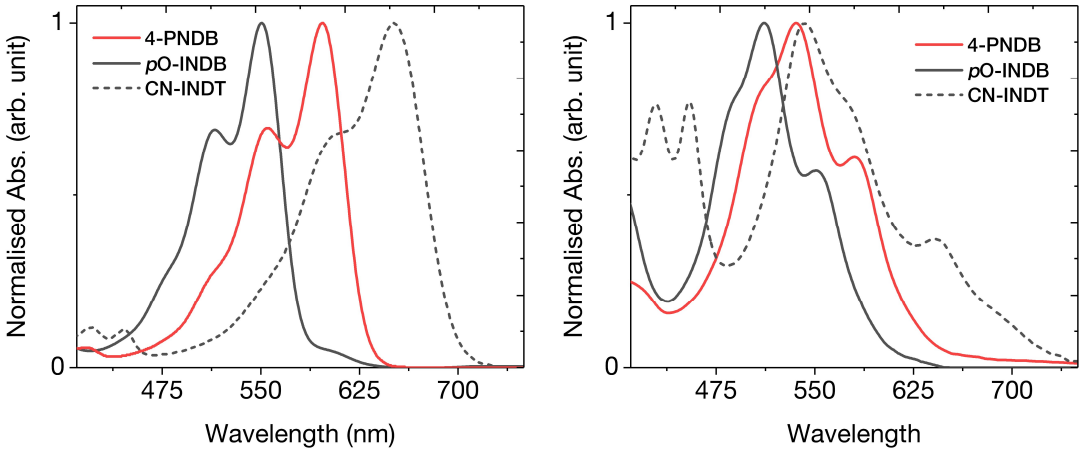


**Figure 5.36** Normalised solution (left) and thin-film (right) UV-vis absorbance spectra of 4-pyridylnaphthyridine benzene (**4PNDB**) shown in red. The absorbance of the corresponding indolonaphthyridine compound (*p*-OINDB, **2.13**) is shown in black, and the corresponding absorbance of **CN-INDT** shown in black dash.

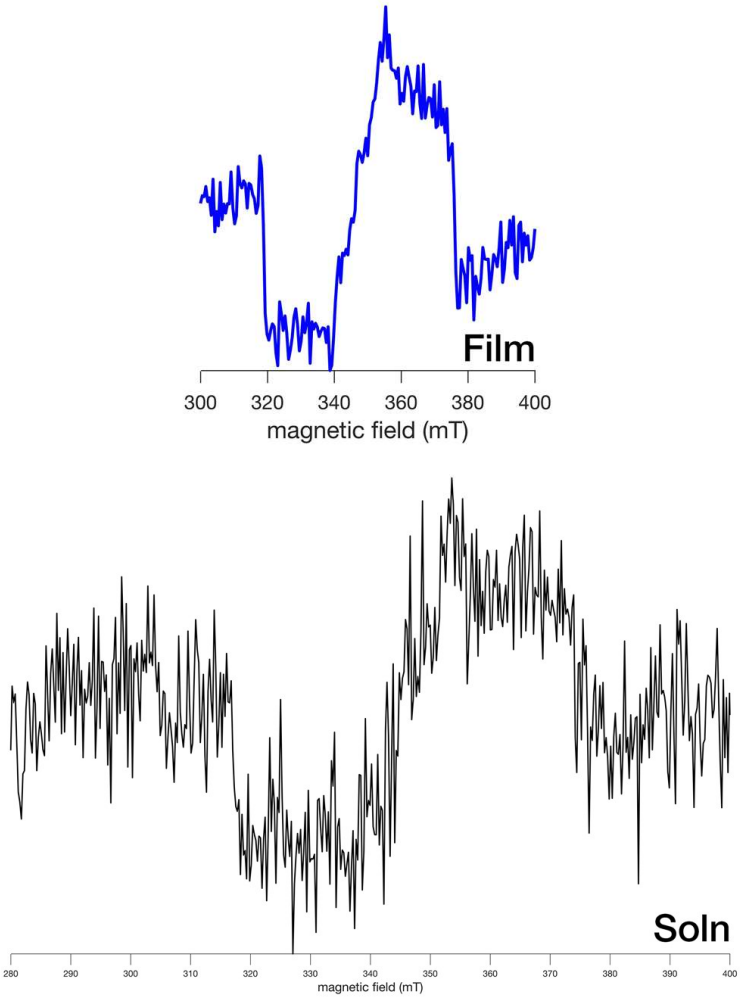


**Figure 5.37** Thin-film (top) and solution (bottom) EPR spectra of **4PNDB**

## 5.5 Conclusions & Future Prospects

An in-depth study into the structure-property relationships of indolonaphthyridines has revealed that chemical functionalisation of the indigoid benzene rings with electron withdrawing functionality results in low triplet energies, and in many candidates the vital requirement of $2T_1 < S_1$ for singlet fission is met. Initial computational calculations on indolonaphthyridine benzene (INDB) compounds revealed difficulty in meeting the above criteria, however the best theoretical candidate was chosen and synthesised, however EPR experiments revealed triplet excitations were likely only occurring through ISC and not SF.

Theoretical analysis of indolonaphthyridine thiophene (INDT) compounds revealed that $2T_1 < S_1$ was met with considerable more ease, although optical band gaps were predicted to be narrow. Six INDT candidates were synthesised and EPR studies on five of them revealed that three structures exhibited evidence which strongly suggests SF is occurring. These six materials are now being investigated with transient absorption spectroscopy to probe their excited state dynamics. The six compounds exhibited unique UV-vis absorptions over 400–700 nm, showcasing the excellent tuneability of the optical properties of the materials using chemical functionalisation.

Crucially, the analysis of the aromaticity of INDT compounds in their triplet state were calculated and revealed large aromatic character in the 5-membered ring, as hypothesised by applying Baird's rule to the indolonaphthyridine framework. The method was also applied to TIPS-pentacene, which exhibited a clear decrease in aromaticity in its triplet state. Additionally, the stability of the synthesised INDT compounds in air and ambient light was investigated and showed impressive stability after 31 days, whereas TIPS-pentacene fully degraded after 4 days. This confirmed that excited state aromaticity is a superior method for achieving low triplet energies without compromising chemical stability.

Finally, in an attempt to synthesise wider band gap SF candidates, pyridyl indolonaphthyridine benzene compounds were assessed and the best SF candidate synthesised. The pyridyl candidate exhibited a wider band gap than the indolonaphthyridine thiophene compounds, however preliminary EPR experiments cannot confirm nor disprove the presence of SF in this system.

In future work, it is of vital importance to tackle the issue of the low yielding condensation reaction of insoluble indigos and aromatic acetyl chlorides. The first steps toward this have already been taken in synthetic strategies towards alkylated indigos. In work that has not been covered in this thesis, molybdenum hexacarbonyl is proficient at oxidatively

coupling alkylated indoles to give alkylated indigo **5.66** in typical yield (33% unoptimized). This indigo was obtained in very high purity due to its high degree of solubility, and its reaction with 2-thiophenylacetyl chloride proceeded extremely well giving the INDT compound **5.67** in 40% yield in just 3 h (**Scheme 5.11**). This incredible yield demonstrated fully how the poor solubility of the indigos has been the limiting factor in these condensation reactions.

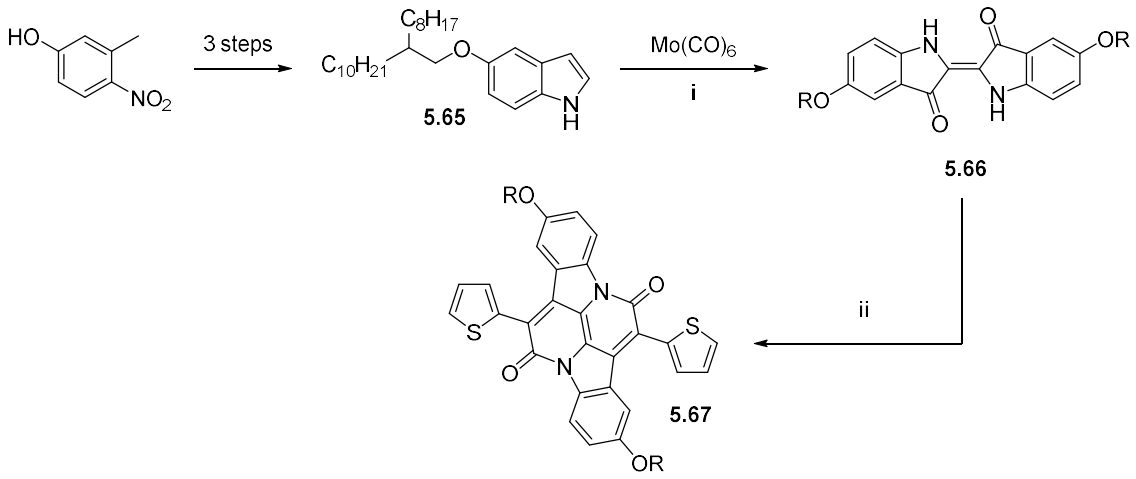


**Scheme 5.11** Route to alkylated indigo **5.66** and the relatively extremely high yielding dual annulation-condensation reaction with thiophenylacetyl chloride
(i) Cumene hydroperoxide, *tert*-BuOH, AcOH, 90 °C, 1 h, 33%; (ii) 2-Thiophenylacetyl chloride, xylenes, 165 °C, 1 h, 40%; (unoptimized yields)

Secondly, the synthesis of an indolonaphthyridine with $\mathrm{T}:\mathrm{S} < 0.5$ and an optical band gap equal to or greater than cibalackrot remains elusive. Although solubilising the indigo core is crucial, future synthesis will need to shift focus to alkyl chains instead of alkoxy, whose stronger electron donating character leads to a large narrowing of $E_\mathrm{g}$ (**Figure 5.38**).

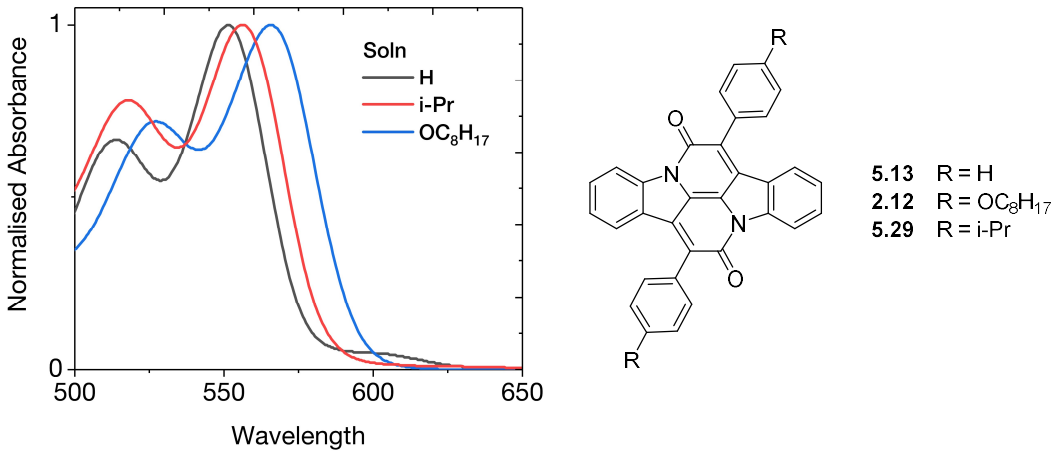


**Figure 5.38** Solution UV-vis absorbance spectra of Cibalackrot (black) and functionalised compounds where R is alkoxy (blue) or alkyl (red) showing greater narrowing of $E_\mathrm{g}$ with electron donating functional groups

# VI

*Experimental Procedures*

## 6.1 Universal Information

Reactions *under normal atmospheric conditions* were carried out in clean but untreated glassware and with HPLC grade solvent. Water was deionised when used as a reagent or solvent, but not during work-ups. Reactions using anhydrous solvents/conditions were carried out using oven-dried glassware, cooled under vacuum and backfilled with argon. Where chemicals and solvents were purchased from a supplier, they were used without further purification unless otherwise stated. Thin-layer chromatography was carried out on Merck Keiselgel aluminium-backed plates coated with silica, with components being visualised using combinations of ultra-violet light and potassium permanganate stain. Column chromatography was carried out using either BDH (40-60 μm) silica or on a Biotage Isolara 4 using Biotage SNAP cartridges. The terms *flash* or *dry-flash* indicate that the silica was not pre-wetted into a gel prior to crude loading, typically the case for large-scale purifications above 5 g. The term *short silica plug* refers to a length of 1-2 inches and a variable width appropriate to the scale of the purification. Indolonaphthyridines tended to require several column chromatography purifications to attain high purity.

$^{1}$H NMR spectra were recorded at 300 MHz on a Bruker Avance 300, 400 MHz on a Bruker Avance 400 spectrometer or at 600 MHz on a Bruker Avance 600 spectrometer in the stated solvent using residual protic solvent $CDCl_3$ (δ = 7.26 ppm, s), DMSO (δ = 2.56 ppm, qn), $d_6$-acetone (δ = 2.05, s) or $D_2O$ (δ = 4.79, s) as the internal standard. Chemical shifts are quoted in ppm using the following abbreviations: s, singlet; d, doublet; t, triplet; q, quartet; qn, quintet; m, multiplet; br, broad or a combination of these. The coupling constants (*J*) were measured in Hertz (Hz). $^{13}$C NMR spectra were

recorded on similar spectrometers in the stated solvent using the central reference of $CHCl_3$ (δ = 77.0 ppm, t), DMSO (δ = 39.52 ppm, septet) as the internal standard. Chemical shifts are reported to the nearest 0.1 ppm. Mass spectra were obtained using either a VG70-SE or MAT 900XP spectrometer at the Department of Chemistry, University College London. X-ray diffraction (XRD) measurements were carried out with a Bruker D4 Endeavour diffractometer equipped with a nickel-filtered Cu Kα1 beam and a scintillation counter detector and post-sample graphite monochromator, using a current of 30 mA and an accelerating voltage of 40 kV. UV-vis spectra were recorded on a Perkin-Elmer Lambda 950 spectrophotometer. A dagger symbol (†) is used after a citation to indicate that the observed data is in good accordance with literature values given in that citation. Organic photovoltaic devices were made by spin coating PEDOT:PSS onto pre-cleaned, patterned indium tin oxide (ITO) substrates. The photoactive layer was deposited by spin coating a 1:2 solution of polymer:PC[70]BM from 4:1 $CHCl_3$:ODCB solution (10 mg/mL at 1000 RPM). The active layer was allowed to dry under an inert atmosphere. The counter electrode of LiF (1 nm) and aluminum (100 nm) was deposited by vacuum evaporation at $3 \times 10^{-7}$ mbar. J-V characteristics were measured under ~100 mW/cm$^2$ white light from a tungsten-halogen lamp filtered by a Schott GG385 UV filter and a Hoya LB120 daylight filter, using a Keithley 2400 source meter. Short circuit currents under AM1.5G conditions were obtained from the spectral response and convolution with the solar spectrum. Spectral response was measured under operation conditions using bias light from a 532 nm solid state laser.

## 6.2
## *Experimental Procedures for Chapter II*

**7,14-diphenyldiindolo[3,2,1-*de*:3',2',1'-*ij*][1,5]naphthyridine-6,13-dione (2.3)**
also ***Cibalackrot***

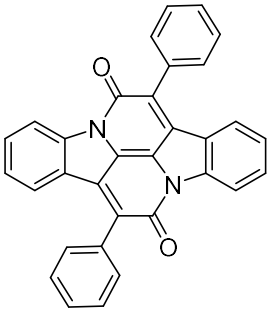

Under normal atmospheric conditions, phenylacetyl chloride (5 mL) was added to a suspension of indigo (1 g) in mixed xylenes (100 mL) heated at 165 °C. The reaction was heated overnight and then xylenes were removed *in vacuo*. The crude residue was taken up in warm chloroform (200 mL) and eluted with chloroform through a 2-inch plug of silica gel. The fractions containing the product (light pink) were concentrated *in vacuo* and taken up in a minimum volume of ethyl acetate and collected by vacuum filtration giving the title compound as a brick-red solid (70 mg, 4%).

**$^1$H NMR** (600 MHz, $CDCl_3$) δ 8.51 (d, *J* = 8.0 Hz, 2H), 7.73 (d, *J* = 7.2 Hz, 4H), 7.63 – 7.51 (m, 10H), 7.22 (t, *J* = 7.6 Hz, 2H) **$^{13}$C NMR** unobtainable due to low solubility **HRMS** Found (EI): $[MH]^+$ 463.1439, $C_{32}H_{19}N_2O_2$ requires 463.1447

### Ethyl 2-(4-hydroxyphenyl)acetate (2.5) [271†]

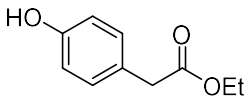


Under normal atmospheric conditions, 4-hydroxyphenyl acetic acid (10 g, 65.7 mmol) was dissolved in ethanol (120 mL). Sulphuric acid (99%, 1 mL) was added and the reaction was heated at reflux for 3 h. The reaction mixture was then poured into brine (240 mL) and extracted with diethyl ether (3 × 75 mL). The combined organic extracts were dried over $MgSO_4$ and concentrated *in vacuo* to give the title compound as a pale yellow oil (11.69 g, 99%).

**$^1$H NMR** (400 MHz, $CDCl_3$) δ 7.12 (d, *J* = 8.6, 2H), 6.74 (d, *J* = 8.6, 2H), 4.15 (q, *J* = 7.1, 2H), 3.54 (s, 2H), 1.25 (t, *J* = 7.1, 3H) **LRMS** (EI+) *m/z* 180 $[M]^+$

### 2-Octyl-1-dodecyl bromide [272†]

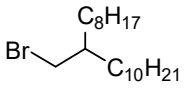


Under normal atmospheric conditions at 0 °C, N-bromosuccinimide (21.5 g, 0.12 mol) was added portionwise to a solution of 2-octyldodecanol (32.4 g, 0.11 mol) and triphenylphosphine (31.7 g, 0.12 mol) in DCM (550 mL). The reaction was allowed to warm to RT and stirred for 12 h. Solvent was then removed *in vacuo* and the residue taken up in hexane and passed through a short silica plug. The filtrate was then concentrated *in vacuo* to give the title compound as a colourless oil (31.7 g, 80%).

**$^1$H NMR** (400 MHz, $CDCl_3$) δ 3.47 (d, *J* = 4.8 Hz, 2H), 1.66 – 1.59 (m, 1H), 1.43 – 1.20 (m, 32H), 0.90 (t, *J* = 6.8 Hz, 6H) **LRMS** (CI+) *m/z* 361 $[M]^+$

### Ethyl 2-(4-((2-octyldodecyl)oxy)phenyl)acetate (2.7)

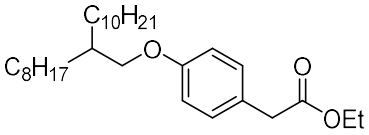


To a solution of phenol **2.5** (11.6 g, 64 mmol) and 2-octyl-1-dodecyl bromide (29.7 g, 82 mmol) in anhydrous DMF (330 mL) was added potassium carbonate (27.6 g, 0.2 mol). The reaction was heated to 80 °C for 12 h, then neutralised by the addition of 6M hydrochloric acid (20 mL). The resulting suspension was filtered and the filtrate was extracted with diethyl ether (3 × 100 mL). The combined organic extracts were washed

with water (2 × 100 mL) then brine (2 × 100 mL), dried over $MgSO_4$ and concentrated *in vacuo*. The crude residue was purified by dry-flash chromatography eluting initially with hexane to remove excess 2-octyl-1-dodecyl bromide, then with 10% ethyl acetate in hexane ($R_F$ = 0.6) to give the title compound as a pale yellow oil (19.3 g, 64%).

**$^1$H NMR** (400 MHz, $CDCl_3$) δ 7.18 (d, *J* = 8.7, 2H), 6.85 (d, *J* = 8.7, 2H), 4.14 (q, *J* = 7.1, 2H), 3.80 (d, *J* = 5.7, 2H), 3.54 (s, 2H), 1.82 – 1.68 (m, 1H), 1.48 – 1.38 (m, 2H), 1.38 – 1.18 (m, 33H), 0.93 – 0.82 (m, 6H) **$^{13}$C NMR** (100 MHz, $CDCl_3$) δ 172.1, 158.6, 130.2, 125.9, 114.6, 70.9, 60.9, 40.6, 38.0, 32.0, 31.4, 30.1, 29.8, 29.7, 29.4, 26.9, 22.8, 22.7, 14.3, 14.2 **HRMS** Found (CI+): $[M]^+$ 460.3912, $C_{30}H_{52}O_3$ requires 460.3911

### 2-(4-(Octyloxy)phenyl)acetic acid (2.8) [273†]

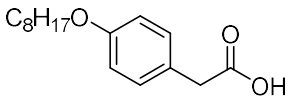


Under normal atmospheric conditions, 1-bromooctane (4 mL, 23 mmol) was added to a solution of 4-hydroxyphenylacetic acid (1.74 g, 11.4 mmol) and potassium hydroxide (1.57 g, 27.4 mmol) in ethanol (7.5 mL) and the reaction was heated at reflux for 12 h. A 13 M solution of potassium hydroxide (1 mL) was then added and the reaction heated at reflux for a further 1.5 h. The reaction was then cooled and acidified with 2M HCl to pH 2 precipitating a white solid, which was collected by filtration to give the title compound as a greasy white solid (2.53 g, 84%).

**$^1$H NMR** (600 MHz, $CDCl_3$) δ 7.17 (d, *J* = 8.6 Hz, 2H), 6.85 (d, *J* = 8.6 Hz, 2H), 3.92 (t, *J* = 6.6 Hz, 2H), 3.57 (s, 2H), 1.79 – 1.72 (m, 2H), 1.47 – 1.39 (m, 2H), 1.38 – 1.22 (m, 9H), 0.88 (t, *J* = 7.0 Hz, 3H) **LRMS** (CI+) *m/z* 265 $[MH]^+$

### 2-(4-((2-Octyldodecyl)oxy)phenyl)acetic acid (2.9)

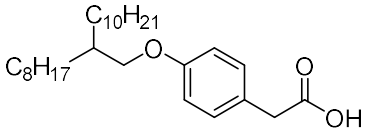


Under normal atmospheric conditions, aqueous sodium hydroxide (4M, 80 mL) was added to ethyl ester **2.7** (19.2 g, 42 mmol) in ethanol (80 mL) and the reaction was stirred for 4 h. The reaction was then acidified and organics extracted with diethyl ether (3 × 100 mL). The combined organic extracts were, washed with brine (2 × 50 mL), dried over $MgSO_4$ and concentrated *in vacuo* to give the title compound as a pale yellow oil that solidifies partially on standing (17.9 g, 99%).

**$^1$H NMR** (400 MHz, $CDCl_3$) δ 7.18 (d, *J* = 8.7, 2H), 6.85 (d, *J* = 8.7, 2H), 3.80 (d, *J* = 5.7, 2H), 3.58 (s, 2H), 1.81 – 1.70 (m, 1H), 1.48 – 1.38 (m, 2H), 1.38 – 1.19 (m, 31H), 0.88 (t, *J* = 6.8, 6H) **$^{13}$C NMR** (100 MHz, $CDCl_3$) δ 177.3, 158.8, 130.4, 125.0, 114.7, 70.9, 40.1, 38.0, 32.0, 31.4, 30.1, 29.8, 29.7, 29.4, 26.9, 22.8, 22.8, 14.2 **HRMS** Found (EI+): $[M]^+$ 432.3599, $C_{28}H_{48}O_3$ requires 432.3598

### 7,14-Bis(4-(octyloxy)phenyl)diindolo[3,2,1-*de*:3',2',1'-*ij*][1,5]naphthyridine-6,13-dione (2.12)

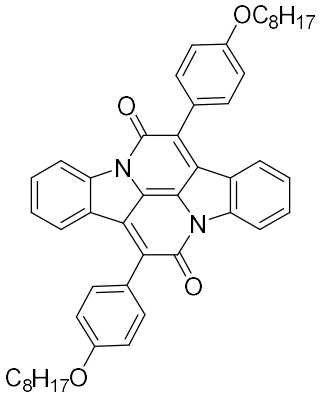


To a solution of carboxylic acid **2.8** (2.53 g, 10 mmol) dissolved in anhydrous DCM (5 mL) at RT was added two drops of anhydrous DMF and then excess thionyl chloride. The reaction was heated at reflux until complete by $^1$H NMR (~3 h). The reaction was then cooled and all volatiles removed *in vacuo* to give the corresponding acetyl chloride **2.10** as a viscous luminous yellow oil which was used immediately without further purification.

Under normal atmospheric conditions, a suspension of indigo (0.23 g, 0.87 mmol) in xylenes (20 mL) was heated to 165 °C. **2.10** was then added in one portion and the reaction heated for 12 h. Xylenes were then removed *in vacuo* and the crude residue was purified by dry-flash chromatography eluting with 0→100% chloroform in hexane. The fractions containing the product (luminous pink spot, $R_F$ = 0.3 in $CHCl_3$) were combined and concentrated *in vacuo* and the residue taken up in a minimum volume of ethyl acetate and collected by vacuum filtration giving the title compound as a brick red solid (293 mg, 47%).

**$^1$H NMR** (600 MHz, $CDCl_3$) δ 8.51 (d, *J* = 8.1 Hz, 2H, H7), 7.70 – 7.65 (m, 6H), 7.55 (t, *J* = 7.7 Hz, 2H), 7.22 (t, *J* = 7.4 Hz, 2H), 7.09 (d, *J* = 8.7 Hz, 4H), 4.08 (t, *J* = 6.5 Hz, 4H), 1.90 – 1.81 (m, 4H), 1.52 – 1.47 (m, 4H), 1.43 – 1.20 (m, 16H), 0.91 (t, *J* = 6.9 Hz, 6H) $R_F$ = 0.35 ($CHCl_3$) **$^{13}$C NMR** (150 MHz, $CDCl_3$) δ 160.1, 159.9, 144.7, 132.0, 131.8, 131.5,

130.9, 126.1, 125.6, 125.5, 122.1, 117.7, 114.6, 68.3, 32.0, 29.5, 29.4, 26.2, 22.8, 14.3 **HRMS** Found ($CI^+$): [M]+ 718.37787, $C_{48}H_{50}N_2O_4$ requires 718.37706

### 7,14-Bis(4-((2-octyldodecyl)oxy)phenyl)diindolo[3,2,1-*de*:3',2',1'-*ij*][1,5]naphthyridine-6,13-dione (2.13)

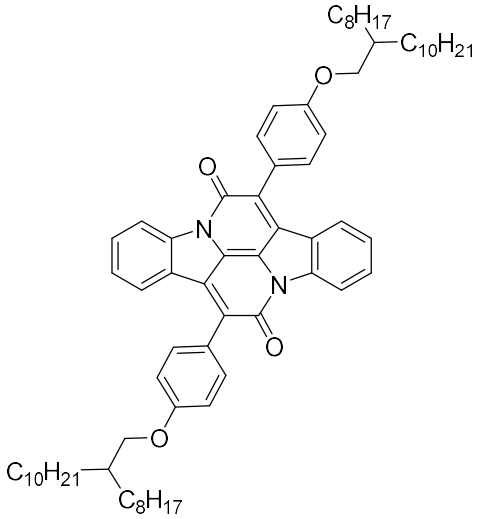


To a solution of acetic acid **2.9** (4.91 g, 23 mmol) dissolved in anhydrous DCM (10 mL) at RT was added two drops of anhydrous DMF and then excess thionyl chloride. The reaction turned yellow immediately and was heated until complete by $^1$H NMR (~3 h). The reaction was then cooled and all volatiles removed *in vacuo* to give the corresponding acetyl chloride **2.11** as a viscous luminous yellow oil which was used immediately without further purification.

Under normal atmospheric conditions, a suspension of indigo (3.0 g, 12 mmol) in xylenes (250 mL) was heated to 165 °C (reflux). Acetyl chloride **2.11** was then added in one portion and the reaction heated for 12 h. Xylenes were then removed *in vacuo* and the crude residue was purified by dry-flash chromatography eluting with 0→100% chloroform in hexane. The fractions containing the product (luminous pink spot, $R_F$ = 0.5 in $CHCl_3$) were combined and concentrated *in vacuo* and the residue taken up in a minimum volume of ethyl acetate and collected by vacuum filtration giving the title compound as a brick-red solid (40 mg, 0.3%).

**$^1$H NMR** (600 MHz, $CDCl_3$) δ 8.52 (d, *J* = 8.0 Hz, 2H), 7.71 (d, *J* = 8.0 Hz, 2H), 7.68 (d, *J* = 8.7 Hz, 4H), 7.55 (t, *J* = 7.7 Hz, 2H), 7.23 (t, *J* = 7.7 Hz, 2H), 7.10 (dd, *J* = 8.7 Hz, 4H), 3.96 (d, *J* = 5.6 Hz, 4H), 1.89 – 1.82 (m, 2H), 1.53 – 1.46 (m, 4H), 1.46 – 1.41 (m, 4H), 1.41 – 1.35 (m, 8H), 1.34 – 1.21 (m, 48H), 0.92 – 0.86 (m, 12H) **$^{13}$C NMR** (150 MHz, $CDCl_3$) δ 160.4, 159.9, 144.7, 131.9, 131.7, 131.4, 131.0, 126.1, 126.0, 125.6, 125.5,

122.0, 117.7, 114.7, 71.2, 38.1, 32.0, 31.5, 30.2, 29.8, 29.7, 29.5, 27.0, 22.8, 14.2 **HRMS** Found (MALDI): $[MH]^+$ 1055.3281, $C_{72}H_{99}N_2O_4$ requires 1055.7605

*also furnished...*

**7-(4-((2-Octyldodecyl)oxy)phenyl)-6*H*-pyrido[1,2-*a*:3,4-*b*']diindole-6,13(12*H*)-dione**

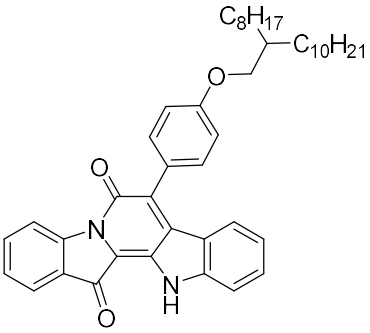


The fractions containing the half-annulated compound (dark purple spot, $R_F$ = 0.2 in $CHCl_3$) were combined and concentrated *in vacuo* and the residue taken up in a minimum volume of ethyl acetate and collected by vacuum filtration giving the title compound as a dark purple solid (1.5 g, 20%).

**$^1$H NMR** (600 MHz, $CDCl_3$) δ 8.87 (s br, 1H), 8.70 (d, *J* = 8.1 Hz, 1H), 7.85 (d, *J* = 7.5 Hz, 1H), 7.63 (t, *J* = 7.8 Hz, 1H), 7.54 (d, *J* = 8.7 Hz, 2H), 7.43 (t, *J* = 7.6 Hz, 1H), 7.35 – 7.29 (m, 2H), 7.24 (d, *J* = 8.1 Hz, 1H), 7.09 (d, *J* = 8.7 Hz, 2H), 6.94 (t, *J* = 7.6 Hz, 1H), 3.95 (d, *J* = 5.6 Hz, 2H), 1.89 – 1.78 (m, 1H), 1.52 – 1.46 (m, 2H), 1.47 – 1.40 (m, 2H), 1.40 – 1.35 (m, 4H), 1.34 – 1.24 (m, 24), 0.92 – 0.86 (m, 6H) **$^{13}$C NMR** (150 MHz, $CDCl_3$) δ 181.7, 160.5, 157.9, 147.1, 146.1, 137.2, 135.9, 135.6, 131.6, 131.3, 130.2, 126.3, 125.5, 125.3, 124.0, 121.6, 120.8, 118.5, 114.9, 111.4, 71.2, 38.1, 32.0, 31.5, 30.2, 29.8, 29.7, 29.5, 27.0, 22.8, 14.3 **HRMS** Found (MALDI): $[MH]^+$ 659.4047, $C_{44}H_{55}N_2O_3$ requires 659.4213

**4-Methoxy-2-nitrobenzaldehyde (2.18)** [274†]

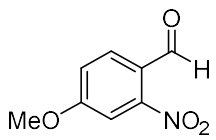


To a solution of 4-methyl-3-nitrophenol (0.5 g, 3.3 mmol) in anhydrous DMF (3.3 mL) was added *N*,*N*-dimethylformamide dimethyl acetal (2.2 mL, 0.17 mol) and the reaction was heated under argon at 135 °C for 72 h. The reaction was then cooled and added dropwise under normal atmospheric conditions into a vigorously stirred suspension of

sodium periodate (3.53 g, 0.17 mol) in $H_2O$ (11.0 mL) and DMF (5.5 mL). The reaction was stirred for 3 h then filtered and the filter cake washed thoroughly with toluene. The organic layer was separated from the filtrate and washed with water (100 mL), brine (100 mL) and then dried over $MgSO_4$ and concentrated *in vacuo*. The crude residue was purified by column chromatography on silica gel eluting with 10% ethyl acetate in hexane ($R_F$ = 0.2) to give the title compound as a yellow solid (0.3 g, 50%).

**$^1$H NMR** (400 MHz, $CDCl_3$) δ 10.33 (s, 1H), 8.02 (d, *J* = 8.7 Hz, 1H), 7.55 (d, *J* = 2.5 Hz, 1H), 7.26 (dd, *J* = 8.7, 2.5 Hz, 1H), 3.99 (s, 3H) **LRMS** (CI+) *m/z* 182 $[MH]^+$

### (*E*)-6,6'-Dimethoxy-[2,2'-biindolinylidene]-3,3'-dione (2.19)
*also* **6,6'-Dimethoxyindigo**

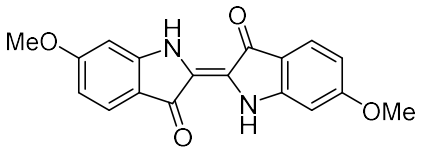


Under normal atmospheric conditions, 4-methoxy-2-nitrobenzaldehyde (0.3 g, 1.7 mmol) was dissolved in acetone (4.5 mL) and cooled to -10 °C. With vigorous stirring, a 0.2M solution of potassium hydroxide (0.6 mL) was added dropwise over 15 min. The solution turned pale yellow/orange and a suspension formed. After 30 min the solution was warmed to 5 °C and a 0.4M solution of potassium hydroxide (4.5 mL) was added dropwise. The reaction was covered and allowed to warm to room temperature and stirred for 24 h. The solid was then collected by vacuum filtration and washed with methanol to give the title compound as a blue solid (19 mg, 7%).

**$^1$H NMR** (400 MHz, $CDCl_3$) δ 8.86 (s, 2H, NH), 7.66 (d, *J* = 8.6 Hz, 2H, H4), 6.54 (dd, *J* = 8.6, 2.0 Hz, 2H, H5), 6.50 (d, *J* = 2.0 Hz, 2H, H7), 3.92 (s, 6H, $CH_3$) **$^{13}$C NMR** unavailable due to poor solubility **HRMS** Found (EI): $[M]^+$ 322.0959, $C_{18}H_{14}N_2O_4$ requires 322.0954

### 3,10-Dimethoxy-7,14-di(thiophen-2-yl)diindolo[3,2,1-*de*:3',2',1'-*ij*][1,5]naphthyridine-6,13-dione (2.20)

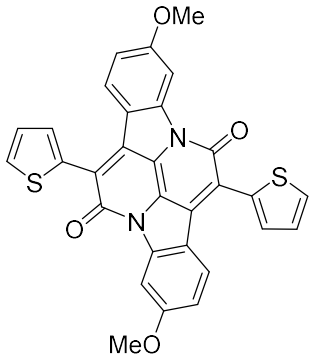


A solution of 2-(thiophen-2-yl)acetyl chloride (0.24 mL, 1.9 mmol) and 6,6'-dimethoxyindigo (54.4 mg, 0.17 mmol) in xylene (3.9 mL) was heated to reflux at 165 °C for 24 h. The reaction was then cooled to room temperature, and the precipitate was collected by filtration under reduced pressure with methanol washings to give the title compound as a black solid (50 mg, 56%).

**$^1$H & $^{13}$C NMR** unobtainable due to poor solubility **HRMS** Found (EI): [M]+ 534.0704, $C_{30}H_{18}N_2O_2S_2$ requires 534.0708

### 2-(3-Methyl-4-nitrophenoxy)tetrahydro-2*H*-pyran (2.22)

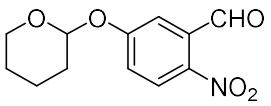


5-hydroxy-2-nitrobenzaldehyde (5.09 g, 31 mmol) and 3,4-dihydro-2*H*-pyran (13.7 mL, 0.15 mol) was dissolved in a 4:1 solution of dichloromethane:hexane (61 mL). *p*-Toluenesulfonic acid (58 mg, 1 mol%) was suspended in dichloromethane (15 mL) and a few drops of pyridine were added. The acidic mixture was then added in one portion and the reaction stirred for 12 h. Solvent and unreacted 3,4-dihydro-2*H*-pyran were then removed *in vacuo* and the crude residue purified by flash chromatography on silica gel eluting with 20% ethyl acetate in hexane ($R_F$ = 0.3) to give the pure product as a yellow oil (7.66 g, 100%).

**$^1$H NMR** (400 MHz, $CDCl_3$) δ 10.49 (s, 1H), 8.17 (d, *J* = 9.0 Hz, 1H), 7.51 (d, *J* = 2.8 Hz, 1H), 7.33 (dd, *J* = 9.0, 2.8 Hz, 1H), 5.62 (t, *J* = 2.8 Hz, 1H), 3.84 – 3.74 (m, 1H), 3.71 – 3.63 (m, 1H), 1.96 – 1.90 (m, 2H), 1.80 – 1.69 (m, 2H), 1.68 – 1.62 (m, 2H) **LRMS** (CI+) *m/z* 252 $[MH]^+$

**(*E*)-5,5'-bis((tetrahydro-2*H*-pyran-2-yl)oxy)-[2,2'-biindolinylidene]-3,3'-dione**
*also* **5,5'-Bis(tetrahydropyran)indigo (2.23)**

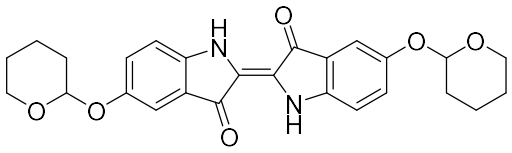

Aldehyde **2.22** (2.3 g) was dissolved in acetone (34.5 mL) and cooled to -10 °C. With vigorous stirring, a 0.2 M solution of potassium hydroxide (4.6 mL) was added dropwise over 15 min, turning the solution pale yellow. After 30 min the solution was warmed to 5 °C and a 0.4 M solution of potassium hydroxide (34.5 mL) was added dropwise, slowly. When half of this solution was added the reaction turned deep green, once addition was complete the reaction was a dark green/blue colour. After addition, the reaction was covered and allowed to warm to room temperature and stir for 24 h. The solid was then collected by vacuum filtration and washed with methanol until washings ran colourless to give a blue solid (0.72 g, 34%). **$^1$H NMR** (600 MHz, $CDCl_3$) δ 8.76 (s, 2H), 7.42 (d, *J* = 2.5 Hz, 2H), 7.22 (dd, *J* = 8.7, 2.5 Hz, 2H), 6.96 (d, *J* = 8.7 Hz, 2H), 5.34 (t, *J* = 3.3 Hz, 2H), 3.97 – 3.88 (m, 2H), 3.68 – 3.58 (m, 2H), 2.04 – 1.94 (m, 4H), 1.92 – 1.82 (m, 4H), 1.73 – 1.63 (m, 4H) **$^{13}$C NMR** unavailable due to low solubility **HRMS** Found (CI+): $[MH]^+$ 463.1863, $C_{26}H_{27}N_2O_6$ requires 463.1869

**2,9-Dihydroxy-7,14-di(thiophen-2-yl)diindolo[3,2,1-*de*:3',2',1'-*ij*][1,5]naphthyridine-6,13-dione (2.24)**
*also* **OH-INDT**
*via* ***tetrahydropyran*** *protecting group strategy*

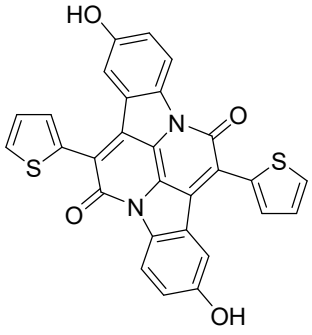

Indigo **2.23** (2.2 g, 4.8 mmol) and 2-(thiophen-2-yl)acetyl chloride (3.6 mL, 29 mmol) were dissolved in anhydrous xylene (96 mL) and the reaction was heated at reflux for 24 h. Solvent was removed *in vacuo* to give a black residue, which was taken up in methanol and the yellow methanol washings carefully decanted off, to leave the black solid in the flask. After five methanol washings the solid was suspended in methanol and, with

stirring, 5% sodium hydroxide solution (20 mL) was added. The solution immediately turned dark red and then black and allowed to stir for 12 h. 6M hydrochloric acid (4.1 mL, 24.8 mmol) was then added to neutralise the reaction. The methanol and water were then removed *in vacuo* and the resulting residue was washed with a small amount of water which was carefully decanted off, to remove any salts. The solid was then taken up in acetone and filtered off under reduced pressure. The resulting dark solid was washed with water, acetone then methanol, then air dried to give a black solid (0.7 g, 29%).

**$^1$H NMR** (600 MHz, DMSO) δ 10.03 (s, 2H), 8.22 (d, *J* = 8.7 Hz, 2H), 7.96 (d, *J* = 4.5 Hz, 2H), 7.74 (d, *J* = 3.6 Hz, 2H), 7.53 (d, *J* = 2.4 Hz, 2H), 7.35 (dd, *J* = 4.5, 3.6 Hz, 2H), 7.07 (dd, *J* = 8.7, 2.4 Hz, 2H) **$^{13}$C NMR** unavailable due to high aggregation **HRMS** Found (ES+): $[MH]^+$ 507.0482, $C_{28}H_{15}N_2O_4S_2$ requires 507.0473

### 2,9-Bis((2-octyldodecyl)oxy)-7,14-di(thiophen-2-yl)diindolo[3,2,1-*de*:3',2',1'-*ij*][1,5]naphthyridine-6,13-dione (2.25)

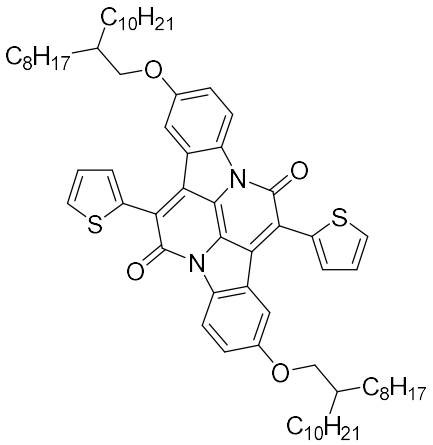


To a solution of **2.24** (266 mg, 0.53 mmol) and 2-octyl-1-dodecyl bromide (473 mg, 1.3 mmol) in anhydrous DMF (10.5 mL) was added potassium carbonate (1.02 g, 7.4 mmol) and the reaction was heated at 80 °C with stirring for 24 h. The reaction was then cooled and poured into brine (50 mL) and the product extracted with chloroform (5 × 30 mL). The combined organic extracts were washed with brine (3 × 30 mL), dried over $MgSO_4$, concentrated *in vacuo*. The crude residue was purified by flash chromatography on silica gel eluting with 50% chloroform in hexane ($R_F$ = 0.2) to give a purple oil (0.5 g, 89%).

**$^1$H NMR** (600 MHz, $CDCl_3$) δ 8.40 (d, *J* = 8.9, 2H), 7.74 (dd, *J* = 3.6, 0.8, 2H), 7.69 (dd, *J* = 5.1, 0.8, 2H), 7.65 (d, *J* = 2.5, 2H), 7.27 – 7.24 (m, 2H), 7.08 (dd, *J* = 8.9, 2.5, 2H), 3.81 (d, *J* = 5.8, 4H), 1.81 – 1.73 (m, 2H), 1.47 – 1.40 (m, 4H), 1.40 – 1.35 (m, 4H), 1.35 – 1.20 (m, 56H), 0.90 – 0.84 (m, 12H) **$^{13}$C NMR** (150 MHz, $CDCl_3$) δ 158.5, 158.0, 138.0,

134.8, 130.3, 130.2, 130.1, 127.1, 126.3, 125.1, 122.5, 118.4, 118.3, 111.0, 71.9, 38.0, 32.0, 31.4, 30.2, 29.8, 29.7, 29.5, 26.9, 22.8, 14.3 **LRMS** (ES-) *m/z* 1066 $[M-H]^-$

**7,14-Bis(5-bromothiophen-2-yl)-2,9-bis((2-octyldodecyl)oxy)diindolo[3,2,1-*de*:3',2',1'-*ij*][1,5]naphthyridine-6,13-dione (2.26)**
*also* **INDT**

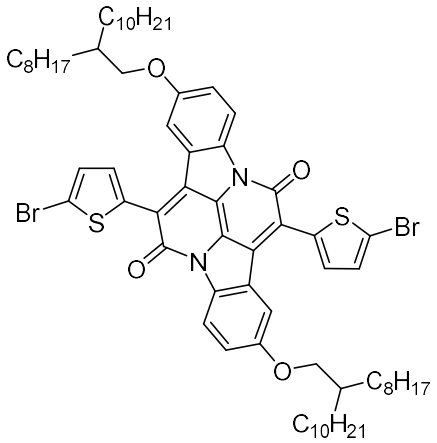


To a solution of compound **2.25** (170 mg, 0.16 mmol) in DCM (21 mL) cooled to 0 °C under argon was added recrystallised N-Bromosuccinimide (56.6 mg, 0.32 mmol). The system was allowed to warm naturally to RT overnight. Solvent was removed *in vacuo* and the crude residue was purified by column chromatography on silica gel eluting with 25→100% chloroform in hexane ($R_F$ = 0.3). Fractions containing the product were concentrated *in vacuo* to give a waxy film which was suspended in methanol and collected by vacuum filtration to give the title compound as a blue waxy solid (139 mg, 71%). If scratching the compound in methanol gave a single lump of material, particles of the compound were isolated by suspending the waxy film in a minimum volume of pentane, leaving the suspension to stand for 15 min, then adding cold methanol.

**$^1$H NMR** (600 MHz, $CDCl_3$) δ 8.34 (d, *J* = 8.9, 2H), 7.67 (d, *J* = 2.4, 2H), 7.54 (d, *J* = 3.9, 2H), 7.21 (d, *J* = 3.9, 2H), 7.07 (dd, *J* = 8.9, 2.4, 2H), 3.83 (d, *J* = 5.7, 4H), 1.83 – 1.75 (m, 2H), 1.48 – 1.41 (m, 4H), 1.41 – 1.36 (m, 4H), 1.36 – 1.17 (m, 56H), 0.91 – 0.83 (m, 12H) **$^{13}$C NMR** (150 MHz, $CDCl_3$) δ 158.1, 137.6, 136.6, 123.0, 129.2, 129.0, 126.8, 124.4, 122.4, 118.7, 111.0, 72.0, 51.0, 38.0, 32.0, 31.4, 30.2, 29.8, 29.5, 27.0, 22.8, 14.3 **HRMS** Found (ES-): $[M-H]^-$ 1221.4817, $C_{68}H_{91}Br_2N_2O_4S_2$ requires 1221.4787

**INDT-T**

*via THP-method*

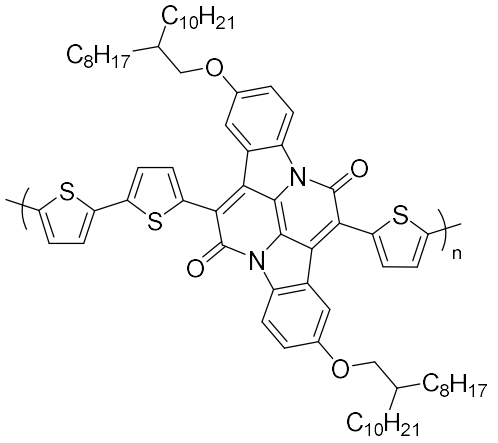


In a dry degassed 10 mL microwave vial was mixed **2.26** (60.1 mg, 49.1 µmol), tris(dibenzylideneacetone)dipalladium(0) (2.6 mg, 2.8 µmol, 6 mol%), tri(o-tolyl)phosphine (3.47 mg, 11.4 µmol) and 2,5-bis(trimethylstannyl)thiophene (20.15 mg, 49.1 µmol). Anhydrous chlorobenzene (2.5 mL) was added via syringe and the solution degassed with argon for 30 min. The vial was then placed in a microwave reactor and heated as follows: 10 min at 100 °C, 5 min at 120 °C, 5 min at 140 °C, 5 min at 160 °C and 20 min at 180 °C. The vial was then allowed to cool and the reaction had changed colour from sapphire blue to turquoise. The reaction mixture was added dropwise slowly into rapidly stirring methanol (70 mL) and allowed to stir for 2 h, forming fine dark blue fibres. The polymeric material was then filtered under reduced pressure into a cellulose thimble and washed with methanol then acetone. The polymer was purified by soxhlet extraction as follows: acetone for 12 h, hexane for 12 h and chloroform for 12 h. The chloroform was then concentrated to give a turquoise plastic-like film on the round bottomed flask. This film was dissolved in a minimum volume of hot chlorobenzene (~2.5 mL) then added dropwise slowly into rapidly stirring methanol cooled to 0 °C. Once addition was complete the methanol was stirred for 30 min then filtered under vacuum, washing carefully with methanol then a small amount of acetone then allowed to dry, forming a dark blue film. The polymer was air dried for 1 h then placed in a vial and dried under vacuum for 12 h (49 mg, 87%).

### 5-(Benzyloxy)-2-nitrobenzaldehyde (2.27) [275†]

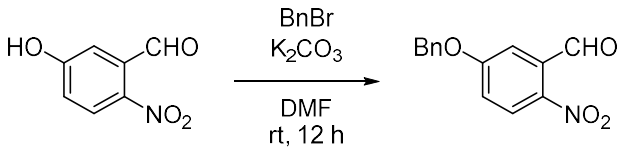


Under argon, a solution of 5-hydroxy-2-nitrobenzaldehyde (2.72 g, 16.3 mmol) and potassium carbonate (2.48, 17.9 mmol) in anhydrous *N*,*N*-dimethylformamide (82 mL) was stirred at RT for 30 min. Benzyl bromide (3.9 mL, 32.6 mmol) was then added and the reaction stirred for 12 h. The reaction was quenched with saturated $NaHCO_3$ solution (100 mL) and then poured into a separating funnel containing water (250 mL) and diethyl ether (250 mL). The organic layer was separated and the aqueous layer washed with diethyl ether (100 mL). The combined organic extracts were combined and washed with brine (3 × 100 mL), dried over magnesium sulphate and concentrated *in vacuo*. The crude residue was purified by dry-flash chromotography using 10% ethyl acetate in hexanes as an eluent ($R_F$ = 0.2) to give the title compound as a pale-yellow solid (4.11 g, 98%).

**$^1$H NMR** (500 MHz, $CDCl_3$) δ 10.48 (s, 1H), 8.16 (d, *J* = 9.1, 1H), 7.44 – 7.34 (m, 7H), 7.21 (dd, *J* = 9.1, 2.9, 1H), 5.21 (s, 2H) **LRMS** (ESI+) *m/z* 258 $[MH]^+$

### (*E*)-5,5'-bis(benzyloxy)-[2,2'-biindolinylidene]-3,3'-dione (2.28)

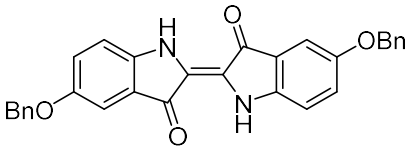


5-(benzyloxy)-2-nitrobenzaldehyde (4.0 g) was dissolved in acetone (60 mL) and cooled to -10 °C. With vigorous stirring, a 0.2 M solution of potassium hydroxide (8 mL) was added dropwise over 15 min, turning the solution pale yellow. After 30 min the solution was warmed to 5 °C and a 0.4 M solution of potassium hydroxide (60 mL) was added dropwise, slowly. When half of this solution was added the reaction turned deep green, once addition was complete the reaction was a dark green/blue colour. After addition the reaction was covered and allowed to warm to room temperature and stir for 24 h. The solid was then collected by vacuum filtration and washed with methanol until washings ran colourless to give a blue solid (1.94 g, 53%).

**$^1$H/$^{13}$C NMR** unavailable due to poor solubility **LRMS** (ESI+) *m/z* 475 $[MH]^+$

**2,9-Bis(benzyloxy)-7,14-di(thiophen-2-yl)diindolo[3,2,1-*de*:3',2',1'-*ij*][1,5]naphthyridine-6,13-dione (2.29)**

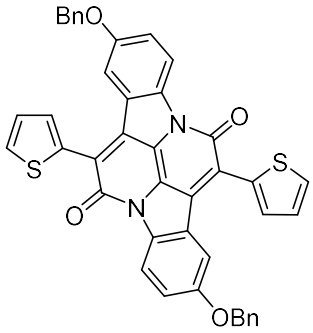


Indigo **2.28** (1.94 g, 4.1 mmol), and 2-(thiophen-2-yl)acetyl chloride (3.0 mL, 24.6 mmol) were dissolved in anhydrous xylene (82 mL) and the reaction heated to reflux for 48 h. The precipitate was isolated by vacuum filtration and washed with chloroform until the filtrate ran colourless, then washed with acetone until the filtrate ran very light pink, then air dried to give a dark purple solid (0.77 g, 27%).

**$^1$H NMR** (600 MHz, $CDCl_3$) δ 8.44 (d, *J* = 8.9, 2H), 7.70 (d, *J* = 2.4, 2H), 7.68 (d, *J* = 5.0, 2H), 7.63 (d, *J* = 3.1, 2H), 7.41 (m, 8H), 7.36 (m, 2H), 7.22 (m, 2H), 7.19 (dd, *J* = 8.9, 2.4, 2H), 5.08 (s, 4H) **$^{13}$C NMR** (150 MHz, $CDCl_3$) δ 158.5, 157.2, 138.3, 136.3, 134.7, 130.3, 130.1, 130.1, 128.8, 128.4, 127.6, 127.2, 126.6, 125.1, 122.5, 118.9, 118.4, 111.3, 70.7 **HRMS** Found (EI): $[M]^+$ 686.13306, $C_{42}H_{26}N_2O_4S_2$ requires 686.13340

**2,9-Dihydroxy-7,14-di(thiophen-2-yl)diindolo[3,2,1-*de*:3',2',1'-*ij*][1,5]naphthyridine-6,13-dione (2.24)**
*also* **OH-INDT**, *via* ***benzyl*** *protecting group strategy*

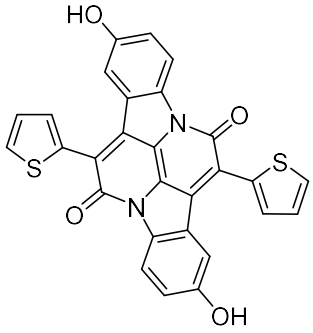


To a suspension of compound **2.29** (0.57 g, 0.83 mmol) in anhydrous DCM (25 mL) under argon was added excess iodotrimethylsilane (1.8 mL, 12.5 mmol). The reaction was stirred at RT until quenched extracts did not dissolve in chloroform (5 days) but did dissolve in DMSO. The reaction was quenched with methanol and filtered under reduced pressure to give a light purple solid (0.37 g, 88%).

*Data in agreement with data reported for synthesis via Bn protecting groups*

**INDT-T**

*via Bn-method*

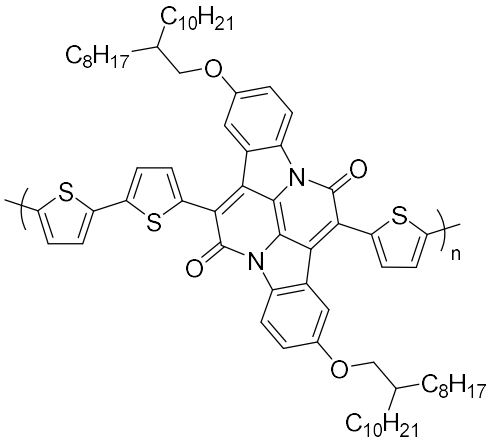


**2.26** (80 mg, 65.4 µmol), 2,5-bis(trimethylstannyl)thiophene (26.8 mg, 65.4 µmol), tris(dibenzylideneacetone)dipalladium(0) (3.0 mg, 3.3 µmol, 5 mol%) and tri(o-tolyl)phosphine (4.0 mg, 13.1 µmol) were added to a dry 10 mL microwave vial equipped with a stirrer bar and sealed. Chlorobenzene (2.5 mL) was added via syringe and the solution degassed with argon for 30 min. The vial was then placed in a microwave reactor and heated as follows: 10 min at 100 °C, 5 min at 120 °C, 5 min at 140 °C, 5 min at 160 °C and 20 min at 180 °C. The vial was then allowed to cool and the reaction had changed colour from sapphire blue to turquoise. The reaction mixture was added dropwise slowly into rapidly stirring methanol (70 mL) and allowed to stir for 2 h, forming fine dark blue fibres. The polymeric material was then filtered under reduced pressure into a cellulose thimble and washed with methanol then acetone. The polymer was purified by soxhlet extraction as follows: acetone for 12 h, hexane for 12 h and chloroform for 12 h. The chloroform was then concentrated to give a turquoise plastic-like film on the round bottomed flask. This film was dissolved in a minimum volume of hot chlorobenzene (~2.5 mL) then added dropwise slowly into rapidly stirring methanol cooled to 0 °C. Once addition was complete the methanol was stirred for 30 min then filtered under vacuum, washing carefully with methanol then a small amount of acetone then allowed to dry, forming a dark blue film. The polymer was air dried for 1 h then placed in a vial and dried under vacuum for 12 h (59 mg, 78%).

**INDT-BT**

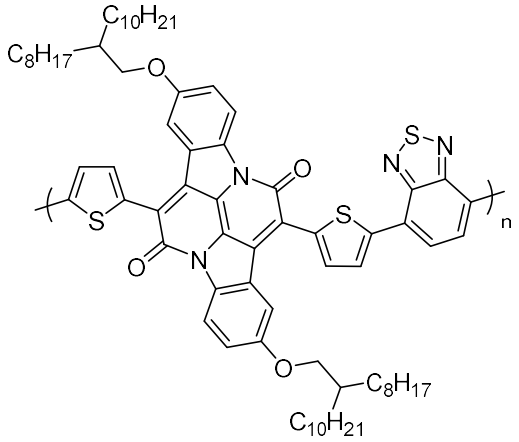

4,7-Bis(4,4,5,5-tetramethyl-1,3,2-dioxaborolan-2-yl)benzo[c][1,2,5]thiadiazole (25.4 mg, 65.4 µmol), **2.26** (79.9 mg, 65.4 µmol), tetrakis(triphenylphosphine)palladium(0) (1.5 mg, 1.31 µmol, 2 mol%) were added to a 10 mL microwave vial equipped with a stirrer bar and sealed and degassed. A degassed solution of Aliquot 336 in toluene (2.2 mL) was added via syringe and the solution further degassed with argon for 30 min. A degassed solution of 1M $Na_2CO_3$ (0.44 mL) was then added and the reaction was heated to 125 °C for 3 days. The reaction mixture was cooled and added dropwise slowly into rapidly stirring methanol (70 mL) and allowed to stir for 1 h. The polymeric material was then filtered under reduced pressure into a cellulose thimble and washed with methanol then acetone. The polymer was purified by soxhlet extraction as follows: acetone for 12 h, hexane for 12 h and chloroform for 12 h. The chloroform was then concentrated to give a turquoise plastic-like film on the round bottomed flask. This film was dissolved in a minimum volume of hot chlorobenzene (~2.5 mL) then added dropwise slowly into rapidly stirring methanol. Once addition was complete the methanol was stirred for 30 min then filtered under vacuum, washing carefully with methanol then a small amount of acetone then allowed to dry, forming a dark green film. The polymer was air dried for 1 h then placed in a vial and dried under vacuum for 12 h (65.9 mg, 84%).

**INDT-P**

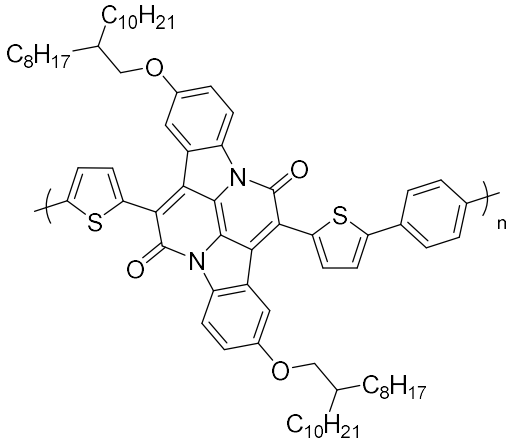


**2.26** (139 mg, 114 μmol), 1,4-benzenediboronic acid bis(pinacol) ester (37.53 mg, 114 μmol), tris(dibenzylideneacetone)dipalladium(0) (4.7 mg, 4.5 mol%) and triphenylphosphine (3.18 mg, 12.1 μmol) were added to a 10 mL microwave vial equipped with a stirrer bar and sealed and degassed. A degassed solution of Aliquot 336 in toluene (2.0 mL) was added via syringe and the solution further degassed with argon for 30 min. A degassed solution of 0.5 mM $K_3PO_4$ (0.23 mL) was then added and the reaction was heated to 125 °C for 3 days. The reaction mixture was cooled and added dropwise slowly into rapidly stirring methanol (80 mL) and allowed to stir for 1 h. The polymeric material was then filtered under reduced pressure into a cellulose thimble and washed with methanol then acetone. The polymer was purified by soxhlet extraction as follows: acetone for 12 h, hexane for 12 h, chloroform for 12 h and chlorobenzene for 12 h. The chlorobenzene was then concentrated to give a turquoise plastic-like film on the round bottomed flask. This film was dissolved in a minimum volume of hot chlorobenzene (~1.5 mL) then added dropwise slowly into rapidly stirring methanol. Once addition was complete the methanol was stirred for 30 min then filtered under vacuum, washing carefully with methanol then a small amount of acetone then allowed to dry, forming a dark blue film. The polymer was air dried for 1 h then placed in a vial and dried under vacuum for 12 h (27.3 mg, 21%).

**INDT-S**

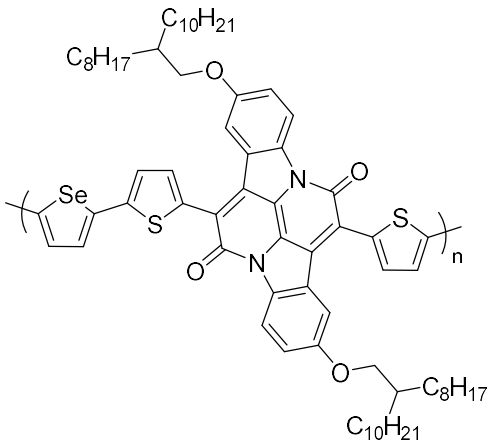


**2.26** (80.0 mg, 65.4 μmol), 2,5-bis(trimethylstannyl)selenophene (29.9 mg, 65.4 μmol), tris(dibenzylideneacetone)dipalladium(0) (3.0 mg, 5 mol%) and tri(o-tolyl)phosphine (4.0 mg, 13.1 μmol) were added to a dry 10 mL microwave vial equipped with a stirrer bar and sealed. Chlorobenzene (2.5 mL) was added via syringe and the solution degassed with argon for 30 min. The vial was then placed in a microwave reactor and heated as follows: 10 min at 100 °C, 5 min at 120 °C, 5 min at 140 °C, 5 min at 160 °C and 20 min at 180 °C. The vial was then allowed to cool. The reaction mixture was added dropwise slowly into rapidly stirring methanol (90 mL) and allowed to stir for 2 h, forming fine dark blue fibres. The polymeric material was then filtered under reduced pressure into a cellulose thimble and washed with methanol then acetone. The polymer was purified by soxhlet extraction as follows: acetone for 12 h, hexane for 12 h and chloroform for 12 h. The chloroform was then concentrated to give a turquoise plastic-like film on the round bottomed flask. This film was dissolved in a minimum volume of hot chlorobenzene (~2 mL) then added dropwise slowly into rapidly stirring methanol. Once addition was complete the methanol was stirred for 30 min then filtered under vacuum, washing carefully with methanol then a small amount of acetone then allowed to dry, forming a blue film. The polymer was air dried for 1 h then placed in a vial and dried under vacuum for 12 h (63.4 mg, 81%).

## 6.3
## *Experimental Procedures for Chapter III*

### Diethyl-2-octyldodecylmalonate (3.9) [97†]

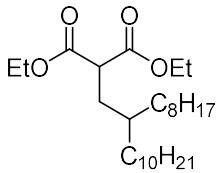


To a fresh solution of sodium ethoxide (1.16 g Na in 100 mL ethanol) under argon was added diethyl malonate (8.06 g, 50 mmol) in one portion and the reaction was heated at reflux for 1 h. To the resulting solution was added 2-octyl-1-dodecyl bromide (20 g, 55 mmol) dropwise and the reaction heated at reflux for 12 h. The reaction was then cooled, diluted with water (200 mL) and extracted with diethyl ether (3 x 100 mL). The combined organic extracts were washed with brine (50 mL), dried over $MgSO_4$ and concentrated *in vacuo* to give the title compound as a yellow oil (20.6 g, 84%).

**$^1$H NMR** (600 MHz, $CDCl_3$) δ 4.19 – 4.08 (m, 4H), 3.46 – 3.32 (m, 1H), 1.81 – 1.75 (m, 2H), 1.39 – 1.06 (m, 39H), 0.88 – 0.78 (m, 6H) **$^{13}$C NMR** (150 MHz, $CDCl_3$) δ 170.0, 61.4, 50.2, 39.9, 39.6, 35.5, 33.3, 33.1, 32.7, 32.0, 31.9, 30.1 29.9, 29.8, 29.7, 29.7, 29.6, 29.5, 29.4, 26.7, 26.6, 26.4, 26.4, 22.8, 14.3, 14.2 **LRMS** *m/z* (EI+) 441 ($MH^+$)

### 2-(2-Octyldodecyl)propanedioic acid (3.11)

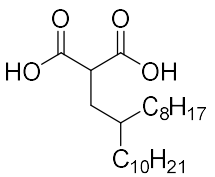


To a solution of diethyl-2-octyldodecylmalonate (12.0 g, 27 mmol) in ethanol (120 mL) was added 2M sodium hydroxide (120 mL) and the reaction was stirred at RT for 12 h. Ethanol was then removed *in vacuo* and the resulting residue acidified and extracted

with diethyl ether (3 x 100 mL). The combined organic extracts were combined, washed with brine (50 mL) and dried over $MgSO_4$ and concentrated *in vacuo*. The crude residue was purified by dry flash chromatography eluting firstly with hexane, then with ethyl acetate to give the title compound as a colourless oil (6.1 g, 57%).

**$^1$H NMR** (600 MHz, $CDCl_3$) δ 11.85 (br s, 2H), 3.50 (t, *J* = 7.5 Hz, 1H), 1.87 (t, *J* = 7.1 Hz, 2H), 1.38 – 1.31 (m, *J* = 12.5 Hz, 1H), 1.31 – 1.17 (m, 27H), 0.86 (t, *J* = 7.0 Hz, 6H) **$^{13}$C NMR** (150 MHz, $CDCl_3$) δ 178.3, 175.58, 49.9, 35.5, 33.2, 33.0, 32.0, 31.9, 30.1, 29.7, 29.4, 26.2, 22.8, 21.1, 20.9, 14.2 **LRMS** *m/z* (EI+) 385 ($MH^+$)

### 4-Octyltetradecanoic acid (3.12)

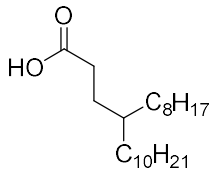


Under argon, neat 2-(2-octyldodecyl)propanedioic acid (6.0 g, 16 mmol) was heated to 190 °C for 2 h. The oil was then cooled and passed through a short silica plug eluting with 50% ethyl acetate in hexane to give the title compound as a colourless oil (3.27 g, 61%).

**$^1$H NMR** (600 MHz, $CDCl_3$) δ 11.29 (br s, 2H), 2.33 – 2.30 (m, 2H), 1.63 – 1.56 (m, 2H), 1.37 – 1.18 (m, 15H), 0.88 (t, *J* = 7.0 Hz, 6H) **$^{13}$C NMR** (150 MHz, $CDCl_3$) δ 181.1, 37.0, 33.3, 32.0, 31.7, 30.2, 29.8, 29.5, 28.5, 26.6, 22.8, 14.2 **LRMS** *m/z* (EI+) 341 ($MH^+$)

### 4-Octyl-1-tetradecanol (3.13)

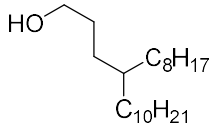


To a solution of 4-octytetradecanoic acid (3.2 g, 9.6 mmol) in anhydrous THF (19 mL) heated to reflux was added a 2M solution of $LiAlH_4$ in THF (4.7 mL) dropwise over 2 h. The reaction was then cooled and quenched with 1M hydrochloric acid solution (100 mL) and the organic material extracted with diethyl ether (3 x 50 mL). The combined organic extracts were washed with brine (50 mL), dried over $MgSO_4$ and concentrated *in vacuo*. The crude residue was passed through a short silica plug eluting with hexane to give the title compound as a colourless oil (2.4 g, 77%).

**$^1$H NMR** (600 MHz, $CDCl_3$) δ 3.60 (t, *J* = 6.8 Hz, 2H), 1.57 – 1.47 (m, 2H), 1.32 – 1.16 (m, 15H), 0.91 – 0.81 (m, 6H) **$^{13}$C NMR** (150 MHz, $CDCl_3$) δ 63.6, 37.3, 33.7, 32.1, 32.0, 30.2, 30.0, 29.9, 29.8, 29.6, 29.5, 26.8, 26.7, 22.8, 14.2 **LRMS** *m/z* (EI+) 326 ($M^+$)

### 4-Octyl-1-tetradecyl bromide (3.14)

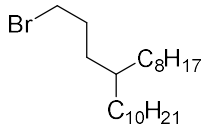


To a solution of 4-octyl-1-tetradecanol (2.3 g, 7.6 mmol) and triphenylphosphine (2.26 g, 8.6 mmol) in DCM (4 mL) cooled to 0 °C was added N-bromosuccinimide (1.52 g, 8.6 mmol) portionwise over 1 h. The reaction was then allowed to warm to RT and stirred for 12 h. The reaction was then concentrated *in vacuo* and the resulting residue taken up in hexane and filtered through a short silica plug eluting with hexane to give the title compound as a colourless oil (2.9 g, quant.).

**$^1$H NMR** (600 MHz, $CDCl_3$) δ 3.39 (t, *J* = 6.9 Hz, 2H), 1.89 – 1.79 (m, 2H), 1.42 – 1.18 (m, 15H), 0.92 – 0.85 (m, 6H) **$^{13}$C NMR** (150 MHz, $CDCl_3$) δ 37.0, 34.6, 33.7, 32.3, 32.1, 30.3, 30.2, 29.9, 29.8, 29.5, 26.7, 26.7, 22.8, 14.3 **LRMS** *m/z* (EI+) 388 ($M^+$)

**2,9-Bis((4-octyltetradecyl)oxy)-7,14-di(thiophen-2-yl)diindolo[3,2,1-*de*:3',2',1'-*ij*][1,5]naphthyridine-6,13-dione (3.16)**

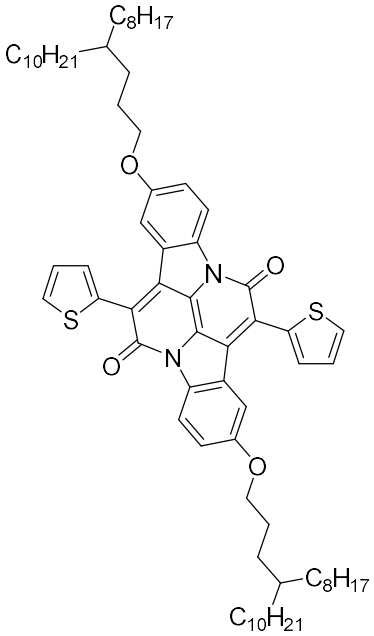


To a solution of **2.24** (505 mg, 1 mmol) and 4-octyl-1-tetradecyl bromide (0.98 g, 2.5 mmol) in anhydrous dimethylformamide (50 mL) was added potassium carbonate (1.3 g, 10 mmol) and the reaction was heated at 80 °C for 12 h. After cooling, inorganic salts were removed by filtration and the filtrate was separated between brine (100 mL) and chloroform (100 mL). The organic layer was extracted with brine (3 × 30 mL), dried over $MgSO_4$ and concentrated *in vacuo*. The crude residue was purified by flash chromatography on silica gel eluting with 40→100% chloroform in hexane to give a purple oily solid (487 mg, 44%).

**$^1$H NMR** (400 MHz, $CDCl_3$) δ 8.43 (d, *J* = 8.9 Hz, 2H), 7.74 (dd, *J* = 3.6, 1.1 Hz, 2H), 7.69 (dd, *J* = 5.1, 1.1 Hz, 2H), 7.66 (d, *J* = 2.5 Hz, 2H), 7.27 (dd, *J* = 4.8, 3.6 Hz, 2H), 7.10 (dd, *J* = 8.9, 2.5 Hz, 2H), 3.93 (t, *J* = 6.7 Hz, 4H), 1.82 – 1.69 (m, 4H), 1.44 – 1.33 (m, 8H), 1.34 – 1.14 (m, 62H), 0.93 – 0.83 (m, 12H) **$^{13}$C NMR** (150 MHz, $CDCl_3$) δ 158.5, 157.7, 138.1, 134.8, 130.3, 130.0, 127.2, 126.4, 125.1, 122.5, 118.3, 111.1, 69.3, 37.3, 33.7, 32.0, 30.2, 29.8, 29.5, 26.8, 26.4, 22.8, 14.2 **HRMS** Found (MALDI): $[MH]^+$ 1123.7342, $C_{72}H_{103}N_2O_4S_2$ requires 1123.7359

**7,14-Bis(5-bromothiophen-2-yl)-2,9-bis((4-octyltetradecyl)oxy)diindolo[3,2,1-*de*:3',2',1'-*ij*][1,5]naphthyridine-6,13-dione (3.17)**

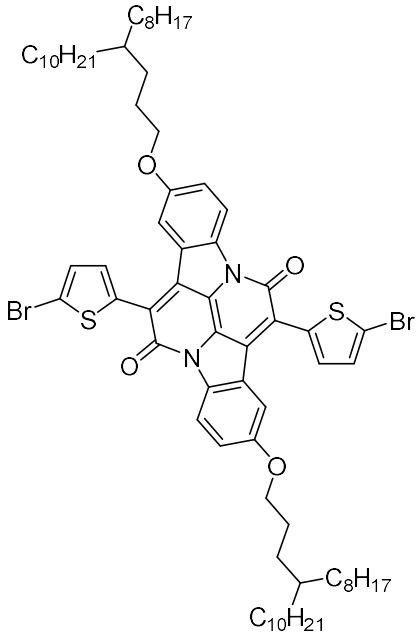


To a solution of **3.16** (450 mg, 0.4 mmol) in dichloromethane (25 mL) at 0 °C was added N-bromosuccinimide (150 mg, 0.84 mmol) in one portion. The reaction was allowed to warm to RT naturally over 12 h and was then concentrated *in vacuo* and the residue purified by column chromatography eluting with 40→100% chloroform in hexane to give the title compound as a purple solid (497 mg, 97%).

**$^1$H NMR** (400 MHz, $CDCl_3$) δ 8.42 (d, *J* = 9.0 Hz, 2H), 7.70 (d, *J* = 2.5 Hz, 2H), 7.56 (d, *J* = 4.0 Hz, 2H), 7.23 (d, *J* = 4.0 Hz, 2H), 7.11 (dd, *J* = 9.0, 2.5 Hz, 2H), 3.96 (t, *J* = 6.6 Hz, 4H), 1.85 – 1.70 (m, 4H), 1.46 – 1.34 (m, 8H), 1.34 – 1.17 (m, 62H), 0.91 – 0.82 (m, 12H) **$^{13}$C-NMR** (150 MHz, $CDCl_3$) δ 158.2, 137.8, 136.6, 129.9, 129.6, 129.5, 129.1, 124.5, 122.6, 118.7, 111.1, 72.0, 51.1, 37.3, 32.0, 30.3, 29.9, 29.5, 26.8, 26.4, 22.8, 14.3 **HRMS** Found (MALDI): $[MH]^+$ 1279.5569, $C_{72}H_{101}Br_2N_2O_4S_2$ requires 1279.5570

**C3-INDTT**

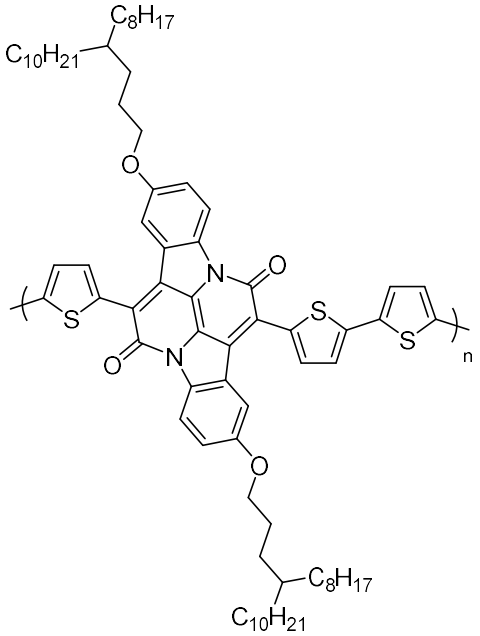


Monomer **3.17** (72.6 mg, 56.8 µmol), 2,5-bis(trimethylstannyl)thiophene (23.3 mg, 56.8 µmol), tris(dibenzylideneacetone)dipalladium(0) (2.0 mg, 2.27 µmol, 4 mol%) and tri(o-tolyl)phosphine (2.75 mg, 9.09 µmol) were added to a dry 10 mL microwave vial equipped with a stirrer bar and sealed. Chlorobenzene (3.0 mL) was added via syringe and the solution was thoroughly degassed. The vial was then placed in a microwave reactor and heated as follows: 10 min at 100 °C, 5 min at 120 °C, 5 min at 140 °C, 5 min at 160 °C and 20 min at 180 °C. The reaction was cooled and poured into rapidly stirring methanol (100 mL). The crude polymeric material was purified by soxhlet extraction as follows: acetone for 12 h, hexane for 12 h and chloroform for 12 h. The chloroform was then concentrated to give a turquoise film which was dissolved in a minimum volume of hot chlorobenzene and then precipitated into rapidly stirring methanol. After stirring for 30 min the polymer was collected by vacuum filtration, and air dried for 1 h. Finally, the polymer was dried under vacuum for 12 h (64 mg, 93%).

**C3-INDTS**

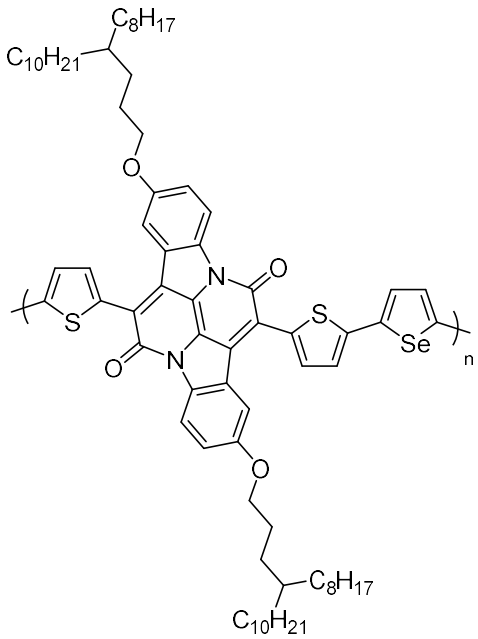


Monomer **3.17** (70.0 mg, 54.7 µmol), 2,5-bis(trimethylstannyl)selenophene (25.2 mg, 54.7 µmol), tris(dibenzylideneacetone)dipalladium(0) (1.9 mg, 2.19 µmol, 4 mol%) and tri(o-tolyl)phosphine (2.65 mg, 8.75 µmol) were added to a dry 10 mL microwave vial equipped with a stirrer bar and sealed. Chlorobenzene (2.8 mL) was added via syringe and the solution degassed with argon for 30 min. The vial was then placed in a microwave reactor and heated as follows: 10 min at 100 °C, 5 min at 120 °C, 5 min at 140 °C, 5 min at 160 °C and 20 min at 180 °C. The reaction was cooled and poured into rapidly stirring methanol (100 mL) and allowed to stir for 30 min. The polymeric material was then filtered under reduced pressure into a cellulose thimble and washed with methanol then acetone. The polymer was purified by soxhlet extraction as follows: acetone for 12 h, hexane for 12 h and chloroform for 12 h. The chloroform was then concentrated and the polymer was dissolved in a minimum volume of hot chlorobenzene and then precipitated into rapidly stirring methanol. After stirring for 30 min the polymer was collected by vacuum filtration, and air dried for 1 h. Finally, the polymer was dried under vacuum for 12 h (59 mg, 86%).

**C3-INDTBT**

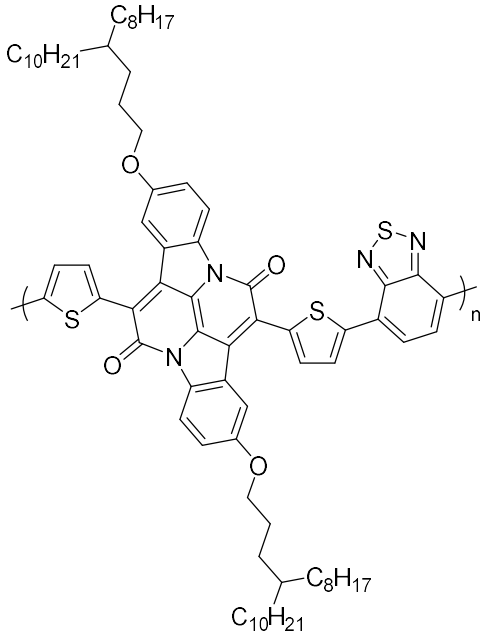


4,7-Bis(4,4,5,5-tetramethyl-1,3,2-dioxaborolan-2-yl)benzo[c][1,2,5]thiadiazole (29.9 mg, 77.8 µmol), tetrakis(triphenylphosphine)palladium(0) (1.8 mg, 2 mol%) and monomer **3.17** (100 mg, 77.8 µmol) were added to a degassed 10 mL microwave vial equipped with a stirrer bar and sealed. A degassed solution of aliquot 336 (2 drops) in toluene (2.5 mL) was added via syringe and the solution further degassed with argon for 30 min. A degassed solution of 1M $Na_2CO_3$ (0.5 mL) was then added and the reaction was heated at 125 °C for 3 days. The reaction mixture was cooled and added dropwise into rapidly stirring methanol (70 mL) and allowed to stir for 1 h. The polymeric material was then filtered under reduced pressure into a cellulose thimble and washed with methanol then acetone. The polymer was purified by soxhlet extraction as follows: acetone for 12 h, hexane for 12 h and chloroform for 12 h. The chloroform was then concentrated to give a turquoise film which was dissolved in a minimum volume of hot chlorobenzene, then precipitated into methanol. After stirring for 30 min the polymer was collected by vacuum filtration, and air dried for 1 h. Finally, the polymer was dried under vacuum for 12 h (81 mg, 83%).

## 6.4
## *Experimental Procedures for Chapter IV*

### 3-Nitro-4-methylphenylammonium hydrosulfate (4.2) [220†]

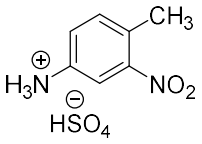


Toluidine (40.0 g, 0.37 mol) was cautiously dissolved in concentrated sulphuric acid (110 mL) and cooled to -10 °C. A solution of concentrated nitric acid (19 mL, 0.43 mol, 70%) in concentrated sulphuric acid (70 mL) was added dropwise insuring the internal temperature did not rise above -5 °C. After 6 h the reaction was poured onto ice (1 kg) precipitating a yellow solid which was collected by vacuum filtration and washed well with cold water. The solid was dried thoroughly to give the title compound as a pale-yellow solid (76.9 g, 83%).

A sample of solid was converted to 3-nitro-4-methylphenylamine for analysis.

**$^1$H NMR** (600 MHz, $CDCl_3$) δ 7.28 (d, *J* = 2.5 Hz, 1H), 7.07 (d, *J* = 8.2 Hz, 1H), 6.80 (dd, *J* = 8.2, 2.5 Hz, 1H), 3.84 (s, 2H), 2.45 (s, 3H) **LRMS** ($Cl^+$) *m/z* 153 $[MH]^+$

### 4-Bromo-2-nitromethylbenzene (4.3) [276†]

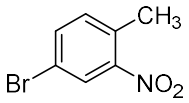


3-Nitro-4-methylphenylammonium hydrosulfate (29.5 g, 0.12 mol) was dissolved in water (129 mL) and hydrobromic acid (38.5 mL, 0.34 mol, 48%) and cooled to -5 °C. An ice-cold solution of sodium nitrite (15.2 g, 0.22 mol) in water (40 mL) was added slowly to the stirred amine, maintaining the temperature below 0 °C, and stirred for 30 min. Separately, copper(I) bromide (17.2 g, 0.12 mol) in hydrobromic acid (23.8 mL, 0.21 mol, 48%) was heated to reflux. The ice-cold diazonium salt was added portionwise to the

copper solution, liberating nitrogen dioxide. The reaction was then heated at reflux for 2 h, cooled and extracted with diethyl ether (3 × 100 mL). The combined organic layers were successively washed with 5% ammonium hydroxide solution (2 × 100 mL), water (100 mL) and brine (100 mL). The organic layer was separated, dried over magnesium sulphate and concentrated *in vacuo* to give a brown oil from which a brown solid separated. Recrystallisation from ethanol yielded 14.8 g (57%) of the title compound as brown crystals.

**$^1$H NMR** (600 MHz, $CDCl_3$) δ 8.12 (d, *J* = 2.0 Hz, 1H), 7.62 (dd, *J* = 8.2, 2.0 Hz, 1H), 7.23 (d, *J* = 8.2 Hz, 1H), 2.55 (s, 3H) **LRMS** (CI+) *m/z* 217/215 $[MH]^+$

### 4-Bromo-2-nitrobenzaldehyde (4.5) [220†]

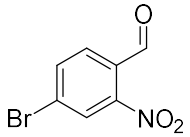


4-Bromo-2-nitromethylbenzene (27.5 g, 0.13 mol) and N,N-dimethylformamide dimethyl acetal (50.6 mL, 0.38 mol) were refluxed in anhydrous dimethylformamide (130 mL) for 3 d under argon. The reaction turned a deep red colour as an enamine was generated. Separately, sodium periodate (81.5 g, 0.38 mol) was dissolved in a 2:1 mixture of $H_2O$:DMF (380 mL). The enamine was cooled to room temperature and the entire contents of the reaction added dropwise to the vigorously stirring periodate solution giving rise to a light brown suspension. If stirring became prevented due to viscosity, $H_2O$/DMF (2:1) was added until stirring resumed. The reaction was stirred for 3 h and then filtered. The filter cake was broken up and washed thoroughly with toluene (300 mL). From the filtrate, the organic layer was separated and washed with water (2 × 200 mL) then brine (2 × 200 mL), dried over magnesium sulphate and concentrated *in vacuo* to give an oil to which hexane was added to crystallise the aldehyde (19.6 g, 67%). Note, if a solid is obtained following concentration, the crude residue is best purified by dry-flash chromatography eluting with 40% ethyl acetate in hexanes.

**$^1$H NMR** (400 MHz, $CDCl_3$) δ 10.39 (s, 1H), 8.27 (d, *J* = 1.8 Hz, 1H), 7.93 (dd, *J* = 8.3, 1.4 Hz, 1H), 7.85 (d, *J* = 8.3 Hz, 1H) **LRMS** (CI+) *m/z* 232/230 $[M]^+$

### (*E*)-6,6'-dibromo-[2,2'-biindolinylidene]-3,3'-dione (4.6)
*also* **6,6'-dibromoindigo**

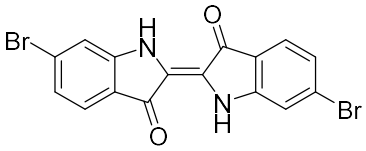

4-bromo-2-nitrobenzaldehyde (19.6 g) was dissolved in acetone (200 mL) and water (200 mL) was added dropwise with vigorous stirring to create a fine suspension. A 1M sodium hydroxide solution (100 mL) was added dropwise, precipitating the purple indigoid. Once addition was complete the reaction was stirred overnight then filtered and washed with acetone. The purple solid was dried thoroughly to give 10.4 g of the title compound (58%).

**$^1$H NMR** (600 MHz, DMSO) δ 7.57 (d, *J* = 8.1 Hz, 2H), 7.55 (s, *J* = 1.1 Hz, 2H), 7.12 (d, *J* = 8.1 Hz, 2H) **$^{13}$C NMR** unobtainable due to low solubility **HRMS** Found (EI): $[M]^+$ 417.8957, $C_{16}H_8Br_2N_2O_2$ requires 417.8953

### 3,10-Dibromo-7,14-bis(4-((2-octyldodecyl)oxy)phenyl)diindolo[3,2,1-*de*:3',2',1'-*ij*][1,5]naphthyridine-6,13-dione (4.7)

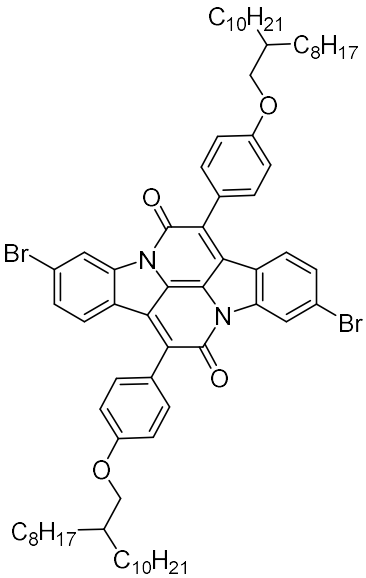

To a solution of acetic acid **2.9** (24 g, 56 mmol) dissolved in anhydrous DCM (110 mL) at RT was added two drops of anhydrous DMF and then excess thionyl chloride. The reaction was heated at reflux until complete by $^1$H NMR (~3 h), after which all volatiles were removed *in vacuo* to give the corresponding acetyl chloride **2.11** as a viscous luminous yellow oil which was used immediately without further purification.

Under normal atmospheric conditions, a suspension of 6,6'-dibromoindigo (5.8 g, 14 mmol) in xylenes (185 mL) was heated to 165 °C. Acetyl chloride **2.11** was then added in one portion and the reaction heated for 12 h. Xylenes were then removed *in vacuo* and the crude residue was purified by dry-flash chromatography eluting with 40% chloroform in hexane ($R_F$ = 0.2, pink). The fractions containing the product were combined and concentrated *in vacuo* and the residue taken up in a minimum volume of ethyl acetate and collected by vacuum filtration giving the title compound as a brilliant-red solid (950 mg, 6%).

**$^1$H NMR** (600 MHz, $CDCl_3$) δ 8.72 (d, *J* = 1.8 Hz, 2H), 7.65 (d, *J* = 8.8 Hz, 4H), 7.58 (d, *J* = 8.5 Hz, 2H), 7.37 (dd, *J* = 8.5, 1.8 Hz, 2H), 7.09 (d, *J* = 8.8 Hz, 4H), 3.96 (d, *J* = 5.6 Hz, 4H), 1.90 – 1.78 (m, 2H), 1.50 – 1.21 (m, 64H), 0.89 (td, *J* = 7.0, 5.3 Hz, 12H) **$^{13}$C NMR** (150 MHz, $CDCl_3$) δ 160.6, 159.6, 145.1, 131.7, 131.0, 130.6, 129.3, 126.3, 126.2, 125.1, 124.5, 122.1, 121.1, 114.7, 71.2, 38.1, 32.1, 31.5, 30.2, 29.8, 29.5, 27.0, 22.8, 14.3 **HRMS** Found (EI): $[MH]^+$ 1211.5818, $C_{72}H_{97}Br_2N_2O_4$ requires 1211.5815

### 7,14-Bis(4-((2-octyldodecyl)oxy)phenyl)-3,10-bis(4,4,5,5-tetramethyl-1,3,2-dioxaborolan-2-yl)diindolo[3,2,1-*de*:3',2',1'-*ij*][1,5]naphthyridine-6,13-dione (4.8)

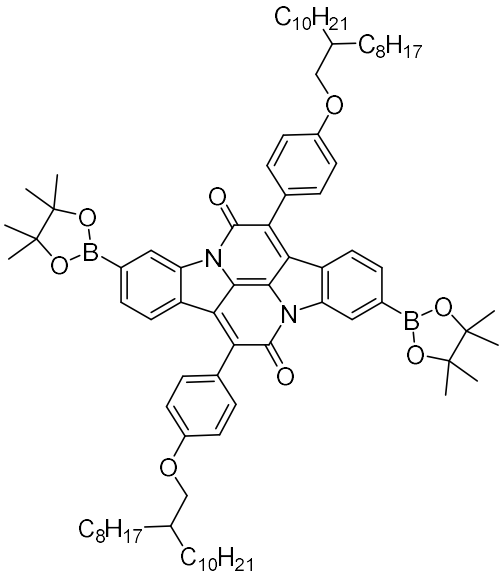


In a dry, degassed microwave vial, a solution of indolonaphthyridine **4.7** (300 mg, 0.25 mmol), [1,1′-bis(diphenylphosphino)ferrocene]dichloropalladium(II) (11 mg, 6 mol%), potassium acetate (145 mg, 1.5 mmol), bis(pinacolato)diboron (151 mg, 0.6 mmol) in anhydrous dioxane (10 mL) was heated to 80 °C under argon for 12 h. The reaction was then cooled and methanol was added. The resulting precipitate was collected by vacuum filtration (282 mg, 87%).

**$^1$H NMR** (600 MHz, $CDCl_3$) δ 8.98 (s, 2H), 7.74 – 7.69 (m, 6H), 7.66 – 7.64 (m, 2H), 7.11 – 7.07 (m, 4H), 3.96 (d, *J* = 5.7 Hz, 4H), 1.90 – 1.81 (m, 2H), 1.54 – 1.47 (m, 4H), 1.47 – 1.20 (m, 84H), 0.91 – 0.86 (m, 12H) **$^{13}$C NMR** (150 MHz, $CDCl_3$) δ 160.4, 159.7, 144.1, 132.3, 131.9, 131.3, 131.0, 128.3, 125.7, 124.6, 123.7, 122.2, 114.5, 84.4, 71.2, 51.1, 38.1, 32.1, 31.5, 30.2, 29.8, 29.5, 27.0, 25.0, 22.8, 14.3 **HRMS** Found (EI): $[MH]^+$ 1307.9308, $C_{84}H_{121}B_2N_2O_8$ requires 1307.9309

### XINDP-DPP (*also* XDPP)

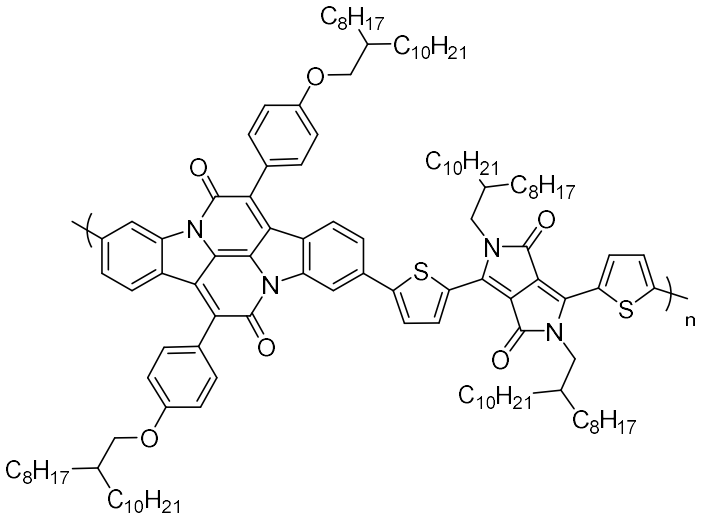


3,6-Bis(5-bromothiophen-2-yl)-2,5-bis(2-octyldodecyl)-2,5-dihydropyrrolo[3,4-*c*]pyrrole-1,4-dione (109 mg, 0.11 mmol), tetrakis(triphenylphosphine)palladium(0) (12.4 mg, 10 mol%) and monomer **4.8** (140 mg, 0.11 mmol) were added to a degassed 10 mL microwave vial equipped with a stirrer bar and sealed. A degassed solution of aliquot 336 (2 drops) in toluene (3 mL) was added via syringe and the solution further degassed with argon for 30 min. A degassed solution of 1M $K_2CO_3$ (0.6 mL) was then added and the reaction was heated at 125 °C for 3 days. The reaction mixture was cooled and added into rapidly stirring methanol (100 mL) and allowed to stir for 30 min. The polymeric material was then filtered under reduced pressure into a cellulose thimble and washed with methanol then acetone. The polymer was purified by soxhlet extraction as follows: acetone for 12 h, hexane for 12 h and chloroform for 12 h. The chloroform was then concentrated and the plastic film was dissolved in a minimum volume of hot chlorobenzene, then precipitated into methanol. After stirring for 30 min the polymer was collected by vacuum filtration, and air dried for 1 h. Finally, the polymer was dried under vacuum for 12 h (169 mg, 83%).

**XINDP-INDT** (*also* **XINDT**)

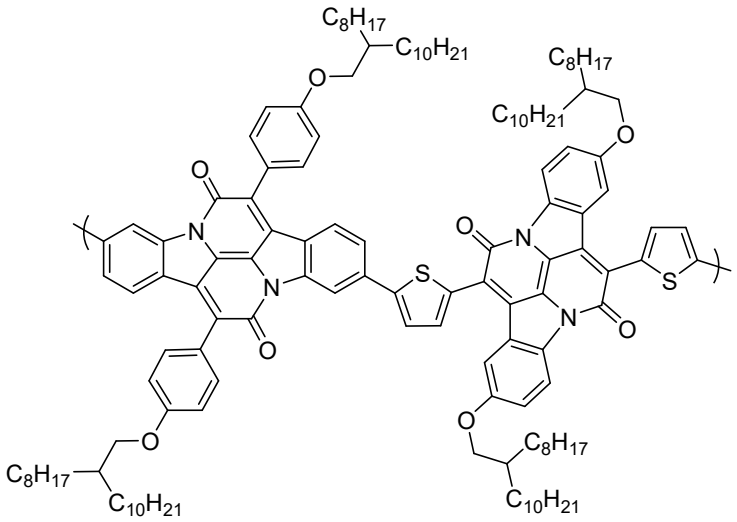


Tetrakis(triphenylphosphine)palladium(0) (6.8 mg, 10 mol%), monomer **4.85.** (76.4 mg, 58.4 µmol) and INDT (**2.26**, 71.6 mg, 58.4 µmol) were added to a degassed 10 mL microwave vial equipped with a stirrer bar and sealed. A degassed solution of aliquot 336 (2 drops) in toluene (1.7 mL) was added via syringe and the solution further degassed with argon for 30 min. A degassed solution of 1M $K_2CO_3$ (0.35 mL) was then added and the reaction was heated at 125 °C for 3 days. The reaction mixture was cooled and added into rapidly stirring methanol (100 mL) and allowed to stir for 30 min. The polymeric material was then filtered under reduced pressure into a cellulose thimble and washed with methanol then acetone. The polymer was purified by soxhlet extraction as follows: acetone for 12 h, hexane for 12 h and chloroform for 12 h. The chloroform was then concentrated and the plastic film was dissolved in a minimum volume of hot chlorobenzene, then precipitated into methanol. After stirring for 30 min the polymer was collected by vacuum filtration, and air dried for 1 h. Finally, the polymer was dried under vacuum for 12 h (107 mg, 86%).

## 6.5
## *Experimental Procedures for Chapter V*

### General Procedure 5.1
***Oxidation of 6-Functionalised Indigoids***

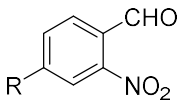


A solution of an *ortho*-nitrotoluene and N,N-dimethylformamide dimethyl acetal (3 equiv.) were heated to 140 °C in anhydrous DMF (1M) under argon for 16 h. The resulting red solution was cooled and added via cannula dropwise to a vigorously stirring solution of sodium periodate (3 equiv.) in $H_2O$:DMF (1M to $NaIO_4$, 2:1) and stirred for 3 h at RT. The solution was filtered and the filter cake washed thoroughly with toluene. From the filtrate, the organic layer was separated, washed with water then brine, then dried over $MgSO_4$ and concentrated *in vacuo*. The crude residues were purified by column chromatography on silica gel eluting with 0→60% ethyl acetate in hexanes.

### General Procedure 5.2
***Synthesis of 6,6'-Functionalised Indigoids***

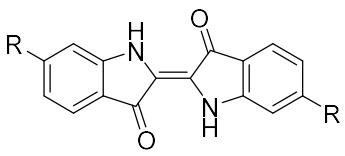


To a solution of an *ortho*-nitrobenzaldehyde dissolved in acetone (10 mL/g) was added deionised water (10 mL/g). If the precursor was a solid, it was precipitated out as a fine suspension; if it was an oil, a turbid solution was formed. To the mixture was added 1M NaOH (5 mL/g) dropwise. All reactions immediately darkened and the corresponding indigo was precipitated. After addition of the base, the reaction was stirred at RT for 4 h,

then the indigo was collected by vacuum filtration and washed with copious amounts of methanol until scrupulously clean.

### General Procedure 5.3

***Synthesis of 6,6'-Functionalised Indolonaphthyridine Thiophenes***

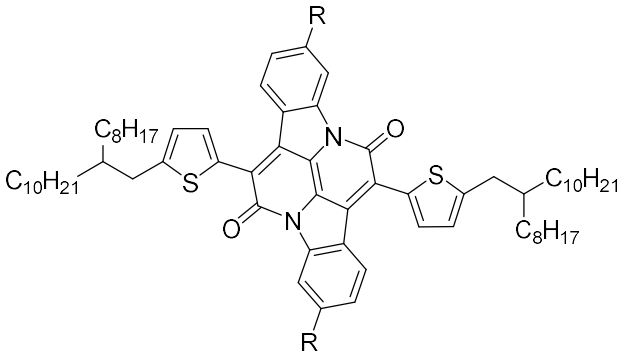


To a solution of thiophenylacetic acid **5.41** in anhydrous DCM (0.1 M) and two drops of anhydrous DMF was added excess thionyl chloride. After completion as monitored by NMR (~3 h), the reaction was cooled and all volatiles were removed $in\ vacuo$ to give the corresponding thiophenylacetyl chloride **5.41** as a luminous yellow oil that was used without further purification.

**Crude $^1$H NMR** (400 MHz, $CDCl_3$) δ 6.79 (d, *J* = 3.4 Hz, 1H), 6.62 (d, *J* = 3.4 Hz, 1H), 4.27 (s, 2H), 2.71 (d, *J* = 6.7 Hz, 2H), 1.65 – 1.55 (m, 1H), 1.28 (d, *J* = 18.2 Hz, 32H), 0.92 – 0.79 (m, 6H)

An indigoid (500 mg) was heated to 165 °C in mixed xylenes (40 mL) under normal atmospheric conditions. Fresh thiophenylacetyl chloride **5.41** (3 g) was then added in one portion and the reaction was heated at reflux for 12 h. The reaction was then cooled, filtered to remove unreacted any unreacted indigoid, and then concentrated $in\ vacuo$. The crude residue was purified by column chromatography eluting with 0→75% chloroform in hexane, then precipitated from n-pentane at -78 °C and collected by filtration or centrifuge. The pure material was passed twice through cotton to remove silica and finally collected by filtration with methanol to give the pure indolonaphthyridine thiophene compound.

**7,14-diphenyldiindolo[3,2,1-*de*:3',2',1'-*ij*][1,5]naphthyridine-6,13-dione (5.13)**
also ***Cibalackrot***

*reproduced from Section* 6.2*, compound* **2.3**

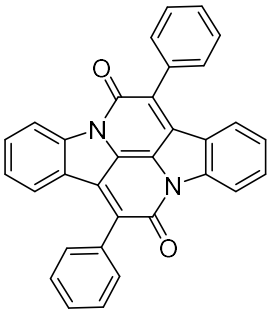


Under normal atmospheric conditions, phenylacetyl chloride (5 mL) was added to a suspension of indigo (1 g) in mixed xylenes (100 mL) heated at 165 °C. The reaction was heated overnight and then xylenes were removed *in vacuo*. The crude residue was taken up in warm chloroform (200 mL) and eluted with chloroform through a 2-inch plug of silica gel. The fractions containing the product (light pink) were concentrated *in vacuo* and taken up in a minimum volume of ethyl acetate and collected by vacuum filtration giving the title compound as a brick-red solid (70 mg, 4%).

*For characterisation, see compound* **2.3**

**7,14-Bis(4-methoxyphenyl)diindolo[3,2,1-*de*:3',2',1'-*ij*][1,5]naphthyridine-6,13-dione (5.27)**

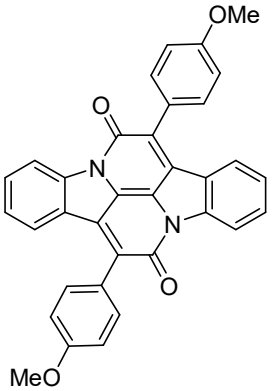


To a solution of 2-(4-methoxyphenyl)acetic acid (3.74 g, 23 mmol) in anhydrous DCM (10 mL) was added two drops of anhydrous DMF, followed by excess thionyl chloride (4.9 mL, 67 mmol). The reaction was heated to reflux for 3h and then volatiles were removed *in vacuo* to the corresponding phenylacetyl chloride **5.24** which was used without further purification.

A suspension of indigo (0.55 g, 2.1 mmol) in xylenes (42 mL) was heated to 165 °C. Acetyl chloride **5.24** was then added in one portion and the reaction heated for a further 12 h. The reaction was then cooled to room temperature, and precipitates were collected by filtration under reduced pressure with methanol washings to give the title compound as a red powder (115 mg, 11%).

**$^1$H NMR** (600 MHz, $CDCl_3$) δ 8.52 (d, *J* = 7.9 Hz, 2H), 7.74 – 7.65 (m, 6H), 7.56 (t, *J* = 7.6 Hz, 2H), 7.25 – 7.21 (m, 2H), 7.12 (d, *J* = 8.2 Hz, 4H), 3.94 (s, 6H) **$^{13}$C NMR** (150 MHz, $CDCl_3$, poor solubility) δ 160.5, 159.9, 144.7, 132.0, 131.8, 126.1, 125.5, 117.8, 114.1, 55.5, 29.8, 14.2 **HRMS** Found (EI): $[M]^+$ 522.1579, $C_{34}H_{22}N_2O_4$ requires 522.1580

### 7,14-Bis(4-bromophenyl)diindolo[3,2,1-*de*:3',2',1'-*ij*][1,5]naphthyridine-6,13-dione (5.28)

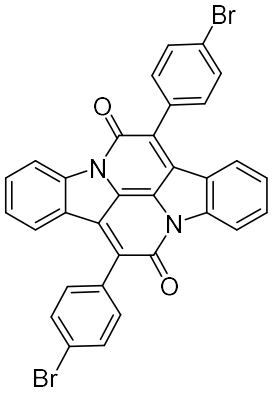


To a solution of 2-(4-bromophenyl)acetic acid (4.9 g, 23 mmol) in anhydrous DCM (10 mL) was added two drops of anhydrous DMF, followed by excess thionyl chloride (4.9 mL, 67 mmol). The reaction was heated to reflux for 3h and then volatiles were removed *in vacuo* to the corresponding phenylacetyl chloride **5.25** which was used without further purification.

A suspension of indigo (0.55 g, 2.1 mmol) in xylenes (42 mL) was heated to 165 °C. Acetyl chloride **5.25** was then added in one portion and the reaction heated for a further 12 h. The reaction was then cooled to room temperature, and precipitates were collected by filtration under reduced pressure with methanol washings to give the title compound as a brown solid (232 mg, 18%).

**$^1$H NMR** (600 MHz, $CDCl_3$) δ 8.50 (d, *J* = 8.2 Hz, 2H), 7.74 (d, *J* = 8.4 Hz, 4H), 7.65 – 7.57 (m, 8H), 7.26 – 7.24 (m, 2H) **$^{13}$C NMR** unavailable due to poor solubility **HRMS** Found (EI): [M]+ 617.9574, $C_{32}H_{16}Br_2N_2O_2$ requires 617.9579

### 7,14-Bis(4-isopropylphenyl)diindolo[3,2,1-*de*:3',2',1'-*ij*][1,5]naphthyridine-6,13-dione (5.29)

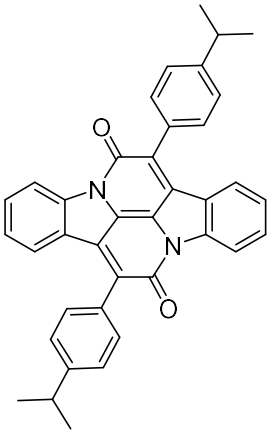

To a solution of 2-(4-isopropylphenyl)acetic acid (1.0 g, 6 mmol) in anhydrous DCM (40 mL) was added two drops of anhydrous DMF, followed by excess thionyl chloride (3 mL). The reaction was heated to reflux for 3h and then volatiles were removed *in vacuo* to the corresponding phenylacetyl chloride **5.26** which was used without further purification.

A suspension of indigo (260 mg g, 0.1 mmol) in xylenes (19 mL) was heated to 165 °C. Acetyl chloride **5.26** was then added in one portion and the reaction heated for a further 12 h. The reaction was then cooled to room temperature, and precipitates were collected by filtration washing with methanol. The crude solid was purified by dry-flash chromatography on silica gel eluting with chloroform to give the title compound as a red solid (7 mg, 13%).

**$^1$H NMR** (600 MHz, $CDCl_3$) δ 8.51 (d, *J* = 8.0 Hz, 2H), 7.67 (dd, *J* = 8.2, 2.0 Hz, 6H), 7.56 (t, *J* = 7.8 Hz, 2H), 7.45 (d, *J* = 8.1 Hz, 4H), 7.24 (t, *J* = 7.7 Hz, 2H), 3.09 – 3.01 (m, 2H), 1.37 (d, *J* = 6.9 Hz, 12 H) **$^{13}$C NMR** (150 MHz, $CDCl_3$) δ 159.8, 150.3, 144.8, 132.1, 131.9, 131.4, 131.0, 130.2, 126.7, 126.1, 126.0, 125.7, 122.2, 117.7, 34.3, 24.1 **HRMS** Found (EI): $[M]^+$ 546.2301, $C_{38}H_{30}N_2O_2$ requires 546.2307

### (*E*)-6,6'-bis(trifluoromethyl)-[2,2'-biindolinylidene]-3,3'-dione (5.31)

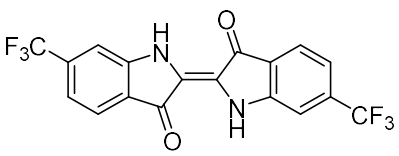

General procedure 5.2 was used with 2-nitro-4-(trifluoromethyl)benzaldehyde (1.0 g), to give the title compound as a blue solid (480 mg, 53%).

**$^1$H NMR** (600 MHz, DMSO) δ 10.96 (s, 1H), 7.84 (d, *J* = 7.9 Hz, 1H), 7.68 (s, 1H), 7.26 (d, *J* = 7,9 Hz, 1H) **$^{13}$C NMR** (150 MHz, DMSO) δ 187.1, 151.9, 134.6 (d), 124.8, 122.9, 121.6, 121.1, 116.6, 110.4 **HRMS** Found (EI): $[MH]^+$ 399.0475, $C_{18}H_9F_6N_2O_2$ requires 399.0568

### 7,14-Bis(4-((2-octyldodecyl)oxy)phenyl)-3,10-bis(trifluoromethyl)diindolo[3,2,1-*de*:3',2',1'-*ij*][1,5]naphthyridine-6,13-dione (5.32)

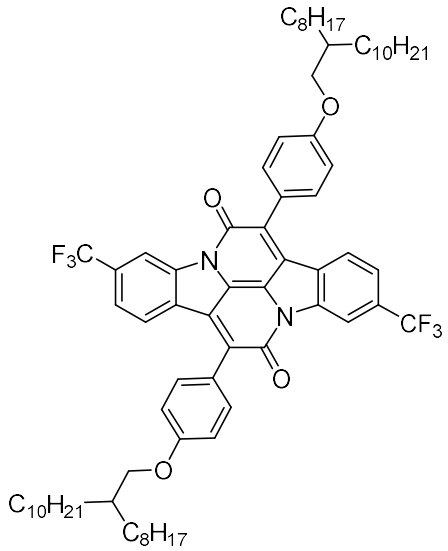


Under normal atmospheric conditions, a suspension of indigo **5.31** (1.5 g, 3.8 mmol) in xylenes (50 mL) was heated to 165 °C. Acetyl chloride **2.11** (6.8 g, 15 mmol) was then added in one portion and the reaction heated for 12 h. Xylenes were then removed *in vacuo* and the crude residue was purified by dry-flash chromatography eluting with 0→100% chloroform in hexane to give the title compound as a purple solid (64 mg, 1.4%).

**$^1$H NMR** (600 MHz, $CDCl_3$) δ 8.84 (s, 2H), 7.88 (d, *J* = 8.2 Hz, 2H), 7.69 (d, *J* = 8.5 Hz, 4H), 7.53 (d, *J* = 8.3 Hz, 2H), 7.12 (d, *J* = 8.6 Hz, 4H), 3.97 (d, *J* = 5.6 Hz, 2H), 1.90 – 1.80 (m, 2H), 1.54 – 1.47 (m, 4H), 1.47 – 1.40 (m, 4H), 1.35 (m, 58H), 0.93 – 0.85 (m, 12H) **$^{13}$C NMR** (150 MHz, $CDCl_3$) δ 160.9, 159.5, 144.2, 133.8, 133.5, 132.5, 131.8, 130.0, 129.1, 125.7, 124.8, 124.5, 123.2, 122.7, 122.3, 114.8, 71.3, 38.1, 32.1, 31.5, 30.2, 29.8, 29.5, 27.0, 22.8, 14.3 **HRMS** Found (EI): $[M]^+$ 1190.7277, $C_{74}H_{96}F_6N_2O_4$ requires 1190.7274

### 2-Octyldodecanoic acid (5.34) [277†]

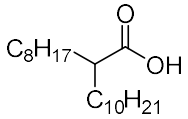


Under normal atmospheric conditions, periodic acid (50 g, 0.22 mol) was stirred in acetonitrile (300 mL) briefly at RT, then cooled to 0 °C. To the mixture was added 2-octyldodecanol (30 g, 0.1 mol) in one portion, followed by the dropwise addition of a solution of pyridinium chlorochromate (430 mg, 2 mol%) in acetonitrile (40 mL). The reaction was then allowed to warm to RT and stirred for 12 h. The reaction was then diluted with ethyl acetate (200 mL) and saturated $NaHCO_3$ solution was carefully added (500 mL). The mixture was then filtered to remove salts and the organic layer was then separated from the filtration and further washed with saturated $NaHCO_3$ solution (100 mL) then brine (100 mL). The organic layer was separated, dried over $MgSO_4$ and concentrated *in vacuo* to give the title compound as a pale-yellow oil from which a white solid separated (25 g, 80%).

**$^1$H NMR** (500 MHz, $CDCl_3$) δ 2.41 – 2.30 (m, 1H), 1.67 – 1.56 (m, 2H), 1.52 – 1.42 (m, 2H), 1.36 – 1.19 (m, 28H), 0.88 (t, *J* = 6.8 Hz, 6H) **LRMS** (EI) *m/z* 312 $[M]^+$

### Methyl 2-(thiophen-2-yl)acetate (5.37)

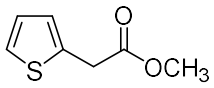


Under normal atmospheric conditions, a solution of 2-(thiophen-2-yl)acetic acid (25 g, 0.18 mol) and conc. sulphuric acid (3 mL) in methanol (350 mL) was heated at reflux for 4 h. The reaction was then cooled, diluted with water (500 mL) and extracted with diethyl ether (200 mL). The ether was separated and washed with brine (2 × 50 mL), dried over $MgSO_4$ and concentrated *in vacuo* to give the title compound as a pale brown oil (25.9 g, 92%).

**$^1$H NMR** (300 MHz, $CDCl_3$) δ 7.24 – 7.19 (m, 1H), 6.99 – 6.92 (m, 2H), 3.85 (s, 2H), 3.73 (s, 3H) **$^{13}$C NMR** (150 MHz, CDCl3) δ 171.1, 135.1, 127.0, 126.9, 125.2, 52.4, 35.3 **HRMS** Found (ES): $[MH]^+$ 157.0368, $C_7H_9O_2S$ requires 157.0323

### 2-Octyldodecanoyl chloride (5.35)

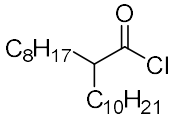


2-Octyldodecanoic acid (16.3 g, 52 mmol), thionyl chloride (20 mL, 0.26 mol) and anhydryous DMF (2 drops) were heated to reflux in anhydrous DCM (100 mL) for 3 h. The reaction was then cooled and all volatiles removed *in vacuo* yielding the title compound as a yellow oil (quant.) that was used immediately and without further purification.

### Methyl 2-(5-(2-octyldodecanoyl)thiophen-2-yl)acetate (5.38)

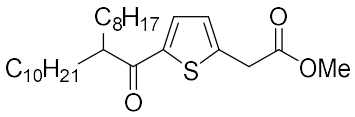


To a solution of acetate **5.37** (5.45 g, 35 mmol) and 2-octyldodecanoyl chloride **5.35** (17.2 g, 52 mmol) in anhydrous DCM (70 mL) under argon at 0 °C was added anhydrous aluminium(III) chloride (7.0 g, 52 mmol) cautiously portion-wise. The reaction was allowed to warm to RT and stirred for 24 h. The reaction was quenched by the careful addition of ice water and the organics were washed with water (100 mL) and brine (2 × 100 mL), allowing emulsions to separate fully. The organic layer was finally separated, dried over $MgSO_4$ and concentrated *in vacuo*. The crude oil was purified by flash chromatography on silica gel eluting with 5% ethyl acetate in hexanes to give the title compound as a brown oil (12.1 g, 76%).

**$^1$H NMR** (300 MHz, $CDCl_3$) δ 7.57 (d, *J* = 3.8 Hz, 1H), 6.98 (d, *J* = 3.8 Hz, 1H), 3.86 (s, 2H), 3.75 (s, 3H), 3.21 – 3.04 (m, 1H), 1.67 – 1.55 (m, 4H), 1.55 – 1.39 (m, 4H), 1.39 – 1.10 (m, 24H), 0.97 – 0.76 (m, 6H) **$^{13}$C NMR** (75 MHz, $CDCl_3$) δ 197.5, 170.1, 145.1, 144.1, 131.6, 128.2, 52.6, 48.3, 35.9, 33.1, 32.0, 29.9, 29.7, 29.6, 29.5, 29.4, 27.8, 22.8, 14.3, 14.2 **HRMS** Found (ES): $[MH]^+$ 451.3209, $C_{27}H_{47}O_3S$ requires 451.3246

### Methyl 2-(5-(2-octyldodecyl)thiophen-2-yl)acetate (5.39)

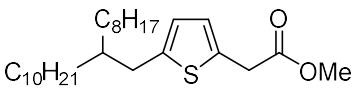


A solution of methyl 2-(5-(2-octyldodecanoyl)thiophen-2-yl)acetate (11.2 g, 27 mmol) and triethylsilane (17.5 mL, 0.11 mol) in trifluoroacetic acid (37 mL) was stirred under argon for 5 days. All the volatiles were removed *in vacuo* and the crude residue was

purified by column chromatography on silica gel eluting with 0→10% ethyl acetate in hexanes to give the title compound as a pale brown oil (10.1 g, 93%), with a small contamination of a silane species which was removed in the subsequent step.

**$^1$H NMR** (600 MHz, $CDCl_3$) δ 6.73 (d, *J* = 3.2 Hz, 1H), 6.58 (d, *J* = 3.2 Hz, 1H), 3.77 (s, 2H), 3.73 (s, 3H), 2.69 (d, *J* = 6.6 Hz, 2H), 1.52 – 1.43 (m, 1H), 1.36 – 1.17 (m, 32H), 0.91 – 0.86 (m, 6H) **$^{13}$C NMR** (150 MHz, $CDCl_3$) δ 171.4, 144.4, 132.5, 126.5, 124.8, 52.4, 39.9, 35.6, 34.5, 33.2, 32.1, 32.0, 30.2, 29.8, 29.7, 29.6, 29.5, 29.4, 26.7, 22.8, 14.3, 14.2 **HRMS** Found (ES): $[M+Na]^+$ 459.3267, $C_{27}H_{48}O_2S$+Na requires 459.3273

### 2-(5-(2-Octyldodecanoyl)thiophen-2-yl)acetic acid (5.40)

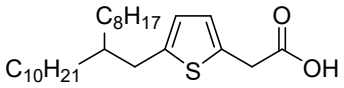


To a solution of methyl 2-(5-(2-octyldodecyl)thiophen-2-yl)acetate (15 g, 34 mmol) in methanol (70 mL) under normal atmospheric conditions was added 4M NaOH (70 mL). After 5 h the reaction was acidified and the solution extracted with diethyl ether (3 × 60 mL). The ethereal extracts were combined and washed with brine, dried over $MgSO_4$ and concentrated *in vacuo*. The crude residue was purified by column chromatography eluting with 0→2% ethyl acetate in hexane to give the title compound as a pale-yellow oil (14.4 g, 99%).

**$^1$H NMR** (400 MHz, $CDCl_3$) δ 6.76 (d, *J* = 3.4 Hz, 1H), 6.60 (d, *J* = 3.4 Hz, 1H), 3.81 (s, 2H), 2.71 (d, *J* = 6.6 Hz, 2H), 1.68 – 1.54 (m, 1H), 1.40 – 1.18 (m, 32H), 0.90 (t, *J* = 6.8 Hz, 6H) **$^{13}$C NMR** (150 MHz, $CDCl_3$) δ 177.4, 144.7, 131.6, 126.9, 124.9, 40.0, 35.5, 34.6, 33.3, 32.1, 31.8, 30.2, 30.1, 29.9, 29.8, 29.5, 26.7, 22.9, 22.8, 14.3 **HRMS** Found (ES): $[MH]^+$ 423.3282, $C_{26}H_{47}O_2S$ requires 423.3297

### 4-Fluoro-2-nitrobenzaldehyde (5.46)

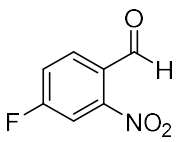


General procedure 5.1 was followed using with 4-fluoro-2-nitrotoluene (5 g, 32 mmol) to give the title compound as an orange oil which solidified on standing (2.4 g, 44%).

**$^1$H NMR** (300 MHz, $CDCl_3$) δ 10.37 (s, 1H), 8.04 (dd, *J* = 8.6, 5.5 Hz, 1H), 7.82 (dd, *J* = 8.0, 2.4 Hz, 1H), 7.55 – 7.44 (m, 1H) **$^{13}$C NMR** (75 MHz, $CDCl_3$) δ 186.7 (s), 166.6 (s), 163.1 (s), 132.3 (d), 127.7 (d), 121.5 (d), 112.6 (d) **LRMS** (EI+) *m/z* 169 $[M]^+$

### (*E*)-6,6'-difluoro-[2,2'-biindolinylidene]-3,3'-dione (5.50)
*also* **6,6'-Difluoroindigo**

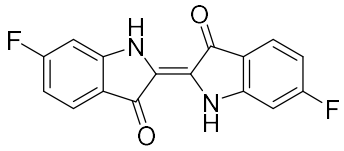

General procedure 5.2 was used with 4-fluoro-2-nitrobenzaldehyde (2.2 g) to give the title compound as a purple solid (924 mg, 48%).

**$^1$H NMR** (400 MHz, DMSO, 60 °C) δ 10.49 (s, 1H), 7.68 (dd, *J* = 8.5, 5.8 Hz, 1H), 7.09 (dd, *J* = 10.1, 2.2 Hz, 1H), 6.80 – 6.71 (m, 1H) **$^{13}$C NMR** unobtainable due to poor solubility **HRMS** Found (EI): $[MH]^+$ 299.4975, $C_{16}H_9F_2N_2O_2$ requires 299.0632

### 4-Chloro-2-nitrobenzaldehyde (5.47)

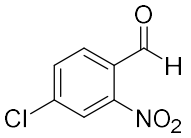

General procedure 5.1 was followed using with 4-chloro-2-nitrotoluene (5 g) to give the title compound as a yellow solid (1.93 g, 36%).

**$^1$H NMR** (300 MHz, $CDCl_3$) δ 10.39 (s, 1H), 8.11 (d, *J* = 1.4 Hz, 1H), 7.94 (d, *J* = 8.3 Hz, 1H), 7.76 (dd, *J* = 8.3, 1.4 Hz, 1H) **$^{13}$C NMR** (75 MHz, $CDCl_3$) δ 187.0, 140.4, 134.3, 131.1, 129.5, 124.9 **LRMS** (EI+) *m/z* 185 $[M]^+$

### (*E*)-6,6'-dichloro-[2,2'-biindolinylidene]-3,3'-dione (5.51)
*also* **6,6'-Dichloroindigo**

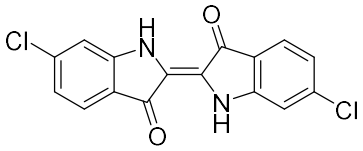

General procedure 5.2 was used with 4-chloro-2-nitrobenzaldehyde (1.8 g) to give the title compound as a purple solid (751 mg, 47%).

**$^1$H/$^{13}$C NMR** unobtainable due to poor solubility **HRMS** Found (EI): $[MH]^+$ 331.3456, $C_{16}H_9Cl_2N_2O_2$ requires 331.0041

### (*E*)-6,6'-dibromo-[2,2'-biindolinylidene]-3,3'-dione (5.52)

*also* **6,6'-Dibromoindigo**, ***Tyrian Purple***

*see Section* 6.4, *compound* **4.6**

### 4-Formyl-3-nitrobenzonitrile (5.49)

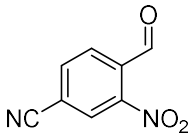


General procedure 5.1 was used with 4-methyl-3-nitrobenzonitrile (5 g) to give the title compound as a yellow solid (3.6 g, 66%).

**$^1$H NMR** (400 MHz, $CDCl_3$) δ 10.47 (s, 1H), 8.45 (t, *J* = 0.9 Hz, 1H), 8.08 (d, *J* = 0.9 Hz, 2H) **$^{13}$C NMR** (150 MHz, $CDCl_3$) δ 186.6, 149.4, 137.4, 134.2, 131.0, 128.3, 117.7, 115.8 **LRMS** (EI+) *m/z* 176 $[M]^+$

### (*E*)-3,3'-dioxo-[2,2'-biindolinylidene]-6,6'-dicarbonitrile (5.53)

*also* **6,6'-Dinitrileindigo**

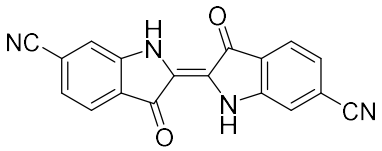


General procedure 5.2 was used with 2-nitro-4-(trifluoromethyl)benzaldehyde (3.5 g) to give the title compound as a purple solid (1.1 g, 36%).

**$^1$H NMR** (600 MHz, DMSO) δ 10.96 (s, 2H), 7.84 (d, *J* = 7.9 Hz, 2H), 7.68 (s, 2H), 7.26 (d, *J* = 7,9 Hz, 2H) **$^{13}$C NMR** (150 MHz, DMSO) δ 187.1, 151.9, 134.6 (d), 124.8, 122.9, 121.6, 121.1, 116.6, 110.4 **HRMS** Found (MALDI): [MH]+ 313.0725, $C_{18}H_9F_2N_4O_2$ requires 313.6926

**7,14-Bis(5-(2-octyldodecyl)thiophen-2-yl)benzo[4,5]pyrrolo[3,2,1-*de*]indolo[3,2,1-*ij*][1,5]naphthyridine-6,13-dione (5.54)**
*also* **H-INDT**

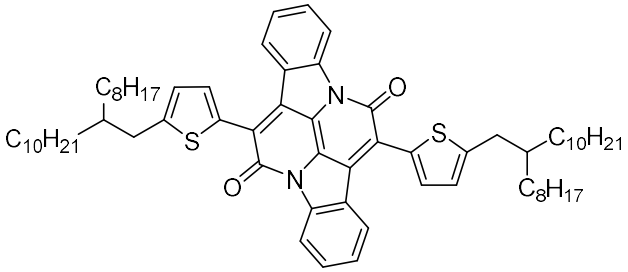


General procedure 5.3 was used with indigo (500 mg) and thiophenylacetyl chloride **5.41** (3 g) in xylenes (40 mL) to give the title compound as a dark purple solid (130 mg, 7%).

**$^1$H NMR** (600 MHz, $CDCl_3$) δ 8.62 (d, *J* = 7.7 Hz, 2H), 8.27 (d, *J* = 7.7 Hz, 2H), 7.62 (d, *J* = 3.6 Hz, 2H), 7.59 (t, *J* = 7.7 Hz, 2H), 7.32 (t, *J* = 7.7 Hz, 2H), 6.94 (d, *J* = 3.6 Hz, 2H), 2.89 (d, *J* = 6.7 Hz, 4H), 1.76 (m, 2H), 1.41 – 1.22 (m, 66H), 0.92 – 0.84 (m, 12H) **$^{13}$C NMR** (150 MHz, $CDCl_3$) δ 159.1, 150.6, 144.1, 132.6, 132.0, 130.3, 129.5, 126.2, 125.2, 125.1, 124.9, 121.9, 117.9, 40.2, 35.0, 33.5, 32.0, 30.1, 29.8, 29.8, 29.5, 26.8, 22.8, 14.3 **HRMS** Found (MALDI): $[MH]^+$ 1035.5973, $C_{68}H_{95}N_2O_2S_2$ requires 1035.6835

**3,10-Difluoro-7,14-bis(5-(2-octyldodecyl)thiophen-2-yl)diindolo[3,2,1-*de*:3',2',1'-*ij*][1,5]naphthyridine-6,13-dione (5.55)**
*also* **F-INDT**

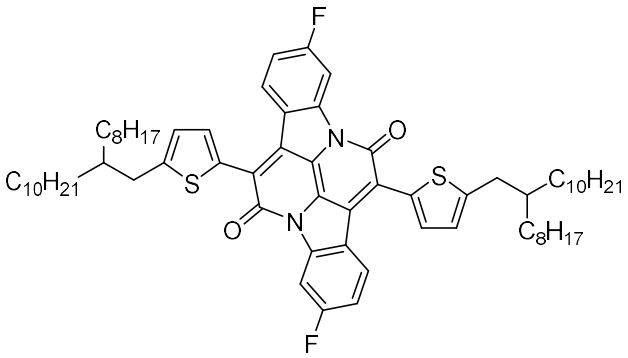


General procedure 5.3 was used with 6,6'-difluoroindigo (500 mg) and thiophenylacetyl chloride **5.41** (3 g) in xylenes (40 mL) to give the title compound as a dark purple solid (124 mg, 7%).

**$^1$H NMR** (600 MHz, $CDCl_3$) δ 8.33 (dd, *J* = 8.7, 2.4 Hz, 2H), 8.23 (dd, *J* = 8.7, 5.2 Hz, 2H), 7.57 (d, *J* = 3.6 Hz, 2H), 7.03 (td, *J* = 8.7, 2.4 Hz, 2H), 6.93 (d, *J* = 3.6 Hz, 2H), 2.88 (d, *J* = 6.7 Hz, 4H), 1.77 (s, 2H), 1.40 – 1.19 (m, 64H), 0.93 – 0.83 (m, 12H) **$^{13}$C NMR** (150 MHz, $CDCl_3$) δ 165.8, 164.2, 158.9, 150.9, 145.2, 132.2, 130.3, 128.8, 126.2, 125.0,

122.3, 122.2, 113.6, 113.5, 106.3, 106.1, 40.2, 35.0, 33.5, 32.1, 31.7, 30.1, 29.8, 29.5, 26.8, 22.8, 14.3 **HRMS** Found (MALDI): $[MH]^+$ 1071.7108, $C_{68}H_{93}F_2N_2O_2S_2$ requires 1071.6647

### 3,10-Dichloro-7,14-bis(5-(2-octyldodecyl)thiophen-2-yl)diindolo[3,2,1-*de*:3',2',1'-*ij*][1,5]naphthyridine-6,13-dione (5.56)

*also* **Cl-INDT**

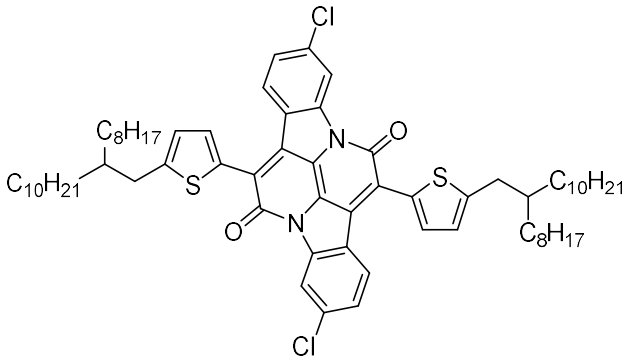


General procedure 5.3 was used with 6,6'-dichloroindigo (500 mg) and thiophenylacetyl chloride **5.41** (3 g) in xylenes (40 mL) to give the title compound as a dark purple solid (91 mg, 6%).

**$^1$H NMR** (600 MHz, $CDCl_3$) δ 8.63 (d, *J* = 2.0 Hz, 2H), 8.19 (d, *J* = 8.5 Hz, 2H), 7.58 (d, *J* = 3.6 Hz, 2H), 7.30 (dd, *J* = 8.5, 2.0 Hz, 2H), 6.94 (d, *J* = 3.6 Hz, 1H), 2.88 (d, *J* = 6.7 Hz, 4H), 1.81 – 1.72 (m, 2H), 1.43 – 1.20 (m, 64H), 0.91 – 0.84 (m, 12H) **$^{13}$C NMR** (150 MHz, $CDCl_3$) δ 158.8, 151.3, 144.4, 138.1, 132.3, 130.5, 128.3, 126.6, 125.5, 125.1, 125.0, 124.6, 121.9, 118.4, 40.3, 35.0, 33.5, 32.0, 30.1, 29.8, 29.5, 26.8, 14.3 **HRMS** Found (MALDI): $[MH]^+$ 1103.9638, $C_{68}H_{93}Cl_2N_2O_2S_2$ requires 1103.6056

**3,10-Dibromo-7,14-bis(5-(2-octyldodecyl)thiophen-2-yl)diindolo[3,2,1-*de*:3',2',1'-*ij*][1,5]naphthyridine-6,13-dione (5.57)**
*also* **Br-INDT**

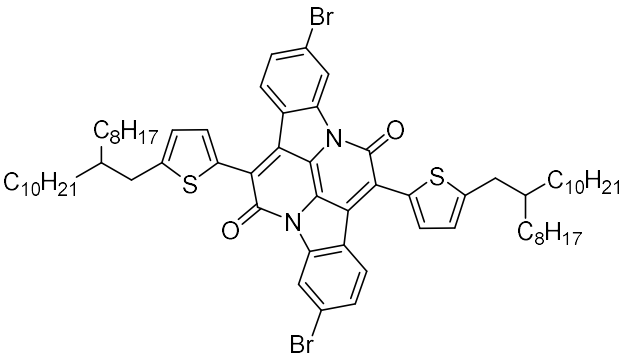


General procedure 5.3 was used with 6,6'-dibromoindigo (500 mg) and thiophenylacetyl chloride (3 g) in xylenes (40 mL) to give the title compound as a dark purple solid (84 mg, 6%).

**$^1$H NMR** (600 MHz, $CDCl_3$) δ 8.83 (d, *J* = 1.7 Hz, 2H), 8.14 (d, *J* = 8.5 Hz, 2H), 7.59 (d, *J* = 3.6 Hz, 2H), 7.46 (dd, *J* = 8.5, 1.7 Hz, 2H), 6.94 (d, *J* = 3.6 Hz, 2H), 2.89 (d, *J* = 6.7 Hz, 4H), 1.81 – 1.73 (m, 2H), 1.42 – 1.16 (m, 64H), 0.91 – 0.82 (m, 12H) **$^{13}$C NMR** (150 MHz, $CDCl_3$) δ 158.7, 151.4, 144.3, 132.3, 130.6, 129.5, 128.1, 126.1, 125.7, 125.1, 125.0, 121.7, 121.2, 40.3, 35.1, 33.5, 32.1, 30.2, 29.9, 29.8, 29.5, 26.8, 22.8, 14.3 **HRMS** Found (MALDI): $[MH]^+$ 1194.0143, $C_{68}H_{93}Br_2N_2O_2S_2$ requires 1193.5035

**7,14-Bis(5-(2-octyldodecyl)thiophen-2-yl)-6,13-dioxo-6,13-dihydrodiindolo[3,2,1-*de*:3',2',1'-*ij*][1,5]naphthyridine-3,10-dicarbonitrile**
*also* **CN-INDT (5.58)**

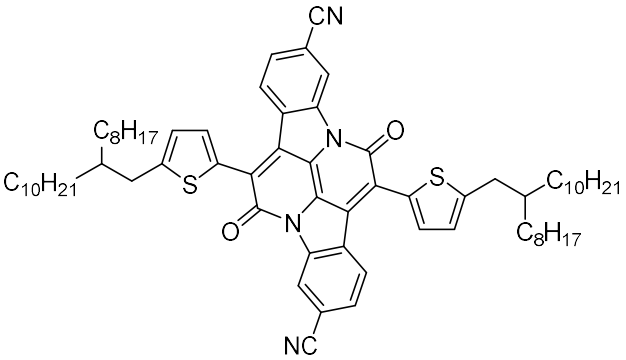


To a dry degassed microwave vial was added Br-INDT **5.57** (100 mg), excess CuCN (100 mg) and anhydrous DMF (5 mL). The reaction was heated at 150 °C for 12 h, then cooled and methanol (15 mL) added. Precipitates were collected by vacuum filtration and the filtrate discarded responsibly. The filter cake was washed with chloroform to extract organics (the filter cake was then discarded responsibly) and the filtrate

concentrated *in vacuo*. The crude residue typically consisted of a 1:3:3 (by $^1$H NMR) mixture of precursor/mono-nitrile/di-nitrile, which were separated by column chromatography on silica gel eluting with 50→100% chloroform in hexane to give **CN-INDT** (30 mg, 35%) and **Br/CN-INDT** (29 mg, 32%).

**$^1$H NMR** (600 MHz, $CDCl_3$) δ 8.96 (s, 2H), 8.46 (d, *J* = 8.2 Hz, 2H), 7.68 – 7.62 (m, 4H), 7.00 (d, *J* = 3.6 Hz, 2H), 2.91 (d, *J* = 6.7 Hz, 4H), 1.84 – 1.74 (m, 2H), 1.42 – 1.19 (m, 64H), 0.91 – 0.84 (m, 12H) **$^{13}$C NMR** (150 MHz, $CDCl_3$) δ 158.6, 153.1, 143.1, 132.1, 131.4, 130.2, 130.0, 127.0, 126.7, 125.6, 125.3, 121.9, 121.2, 117.9, 114.8, 40.3, 35.1, 33.5, 32.1, 30.1, 29.8, 29.5, 26.8, 22.8, 14.3 **HRMS** Found (MALDI): $[MH]^+$ 1085.4784, $C_{70}H_{92}N_4O_2S_2$ requires 1085.6740

### 10-Bromo-7,14-bis(5-(2-octyldodecyl)thiophen-2-yl)-6,13-dioxo-6,13-dihydrodiindolo[3,2,1-*de*:3',2',1'-*ij*][1,5]naphthyridine-3-carbonitrile *also* Br/CN-INDT (5.59)

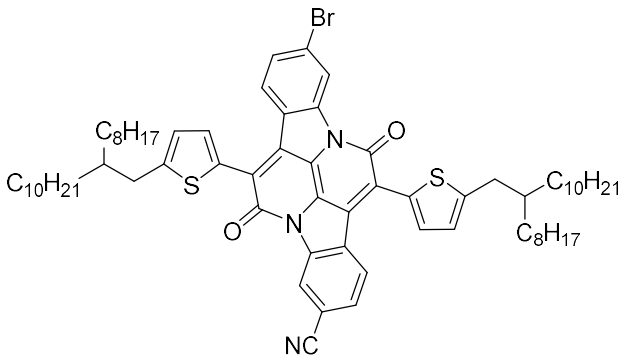


**$^1$H NMR** (600 MHz, $CDCl_3$) δ 8.93 (d, *J* = 1.1 Hz, 1H), 8.84 (d, *J* = 1.8 Hz, 1H), 8.43 (d, *J* = 8.2 Hz, 1H), 8.16 (d, *J* = 8.5 Hz, 1H), 7.64 – 7.60 (m, 3H), 7.49 (dd, *J* = 8.5, 1.8 Hz, 1H), 6.97 (dd, *J* = 11.9, 3.6 Hz, 2H), 2.90 (dd, *J* = 6.0, 6.0 Hz, 4H), 1.83 – 1.73 (m, 2H), 1.42 – 1.20 (m, *J* = 37.1, 22.6 Hz, 64H), 0.91 – 0.84 (m, 12H) **$^{13}$C NMR** (150 MHz, $CDCl_3$) δ 158.9 158.5, 152.4, 145.2, 144.3, 143.3, 132.2, 132.1, 131.0, 130.8, 130.1, 129.8, 129.6, 128.4, 127.1, 126.4, 125.8, 125.4, 125.3, 124.9, 121.9, 121.4, 121.0, 117.9, 114.8, 40.3, 35.1, 35.0, 33.5, 32.0, 30.1, 29.8, 29.8, 29.8, 29.5, 26.8, 22.8, 14.3 **HRMS** Found (MALDI): $[MH]^+$ 1138.1582, $C_{69}H_{93}BrN_3O_2S_2$ requires 1138.5892

### 3-((Carboxymethyl)amino)picolinic acid (5.61)

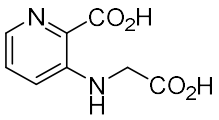

Anhydrous potassium carbonate (38.6 g, 0.28 mol) was added portion-wise to a solution of 3-aminopicolinic acid (25.0 g, 0.18 mol) and chloroacetic acid (18.4 g, 0.20 mol) in deionised water (600 mL) under argon. The resulting solution was stirred at 95 °C under argon for 12 h, then cooled on ice and acidified with 24% hydrochloric acid (62 g). The resulting precipitate was collected by filtration, washed sparingly with ethanol and air dried to give the title compound as a dusty brown solid (13.0 g, 37%).

**$^1$H NMR** (600 MHz, DMSO) δ 8.28 (s br, 1H), 7.88 (dd, *J* = 4.4, 1.2 Hz, 1H), 7.46 (dd, *J* = 8.7, 4.4 Hz, 2H), 7.22 (dd, *J* = 8.7, 1.2 Hz, 2H), 4.34 (s br, 1H), 4.05 (s, 2H) **$^{13}$C NMR** (150 MHz, DMSO) δ 171.4, 167.4, 146.7, 134.1, 128.7, 127.0, 121.5, 43.7 **HRMS** Found (EI): $[MH]^+$ 197.0563, $C_8H_9N_2O_4$ requires 197.0562

### 1-Acetyl-1*H*-pyrrolo[3,2-*b*]pyridin-3-yl acetate (5.62)
*also* **3-Acetoxy-1-acetyl-1,4-diazaindene**

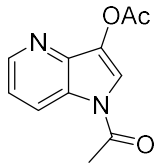

A suspension of picolinic acid **5.61** (12.7 g, 64.7 mmol) and freshly fused potassium acetate (15.9 g, 0.16 mol) in acetic anhydride (85 mL) under argon was submerged in a preheated oil bath at 130 °C for 1 h. The reaction was then cooled and diluted with acetone (250 mL) and the insoluble potassium acetate removed by filtration. The filtrate was concentrated *in vacuo* and the solid crude residue was purified by dry-flash chromatography (dry-loading from DCM was necessary) eluting with ethyl acetate ($R_F$ = 0.5) to afford the title compound as a pale brown solid (11.0 g, 78%).

**$^1$H NMR** (600 MHz, DMSO) δ 8.61 (dd, *J* = 8.4, 1.2 Hz, 1H), 8.52 (dd, *J* = 4.7, 1.2 Hz, 1H), 8.23 (s, 1H), 7.41 (dd, *J* = 8.4, 4.7 Hz, 1H), 2.65 (s, 3H), 2.39 (s, 3H) **$^{13}$C NMR** (150 MHz, DMSO) δ 169.7, 168.3, 146.1, 140.6, 132.9, 126.5, 123.4, 120.5, 119.9, 23.3, 20.4 **HRMS** Found (EI): $[MH]^+$ 219.0769, $C_{11}H_{11}N_2O_3$ requires 219.0770

**(*E*)-[2,2'-bipyrrolo[3,2-*b*]pyridinylidene]-3,3'(1*H*,1'*H*)-dione (5.63)**
*also* **4-Azaindigo**

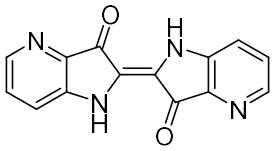

Diazaindene **5.62** (9.95 g) was stirred in 28% ammonia water (100 mL) under normal atmospheric conditions, precipitating the blue indigoid. After 12 h, the solution was diluted with water (100 mL) and the precipitate collected, sonicated well in methanol to remove impurities and isolated and dried by vacuum filtration giving the title compound as a blue solid (2.2 g, 37%).

**$^1$H NMR** (600 MHz, DMSO) δ 10.81 (s br, 2H), 8.31 (dd, *J* = 4.4, 1.1 Hz, 2H), 7.75 (dd, *J* = 8.3, 1.1 Hz, 2H), 7.46 (dd, *J* = 8.3, 4.4 Hz, 2H) **$^{13}$C NMR** unobtainable due to poor solubility **HRMS** Found (EI): $[MH]^+$ 265.0771, $C_{14}H_9N_4O_2$ requires 265.0726

**7,14-Bis(4-((2-octyldodecyl)oxy)phenyl)pyrido[2',3':4,5]pyrrolo[3,2,1-*de*]pyrido[2',3':4,5]pyrrolo[3,2,1-*ij*][1,5]naphthyridine-6,13-dione (5.64)**
*also* **4-PNDB**

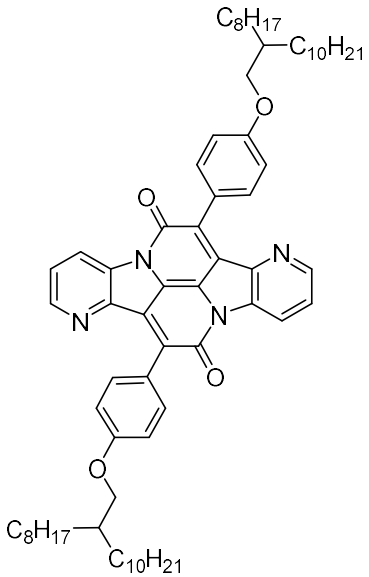

To a solution of phenylacetic acid **2.9** (13 g, 30 mmol) in anhydrous DCM (60 mL) under argon was added excess thionyl chloride (11 mL) and the reaction heated at reflux for 3 h. All volatiles were removed *in vacuo* giving the corresponding phenylacetyl chloride (**2.11**, quant.) as a viscous yellow oil that was used immediately without further purification.

Under normal atmospheric conditions, a suspension of 4-azaindigo (1.0 g, 3.8 mmol) in xylenes (50 mL) was heated to 165 °C. Acetyl chloride **2.11** was added all at once and the reaction was heated for 12 h. Xylenes were then removed *in vacuo* and the resulting crude residue purified by dry-flash chromatography eluting with chloroform, collecting the purple coloured fractions containing the product ($R_F$ = 0.4). The residue obtained from concentrating these fractions were then combined and then further purified by column chromatography eluting with THF (0→15%) in hexanes to give the title compound as a purple solid (15 mg, 0.4%).

**$^1$H NMR** (600 MHz, $CDCl_3$) δ 8.79 (dd, *J* = 8.2, 1.5 Hz, 2H), 8.58 (dd, *J* = 4.8, 1.5 Hz, 2H), 8.00 (d, *J* = 8.8 Hz, 4H), 7.47 (dd, *J* = 8.2, 4.8 Hz, 2H), 7.08 (d, *J* = 8.8 Hz, 4H), 3.96 (d, *J* = 5.6 Hz, 4H), 1.87 – 1.80 (m, 2H), 1.52 – 1.45 (m, 4H), 1.43 – 1.19 (m, 66H), 0.92 – 0.87 (m, 6H) **$^{13}$C NMR** (150 MHz, $CDCl_3$) δ 167.9, 161.0, 159.6, 147.5, 145.9, 139.2, 133.1, 132.7, 132.5, 131.0, 128.9, 128.7, 124.7, 124.5, 124.3, 121.4, 113.9, 70.9, 68.3, 38.8, 38.1, 32.1, 31.5, 30.5, 30.2, 29.8, 29.5, 29.0, 27.0, 23.8, 23.1, 22.8, 14.3 **HRMS** Found (EI): $[MH]^+$ 1057.7552, $C_{70}H_{97}N_4O_4$ requires 1057.7510

### 5-((2-octyldodecyl)oxy)-1*H*-indole (5.65)

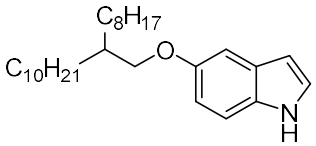


To a solution of 2-methyl-1-nitro-4-((2-octyldodecyl)oxy)benzene (10 g, 23 mmol) and *N*,*N*-dimethylformamide dimethyl acetal (3.7 mL, 28 mol) in anhydrous DMF (12 mL) under argon was added pyrrolidine (2.3 mL, 28 mmol). The reaction was heated at 100 °C for 16 h, then concentrated *in vacuo* to give the equivalent pyrrolidine enamine as a viscous red oil which was used without further purification as a reactive intermediate.

**Crude $^1$H NMR** (400 MHz, $CDCl_3$) δ 7.95 (d, *J* = 9.2 Hz, 1H), 7.22 (d, *J* = 13.4 Hz, 1H), 6.81 (d, *J* = 2.6 Hz, 1H), 6.47 (dd, *J* = 9.2, 2.6 Hz, 1H), 6.04 (d, *J* = 13.4 Hz, 1H), 3.86 (d, *J* = 5.6 Hz, 2H), 3.33 (t, *J* = 6.7 Hz, 4H), 1.98 – 1.91 (m, 4H), 1.46 – 1.34 (m, 4H), 1.28 (m, 29H), 0.86 (t, *J* = 6.8 Hz, 6H)

Under normal atmospheric conditions, a solution of the enamine (assumed 23 mmol) in DCM (110 mL) was added dropwise to a suspension of zinc dust (6.0 g, 92 mmol) in glacial acetic acid (5.3 mL, 92 mmol) and DCM (110 mL) at 0 °C. The reaction was allowed to warm naturally to RT, then poured into 2M HCl (220 mL). The solution was passed through a short pad of celite and the filtrate was extracted with DCM (2 × 50 mL). The combined organic layers were then washed with brine (2 × 100 mL), dried over

$MgSO_4$ and concentrated *in vacuo*. The crude residue was purified twice by column chromatography, firstly eluting with 50→100% toluene in hexane, then 0→100% chloroform in hexane to give the title compound as a colourless oil (6.3 g, 66%).

**$^1$H NMR** (400 MHz, $CDCl_3$) δ 8.03 (s br, 1H), 7.27 (d, *J* = 8.7 Hz, 2H), 7.17 (t, *J* = 2.8 Hz, 1H), 7.10 (d, *J* = 2.4 Hz, 1H), 6.87 (dd, *J* = 8.7, 2.4 Hz, 1H), 6.46 (ddd, *J* = 3.0, 2.0, 0.9 Hz, 1H), 3.87 (d, *J* = 5.8 Hz, 2H), 1.88 – 1.73 (m, 1H), 1.51 – 1.42 (m, 2H), 1.42 – 1.18 (m, 29H), 0.93 – 0.83 (m, 6H) **$^{13}$C NMR** (150 MHz, $CDCl_3$) δ 154.1, 131.0, 128.4, 124.8, 113.2, 111.7, 103.5, 102.5, 71.9, 38.2, 32.1, 31.6, 30.2, 29.8, 29.5, 27.0, 22.8, 14.3 **HRMS** Found (ESI): $[MH]^+$ 414.3727, $C_{28}H_{48}NO$ requires 414.3736

### (*E*)-5,5'-bis((2-octyldodecyl)oxy)-[2,2'-biindolinylidene]-3,3'-ione (5.66) *also* 5,5'-Bis(octyldodecyloxy)indigo

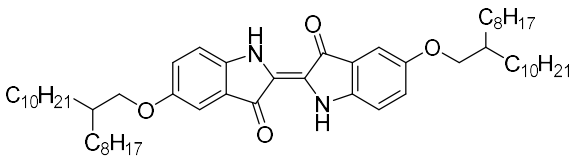


Under normal atmospheric conditions, a solution of indole **5.65** (2 g, 4.8 mmol), acetic acid (0.02 mL, 10 mol%), cumene hydroperoxide (2 mL, 80%, 9.6 mmol) and molybdenumhexacarbonyl (1.2 mg, 0.1 mol%) in *tert*-butyl alcohol (8.4 mL) was placed in an oil bath preheated at 90 °C for 1 h. The reaction was then concentrated *in vacuo* and the crude residue was purified by column chromatography eluting with 50→100% chloroform in hexane to give the title compound as a waxy blue solid (667 mg, 33%).

**$^1$H NMR** (600 MHz, $CDCl_3$) δ 8.72 (s, 1H), 7.18 (d, *J* = 2.4 Hz, 1H), 7.12 (dd, *J* = 8.7, 2.6 Hz, 1H), 6.96 (d, *J* = 8.7 Hz, 1H), 3.82 (d, *J* = 5.7 Hz, 2H), 1.81 – 1.73 (m, *J* = 12.2, 6.0 Hz, 1H), 1.49 – 1.40 (m, 3H), 1.40 – 1.19 (m, 41H), 0.91 – 0.84 (m, 8H) **$^{13}$C NMR** (150 MHz, $CDCl_3$) δ 188.8, 154.5, 146.9, 126.0, 122.6, 120.3, 113.2, 106.7, 71.9, 38.1, 32.1, 32.0, 31.4, 30.2, 29.8, 29.7, 29.5, 26.9, 22.8, 14.3 **HRMS** Found (MADLI): $[M]^+$ 854.6908, $C_{56}H_{90}N_2O_4$ requires 854.5870

**2,9-Bis((2-octyldodecyl)oxy)-7,14-di(thiophen-2-yl)diindolo[3,2,1-*de*:3',2',1'-*ij*][1,5]naphthyridine-6,13-dione (5.67/2.25)**

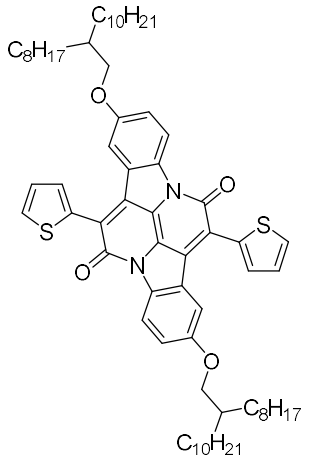


Under normal atmospheric conditions, 2-thiopheneacetyl chloride (0.4 mL, 3 mmol) was added to a solution of indigo **5.66** (660 mg, 0.7 mmol) in xylenes (33 mL) at 165 °C. The reaction was monitored by TLC and at completion (3 h) the xylenes were removed *in vacuo*. The crude residue was purified by column chromatography eluting with 0→100% chloroform in hexane. The residue from chromatography was washed with methanol, then hot ethanol, and finally taken up in cold methanol and collected with filtration to give the title compound as a waxy dark purple solid (330 mg, 40%).

*For characterisation, see compound* **2.25**

# VII

*References*


(1) Chiang, C. K.; Fincher, C. R.; Park, Y. W.; Heeger, A. J.; Shirakawa, H.; Louis, E. J.; Gau, S. C.; MacDiarmid, A. G. *Phys. Rev. Lett.* **1977**, *39* (17), 1098–1101.

(2) Shirakawa, H.; Louis, E. J.; MacDiarmid, A. G.; Chiang, C. K.; Heeger, A. J. *J. Chem. Soc. Chem. Commun.* **1977**, No. 16, 578–580.

(3) Tang, C. W. *Appl. Phys. Lett.* **1986**, *48* (2), 183–185.

(4) Tang, C. W.; VanSlyke, S. A. *Appl. Phys. Lett.* **1987**, *51* (12), 913–915.

(5) Tsumura, A.; Koezuka, H.; Ando, T. *Synth. Met.* **1988**, *25* (1), 11–23.

(6) Zaumseil, J.; Sirringhaus, H. *Chem. Rev.* **2007**, *107* (4), 1296–1323.

(7) Lu, L.; Zheng, T.; Wu, Q.; Schneider, A. M.; Zhao, D.; Yu, L. *Chem. Rev.* **2015**, *115* (23), 12666–12731.

(8) Sasabe, H.; Kido, J. *J. Mater. Chem. C* **2013**, *1* (9), 1699–1707.

(9) Heck, R. F. *J. Am. Chem. Soc.* **1969**, *91* (24), 6707–6714.

(10) Mc Cartney, D.; Guiry, P. J. *Chem. Soc. Rev.* **2011**, *40* (10), 5122–5150.

(11) Fujiwara, Y.; Moritani, I.; Danno, S.; Asano, R.; Teranishi, S. *J. Am. Chem. Soc.* **1969**, *91* (25), 7166–7169.

(12) Moritanl, I.; Fujiwara, Y. *Tetrahedron Lett.* **1967**, *8* (12), 1119–1122.

(13) Negishi, E.; King, A. O.; Okukado, N. *J. Org. Chem.* **1977**, *42* (10), 1821–1823.

(14) Haas, D.; Hammann, J. M.; Greiner, R.; Knochel, P. *ACS Catal.* **2016**, *6* (3), 1540–1552.

(15) Hatanaka, Y.; Hiyama, T. *J. Org. Chem.* **1988**, *53* (4), 918–920.

(16) Nakao, Y.; Hiyama, T. *Chem. Soc. Rev.* **2011**, *40* (10), 4893–4901.

(17) Sonogashira, K.; Tohda, Y.; Hagihara, N. *Tetrahedron Lett.* **1975**, *16* (50), 4467–4470.

(18) Chinchilla, R.; Nájera, C. *Chem. Rev.* **2007**, *107* (3), 874–922.

(19) Guram, A. S.; Buchwald, S. L. *J. Am. Chem. Soc.* **1994**, *116* (17), 7901–7902.

(20) Paul, F.; Patt, J.; Hartwig, J. F. *J. Am. Chem. Soc.* **1994**, *116* (13), 5969–5970.

(21) Sunesson, Y.; Limé, E.; Nilsson Lill, S. O.; Meadows, R. E.; Norrby, P.-O. *J. Org. Chem.* **2014**, *79* (24), 11961–11969.

(22) Tamao, K.; Sumitani, K.; Kumada, M. *J. Am. Chem. Soc.* **1972**, *94* (12), 4374–4376.

(23) Corriu, R. J. P.; Masse, J. P. *J. Chem. Soc.{,} Chem. Commun.* **1972**, No. 3, 144a–144a.

(24) Nicolaou, K. C.; Bulger, P. G.; Sarlah, D. *Angew. Chemie Int. Ed.* **2005**, *44* (29), 4442–4489.

(25) Kikukawa, K.; Matsuda, T. *Chem. Lett.* **1977**, *6* (2), 159–162.

(26) Kikukawa, K.; Nagira, K.; Wada, F.; Matsuda, T. *Tetrahedron* **1981**, *37* (1), 31–36.

(27) Taylor, J. G.; Moro, A. V.; Correia, C. R. D. *European J. Org. Chem.* **2011**, *2011* (8), 1403–1428.

(28) Miyaura, N.; Yamada, K.; Suzuki, A. *Tetrahedron Lett.* **1979**, *20* (36), 3437–3440.

(29) Miyaura, N.; Suzuki, A. *J. Chem. Soc.{,} Chem. Commun.* **1979**, No. 19, 866–867.

(30) Miyaura, N.; Suzuki, A. *Chem. Rev.* **1995**, *95* (7), 2457–2483.

(31) Milstein, D.; Stille, J. K. *J. Am. Chem. Soc.* **1978**, *100* (11), 3636–3638.

(32) Milstein, D.; Stille, J. K. *J. Am. Chem. Soc.* **1979**, *101* (17), 4992–4998.

(33) Milstein, D.; Stille, J. K. *J. Org. Chem.* **1979**, *44* (10), 1613–1618.

(34) Farina, V.; Krishnamurthy, V.; Scott, W. J. In *Organic Reactions*; John Wiley & Sons, Inc., 2004.

(35) Thomas, A. A.; Denmark, S. E. *Science* **2016**, *352* (6283), 329 LP-332.

(36) Rissler, J. *Chem. Phys. Lett.* **2004**, *395* (1), 92–96.

(37) Meier, H.; Stalmach, U.; Kolshorn, H. *Acta Polym.* **1997**, *48* (9), 379–384.

(38) Brédas, J. L. *J. Chem. Phys.* **1985**, *82* (8), 3808–3811.

(39) Ma, J.; Li, S.; Jiang, Y. *Macromolecules* **2002**, *35* (3), 1109–1115.

(40) Cheng, Y. J.; Yang, S. H.; Hsu, C. S. *Chem. Rev.* **2009**, *109* (11), 5868–5923.

(41) Wudl, F.; Kobayashi, M.; Heeger, A. J. *J. Org. Chem.* **1984**, *49* (18), 3382–3384.

(42) Conboy, G.; Spencer, H. J.; Angioni, E.; Kanibolotsky, A. L.; Findlay, N. J.; Coles, S. J.; Wilson, C.; Pitak, M. B.; Risko, C.; Coropceanu, V.; Brédas, J.-L.; Skabara, P. J. *Mater. Horiz.* **2016**, *3* (4), 333–339.

(43) Lee, J.; Jang, M.; Lee, S. M.; Yoo, D.; Shin, T. J.; Oh, J. H.; Yang, C. *ACS Appl. Mater. Interfaces* **2014**, *6* (22), 20390–20399.

(44) Müllen, K.; Pisula, W. *J. Am. Chem. Soc.* **2015**, *137* (30), 9503–9505.

(45) Cao, W.; Xue, J. *Energy Environ. Sci.* **2014**, *7* (7), 2123–2144.

(46) You, J.; Dou, L.; Yoshimura, K.; Kato, T.; Ohya, K.; Moriarty, T.; Emery, K.; Chen, C.-C.; Gao, J.; Li, G.; Yang, Y. *Nat Commun* **2013**, *4*, 1446.

(47) He, Z.; Zhong, C.; Su, S.; Xu, M.; Wu, H.; Cao, Y. *Nat Phot.* **2012**, *6* (9), 591–595.

(48) He, Z.; Zhong, C.; Huang, X.; Wong, W.-Y.; Wu, H.; Chen, L.; Su, S.; Cao, Y. *Adv. Mater.*

**2011**, *23* (40), 4636–4643.

(49) Facchetti, A. *Mater. Today* **2007**, *10* (3), 28–37.

(50) Hamadani, B. H.; Gundlach, D. J.; McCulloch, I.; Heeney, M. *Appl. Phys. Lett.* **2007**, *91* (24), 243512.

(51) McCulloch, I.; Heeney, M.; Chabinyc, M. L.; DeLongchamp, D.; Kline, R. J.; Cölle, M.; Duffy, W.; Fischer, D.; Gundlach, D.; Hamadani, B.; Hamilton, R.; Richter, L.; Salleo, A.; Shkunov, M.; Sparrowe, D.; Tierney, S.; Zhang, W. *Adv. Mater.* **2009**, *21* (10–11), 1091–1109.

(52) Wang, S.; Kappl, M.; Liebewirth, I.; Müller, M.; Kirchhoff, K.; Pisula, W.; Müllen, K. *Adv. Mater.* **2012**, *24* (3), 417–420.

(53) Tsao, H. N.; Cho, D. M.; Park, I.; Hansen, M. R.; Mavrinskiy, A.; Yoon, D. Y.; Graf, R.; Pisula, W.; Spiess, H. W.; Müllen, K. *J. Am. Chem. Soc.* **2011**, *133* (8), 2605–2612.

(54) McCulloch, I.; Heeney, M.; Bailey, C.; Genevicius, K.; MacDonald, I.; Shkunov, M.; Sparrowe, D.; Tierney, S.; Wagner, R.; Zhang, W.; Chabinyc, M. L.; Kline, R. J.; McGehee, M. D.; Toney, M. F. *Nat Mater* **2006**, *5* (4), 328–333.

(55) Nielsen, C. B.; Turbiez, M.; McCulloch, I. *Adv. Mater.* **2013**, *25* (13), 1859–1880.

(56) Yuen, J. D.; Fan, J.; Seifter, J.; Lim, B.; Hufschmid, R.; Heeger, A. J.; Wudl, F. *J. Am. Chem. Soc.* **2011**, *133* (51), 20799–20807.

(57) Li, Y.; Sonar, P.; Singh, S. P.; Zeng, W.; Soh, M. S. *J. Mater. Chem.* **2011**, *21* (29), 10829–10835.

(58) Bronstein, H.; Chen, Z.; Ashraf, R. S.; Zhang, W.; Du, J.; Durrant, J. R.; Shakya Tuladhar, P.; Song, K.; Watkins, S. E.; Geerts, Y.; Wienk, M. M.; Janssen, R. A. J.; Anthopoulos, T.; Sirringhaus, H.; Heeney, M.; McCulloch, I. *J. Am. Chem. Soc.* **2011**, *133* (10), 3272–3275.

(59) Lei, T.; Dou, J.-H.; Pei, J. *Adv. Mater.* **2012**, *24* (48), 6457–6461.

(60) Mei, J.; Kim, D. H.; Ayzner, A. L.; Toney, M. F.; Bao, Z. *J. Am. Chem. Soc.* **2011**, *133* (50), 20130–20133.

(61) Zhang, W.; Smith, J.; Watkins, S. E.; Gysel, R.; McGehee, M.; Salleo, A.; Kirkpatrick, J.; Ashraf, S.; Anthopoulos, T.; Heeney, M.; McCulloch, I. *J. Am. Chem. Soc.* **2010**, *132* (33), 11437–11439.

(62) Bronstein, H.; Leem, D. S.; Hamilton, R.; Woebkenberg, P.; King, S.; Zhang, W.; Ashraf, R. S.; Heeney, M.; Anthopoulos, T. D.; Mello, J. de; McCulloch, I. *Macromolecules* **2011**, *44* (17), 6649–6652.

(63) Zhang, X.; Bronstein, H.; Kronemeijer, A. J.; Smith, J.; Kim, Y.; Kline, R. J.; Richter, L. J.; Anthopoulos, T. D.; Sirringhaus, H.; Song, K.; Heeney, M.; Zhang, W.; McCulloch, I.; DeLongchamp, D. M. *Nat. Commun.* **2013**, *4*.

(64) Li, J.; Zhao, Y.; Tan, H. S.; Guo, Y.; Di, C.-A.; Yu, G.; Liu, Y.; Lin, M.; Lim, S. H.; Zhou, Y.; Su, H.; Ong, B. S. *Sci. Rep.* **2012**, *2*, 754.

(65) Zhao, Y.; Guo, Y.; Liu, Y. *Adv. Mater.* **2013**, *25* (38), 5372–5391.

(66) Sun, B.; Hong, W.; Yan, Z.; Aziz, H.; Li, Y. *Adv. Mater.* **2014**, *26* (17), 2636–2642.

(67) Sun, B.; Hong, W.; Aziz, H.; Li, Y. *Polym. Chem.* **2015**, *6* (6), 938–945.

(68) Gruber, M.; Jung, S.-H.; Schott, S.; Venkateshvaran, D.; Kronemeijer, A. J.; Andreasen,

J. W.; McNeill, C. R.; Wong, W. W. H.; Shahid, M.; Heeney, M.; Lee, J.-K.; Sirringhaus, H. *Chem. Sci.* **2015**, *6* (12), 6949–6960.

(69) Park, J. H.; Jung, E. H.; Jung, J. W.; Jo, W. H. *Adv. Mater.* **2013**, *25* (18), 2583–2588.

(70) Chen, Z.; Lee, M. J.; Shahid Ashraf, R.; Gu, Y.; Albert-Seifried, S.; Meedom Nielsen, M.; Schroeder, B.; Anthopoulos, T. D.; Heeney, M.; McCulloch, I.; Sirringhaus, H. *Adv. Mater.* **2012**, *24* (5), 647–652.

(71) Kang, B.; Kim, R.; Lee, S. B.; Kwon, S. K.; Kim, Y. H.; Cho, K. *J. Am. Chem. Soc.* **2016**, *138* (11), 3679–3686.

(72) Dai, Y.-Z.; Ai, N.; Lu, Y.; Zheng, Y.-Q.; Dou, J.-H.; Shi, K.; Lei, T.; Wang, J.-Y.; Pei, J. *Chem. Sci.* **2016**, *7* (9), 5753–5757.

(73) Lei, T.; Dou, J.-H.; Cao, X.-Y.; Wang, J.-Y.; Pei, J. *Adv. Mater.* **2013**, *25* (45), 6589–6593.

(74) *International Energy Outlook 2016*; U.S. Energy Information Administration (EIA), 2016.

(75) Darling, S. B.; You, F. *RSC Adv.* **2013**, *3* (39), 17633–17648.

(76) Global land-ocean temperature index https://climate.nasa.gov/vital-signs/global-temperature/ (accessed Jul 26, 2017).

(77) Reddy, K. G.; Deepak, T. G.; Anjusree, G. S.; Thomas, S.; Vadukumpully, S.; Subramanian, K. R. V; Nair, S. V; Nair, A. S. *Phys. Chem. Chem. Phys.* **2014**, *16* (15), 6838–6858.

(78) Scharber, M. C.; Sariciftci, N. S. *Prog. Polym. Sci.* **2013**, *38* (12), 1929–1940.

(79) OPVIUS http://www.opvius.com (accessed Jul 27, 2017).

(80) Markov, D. E.; Blom, P. W. M. *Phys. Rev. B* **2006**, *74* (8), 85206.

(81) Tamai, Y.; Ohkita, H.; Benten, H.; Ito, S. *J. Phys. Chem. Lett.* **2015**, *6* (17), 3417–3428.

(82) Garbuzov, D. Z.; Forrest, S. R.; Tsekoun, A. G.; Burrows, P. E.; Bulović, V.; Thompson, M. E. *J. Appl. Phys.* **1996**, *80* (8), 4644–4648.

(83) Lunt, R. R.; Giebink, N. C.; Belak, A. A.; Benziger, J. B.; Forrest, S. R. *J. Appl. Phys.* **2009**, *105* (5), 53711.

(84) Sauvé, G.; Fernando, R. *J. Phys. Chem. Lett.* **2015**, *6* (18), 3770–3780.

(85) Zhou, N.; Dudnik, A. S.; Li, T. I. N. G.; Manley, E. F.; Aldrich, T. J.; Guo, P.; Liao, H.-C.; Chen, Z.; Chen, L. X.; Chang, R. P. H.; Facchetti, A.; Olvera de la Cruz, M.; Marks, T. J. *J. Am. Chem. Soc.* **2016**, *138* (4), 1240–1251.

(86) Emmott, C. J. M.; Urbina, A.; Nelson, J. *Sol. Energy Mater. Sol. Cells* **2012**, *97*, 14–21.

(87) Yu, Z.; Xia, Y.; Du, D.; Ouyang, J. *ACS Appl. Mater. Interfaces* **2016**, *8* (18), 11629–11638.

(88) Nardes, A. M.; Kemerink, M.; de Kok, M. M.; Vinken, E.; Maturova, K.; Janssen, R. A. J. *Org. Electron.* **2008**, *9* (5), 727–734.

(89) Jørgensen, M.; Norrman, K.; Krebs, F. C. *Sol. Energy Mater. Sol. Cells* **2008**, *92* (7), 686–714.

(90) Dixon, S. C.; Scanlon, D. O.; Carmalt, C. J.; Parkin, I. P. *J. Mater. Chem. C* **2016**, *4* (29), 6946–6961.

(91) Guo, X.; Zhou, N.; Lou, S. J.; Smith, J.; Tice, D. B.; Hennek, J. W.; Ortiz, R. P.; Navarrete, J. T. L.; Li, S.; Strzalka, J.; Chen, L. X.; Chang, R. P. H.; Facchetti, A.; Marks, T. J. *Nat. Photonics* **2013**, *7* (10), 825–833.

(92) Lee, J.; Chung, J. W.; Yoon, G. B.; Lee, M. H.; Kim, D. H.; Park, J.; Lee, J.-K.; Kang, M. S. *ACS Appl. Mater. Interfaces* **2016**, *8* (44), 30344–30350.

(93) Würthner, F.; Schmidt, R. *ChemPhysChem* **2006**, *7* (4), 793–797.

(94) Wang, C.; Dong, H.; Li, H.; Zhao, H.; Meng, Q.; Hu, W. *Cryst. Growth Des.* **2010**, *10* (9), 4155–4160.

(95) Dong, H.; Wang, C.; Hu, W. *Chem. Commun.* **2010**, *46* (29), 5211–5222.

(96) Moon, H.; Zeis, R.; Borkent, E.-J.; Besnard, C.; Lovinger, A. J.; Siegrist, T.; Kloc, C.; Bao, Z. *J. Am. Chem. Soc.* **2004**, *126* (47), 15322–15323.

(97) Meager, I.; Ashraf, R. S.; Mollinger, S.; Schroeder, B. C.; Bronstein, H.; Beatrup, D.; Vezie, M. S.; Kirchartz, T.; Salleo, A.; Nelson, J.; McCulloch, I. *J. Am. Chem. Soc.* **2013**, *135* (31), 11537–11540.

(98) McCulloch, I.; Salleo, A.; Chabinyc, M. *Science* **2016**, *352* (6293), 1521–1522.

(99) Bittle, E. G.; Basham, J. I.; Jackson, T. N.; Jurchescu, O. D.; Gundlach, D. J. *Nat. Commun.* **2016**, *7*, 10908.

(100) Horowitz, G. *Adv. Mater.* **1998**, *10* (5), 365–377.

(101) Okachi, T.; Kashiki, T.; Ohya, K. McCulloch, I., Jurchescu, O. D., Kymissis, I., Shinar, R., Torsi, L., Eds.; International Society for Optics and Photonics, 2015; p 95680I.

(102) Natali, D.; Caironi, M. *Adv. Mater.* **2012**, *24* (11), 1357–1387.

(103) Ghazvini Zadeh, E. H.; Tang, S.; Woodward, A. W.; Liu, T.; Bondar, M. V; Belfield, K. D. *J. Mater. Chem. C* **2015**, *3* (33), 8495–8503.

(104) Robb, M. J.; Ku, S.-Y.; Brunetti, F. G.; Hawker, C. J. *J. Polym. Sci. Part A Polym. Chem.* **2013**, *51* (6), 1263–1271.

(105) Wang, E.; Mammo, W.; Andersson, M. R. *Adv. Mater.* **2014**, *26* (12), 1801–1826.

(106) Deng, P.; Zhang, Q. *Polym. Chem.* **2014**, *5* (10), 3298–3305.

(107) Ma, Z.; Sun, W.; Himmelberger, S.; Vandewal, K.; Tang, Z.; Bergqvist, J.; Salleo, A.; Andreasen, J. W.; Inganas, O.; Andersson, M. R.; Muller, C.; Zhang, F.; Wang, E. *Energy Environ. Sci.* **2014**, *7* (1), 361–369.

(108) Osaka, I.; Akita, M.; Koganezawa, T.; Takimiya, K. *Chem. Mater.* **2012**, *24* (6), 1235–1243.

(109) Burke, D. J.; Lipomi, D. J. *Energy Environ. Sci.* **2013**, *6* (7), 2053–2066.

(110) Guo, C.; Sun, B.; Quinn, J.; Yan, Z.; Li, Y. *J. Mater. Chem. C* **2014**, *2* (21), 4289–4296.

(111) Gorner, H.; Pouliquen, J.; Kossanyi, J. *Can. J. Chem. Can. Chim.* **1987**, *65* (4), 708–717.

(112) Rondão, R.; Seixas de Melo, J.; Melo, M. J.; Parola, A. J. *J. Phys. Chem. A* **2012**, *116* (11), 2826–2832.

(113) Irimia-Vladu, M.; Głowacki, E. D.; Troshin, P. A.; Schwabegger, G.; Leonat, L.; Susarova, D. K.; Krystal, O.; Ullah, M.; Kanbur, Y.; Bodea, M. A.; Razumov, V. F.; Sitter, H.; Bauer, S.; Sariciftci, N. S. *Adv. Mater.* **2012**, *24* (3), 375–380.

(114) Klimovich, I. V; Leshanskaya, L. I.; Troyanov, S. I.; Anokhin, D. V; Novikov, D. V; Piryazev, A. A.; Ivanov, D. A.; Dremova, N. N.; Troshin, P. A. *J. Mater. Chem. C* **2014**, *2* (36), 7621–7631.

(115) Engi, G. *Angew. Chemie* **1914**, *27* (20), 144–148.

(116) Glowacki, E. D.; Leonat, L.; Voss, G.; Bodea, M.; Bozkurt, Z.; Irimia-Vladu, M.; Bauer, S.; Sariciftci, N. S. In *Proc. SPIE 8118, Organic Semiconductors in Sensors and Bioelectronics IV, 81180M*; 2011; Vol. 8118, p 81180M–81180M–10.

(117) He, B.; Pun, A. B.; Zherebetskyy, D.; Liu, Y.; Liu, F.; Klivansky, L. M.; McGough, A. M.; Zhang, B. A.; Lo, K.; Russell, T. P.; Wang, L.; Liu, Y. *J. Am. Chem. Soc.* **2014**, *136* (42), 15093–15101.

(118) Klein, M. F. G.; Pasker, F. M.; Kowarik, S.; Landerer, D.; Pfaff, M.; Isen, M.; Gerthsen, D.; Lemmer, U.; Höger, S.; Colsmann, A. *Macromolecules* **2013**, *46* (10), 3870–3878.

(119) Chen, H.; He, C.; Yu, G.; Zhao, Y.; Huang, J.; Zhu, M.; Liu, H.; Guo, Y.; Li, Y.; Liu, Y. *J. Mater. Chem.* **2012**, *22* (9), 3696–3698.

(120) Huang, Z.; Fregoso, E. C.; Dimitrov, S.; Tuladhar, P. S.; Soon, Y. W.; Bronstein, H.; Meager, I.; Zhang, W.; McCulloch, I.; Durrant, J. R. *J. Mater. Chem. A* **2014**, *2* (45), 19282–19289.

(121) Heravi, M. M.; Hajiabbasi, P. *Monatshefte für Chemie - Chem. Mon.* **2012**, *143* (12), 1575–1592.

(122) Baeyer, A.; Drewsen, V. *Berichte der Dtsch. Chem. Gesellschaft* **1882**, *15* (2), 2856–2864.

(123) Glowacki, E. D.; Apaydin, D. H.; Bozkurt, Z.; Monkowius, U.; Demirak, K.; Tordin, E.; Himmelsbach, M.; Schwarzinger, C.; Burian, M.; Lechner, R. T.; Demitri, N.; Voss, G.; Sariciftci, N. S. *J. Mater. Chem. C* **2014**, *2* (38), 8089–8097.

(124) Ashburn, B. O.; Carter, R. G. *Angew. Chemie Int. Ed.* **2006**, *45* (40), 6737–6741.

(125) Sawatari, N.; Sakaguchi, S.; Ishii, Y. *Tetrahedron Lett.* **2003**, *44* (10), 2053–2056.

(126) Phillips, B. T.; Hartman, G. D. *J. Heterocycl. Chem.* **1986**, *23* (3), 897–899.

(127) Rajeshwaran, G. G.; Mohanakrishnan, A. K. *Org. Lett.* **2011**, *13* (6), 1418–1421.

(128) Lankalapalli, R. S.; Ouro, A.; Arana, L.; Gómez-Muñoz, A.; Bittman, R. *J. Org. Chem.* **2009**, *74* (22), 8844–8847.

(129) Ramalingam, B. M.; Saravanan, V.; Mohanakrishnan, A. K. *Org. Lett.* **2013**, *15* (14), 3726–3729.

(130) Michael R Naffziger; Bradley O. Ashburn; Johanna R. Perkins, and; Carter*, R. G. **2007**.

(131) Wang, Y.; Ai, J.; Liu, G.; Geng, M.; Zhang, A.; Bode, C.; Chen, A.; Choquette, D.; Dussault, I.; Hirai, S.; Kaplan-Lefko, P.; Larrow, J. F.; Lin, M.-H. J.; Lohman, J.; Potashman, M. H.; Rex, K.; Santostefano, M.; Shah, K.; Shimanovich, R.; Springer, S. K.; Teffera, Y.; Yang, Y. J.; Zhang, Y. H.; Harmange, J. C. *Org. Biomol. Chem.* **2011**, *9* (17), 5930.

(132) Raju, P.; Gobi Rajeshwaran, G.; Nandakumar, M.; Mohanakrishnan, A. K. *European J. Org. Chem.* **2015**, *2015* (16), 3513–3523.

(133) Belov, P.; Campanella, V. L.; Smith, A. W.; Priefer, R. *Tetrahedron Lett.* **2011**, *52* (21), 2776–2779.

(134) Paley, D. W.; Sedbrook, D. F.; Decatur, J.; Fischer, F. R.; Steigerwald, M. L.; Nuckolls,

C. *Angew. Chemie - Int. Ed.* **2013**, *52* (17), 4591–4594.

(135) Basak, T.; Grudzie, K.; Barbasiewicz, M. *Eur. J. Inorg. Chem.* **2016**, *2016* (21), 3513–3523.

(136) Zniber, R.; Achour, R.; Cherkaoui, M. Z.; Donnio, B.; Gehringer, L.; Guillon, D. *J. Mater. Chem.* **2002**, *12* (8), 2208–2213.

(137) Guo, J.; Zhuang, J.; Wang, F.; Raghupathi, K. R.; Thayumanavan, S. *J. Am. Chem. Soc.* **2014**, *136* (6), 2220–2223.

(138) T. W. Green, P. G. M. W. *Protective Groups in Organic Synthesis*; Wiley-Interscience: New York, 1999.

(139) Grzybowski, M.; Gryko, D. T. *Adv. Opt. Mater.* **2015**, *3* (3), 280–320.

(140) Li, C.; Bo, Z. In *New Chemistry for Organic Photovoltaic Materials*; Royal Society of Chemistry, 2015; pp 1–31.

(141) Leong, W. L.; Welch, G. C.; Kaake, L. G.; Takacs, C. J.; Sun, Y.; Bazan, G. C.; Heeger, A. J. *Chem. Sci.* **2012**, *3* (6), 2103.

(142) Mateker, W. R.; Douglas, J. D.; Cabanetos, C.; Sachs-Quintana, I. T.; Bartelt, J. A.; Hoke, E. T.; El Labban, A.; Beaujuge, P. M.; Fréchet, J. M. J.; McGehee, M. D.; Allara, D. L.; Koch, N.; Brütting, W.; Manca, J.; Vanderzande, D. J. M. *Energy Environ. Sci.* **2013**, *6* (8), 2529.

(143) Erwin, M. M.; McBride, J.; Kadavanich, A. V.; Rosenthal, S. J. *Thin Solid Films* **2002**, *409* (2), 198–205.

(144) Yang, L.; Yu, Y.; Gong, Y.; Li, J.; Ge, F.; Jiang, L.; Gao, F.; Dan, Y. *Polym. Chem.* **2015**, *6* (39), 7005–7014.

(145) Li, W.; Hendriks, K. H.; Wienk, M. M.; Janssen, R. J. .

(146) Choi, J.; Song, H.; Kim, N.; Kim, F. S. *Semicond. Sci. Technol.* **2015**, *30* (6), 64002.

(147) Qian, G.; Wang, Z. Y. *Chem. – An Asian J.* **2010**, *5* (5), 1006–1029.

(148) Hendriks, K. H.; Li, W.; Wienk, M. M.; Janssen, R. A. J. *J. Am. Chem. Soc.* **2014**, *136* (34), 12130–12136.

(149) Bronstein, H.; Collado-Fregoso, E.; Hadipour, A.; Soon, Y. W.; Huang, Z.; Dimitrov, S. D.; Ashraf, R. S.; Rand, B. P.; Watkins, S. E.; Tuladhar, P. S.; Meager, I.; Durrant, J. R.; McCulloch, I. *Adv. Funct. Mater.* **2013**, *23* (45), 5647–5654.

(150) Dimitrov, S. D.; Bakulin, A. A.; Nielsen, C. B.; Schroeder, B. C.; Du, J.; Bronstein, H.; McCulloch, I.; Friend, R. H.; Durrant, J. R. *J. Am. Chem. Soc.* **2012**, *134* (44), 18189–18192.

(151) Wang, Y.; Michinobu, T. *J. Mater. Chem. C* **2016**, *4* (26), 6200–6214.

(152) Hollinger, J.; Gao, D.; Seferos, D. S. *Isr. J. Chem.* **2014**, *54* (5–6), 440–453.

(153) Ngai, J. H. L.; Leung, L. M.; So, S. K.; Lee, H. K. H. *Org. Electron.* **2016**, *32*, 258–266.

(154) Voss, G.; Gradzielski, M.; Heinze, J.; Reinke, H.; Unverzagt, C. *Helv. Chim. Acta* **2003**, *86* (6), 1982–2004.

(155) "Indigo - chemical synthesis" http://www.chriscooksey.demon.co.uk/indigo/chem.html (accessed Sep 17, 2016).

(156) Weber, W. P. In *Silicon Reagents for Organic Synthesis*; Weber, W. P., Ed.; Springer Berlin Heidelberg: Berlin, Heidelberg, 1983; pp 21–39.

(157) Vezie, M. S.; Few, S.; Meager, I.; Pieridou, G.; Dorling, B.; Ashraf, R. S.; Goni, A. R.; Bronstein, H.; McCulloch, I.; Hayes, S. C.; Campoy-Quiles, M.; Nelson, J. *Nat Mater* **2016**, *15* (7), 746–753.

(158) Tsai, C. H.; Fortney, A.; Qiu, Y.; Gil, R. R.; Yaron, D.; Kowalewski, T.; Noonan, K. J. T. *J. Am. Chem. Soc.* **2016**, *138* (21), 6798–6804.

(159) Dimitrov, S. D.; Huang, Z.; Deledalle, F.; Nielsen, C. B.; Schroeder, B. C.; Ashraf, R. S.; Shoaee, S.; McCulloch, I.; Durrant, J. R. *Energy Environ. Sci.* **2014**, *7* (3), 1037–1043.

(160) Richards, T. J.; Sirringhaus, H. *J. Appl. Phys.* **2007**, *102* (9), 94510.

(161) Rentenberger, S.; Vollmer, A.; Zojer, E.; Schennach, R.; Koch, N. *J. Appl. Phys.* **2006**, *100* (5), 53701.

(162) Stadlober, B.; Haas, U.; Gold, H.; Haase, A.; Jakopic, G.; Leising, G.; Koch, N.; Rentenberger, S.; Zojer, E. *Adv. Funct. Mater.* **2007**, *17* (15), 2687–2692.

(163) Zhou, Y.; Fuentes-Hernandez, C.; Shim, J.; Meyer, J.; Giordano, A. J.; Li, H.; Winget, P.; Papadopoulos, T.; Cheun, H.; Kim, J.; Fenoll, M.; Dindar, A.; Haske, W.; Najafabadi, E.; Khan, T. M.; Sojoudi, H.; Barlow, S.; Graham, S.; Brédas, J.-L.; Marder, S. R.; Kahn, A.; Kippelen, B. *Science* **2012**, *336* (6079), 327–332.

(164) Bolognesi, A.; Di Carlo, A.; Lugli, P. *Appl. Phys. Lett.* **2002**, *81* (24), 4646–4648.

(165) Simonetti, O.; Giraudet, L.; Maurel, T.; Nicolas, J. L.; Belkhir, A. *Org. Electron.* **2010**, *11* (8), 1381–1393.

(166) Giraudet, L.; Simonetti, O. *Org. Electron.* **2011**, *12* (1), 219–225.

(167) Smilgies, D.-M. *J. Appl. Crystallogr.* **2009**, *42* (6), 1030–1034.

(168) Rivnay, J.; Toney, M. F.; Zheng, Y.; Kauvar, I. V; Chen, Z.; Wagner, V.; Facchetti, A.; Salleo, A. *Adv. Mater.* **2010**, *22* (39), 4359–4363.

(169) Meager, I.; Nikolka, M.; Schroeder, B. C.; Nielsen, C. B.; Planells, M.; Bronstein, H.; Rumer, J. W.; James, D. I.; Ashraf, R. S.; Sadhanala, A.; Hayoz, P.; Flores, J.-C.; Sirringhaus, H.; McCulloch, I. *Adv. Funct. Mater.* **2014**, *24* (45), 7109–7115.

(170) Shahid, M.; McCarthy-Ward, T.; Labram, J.; Rossbauer, S.; Domingo, E. B.; Watkins, S. E.; Stingelin, N.; Anthopoulos, T. D.; Heeney, M. *Chem. Sci.* **2012**, *3* (1), 181–185.

(171) Ashraf, R. S.; Meager, I.; Nikolka, M.; Kirkus, M.; Planells, M.; Schroeder, B. C.; Holliday, S.; Hurhangee, M.; Nielsen, C. B.; Sirringhaus, H.; McCulloch, I. *J. Am. Chem. Soc.* **2015**, *137* (3), 1314–1321.

(172) Chen, Z.; Lemke, H.; Albert-Seifried, S.; Caironi, M.; Nielsen, M. M.; Heeney, M.; Zhang, W.; McCulloch, I.; Sirringhaus, H. *Adv. Mater.* **2010**, *22* (21), 2371–2375.

(173) Venkateshvaran, D.; Nikolka, M.; Sadhanala, A.; Lemaur, V.; Zelazny, M.; Kepa, M.; Hurhangee, M.; Kronemeijer, A. J.; Pecunia, V.; Nasrallah, I.; Romanov, I.; Broch, K.; McCulloch, I.; Emin, D.; Olivier, Y.; Cornil, J.; Beljonne, D.; Sirringhaus, H. *Nature* **2014**, *515* (7527), 384–388.

(174) Jackson, N. E.; Savoie, B. M.; Kohlstedt, K. L.; Olvera de la Cruz, M.; Schatz, G. C.; Chen, L. X.; Ratner, M. A. *J. Am. Chem. Soc.* **2013**, *135* (28), 10475–10483.

(175) Yan, H.; Chen, Z.; Zheng, Y.; Newman, C.; Quinn, J. R.; Dotz, F.; Kastler, M.; Facchetti,

A. *Nature* **2009**, *457* (7230), 679–686.

(176) Anthony, J. E.; Facchetti, A.; Heeney, M.; Marder, S. R.; Zhan, X. *Adv. Mater.* **2010**, *22* (34), 3876–3892.

(177) Hwang, Y.-J.; Earmme, T.; Courtright, B. A. E.; Eberle, F. N.; Jenekhe, S. A. *J. Am. Chem. Soc.* **2015**, *137* (13), 4424–4434.

(178) Wang, J.; Ueda, M.; Higashihara, T. *J. Polym. Sci. Part A Polym. Chem.* **2014**, *52* (8), 1139–1148.

(179) Schuettfort, T.; Thomsen, L.; McNeill, C. R. *J. Am. Chem. Soc.* **2013**, *135* (3), 1092–1101.

(180) Back, J. Y.; Yu, H.; Song, I.; Kang, I.; Ahn, H.; Shin, T. J.; Kwon, S. K.; Oh, J. H.; Kim, Y. H. *Chem. Mater.* **2015**, *27* (5), 1732–1739.

(181) Li, J.; Qiao, X.; Xiong, Y.; Li, H.; Zhu, D. *Chem. Mater.* **2014**, *26* (19), 5782–5788.

(182) Lei, T.; Wang, J.-Y.; Pei, J. *Acc. Chem. Res.* **2014**, *47* (4), 1117–1126.

(183) Wang, C.; Qin, Y.; Sun, Y.; Guan, Y.-S.; Xu, W.; Zhu, D. *ACS Appl. Mater. Interfaces* **2015**, *7* (29), 15978–15987.

(184) Shin, J.; Park, G. E.; Lee, D. H.; Um, H. A.; Lee, T. W.; Cho, M. J.; Choi, D. H. *ACS Appl. Mater. Interfaces* **2015**, *7* (5), 3280–3288.

(185) Podzorov, V. *Nat Mater* **2013**, *12* (11), 947–948.

(186) Kanimozhi, C.; Yaacobi-Gross, N.; Chou, K. W.; Amassian, A.; Anthopoulos, T. D.; Patil, S. *J. Am. Chem. Soc.* **2012**, *134* (40), 16532–16535.

(187) Hendriks, K. H.; Heintges, G. H. L.; Gevaerts, V. S.; Wienk, M. M.; Janssen, R. A. J. *Angew. Chemie - Int. Ed.* **2013**, *52* (32), 8341–8344.

(188) Loser, S.; Bruns, C. J.; Miyauchi, H.; Ortiz, R. P.; Facchetti, A.; Stupp, S. I.; Marks, T. J. *J. Am. Chem. Soc* **2011**, *133*, 8142–8145.

(189) Fallon, K. J.; Wijeyasinghe, N.; Yaacobi-Gross, N.; Ashraf, R. S.; Freeman, D. M. E.; Palgrave, R. G.; Al-Hashimi, M.; Marks, T. J.; McCulloch, I.; Anthopoulos, T. D.; Bronstein, H. *Macromolecules* **2015**, *48* (15), 5148–5154.

(190) Fallon, K. J.; Wijeyasinghe, N.; Manley, E. F.; Dimitrov, S. D.; Yousaf, S. A.; Ashraf, R. S.; Duffy, W.; Guilbert, A. A. Y.; Freeman, D. M. E.; Al-Hashimi, M.; Nelson, J.; Durrant, J. R.; Chen, L. X.; McCulloch, I.; Marks, T. J.; Clarke, T. M.; Anthopoulos, T. D.; Bronstein, H. *Chem. Mater.* **2016**, *28* (22), 8366–8378.

(191) Steyrleuthner, R.; Di Pietro, R.; Collins, B. A.; Polzer, F.; Himmelberger, S.; Schubert, M.; Chen, Z.; Zhang, S.; Salleo, A.; Ade, H.; Facchetti, A.; Neher, D. *J. Am. Chem. Soc.* **2014**, *136* (11), 4245–4256.

(192) Kawabata, K.; Saito, M.; Osaka, I.; Takimiya, K. *J. Am. Chem. Soc.* **2016**, *138* (24), 7725–7732.

(193) Schroeder, B. C.; Chiu, Y.-C.; Gu, X.; Zhou, Y.; Xu, J.; Lopez, J.; Lu, C.; Toney, M. F.; Bao, Z. *Adv. Electron. Mater.* **2016**, *2* (7), 1600104.

(194) Chen, S.; Sun, B.; Hong, W.; Aziz, H.; Meng, Y.; Li, Y. *J. Mater. Chem. C* **2014**, *2* (12), 2183–2190.

(195) Krapcho, A. P.; Weimaster, J. F.; Eldridge, J. M.; Jahngen, E. G. E.; Lovey, A. J.; Stephens, W. P. *J. Org. Chem.* **1978**, *43* (1), 138–147.

(196) Krapcho, A. P.; Jahngen, E. G. E.; Lovey, A. J.; Short, F. W. *Tetrahedron Lett.* **1974**, *15* (13), 1091–1094.

(197) Krapcho, A. P.; Glynn, G. A.; Grenon, B. J. *Tetrahedron Lett.* **1967**, *8* (3), 215–217.

(198) Meijer, E. J.; Detcheverry, C.; Baesjou, P. J.; van Veenendaal, E.; de Leeuw, D. M.; Klapwijk, T. M. *J. Appl. Phys.* **2003**, *93* (8), 4831–4835.

(199) Swager, T. M.; Grubbs, R. H. *J. Am. Chem. Soc.* **1987**, *109* (3), 894–896.

(200) Heeney, M.; Bailey, C.; Genevicius, K.; Shkunov, M.; Sparrowe, D.; Tierney, S.; McCulloch, I. *J. Am. Chem. Soc.* **2005**, *127* (4), 1078–1079.

(201) Zhang, W.; Mao, Z.; Zheng, N.; Zou, J.; Wang, L.; Wei, C.; Huang, J.; Gao, D.; Yu, G. *J. Mater. Chem. C* **2016**, *4* (39), 9266–9275.

(202) Van Pruissen, G. W. P.; Brebels, J.; Hendriks, K. H.; Wienk, M. M.; Janssen, R. A. J. *Macromolecules* **2015**, *48* (8), 2435–2443.

(203) Ganguly, A.; Zhu, J.; Kelly, T. L. *J. Phys. Chem. C* **2017**, *121* (17), 9110–9119.

(204) Voortman, T. P.; Bartesaghi, D.; Koster, L. J. A.; Chiechi, R. C. *Macromolecules* **2015**, *48* (19), 7007–7014.

(205) Romero-Servin, S.; Lozano-Hernández, L.-A.; Maldonado, J.-L.; Carriles, R.; Ramos-Ortíz, G.; Pérez-Gutiérrez, E.; Scherf, U.; Zolotukhin, G. M. *Polymers* . 2016.

(206) Aparicio-Ixta, L.; Ramos-Ortiz, G.; Pichardo-Molina, J. L.; Maldonado, J. L.; Rodriguez, M.; Tellez-Lopez, V. M.; Martinez-Fong, D.; Zolotukhin, M. G.; Fomine, S.; Meneses-Nava, M. A.; Barbosa-Garcia, O. *Nanoscale* **2012**, *4* (24), 7751–7759.

(207) Voortman, T. P.; de Gier, H. D.; Havenith, R. W. A.; Chiechi, R. C. *J. Mater. Chem. C* **2014**, *2* (17), 3407–3415.

(208) Li, X.; Zhang, X.; Li, W.; Wang, Y.; Liu, T.; Zhang, B.; Yang, W. *J. Mater. Chem.* **2011**, *21* (11), 3916–3924.

(209) Maeda, T.; Tsukamoto, T.; Seto, A.; Yagi, S.; Nakazumi, H. *Macromol. Chem. Phys.* **2012**, *213* (24), 2590–2597.

(210) Kayser, L. V; Hartigan, E. M.; Arndtsen, B. A. *ACS Sustain. Chem. Eng.* **2016**, *4* (12), 6263–6267.

(211) Barik, S.; Valiyaveettil, S. *J. Polym. Sci. Part A Polym. Chem.* **2014**, *52* (15), 2217–2227.

(212) Preis, E.; Scherf, U. *Macromol. Rapid Commun.* **2006**, *27* (14), 1105–1109.

(213) Wang, H.; Helgeson, R.; Ma, B.; Wudl, F. *J. Org. Chem.* **2000**, *65* (18), 5862–5867.

(214) Fang, Q.; Yamamoto, T. *J. Polym. Sci. Part A Polym. Chem.* **2004**, *42* (11), 2686–2697.

(215) McGovern, P. E.; Michel, R. H. *Anal. Chem.* **1985**, *57* (14), 1514A–1522A.

(216) Friedländer, P. *Berichte der Dtsch. Chem. Gesellschaft* **1909**, *42* (1), 765–770.

(217) Schatz, P. F. *J. Chem. Educ.* **2001**, *78* (11), 1442.

(218) Wolk, J. L.; Frimer, A. A. *Molecules* **2010**, *15* (8), 5561–5580.

(219) Cooksey, C. J. *Molecules* **2001**, *6* (9), 736–769.

(220) Imming, P.; Imhof, I.; Zentgraf, M. *Synth. Commun.* **2001**, *31* (23), 3721–3727.

(221) National Renewable Energy Laboratory (NREL) Best Research-Cell Efficiencies Chart https://www.nrel.gov/pv/assets/images/efficiency-chart.png (accessed Jun 25, 2017).

(222) Shockley, W.; Queisser, H. J. *J. Appl. Phys.* **1961**, *32* (3), 510–519.

(223) Reference Solar Spectral Irradiance: ASTM G-173 http://rredc.nrel.gov/solar/spectra/am1.5/astmg173/astmg173.html (accessed Jun 13, 2017).

(224) Byrnes, S. J. The Shockley-Queisser limit http://sjbyrnes.com/sq.html (accessed Nov 24, 2016).

(225) Hanna, M. C.; Nozik, A. J. *J. Appl. Phys.* **2006**, *100* (7), 74510.

(226) Scholes, G. D. *J. Phys. Chem. A* **2015**, *119* (51), 12699–12705.

(227) Wang, R.; Zhang, C.; Zhang, B.; Liu, Y.; Wang, X.; Xiao, M. **2015**, *6*, 8602.

(228) Monahan, N. R.; Sun, D.; Tamura, H.; Williams, K. W.; Xu, B.; Zhong, Y.; Kumar, B.; Nuckolls, C.; Harutyunyan, A. R.; Chen, G.; Dai, H.-L.; Beljonne, D.; Rao, Y.; ZhuX.-Y. *Nat Chem* **2017**, *9* (4), 341–346.

(229) Smith, M. B.; Michl, J. *Chem. Rev.* **2010**, *110* (11), 6891–6936.

(230) Conte, M.; MacKay, W. W. *An Introduction to the Physics of Particle Accelerators (2nd Edition)*; World Scientific Publishing Co Inc, 2008.

(231) Tayebjee, M. J. Y.; Sanders, S. N.; Kumarasamy, E.; Campos, L. M.; Sfeir, M. Y.; McCamey, D. R. *Nat Phys* **2017**, *13* (2), 182–188.

(232) Sanders, S. N.; Kumarasamy, E.; Pun, A. B.; Trinh, M. T.; Choi, B.; Xia, J.; Taffet, E. J.; Low, J. Z.; Miller, J. R.; Roy, X.; Zhu, X.-Y.; Steigerwald, M. L.; Sfeir, M. Y.; Campos, L. M. *J. Am. Chem. Soc.* **2015**, *137* (28), 8965–8972.

(233) Sanders, S. N.; Kumarasamy, E.; Pun, A. B.; Steigerwald, M. L.; Sfeir, M. Y.; Campos, L. M. *Chem* **2016**, *1* (3), 505–511.

(234) Sanders, S. N.; Kumarasamy, E.; Pun, A. B.; Appavoo, K.; Steigerwald, M. L.; Campos, L. M.; Sfeir, M. Y. *J. Am. Chem. Soc.* **2016**, *138* (23), 7289–7297.

(235) Zimmerman, P. M.; Zhang, Z.; Musgrave, C. B. *Nat Chem* **2010**, *2* (8), 648–652.

(236) Zimmerman, P. M.; Bell, F.; Casanova, D.; Head-Gordon, M. *J. Am. Chem. Soc.* **2011**, *133* (49), 19944–19952.

(237) Tabachnyk, M.; Karani, A. H.; Broch, K.; Pazos-Outón, L. M.; Xiao, J.; Jellicoe, T. C.; Novák, J.; Harkin, D.; Pearson, A. J.; Rao, A.; Greenham, N. C.; Böhm, M. L.; Friend, R. H. *APL Mater.* **2016**, *4* (11), 116112.

(238) Wilson, M. W. B.; Rao, A.; Johnson, K.; Gélinas, S.; di Pietro, R.; Clark, J.; Friend, R. H. *J. Am. Chem. Soc.* **2013**, *135* (44), 16680–16688.

(239) Korovina, N. V; Das, S.; Nett, Z.; Feng, X.; Joy, J.; Haiges, R.; Krylov, A. I.; Bradforth, S. E.; Thompson, M. E. *J. Am. Chem. Soc.* **2016**, *138* (2), 617–627.

(240) Fujihashi, Y.; Chen, L.; Ishizaki, A.; Wang, J.; Zhao, Y. *J. Chem. Phys.* **2017**, *146* (4), 44101.

(241) Musser, A. J.; Maiuri, M.; Brida, D.; Cerullo, G.; Friend, R. H.; Clark, J. *J. Am. Chem. Soc.* **2015**, *137* (15), 5130–5139.

(242) Ullah, M.; Yambem, S. D.; Moore, E. G.; Namdas, E. B.; Pandey, A. K. *Adv. Electron.*

*Mater.* **2015**, *1* (12), 1500229–n/a.

(243) Ma, L.; Zhang, K.; Kloc, C.; Sun, H.; Michel-Beyerle, M. E.; Gurzadyan, G. G. *Phys. Chem. Chem. Phys.* **2012**, *14* (23), 8307–8312.

(244) Wen, X.; Yu, P.; Yuan, C.-T.; Ma, X.; Tang, J. *J. Phys. Chem. C* **2013**, *117* (34), 17741–17747.

(245) Nichols, V. M.; Rodriguez, M. T.; Piland, G. B.; Tham, F.; Nesterov, V. N.; Youngblood, W. J.; Bardeen, C. J. *J. Phys. Chem. C* **2013**, *117* (33), 16802–16810.

(246) Schrauben, J. N.; Zhao, Y.; Mercado, C.; Dron, P. I.; Ryerson, J. L.; Michl, J.; Zhu, K.; Johnson, J. C. *ACS Appl. Mater. Interfaces* **2015**, *7* (4), 2286–2293.

(247) Clar, E. Rondia, D., Cooke, M., Haroz, R. K., Eds.; Springer Netherlands: Dordrecht, 1983; pp 49–58.

(248) Solà, M. *Front. Chem.* **2013**, *1*, 22.

(249) Clar, E.; Zander, M. *J. Chem. Soc.* **1958**, No. 0, 1861–1865.

(250) Poater, J.; Bofill, J. M.; Alemany, P.; Solà, M. *J. Phys. Chem. A* **2005**, *109* (47), 10629–10632.

(251) Abe, M. *Chem. Rev.* **2013**, *113* (9), 7011–7088.

(252) Hückel, E. *Zeitschrift für Phys.* **1931**, *70* (3), 204–286.

(253) Hückel, E. *Zeitschrift für Phys.* **1931**, *72* (5), 310–337.

(254) Hückel, E. *Zeitschrift für Phys.* **1932**, *76* (9), 628–648.

(255) Roberts, J. D.; Streitwieser, A.; Regan, C. M. *J. Am. Chem. Soc.* **1952**, *74* (18), 4579–4582.

(256) Baird, N. C. *J. Am. Chem. Soc.* **1972**, *94* (14), 4941–4948.

(257) Möllerstedt, H.; Piqueras, M. C.; Crespo, R.; Ottosson, H. *J. Am. Chem. Soc.* **2004**, *126* (43), 13938–13939.

(258) Smith, M. B.; Michl, J. *Annu. Rev. Phys. Chem.* **2013**, *64* (1), 361–386.

(259) Mou, W.; Hattori, S.; Rajak, P.; Shimojo, F.; Nakano, A. *Appl. Phys. Lett.* **2013**, *102* (17), 173301.

(260) Wolff, L. *Justus Liebigs Ann. Chem.* **1912**, *394* (1), 86–108.

(261) Hutchins, R. O.; Milewski, C. A.; Maryanoff, B. E. *J. Am. Chem. Soc.* **1973**, *95* (11), 3662–3668.

(262) Ellis, G. P.; Romney-Alexander, T. M. *Chem. Rev.* **1987**, *87* (4), 779–794.

(263) Sung, Y. M.; Yoon, M.-C.; Lim, J. M.; Rath, H.; Naoda, K.; Osuka, A.; Kim, D. *Nat Chem* **2015**, *7* (5), 418–422.

(264) Chen, Z.; Wannere, C. S.; Corminboeuf, C.; Puchta, R.; Schleyer, P. von R. *Chem. Rev.* **2005**, *105* (10), 3842–3888.

(265) Schleyer, P. von R.; Maerker, C.; Dransfeld, A.; Jiao, H.; Hommes, N. J. R. van E. *J. Am. Chem. Soc.* **1996**, *118* (26), 6317–6318.

(266) Sun, H.; An, K.; Zhu, J. *Chem. – An Asian J.* **2016**, *11* (2), 234–240.

(267) Fallah-Bagher-Shaidaei, H.; Wannere, C. S.; Corminboeuf, C.; Puchta, R.; Schleyer, P. v. R. *Org. Lett.* **2006**, *8* (5), 863–866.

(268) Sucharda, E. *Berichte der Dtsch. Chem. Gesellschaft (A B Ser.* **1925**, *58* (8), 1727–1729.

(269) Sucharda, E. *Berichte der Dtsch. Chem. Gesellschaft (A B Ser.* **1925**, *58* (8), 1724–1727.

(270) Willette, R. E. *J. Chem. Soc.* **1965**, 5874–5876.

(271) Bozzini, T.; Botta, G.; Delfino, M.; Onofri, S.; Saladino, R.; Amatore, D.; Sgarbanti, R.; Nencioni, L.; Palamara, A. T. *Bioorg. Med. Chem.* **2013**, *21* (24), 7699–7708.

(272) Chang, H.-C.; Shiozaki, T.; Kamata, A.; Kishida, K.; Ohmori, T.; Kiriya, D.; Yamauchi, T.; Furukawa, H.; Kitagawa, S. *J. Mater. Chem.* **2007**, *17* (39), 4136–4138.

(273) Takuya, H.; Koji, K.; Shinji, I. Dithiazole compounds, matrix metalloprotease inhibitors and external preparations for the skin. EP1422224, 2004.

(274) Katritzky, A. R.; Xu, Y.-J.; Vakulenko, A. V; Wilcox, A. L.; Bley, K. R. *J. Org. Chem.* **2003**, *68* (23), 9100–9104.

(275) Skiles, J. W.; Cava, M. P. *J. Org. Chem.* **1979**, *44* (3), 409–412.

(276) Yao, M.-L.; Reddy, M. S.; Yong, L.; Walfish, I.; Blevins, D. W.; Kabalka, G. W. *Org. Lett.* **2010**, *12* (4), 700–703.

(277) Rumer, J. W.; Dai, S.-Y.; Levick, M.; Biniek, L.; Procter, D. J.; McCulloch, I. *J. Polym. Sci. Part A Polym. Chem.* **2013**, *51* (6), 1285–1291.

*Would you tell me, please,*
*which way I ought to go from here?*

*– That depends a good deal*
*on where you want to get to.*

*I don't much care where...*

*– Then it doesn't much matter which way you go.*

. *..So long as I get somewhere.*

*– Oh, you're sure to do that,*
*if only you walk long enough.*

# VIII

*Appendixes*